Study of Scattering and Trapping of Water Waves in Two-layer Fluids for Various Types of Structure Configurations and Sea-beds

by

Koushik Kanti Barman

DEPARTMENT OF MATHEMATICS
INDIAN INSTITUTE OF TECHNOLOGY GUWAHATI
GUWAHATI-781039, INDIA

April, 2022

TH-2746_176123008

TH-2746_176123008

Study of Scattering and Trapping of Water Waves in Two-layer Fluids for Various Types of Structure Configurations and Sea-beds

A Thesis submitted
in partial fulfillment of the requirements
for the degree of

DOCTOR OF PHILOSOPHY

by

Koushik Kanti Barman

(Roll No: 176123008)

DEPARTMENT OF MATHEMATICS
INDIAN INSTITUTE OF TECHNOLOGY
GUWAHATI
GUWAHATI-781039, INDIA

April, 2022

TH-2746_176123008

TH-2746_176123008

Dedicated to

my mother Smt. Bina Barman

and

my father Shri Kamal Kanti Barman

"The last dream I had was about my late parents smiling –
giving me a limitless contentment that they are resting in peace"

TH-2746_176123008

TH-2746_176123008

Declaration

I do hereby declare that this thesis entitled **Study of Scattering and Trapping of Water Waves in Two-layer Fluids for Various Types of Structure Configurations and Sea-beds** is a presentation of my original research work done under the supervision of **Dr. Swaroop Nandan Bora**, Professor, Department of Mathematics, Indian Institute of Technology Guwahati for the award of the degree of Doctor of Philosophy and this work has not been submitted elsewhere for a degree.

April, 2022

Koushik Kanti Barman
Roll No. 176123008
Department of Mathematics
Indian Institute of Technology Guwahati

TH-2746_176123008

TH-2746_176123008

Certificate

It is to certify that the work contained in this thesis entitled **Study of Scattering and Trapping of Water Waves in Two-layer Fluids for Various Types of Structure Configurations and Sea-beds** has been carried out by **Koushik Kanti Barman**, a student in the Department of Mathematics, Indian Institute of Technology Guwahati, under my supervision for the award of the degree of Doctor of Philosophy and this work has not been submitted elsewhere for a degree.

April, 2022

Dr. Swaroop Nandan Bora
Professor
Department of Mathematics
Indian Institute of Technology Guwahati

TH-2746_176123008

TH-2746_176123008

Acknowledgements

Writing a dissertation is a long and arduous procedure, and cannot be completed on one's own. I faced many obstacles and challenges on a personal ground that would have hampered my academics, but a group of people behind me made me feel at ease and helped me realize my dream. And they definitely need to be acknowledged! I want to express my gratitude to everyone who has helped, mentored, and supported me along the way.

First and foremost, I would like to thank God for the blessings, strength, and ability to undertake and complete my Ph.D. thesis satisfactorily.

Secondly, I offer my sincere thanks and gratitude to my supervisor Prof. Swaroop Nandan Bora for the constant support and valuable advice since the beginning of this journey. I was lucky enough to be chosen as a research scholar by him. I was given great intellectual autonomy and was left to discover my path without interference. Without his extensive knowledge, persistent encouragement, and support, this work would not have been feasible.

I want to express my gratitude to my Doctoral Committee members Prof. Durga Chandra Dalal, Prof. Natesan Srinivasan, and Prof. Rajen Kumar Sinha for their insightful comments and suggestions during this entire journey. My sincere gratitude is also due to all other faculty members of the department. I would also like to thank the office staff of our department.

I want to thank my seniors, Dr. Santu Das, Dr. Sunanda Saha, Dr. Somnath Ghosh, Dr. Sunil Das, Dr. Ayan Chanda, Dr. Rakesh Jana, Dr. Koyel Chakravarty, Dr. Abhijit Sarkar, Dr. Swapnendu Panda, Dr. Madhusudhan Bera, Dr. Devanand Jaiswal, Dr. Mriganka Biswas and Dr. Shamik Das. I also thank my colleagues and friends, Nilay Da, Mrityunjoy, Bibhuti, Ravi, Harpreet, Palak, Molecule, Shyam, Avijit, Shilpi, Shiva, Matap, for their generosity and support. I have been fortunate enough to work with you all over the years.

I owe my parents Late Kamal Kanti Barman (Baba) and Late Bina Barman (Maa), a debt of gratitude for providing me with the necessary foundation of life and believing in my abilities, and allowing me to achieve my goal. Maa! Baba! 'Dabbu loves you a lot.' I would also like to thank my sister Mrs. Nirupama Barman and my brother-in-law Mr. Suman Saha for the love and support.

"There is a 'He' in every 'She' ", an adage once said. I would want to express my gratitude to Krisangi Saikia, who has been incredibly supportive of me throughout this entire process and has made several sacrifices to assist me in reaching this stage. She gave me the necessary breaks from philosophy and the determination to finish my degree as quickly as possible. Didi, Jiju, Krisangi, and my parents deserve special recognition for

TH-2746_176123008

their unwavering support and encouragement. I doubt I would be in this position now if I did not have such a strong team behind me.

Last but not the least, I would want to express my gratitude to my relatives, particularly Ranidi, Rajkumarda, my childhood buddy Subhajit, and Mainak, for their spiritual support during the composition of my thesis and my life in general. I am also grateful to the Ministry of Education (earlier known as the Ministry of Human Resource Development) for the financial assistance. I would like to thank IIT Guwahati for providing such a positive atmosphere where one can feel at ease and work diligently.

April, 2022 **Koushik Kanti Barman**

TH-2746_176123008

Abstract

The notion of porous media is being increasingly used in a growing number of fields in applied science and engineering. Filtration, acoustics, geomechanics, soil mechanics, rock mechanics, petroleum engineering, construction engineering, hydrogeology, geophysics, biology, biophysics, material science, and some other disciplines are among them. Porous structures can produce a calm zone by reducing the impact of waves on and around harbours, ports, inlets, rigid breakwaters, and other structures, and have therefore become an important research area. Porous structures have numerous applications in coastal areas in general, and in shoreline and harbour regions in particular, including (i) its use as breakwaters to protect harbours, inlets, and beaches from harsh wave impact in order to create a quiet water region for mooring and/or manoeuvring vessels, (ii) providing shelter and safety for various operations, such as cargo handling operations at the harbour, and (iii) as dissipating sea-walls near harbours to attenuate wave energy. These structures are very flexible, reusable, and can develop low-cost wave attenuation and protection systems. Porous bodies are generally used as coastal and offshore structures for various applications. Examples are breakwater, barrier, semi-submersibles, and wave power energy conversion systems. The main objective of this thesis is to investigate the wave reflection and transmission, forces, wave run-up, and hydrodynamic coefficients due to the presence of two-dimensional and one-dimensional porous structures in water of various bottom profiles in a two-layer fluid within the framework of linear water wave theory. A reasonable emphasis has been laid on wave attenuation so as to propose reasonably appropriate structures for this purpose.

This study considers two layers of an immiscible fluid to be incompressible, homogeneous and inviscid undergoing an irrotational motion. In our first work, we consider wave interaction with a porous structure over a step-type rigid bottom. We consider two cases: (i) a single-chamber porous structure, (ii) a two-chamber structure with different porosity

TH-2746_176123008

and friction. We also discuss the porous bottom as a particular case. In continuation, we consider a caisson type two-block structure over a porous bottom in our second work. This case investigates scattering phenomenon as well as trapping. Further, a perforated wall is considered in front of the structure as a particular case. The impact of bottom porosity is also analysed. It leads to the finding that a composite porous structure produces better wave dissipation. Next, we attempt a scattering problem in an ocean due to a caisson type two-chamber and multi-chamber structures with a perforated front wall over an elastic bottom in our third and fourth works. The change of bottom profile, as well as the scattering phenomenon are studied elaborately. The subsequent study explores the problem related to the scattering of linear waves with a composite structure consisting of multiple chambers over the elastic bottom. It establishes the significant role of the porous structure as well as of the elastic bottom in reducing the waveload. We mainly focus on scattering coefficients and hydrodynamic coefficients such as waveload, elevation, etc. The variation of the bottom profile is handled by profoundly analysing the dispersion relations as well as its effect in hydrodynamic coefficients. This kind of study also leads us to find the optimum width with suitable structural configuration, which produces a more efficient porous structure possessing both reflective and dissipative characteristics. By an appropriate selection of structural height, width, porosity and porous impedance parameter, one can find (i) the maximum wave reflection by the structure, (ii) the maximum dissipation of energy by the porous body, and (iii) the minimum value of the waveload on the end sea-wall. We also find that a composite porous structure is more efficient in producing higher reflection and lower waveload compared to a simple kind of structure.

In the later part of the thesis, scattering problems pertaining to thin structures are taken up, and the associated hydrodynamic coefficients are evaluated. We basically analyse the dispersion relation and scattering phenomenon. In our fifth work, we begin by considering a thin poro-elastic barrier over the porous bottom in front of a partially reflecting sea wall. We adopt the least square technique for calculating the unknown coefficients. The dead water analogue upon porous bottom is also investigated. Appropriate edge conditions are selected for attaining suitable reflective and dissipative characteristics. Consequently, we consider a porous wavemaker over a porous bottom in the sixth work. We analyse the scattering as well as radiation due to the motion(oscillation) of the porous wavemaker. Least square technique is used to find reflection, transmission coefficients and added mass, damping coefficient. The hydrodynamic coefficients, namely, added mass and damping coefficients, are analyzed, and, it is found that the porosity of the barrier is crucial for suitable energy dissipation. In the seventh work, the impact of water wave on a moored floating elastic plate is analyzed in the presence of a thick porous structure as a breakwater. Matched eigenfunction technique is used to obtain the solution, and consequently, reflection by the porous structure, plate deflection, bending moment etc. are analyzed. Various types of edge conditions are analyzed and this study

suggests that clamped-free and clamped moored conditions are appropriate choices for the structure, which presents a porous structure which is more efficient in possessing both reflective and dissipative characteristics. The structural elevation is examined for different elastic parameters of the structure, and minimum structural elevation can be achieved by the highly porous structures with higher flexural rigidity.

In all cases, the results are validated by comparing with available results as far as possible, and these point towards the effectiveness of the present model for each case in investigating such ocean engineering problems.

TH-2746_176123008

TH-2746_176123008

Contents

TH-2746_176123008

TH-2746_176123008

TH-2746_176123008

TH-2746_176123008

List of Figures

TH-2746_176123008

TH-2746_176123008

TH-2746_176123008

TH-2746_176123008

TH-2746_176123008

TH-2746_176123008

TH-2746_176123008

TH-2746_176123008

TH-2746_176123008

भारतीय प्रौद्योगिकी संस्थान गुवाहाटी
Indian Institute of Technology Guwahati

List of Tables

TH-2746_176123008

TH-2746_176123008

CHAPTER 1

Introduction

1.1 Preamble

A fluid is a substance that deforms constantly under shear stress, or, to put it in another way, one that does not have a specific shape. Fluid mechanics deals with fluids in motion and at rest, as well as the effect of the fluid on the boundaries, which may be either solid surfaces or fluid-fluid interfaces. When it comes to the various uses of fluids in the world of science and technology ranging from regulating the passage of air through the lungs to pumping water through a pipeline, there is no limit to the variety of fluid applications. Our environment consists of mostly fluids. Most fundamental concepts of conservation of mass, energy, and momentum of applied mechanics are utilised to study fluid behaviour. Fluid properties such as density, volume, temperature, and pressure are all influenced by the one key assumption termed as *Continuum Hypothesis*. It is considered that fluids are made up of continuous matter, which allows fluid features to be defined in infinitesimally small areas and to change continuously from one point to the next. The fluid velocity matches the solid boundary velocity when it reaches a solid barrier. The outermost molecules of the fluid may be seen as adhering to the surfaces it passes across. Mathematically, when a boundary value problem is prescribed with a known solution at certain points, then that condition is called *Dirichlet boundary condition*. Matching the boundary velocity across a rigid barrier in fluid flow problem leads to *Neumann boundary condition*. The term *no-slip condition* is used to describe such no flow boundary condition in fluid mechanics. As far as fluid mechanics is concerned, there are two methods of investigation that may be used. An initial approach known as the *Lagrangian type* involves the tracking of the movement of a single fluid particle from an initial location. It is also possible to specify

TH-2746_176123008

the mechanics in an *Eulerian way*, which uses a fixed spatial coordinate system and looks at fluid properties as time-dependent functions of flow velocity. Although the Lagrangian specification is useful in certain cases, but it may take some time to analyse and does not instantly reveal the spatial gradients of velocity within the fluid. Therefore, Eulerian specifications are often preferred. *Streamlines*, *pathlines*, and *streaklines* are three common curves used in the Eulerian description of fluid motion. Using these curves as a starting point for monitoring seed particles or dye filaments in experiments is a common technique in fluid dynamics research. At all times, a *streamline*'s curve is tangent to the fluid velocity of the flow field. It is known as a *streakline* when the path of all fluid particles passing through a given area is traced out. A *pathline* is the path that a particle takes while it moves. One may find path lines and streaklines at the same spot.

When there is a steady stream, *viscosity* is the fluid attribute that makes a fluid more resistant to shear forces. Theoretical investigations of fluid mechanics often begin with the concept of an *ideal fluid*, where two contacting layers experience no *tangential forces* (i.e., shearing stresses) but only *normal forces* (i.e., pressure). It implies that there is no internal resistance in an ideal fluid. *Real fluids*, on the other hand, are susceptible to both tangential and normal stresses in their inner layers. Tangential forces explain the existence of viscosity in a fluid. Various characteristics of a fluid flow allow for a plethora of classifications. When pressure and temperature fluctuate, the density of a fluid changes substantially, but when pressure and temperature do not change, the density of a fluid remains the same. As an example, the *Mach number* (the ratio of an object's speed to the local speed of sound) is employed in aerodynamics as a measure of compressible and incompressible flows. Negligible viscosity flow is referred to as a *non-viscous* or *inviscid* flow of the fluid, else the fluid is termed as *viscous* which describes a fluid having resistance to deform. While *unsteady flow* is characterised by a change in the properties of the fluid over time, a *steady flow* is the one in which the fluid properties remain constant over time. Recirculation, whirling, and unpredictability in the fluid are all factors that contribute to the formation of *turbulence*. *Laminar fluid flow* occurs when there is little or no turbulence in the fluid stream. Fluid is categorised into two groups based on the mathematical connection between stress and strain: *Newtonian fluids* (water, air, etc.) and *non-Newtonian fluids* (blood, polymer, etc.). There is a very close linear connection between stress (internal force) and strain (normalised measure of deformation) for a Newtonian fluid. For a non-Newtonian fluid, stress and strain are not related to each other. *Subsonic*, *transonic*, *supersonic*, and *hypersonic* are all types of fluid flow based on the flow velocity (*Mach number*). If curl $\vec{v} = 0$ in a flow field with a velocity vector $\vec{v}$, the flow is called *irrotational*; otherwise, it is called *rotational*. A scalar function must be present in order that a flow is irrotational. It is called the velocity potential usually with the notation Φ. Laplacian of the velocity potential must be zero if the flow is both irrotational and incompressible, resulting in an equation of continuity for a potential flow.

TH-2746_176123008

The water wave theory of Airy was developed under the assumption of incompressible fluid with inviscid and irrotational flow. A similar assumption is being followed in our research which leads to the ideal fluid by definition. However, water in real life is not an ideal fluid. Moreover, practically water is an incompressible fluid with negligible viscosity. In this context, water can be assumed as an ideal fluid.

In physics, mathematics and related fields, a wave is always in disruption (change from equilibrium position) of one or more fields in which values regularly bounce around a stable equilibrium (resting) value. Waves are of two types such as *mechanical* and *electromagnetic*. In a mechanical wave, the stress and strain fields vary around a point of mechanical equilibrium (water wave, sound wave, etc.). In an electromagnetic wave, the electric and magnetic fields are alternating. Electromagnetic waves (light) are made up of fluctuating electric and magnetic fields that travel across space. Electromagnetic waveforms include radio waves, infra-red and visible light, ultraviolet and gamma rays, as well as X-rays and other diagnostic imaging modalities. When we throw a stone into a pond, we can see ripples which is a primary example of water waves in action. Examples of a few more such incidence include ripples on a lake's surface caused by the motion of wind, ripples due to movement of ships in the ocean etc. These waves oscillate at very small frequencies. There are, however, certain exceptions to the rule. Amplitude of waves is not always small, but it may still be perceptible in certain situations. In addition to tsunamis and tidal waves, other high-energy waves include rogue waves.

Researchers have lately proposed a variety of porous breakwaters for the protection of coastal regions and developmental sites. Reduced wave stresses and run-up may be achieved by porous structures. Additionally, these structures are often used to create floating airports, bridges, piers, docks, and wave power conversion systems, among other things. The use of porous structures in the construction of coastal and offshore structures has been found to be more suited. Structures in a sea must resist a variety of atmospheric conditions. As a consequence, hydrodynamic research has focused on building optimal systems in order to find a way to minimise significant hydrodynamic ramifications. When a problem with water wave mechanics arises, it is common to look at water in a region that is bounded by a free surface (in touch with the atmosphere), a rigid surface, a porous surface, or any other media. In addition, for the sake of convenience, we may consider virtual boundaries. The wave interaction with a large floating ice sheet, which may be considered as a massive elastic plate following the Euler-Bernoulli beam equation, is of equal importance in the polar marginal ice zone. A hydroelastic model is necessary in many circumstances when structures are believed to be flexible. Many hydrodynamic factors demand investigation. Several of these structures have advantages over conventional rigid structures because they are recyclable, ecologically friendly, and cost-effective. There has been a reasonable advancement in the knowledge of the dynamics of ocean surface waves and their influence on ocean structures during the past several decades. Different

TH-2746_176123008

physical conditions lead to different solutions. Laplace's equation, Helmholtz or modified Helmholtz equations are mainly used to describe wave motion in water with Dirichlet type (no derivative) or Neumann type (only derivative) or mixture of derivative and non-derivative boundary conditions. Analysis of Fourier transform, complex function theory, Green's function technique, boundary integral equation method, the least square approximation method, the wide spacing approximation method, and integral transform method can all be utilized as the solution procedures. The same theory holds for the stationary phase as well. In addition, it may be used for porous regions.

A long history of water waves can be found in Craik [23], who wrote extensively on water wave theory. A hypothesis of water waves was initially proposed by Sir Isaac Newton in the 17th century. He suggested a dubious analogy with oscillations in a U-tube and properly deduced that the frequency of deep sea waves was related to the square root of the "breadth of the wave" in Book II, Prop. XLV of *Principia* (1687). Wilhelm-Jacobs Gravesande (1721) and Charles Bossut (1786) also endorsed Newton's hypothesis later. Then, Joseph Louis Lagrange (1781, 1786) came up with the linearized governing equations for small-amplitude waves and found the solution to long plane waves in shallow water. In '*Mechanique Analitique*' (1788), precisely the same theory was established. Lagrange (1786) said that, for shallow water waves, "the speed of propagation of waves will be that which a heavy body would acquire in falling from ... half the height of the water in canal", i.e., $(gh)^{1/2}$, where g represents gravitational acceleration and h denotes liquid depth. Only a handful of publications prior to 1800 dealt with wave motion. MḞlaugergues (1793) and Francois de la Coudraye (1796) created exceptional works, which were subsequently summarised by Weber and Weber (1825). The first accurate nonlinear solution for waves with limited amplitude in deep sea was described by Franz Joseph von Gerstner (1802). Because the motion was not irrotational, the Gerstner wave solution has long been disregarded; even now, it is considered a curiosity rather than a conclusion of practical significance because of this. W. J. Macquorn Rankine (1863) was the one who discovered it on his own. In December, 1813, the French *Academie des Sciences* launched a mathematical prize competition on the propagation of surface waves in fluids of infinite depths. It was in July 1815 when Augustin-Louis Cauchy filed his submission and in August, Simeon D. Poisson, one of the judges, lodged a memoir of his own to document his independent work. The prize was awarded to Cauchy in 1816. Poisson's narrative was published in 1818, while Cauchy's work was finally published in 1827, with 188 more pages of annotations. Horace Lamb presented the Cauchy-Poisson analysis, but confined it to two-dimensional disturbances in "Hydrodynamics" (1895). This book was originally written in 1908 as a short, unfinished, and tiny print book, but he revised it in 1916 for a more comprehensive treatment. The Cauchy-Poisson analysis is currently recognised as an important milestone in the theory of initial value problems.

Ernst Heinrich Weber and Wilhelm Eduard Weber wrote a radically distinct study

TH-2746_176123008

on waves: *Wellenlehre auf Experimente gegrundet* (1825). A collection of samples and remarks from Webers' meticulous laboratory studies on periodic wavetrains in a channel are included in this book. Sir John Robinson and John Scott Russell [86] published a ground-breaking paper in 1837 on the ocean, rivers, and canals wave properties. Nonlinear solitary waves were discovered in these investigations. His newly discovered solitary wave, tides and bores; oscillatory waves, or periodic wave trains; and capillary and corpuscular sounds moving through water were among the four kinds of waves they had identified. A linear shallow water wave with a lengthy period of time and a short depth and breadth was the focus of the demonstration of George Green [38] in the following year. When Philip Kelland [47] studied long waves of small amplitude in 1840, he found that the wave speed was correctly calculated. In 1847, Samuel Earnshaw [35] began using discontinuous expressions to depict a single wave. There has been a dearth of success in finding generic solutions to hydrodynamic equations, and the necessity to focus on specific movements based on experimental assumptions was emphasised by him. Toward the end of the year, a nonlinear theory known as Stokes' theory by George Gabriel Stokes [96] was produced. Bernard Rayleigh [83] discovered in 1876 that Earnshaw's solution was not for irrotational flow, and he also found the correct approximate solution. In 1841, George Biddell Airy's lengthy and famous essay "Tides and Waves" was published in the *Encyclopaedia Metropolitana*. As a mathematician and astronomer, Airy's scientific reputation was already well-known. Water wave theory has long regarded Airy's essay as a significant contribution.

Laplace's equation is used as the governing equation for boundary value problems in a range of maritime engineering applications. The Helmholtz equation, or a modified version of it, also regulates several processes. The available boundary conditions and matching conditions are used to solve the problem depending on its nature. It is, therefore, possible to calculate and analyse several critical characteristics of the relevant quantities such as forces, moments and wave run-up and hydrodynamic coefficients. The linearized water wave theory equations for constant depth are described briefly in the next section.

1.2 Relevant equations and conditions

There are a number of equations that will be discussed in this section. These definitions and descriptions of water waves are helpful in learning the fundamentals of water wave theory. Different boundary conditions may be obtained and explained using linearized water wave theory. Water wave mechanics issues are often described using linear wave theory, which deals with small-amplitude waves. Homogeneous, incompressible and non-viscous fluids are assumed to be in motion. Sea-bed is usually assumed to be flat and impermeable. Length and height of waves, as well as the water depth across which they

TH-2746_176123008

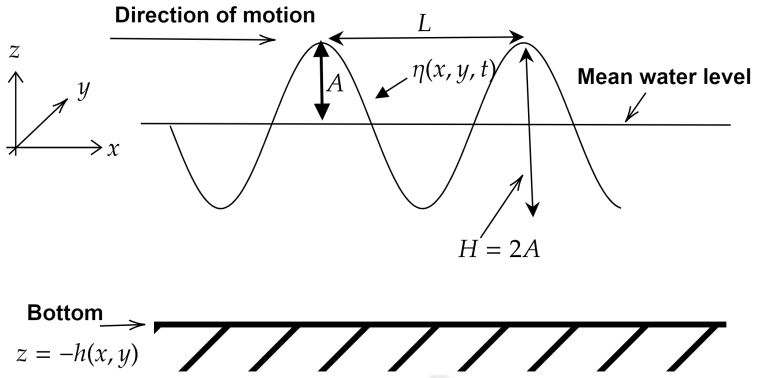

Figure 1.1: Schematic diagram of a typical wave propagation

travel, are significant elements to be considered. Theoretically, all other parameters, such as wave-induced water velocities and accelerations, may be calculated using these values. Two-dimensional coordinates in x and y are taken into consideration in Figure 1.1. On a surface wave, a *crest* is a point where the wave displacement is at its greatest. The smallest or lowest point in a wave cycle is called a *trough*. It is the polar opposite of a crest. The horizontal distance between two consecutive wave crests is the *wavelength* which is represented as L. Following is a list of the notations: h: water depth which is measured from the mean sea level to the sea-bed, $\eta(x,t)$: vertical displacement above the mean water level, $A = \frac{H}{2}$: amplitude where H is the overall amplitude of a wave, T: period of a wave, $k = \frac{2\pi}{L}$: wavenumber, and $\omega = \frac{2\pi}{T}$: angular frequency of a wave.

Ocean waves that are *irregular* or seemingly *random* are common. There are a variety of ways that regular waves (wave components) might combine to produce irregular ones. A regular wave (wave component) is defined by a single frequency (wavelength) and amplitude (height of the wave). *Wind* waves and *swells* are examples of normal water waves. There are many instances of irregular waves such as *surf beats*, *harbour resonance*, *seiche*, and *tsunamis*. It is possible to classify water waves depending on their wavelength. In terms of wave classification, there are two distinct sorts of waves: *deep* and *shallow*. When the wavelength of a water wave exceeds the depth of the water, it is considered shallow (or long wave). Tsunamis and tidal waves are examples of shallow water waves. Deep water waves, on the other hand, have wavelengths that are shorter than the depth of the ocean (or short waves), e.g., rogue wave. There are waves that fall midway between shallow and deep, and they are called *intermediate* water waves. This relative depth of wave characteristics is defined by h/L, where h denotes constant depth. For shallow water wave, this ratio satisfies $h/L < \frac{1}{20}$, for deep water waves, $h/L > \frac{1}{2}$ and for intermediate waves, $\frac{1}{20} < \frac{h}{L} < \frac{1}{2}$. A linearized theory of water waves is used when the wave amplitude is expected to be small in proportion to the theoretical wavelength. In general, waves in

TH-2746_176123008

the ocean are nonlinear. However, the margin of error in most engineering scenarios is quite small even when linear theory is utilised instead of nonlinear theory. With small amplitude waves in mind, linear wave theory is used to describe the majority of water wave dynamics difficulties. The linearized water wave theory is used in tackling the problems in this thesis.

With a velocity $\vec{U}$, the equations for mass and momentum conservation in incompressible fluids with inviscid flow are as follows:

$$\nabla.\vec{U} = 0, \tag{1.1}$$

$$\frac{\partial \vec{U}}{\partial t} + (\vec{U}.\nabla)\vec{U} = \vec{g} - \frac{1}{\rho}\nabla P, \tag{1.2}$$

where ρ is the density of the water, $\vec{g}$ is the gravitational accelaration and P is the hydrodynamic pressure.

Irrotational flows are now considered which results in a scalar function Φ such that

$$\vec{U} = \pm\nabla\Phi. \tag{1.3}$$

Mathematically, both positive and the negative signs are correct in (1.3). However, the gravity wave always flows from higher to lower potential which defines loss of energy. Following this convention, the negative sign is being considered in all our works in this thesis. This Φ is called the velocity potential. Substituting (1.3) in (1.1) gives the equation of continuity for a potential flow as

$$\nabla^2\Phi \quad = \quad 0, \tag{1.4}$$

which is the **Laplace's equation**.

Considering periodic waves with time harmonic motions, the velocity potential can be expressed in Cartesian coordinates (x, y, z) as

$$\Phi(x, y, z, t) = \mathrm{Re}[\phi(x, y, z)\exp(-\mathrm{i}\omega t)], \tag{1.5}$$

with $\phi(x, y, z)$ being the spatial potential function and 'Re' the real part of a function.

Considering gravity to be acting in the negative z-direction, it gives

$$\vec{g} = \nabla(-gz). \tag{1.6}$$

Then equation (1.2) gives

$$\nabla\left[\frac{\partial\Phi}{\partial t} + \frac{1}{2}\nabla\Phi.\nabla\Phi + \frac{P}{\rho} + gz\right] = 0. \tag{1.7}$$

TH-2746_176123008

After carrying out the integration with respect to the spatial variables in real time domain $[0, t]$, it yields

$$\frac{\partial \Phi}{\partial t} + \frac{1}{2}\nabla\Phi.\nabla\Phi + \frac{P}{\rho} + gz = f(t),$$

when the process starts from rest at $t = 0$ and $f(t)$ is the integration constant.

Without loss of generality, $f(t)$ can be combined with the potential $\Phi(x, y, z, t)$ which results in

$$\frac{\partial \Phi}{\partial t} + \frac{1}{2}\nabla\Phi.\nabla\Phi + \frac{P}{\rho} + gz = 0. \tag{1.8}$$

This is called the **Bernoulli's equation** or it may be termed here as the dynamic boundary condition.

Following small amplitude of the motion, the linearised dynamic boundary condition (1.8) at free surface $z = \eta$ becomes

$$\frac{\partial \Phi}{\partial t} + \frac{P}{\rho} + g\eta = 0. \tag{1.9}$$

The kinematic condition is given as the free surface as a material boundary for which a particle on the free surface always remains on the free surface and hence the total derivative of the free surface is zero. In reality, particles are in continuous motion; even due to Brownian motion, a particle will not stay on the free surface. A free surface is actually an idealization; it is a collection of many particles that form a surface. Therefore, the condition at the free surface $z = \eta(x, y, t)$ is given by

$$\frac{\partial \Phi}{\partial z} = \frac{\partial \eta}{\partial t} + \frac{\partial \eta}{\partial x}\frac{\partial \Phi}{\partial x} + \frac{\partial \eta}{\partial y}\frac{\partial \Phi}{\partial y}. \tag{1.10}$$

The linearised kinematic condition (1.10) ultimately takes the form

$$\frac{\partial \Phi}{\partial z} = \frac{\partial \eta}{\partial t} \quad \text{at} \quad z = 0. \tag{1.11}$$

Following linear water wave theory as mentioned earlier, the boundary value problem is governed by

$$\nabla^2\phi \;=\; 0. \tag{1.12}$$

Assuming hydrodynamic pressure to be 0 at the free surface, and combining (1.9) and

TH-2746_176123008

(1.11) gives us the mean free surface condition at $z = 0$ as

$$\frac{\partial \phi}{\partial z} - K\phi = 0, \tag{1.13}$$

where $K = \dfrac{\omega^2}{g}$.

We define a no flow boundary condition for a rigid structure as follows:

$$\frac{\partial \phi}{\partial n} = 0 \qquad \text{on } S, \tag{1.14}$$

where S is surface boundary of the structure and n is the outward normal of the surface.

For an uneven impermeable rigid bottom $z = -h(x, y)$, the boundary condition reduces to

$$\frac{\partial \phi}{\partial z} + \nabla_{x,y} h \cdot \nabla_{x,y} \phi = 0, \tag{1.15}$$

where $\nabla_{x,y} = \left(\dfrac{\partial}{\partial x}, \dfrac{\partial}{\partial y}\right)$.
For a constant bottom, it reduces into

$$\frac{\partial \phi}{\partial z} = 0 \quad \text{at} \quad z = -h. \tag{1.16}$$

The same principle may now be used to two layers of an immiscible fluid with mean free surface at $z = 0$, impermeable bottom at $z = -h$ and linear interface at $z = -h_I$. Considering time harmonic motion of the fluid properties where the syntax remains the same, we add subscripts 1 and 2 to denote the upper and lower layer fluid features, respectively. Hence, the potentials satisfy the governing equation as follows:

$$\nabla^2 \phi_1 = 0, \text{ for } -h_I \leq z \leq 0, \tag{1.17}$$

$$\nabla^2 \phi_2 = 0, \text{ for } -h \leq z \leq -h_I. \tag{1.18}$$

The mean free surface condition at the upper layer gives

$$\frac{\partial \phi_1}{\partial z} - K\phi_1 = 0. \tag{1.19}$$

The impermeable bottom condition at the lower layer gives

$$\frac{\partial \phi_2}{\partial z} = 0. \tag{1.20}$$

Assuming linear interface along the two-layer fluid with elevation $\eta_2(x, y, t)$, the continuity

TH-2746_176123008

of velocity results in

$$\frac{\partial \Phi_1}{\partial z} = \frac{\partial \Phi_2}{\partial z} = \frac{\partial \eta_2}{\partial t}. \tag{1.21}$$

Further, the continuity of momentum from linearised Bernoulli's equation gives another boundary condition as follows:

$$\begin{aligned} P_1 &= P_2, \\ \implies \rho_1 \frac{\partial \Phi_1}{\partial t} - \rho_2 \frac{\partial \Phi_2}{\partial t} &= g(\rho_2 - \rho_1)\eta_2. \end{aligned} \tag{1.22}$$

For time harmonic motions in a two-layer fluid, the conditions (1.21) and (1.22) become

$$\frac{\partial \phi_1}{\partial z} = \frac{\partial \phi_2}{\partial z}, \tag{1.23}$$

$$\rho_1 \left(\frac{\partial \phi_1}{\partial z} - K\phi_1 \right) = \rho_2 \left(\frac{\partial \phi_2}{\partial z} - K\phi_2 \right). \tag{1.24}$$

1.2.1 Solution for the potential in a two-layer fluid

For a two-layer fluid, we consider harmonic motion in the y-direction as well as in time. Hence, the velocity potential $\Phi_j(x, y, z, t)$ for $j = 1, 2$ in each fluid layer can be written as $\Phi_j(x, y, z, t) = \text{Re}\left[\phi_j(x, z)e^{\text{i}(k_y y - \omega t)}\right]$ where $k_y = k_1 \sin\theta$ with k_1 being the incident wavenumber.

For the fluid region, the analytical solution is found by using the method of separation of variables. Substituting Φ_j in equations (1.17) and (1.18), the Laplace's equation gets transformed into a modified Helmholtz equation and subsequently, by applying equations (1.20), (1.21) and (1.23), the spatial potentials can be written as

$$\phi_1(x, z) = e^{\pm \text{i}qx} \frac{\sinh k(h - h_I)(K \sinh kz + k \cosh kz)}{K \cosh kh_I - k \sinh kh_I}, \tag{1.25}$$

$$\phi_2(x, z) = e^{\pm \text{i}qx} \cosh k(z + h), \tag{1.26}$$

where $q = \sqrt{k^2 - k_y^2}$ and $(\pm)$ sign stands for the direction of the waves. Wavenumber k can be found from the dispersion relation, by using equations (1.25) and (1.26) in equation (1.24), as

$$K^2(\rho + \coth kh_I \coth k(h - h_I)) - kK(\coth kh_I + \coth k(h - h_I)) + k^2(1 - \rho) = 0. \tag{1.27}$$

This equation has two pairs of symmetric real roots $k = \pm k_n$, for $n = 1, 2$, denoting the progressive wavemodes and an infinite number of symmetric purely imaginary roots $k = \pm k_n = \pm \text{i}t_n$ for $n = 3, 4, \ldots$, where t_n is a real number (See Appendix B), denoting

TH-2746_176123008

the evanescent modes. Two sorts of solution of potential are produced depending on k.

The potential function for such an n-th mode can be written as

$$\phi_1(x,z) = e^{\pm \mathrm{i}q_n x}\frac{\sinh k_n(h-h_I)(K\sinh k_n z + k\cosh k_n z))}{K\cosh k_n h_I - k\sinh k_n h_I}, \tag{1.28}$$

$$\phi_2(x,z) = e^{\pm \mathrm{i}q_n x}\cosh k_n(z+h). \tag{1.29}$$

Eigenfunction expansion technique is the utilization of the existence of a set of orthogonal eigenfunctions that can be used to construct solutions. The Sturm-Liouville theory provides an infinite sequence of eigenvalue-eigenfunction pairs. If $\{u_n\}_{n=1}^{\infty}$ is the sequence of eigenfunctions of a Sturm-Liouville problem on an interval $[a,\ b]$ on the real axis, and $F(x)$ is any function defined on this interval, one seeks a representation of $F(x)$ in the form

$$F(x) = \sum_{n=1}^{\infty} c_n u_n(x),$$

where the constants $\{c_n\}$ must characterize the function f. MacCamy and Fuchs [60] calculated the force and moment acting on water wave interaction with cylindrical piles by using eigenfunction expansion method. Sollitt and Cross [95] and Madsen [61] used this technique in two-dimensional Cartesian coordinates. Sulisz [97] formulated a theory for variable structure and numerically solved the problem.

Using eigenfunction expansion, considering all the dispersive modes, the potential can also be written in the form

$$\phi(x,z) = \sum_{n=1}^{\infty} e^{\pm \mathrm{i}q_n x} I_n, \tag{1.30}$$

where

$$I_n = \begin{cases} \dfrac{\sinh k_n(h-h_I)(K\sinh k_n z + k\cosh k_n z))}{K\cosh k_n h_I - k\sinh k_n h_I}, & \text{for } h_I < z < 0, \\ \cosh k_n(z+h), & \text{for } h < z < h_I. \end{cases} \tag{1.31}$$

1.3 Fluid flow through porous media

We begin our discussion of flow within a porous medium by defining a porous medium and its many uses. The term "porous medium" refers to a medium or substance that has pores in it. The "matrix" or "frame" refers to the medium's skeleton structure. In most cases, a liquid or gas fills the pores. Foams and other porous media may also be productively analysed by utilising the idea of skeletal structure. For example, aquifers and petroleum reservoirs may be classified as porous media, as can be natural compounds like zeolites,

TH-2746_176123008

organic tissues (bones, cork), and man-made materials like cement and ceramics, which are all porous. Only by assuming that they are porous media, many of their significant features can be explained. Filtration, mechanics, petroleum engineering, bioremediation, and construction engineering are some of the fields that make use of porous media. Other fields include biology and biophysics, geomechanics and geoengineering that also use the concept of porous media. Both *saturated* and *unsaturated* porous media exist in the world of adsorbents. Saturated and unsaturated porous media both have empty spaces that are partly filled with fluid, while the voids in saturated porous media are completely filled. Only a small portion of the space is occupied by the liquid, while the rest is occupied by air. *Porosity* is an essential word that defines how much "empty" space is there in a material. Let us consider a volume V_T of a reasonably large porous medium such that

$$V_T = V_P + V_S,$$

where V_P is the void volume (pore volume) while V_S is the solid material volume. Porosity, which is defined as the ratio of pore volume to total volume, may be represented and denoted as follows:

$$\epsilon = \frac{V_P}{V_T} = \frac{V_T - V_S}{V_T}.$$

Types of porosity

- Primary porosity (The porosity of a rock or any other natural porous material that happens at the depositing time).
- Secondary porosity (The porosity that grows after deposition of the rock or any other natural porous material).

Further, porosity can be categorized into the following six types depending on the size of the pores:

- Total porosity (It is a ratio of the entire pore space in a rock to its bulk volume).
- Effective porosity (It is a measure of the void space that is filled by recoverable oil and gas),
  porosity$= \frac{\text{Vol. of interconnected pores + Vol. of dead end}}{\text{Total or bulk vol. of reservoir rock}}$.
- Dual porosity (It is a conceptual idea that there are two overlapping reservoirs which interact. In fractured rock aquifers, the rock mass and fractures are often simulated as being two overlapping but distinct bodies).
- Microporosity (Pore size is smaller than 2 nanometers in diameter).

TH-2746_176123008

- Mesoporosity (Pore size is greater than 2 nanometers and less than 50 nanometers in diameter).
- Macroporosity (Pore size is greater than 50 nanometers in diameter).

Porosity measuring method

There are several types of methods for finding porosity such as

- Direct method
- Optical method
- Computed tomography method
- Imbibition method
- Gas expansion method.

Motion in three dimensions of small amplitude waves in an undeformable porous medium is studied here with the medium being homogeneous and isotropic. When the seepage fluid velocity $\vec{U}$ and dynamic pressure P are taken into account, the fluid moves according to the continuity equation and the equation of motion such as

$$\nabla.\vec{U} = 0, \tag{1.32}$$

$$m\frac{\partial \vec{U}}{\partial t} + \frac{1}{\rho}\nabla P + f\omega\vec{U} = 0, \tag{1.33}$$

where the innertial coefficient is defined as

$$m = 1 + C_M\frac{1-\epsilon}{\epsilon}, \tag{1.34}$$

with C_M as the added mass coefficient, f is the friction parameter and ϵ is the porosity. The derivation and physical significance of (1.33) and (1.34) are described in Appendix A.

Now similarly, the irrotational flow inside the porous medium results in a pore velocity potential $\Phi(x, y, z, t)$ satisfying

$$\vec{U} = -\nabla\Phi. \tag{1.35}$$

Integrating (1.33) gives the **Bernoulli's equation** for porous medium as follows:

$$m\frac{\partial \Phi}{\partial t} + f\omega\Phi + \frac{P}{\rho} = 0. \tag{1.36}$$

TH-2746_176123008

Considering time harmonic solutions in Cartesian coordinates (x, y, z), $\vec{U}$, P and Φ can be expressed as

$$\vec{U} = u(x, y, z)e^{-\mathrm{i}\omega t}, \quad P = p(x, y, z)e^{-\mathrm{i}\omega t}, \quad \Phi = \phi(x, y, z)e^{-\mathrm{i}\omega t}. \tag{1.37}$$

Substituting these values in (1.32) and (1.35), it results in

$$\nabla^2\phi \;=\; 0, \tag{1.38}$$

which is the governing Laplace's equation.

Further, substituting the values into (1.33) gives

$$\frac{\nabla p}{\rho} - \mathrm{i}\omega\gamma u = 0, \tag{1.39}$$

where $\gamma = m + \mathrm{i}f$. Following small amplitude $\eta(x, y, t)$ of the motion along the free surface and $p = \rho g\eta$, the linearised dynamic boundary condition (1.36) at $z = 0$ becomes

$$\eta = \frac{\mathrm{i}\omega\gamma}{g}\Phi. \tag{1.40}$$

The linearised kinematic condition is

$$\frac{\partial\Phi}{\partial z} = \frac{\partial\eta}{\partial t} \quad \text{at} \quad z = 0. \tag{1.41}$$

Combining (1.40) and (1.41) gives us the mean free surface condition at $z = 0$ as

$$\frac{\partial\phi}{\partial z} - \gamma K\phi = 0. \tag{1.42}$$

For $f = 0$ and $m = 1$, i.e., $\gamma = 1$, the porous medium gets converted into a water region and hence, the corresponding free surface condition (1.42) reduces to

$$\frac{\partial\phi}{\partial z} - K\phi = 0. \tag{1.43}$$

For a constant bottom, we can define the impermeable bottom condition as

$$\frac{\partial\phi}{\partial z} = 0 \quad \text{at} \quad z = -h. \tag{1.44}$$

Similar theory can be applied for the flow in a two-layer porous medium with free surface at $z = 0$, impermeable bottom at $z = -h$ and linear interface at $z = -h_I$. Hence, the

TH-2746_176123008

potentials satisfy the governing equations as follows:

$$\nabla^2\phi_1 = 0, \text{ for } -h_I \le z \le 0, \tag{1.45}$$

$$\nabla^2\phi_2 = 0, \text{ for } -h \le z \le -h_I. \tag{1.46}$$

The mean free surface condition at the upper layer gives

$$\frac{\partial\phi_1}{\partial z} - \gamma K\phi_1 = 0. \tag{1.47}$$

The impermeable bottom condition at the lower layer gives

$$\frac{\partial\phi_2}{\partial z} = 0. \tag{1.48}$$

Further, the continuity of momentum from linearised Bernoulli's equation of *porous medium* gives another pair of boundary conditions as follows:

$$\frac{\partial\phi_1}{\partial z} = \frac{\partial\phi_2}{\partial z}, \tag{1.49}$$

$$\rho_1\left(\frac{\partial\phi_1}{\partial z} - \gamma K\phi_1\right) = \rho_2\left(\frac{\partial\phi_2}{\partial z} - \gamma K\phi_2\right). \tag{1.50}$$

For a two-layer porous medium flow, we consider a harmonic motion in the y-direction as well as in time. Hence, the velocity potential $\Phi_j(x, y, z, t)$ for $j = 1, 2$ in each fluid layer can be written as $\Phi_j(x, y, z, t) = \text{Re}\left[\phi_j(x, z)e^{\text{i}(k_y y - \omega t)}\right]$ where $k_y = k_1 \sin\theta$ with k_1 being the incident wavenumber.

Similarly as in Section 1.2.1, substituting Φ_j in equations (1.45) and (1.46), the Laplace's equation gets transformed into a Helmholtz equation and subsequently, by applying equations (1.47) to (1.50), the spatial potentials can be written as

$$\phi_1(x, z) = e^{\pm \text{i}qx}\frac{\sinh k(h - h_I)(K\gamma \sinh kz + k\cosh kz))}{K\gamma\cosh kh_I - k\sinh kh_I}, \tag{1.51}$$

$$\phi_2(x, z) = e^{\pm \text{i}qx}\cosh k(z + h), \tag{1.52}$$

where $q = \sqrt{k^2 - k_y^2}$ and $(\pm)$ sign stands for the direction of the waves. Wavenumber k can be found from the dispersion relation, by using equations (1.51) and (1.52) in equation (1.50), as

$$K^2\gamma^2(\rho + \coth kh_I \coth k(h - h_I)) - kK\gamma(\coth kh_I + \coth k(h - h_I)) + k^2(1 - \rho) = 0. \tag{1.53}$$

For real γ, this equation has two pairs of symmetric real roots denoting the progressive modes and an infinite number of symmetric purely imaginary roots denoting evanescent

TH-2746_176123008

modes. However, due to complex γ, all the roots are complex of the form $k_n = \pm(a_n + \mathrm{i}b_n)$ with a_n and b_n are real and the existence of the roots can be found in Appendix B. Two sorts of solution of potential are produced depending on k.

The potential function for such an n-th mode can be written as

$$\phi_1(x,z) = e^{\pm \mathrm{i}q_n x} \frac{\sinh k_n(h-h_I)(K\gamma \sinh k_n z + k\cosh k_n z))}{K\gamma \cosh k_n h_I - k \sinh k_n h_I}, \tag{1.54}$$

$$\phi_2(x,z) = e^{\pm \mathrm{i}q_n x} \cosh k_n(z+h). \tag{1.55}$$

Darcy's law for flow in porous media

By Darcy's law, the movement of liquids and gases in porous media may be described. It was laboratory tests that first presented Darcy's law as an empirical connection in 1856.

Incompressible flow through a homogeneous porous medium may be represented by using Darcy's law in terms of laminar stationary flow as

$$\vec{U} = -\frac{\mathcal{K}}{\mu}\nabla P,$$

where, $\vec{U}$ and P represent the velocity and pressure of the fluid passing through the pores, respectively, $\mathcal{K}$ denotes the permeability of the medium and μ is the dynamic viscosity. The relation between particle diameter (d_p) and porosity (ϵ) is defined by the Carman-Kozeny equation as follows:

$$\mathcal{K} = \frac{d_p^2 \gamma^2}{180(1-\gamma)^2}.$$

Permeability has meter^2 as the dimension of measurement. The Darcy number is the ratio of permeability and the total length of the medium. The bigger the Darcy number, the larger the particle diameter and the smaller the pores are. The Darcy number 0 denotes the absence of any fluid in the medium.

Darcy's law applies to fluid flow through porous medium when the structure is thin. The pressure differential across the porous barrier determines the flow velocity. It is now possible to calculate the hydrodynamic pressure $P(x,y,z,t) = \mathrm{Re}\left[p(x,y,z)e^{-\mathrm{i}\omega t}\right]$ from the linearized Bernoulli's equation as $p = \mathrm{i}\rho\omega\phi$, where ρ is the density of the fluid. Therefore, the condition at the interface can be written as

$$W(x,y,z) = \frac{\mathrm{i}b\rho\omega}{\mu}(\phi_+ - \phi_-) = G(\phi_+ - \phi_-), \tag{1.56}$$

where $\pm$ denotes the velocity potentials at the boundary of the porous wall. Dimensionless porous-effect parameter $G = \dfrac{\mathrm{i}b\rho\omega}{\mu}$ is the term used by Chwang in [20], where k is the wavenumber. It may be expressed as $G = G_R + \mathrm{i}G_I$ where G_R signifies the real component

TH-2746_176123008

and G_I denotes the imaginary part, as used by Yu [120]. However, in fact, G always has positive real and imaginary components unless when the resistance effect against flow overcomes the inertial effect of the fluid within the porous material, in which case G becomes real. This is also true when the inertia impact is greater than the resistance effect. According to Chwang [20], G may be considered as a Reynolds number for a flow through the small pores of the wall. As a measure of the porosity of the wall, this number is also used. The wall is impermeable when $G = 0$. There would be no porous wall at all if G approaches infinity since the wall is entirely permeable to fluids at this point in time. For low Reynolds number flow through porous walls, we use Darcy's law. By trial and error, the value of G may be determined for a particular porosity. One may get an idea of the unknown material constant by substituting the obtained G value and other well-known values in this equation. The material constant values for additional porosities are determined via linear extrapolation, resulting in G values. Similar theory can be applied to the porous bottom when the sea-bed is assumed to be a thin porous plate.

1.4 Wave propagation over dissipative sea-beds

Water waves propagating over a non-rigid bed have been seen to be attenuated due to energy dissipation through the bed. When waves in coastal waters are attenuated, the energy dissipation method usually includes some type of bottom contact. Most wave attenuation theories, such as those based on bottom friction or percolation on a permeable substrate, assume that the sea-bed is rigid in its response to water waves. However, there is a mounting evidence that, when waves travel across the sea-bed, tiny deflections in the sea-bed may be created. Waves in the North Sea, according to Bjerrum [10], cause sea-bed deflections of up to 5 cm. Wave energy is always dissipated as a result of internal friction inside the sea-bed when such deflections occur. This process might play a role in explaining wave attenuation on the continental shelf and in coastal seas. Mud, also known as cohesive sediment, is made up of clay particles, silt, (fine) sand, organic matter, gas, and water. Because of the poor permeability and electrochemical attraction of clay particles and organic material, this sediment combination possesses cohesive qualities. The impact of a muddy sea-bed is significant in a variety of real-world applications:

1. Mud deposits have a negative impact on navigation.
2. Unfortunately, many mud deposits are now polluted, putting the ecology at risk and driving up the expense of dredging operations.
3. Mud is also one of the governing forces in the water system's ecological evolution, sculpting the physical and biological landscape. The oxygenation of water is critical for survival, reproduction, and growth of biological organism.
4. Sediment transport: beach erosion and accretion,

TH-2746_176123008

5. Coastal structure weakening,

6. Silt up of navigation channels and ports.

A soil under a weight does not respond to an immediate deflection under that force, but settles gradually at a variable pace, as is well recognised in engineering practice. Clays and sands that have been wet with water show a lot of settlement. The settling is induced by the soil's progressive response to load change. Soil consolidation is the term for this procedure. Sandy beaches are made up of loose material that is porous.

Changes in pressure associated with both mean and oscillatory water wave flows create a groundwater flow of sea water inside the porous medium in the coastal environment. The mean flow has a substantial impact on the creation of the water table. This component also percolates through the porous bottom, influencing the wave pressures on structures that are supported by or extend into the bottom. The oscillatory component of the wave field, on the other hand, contributes to wave damping over a porous beach. The interplay of numerous physical processes, biodiversity and productivity of sandy beaches, sediment transport, and coastal structure stability all require knowledge of both of the aforementioned components. Coastal engineers have been studying the wave-sea-bed interaction extensively in recent years. Gravity water waves travelling through the ocean are well recognised for generating enormous dynamic pressure on the sea-bed. Effective stresses and pore pressure within the soil matrix are further induced by these pressure variations. A sedimentary bed may become unstable when pore pressure exceeds effective stresses, resulting in sea-bed instability such as liquefaction and shear failure, resulting in damage to offshore installations (such as pipelines, soil storage tanks, piers, breakwaters, and so on) caused by wave-induced sea-bed instability rather than construction causes.

Most wave theories in conventional ocean engineering are based on the assumption that waves propagate across a rigid sea-bed. This means that such theories employ the wave pressures calculated from the solution, under the assumption of a rigid sea-bed, as input forces throughout the whole wave-sea-bed interaction. This indicates that, at the sea-bed, the vertical velocity vanishes. As a result, the impacts of sea-bed reaction on wave characteristics are not possible to be investigated. However, the features of sedimentary beds in ocean settings determine wave characteristics, which are significant in ocean engineering. In other words, if the sea-bed is a dissipative medium, the wave properties (such as damping of water waves, wavelength, and wave pressure) may be influenced by the sea-bed reaction (porous or elastic medium). As a result, in order to offer a better assessment of wave properties, the wave field and dissipative flow must be coupled. The major focus of this thesis is on two forms of dissipative beds: (1) porous sea-beds and (2) elastic sea-beds. The sea-bed (porous or elastic) is treated as a boundary, with no consideration given to the motion beyond it. The elastic sea-bed may also be treated as a thin elastic plate (using the Euler-Bernoulli beam equation), which is

TH-2746_176123008

analogous to the issue of wave interaction with big floating constructions, known as Very Large Floating Structures (VLFS).

There are many theories available to deal with a porous bed. For simplicity, we consider the bottom in all works as a porous plate placed over the rigid bottom. The flow inside the plate is considered to be insignificant and we should confine our analysis to porous bottom with fine pores. The water depth is finite and only the boundary condition at the interface between the fluid and the porous sea-bed is used to handle the physical problem as in Martha et al. [66]. The bed permeability has been characterized by a parameter $G = \dfrac{\mathrm{i}b_B\rho_2\omega}{\mu}$ with b_B as the coefficient which has the dimension of length and μ the coefficient of dynamic viscosity [14]. Generally, G is a complex number as defined in [123] and can be represented by $G = G_R + \mathrm{i}G_I$ where G_R contributes to resistance effects and G_I (imaginary part) contributes to inertial effects. Further, it may be noted that, to ensure propagation of progressive wave at the far field in the open water region, G_1 is assumed to be real [63].

1.5 Brief review of previous works

The study of water wave propagation in a two-layer fluid intercepted by a submerged or floating impediment, such as a barrier, breakwater, or any geometric structure, is very essential in coastal and marine engineering. In recent decades, there has been a growing interest in studying this kind of occurrence in order to design suitable porous structures that may be utilised as breakwaters to lessen the effect of waves on shorelines. It is critical to reduce wave forces in order to safeguard different infrastructures as well as shorelines. This creates a relatively peaceful zone along the coast, allowing operations such as vessel anchoring, loading and unloading of goods, and so on to take place without too much disruption. The goal is to create a calm zone with the least amount of wave effect. The term "tranquilly zone" refers to a region where the sea is relatively calm and the power of waves has diminished significantly. When a train of water waves hits an obstruction on any stratum of the ocean, some of the wave is reflected, while some is transferred across it, and the rest is stuck. The use of suitable porous structures to evaluate the corresponding coefficients will provide a clear situation of how to build a serenity zone that will provide a variety of advantages for the smooth operation of activities on and near shorelines.

Jarlan recommended using perforated breakwaters to lessen wave effect on stiff vertical wall breakwaters installed behind it in 1961 [44]. Sollitt and Cross [95] found and analysed the dissipation of wave energy within a porous medium by using an iterative procedure and the linearized friction term f. Following that, Madsen [61] investigated the reflection and transmission of linear shallow water waves owing to a rectangular porous wave-absorber installed on a level ocean bottom using the linearized version of the governing equations

TH-2746_176123008

and the flow resistance formula. Rojanakamthorn et al. [84] employed potential theory to solve a boundary value problem involving porous structures. By studying several forms of rubble-mound breakwaters, which constitute most of the basic porous structures, Sulisz [97] employed boundary element technique to develop numerical solutions to such scattering issues. Dalrymple et al. [25] reported the finding that wavenumbers derived from the dispersion relation inside a porous medium merged in certain situations, and hence the velocity potential within the porous medium could not be represented in terms of eigenfunctions. Yu and Chwang [123] investigated wave propagation through a porous structure by using the virtual work concept developed by Sollitt and Cross [95]. Different approaches for solving the dispersion equation inside a dissipative medium were developed by Mendez and Losada [68] and Chang and Liou [18]. Mendez and Losada [68] utilised a second-order perturbation approach to find higher-order roots, while Chang and Liou [18] used the homotopy perturbation method. The dissipation of wave energy inside porous structures is an important element to be considered while investigating water wave interaction with such structures. For examining regular wave interaction with a caisson-type breakwater with perforated-wall consisting of a perforated front wall and a chamber with an impervious rear wall, Zhu and Zhu [126] developed an impedance analytical technique (IAM). Garrido and Medina [37] proposed a novel semi-empirical model for predicting the reflection coefficient for single and double perforated chamber breakwaters.

Additional research on various forms of porous breakwaters sheds more insight on the subject. In his porous wave-maker theory, Chwang [20] utilised Darcy's law to investigate waves flowing through a porous structure, and Yu [120] extended it by incorporating the inertia effect in the formulation. The thin-plate model was extensively used by Chwang and Lee [21] and Sahoo et al. [91] to examine waves propagating through various porous structures with diverse topologies. The performance of a breakwater with a perforated front wall, an impervious rear wall, and a rock-filled core was studied by Isaacson et al. [44]. Kaligatla et al. [46] and Tabssum et al. [98] examined water wave interaction with porous structures for waves propagating across sea-beds of varying depths. It was shown that a breakwater made up of numerous porous blocks of varying width may effectively reduce wave energy. Zhu [127] studied the reflection and damping of surface waves propagating through a porous material by using wave-induced refraction-diffraction equations. The problem was solved by using the Sollitt and Cross model in combination with the orthogonality of the depth-dependent functions. Das and Bora [32, 33] built on the work of Zhu [127] to investigate wave reflection and damping by a rectangular porous structure with uniform porosity placed on raised single-step and multi-step bottoms. Liu et al. [58] investigated the hydrodynamic performance of a modified horizontal-plate breakwater consisting of a submerged upper horizontal porous plate and a submerged lower horizontal solid plate by computing the reflection coefficient for various depths,

TH-2746_176123008

structure width, and porosity. Sahoo et al. [90] studied the effect of porous structure in the presence of a thin elastic plate.

All these above works focused on wave propagation through or within porous structures mainly in homogeneous fluids only. What was missing and is probably additionally required is to focus on water wave interaction with a porous structure in a stratified ocean which represents a more realistic scenario. Those different strata or layers in ocean form due to differences in temperature and salinity in coastal regions, which results in appreciable changes in water density. Thus, in reality, ocean water is non-homogeneous with respect to space and time. In other words, ocean water is formed by different strata, i.e., density layers, with sharp interfaces. Practically, there are three main 'layers' in an ocean: the surface ocean, the deep ocean, and the seafloor sediments (Thorpe [99]). The surface ocean can be thought of as the upper layer. When scientists refer to the surface ocean, the portion of top 200 meters of the ocean (on average) is referred but the change in depth takes place corresponding to different seasons and latitudes. In general, the surface ocean is much warmer than the deep ocean, and the bottom of the surface ocean is determined by measurements of water temperature and density. The transition into the deep ocean happens when the temperature of water drops and the density increases. The deep ocean is all the seawater that is colder (generally 0-3° C or 32-37.4° F), and thus denser. That is why in our consideration, we assume the depth of the lower layer is more than or equal to the upper layer. In general, deep ocean water, which makes up approximately 90% of the water in the ocean, is homogeneous (it is relatively constant in temperature and salinity from place to place). Because the surface and deep ocean layers are of different densities (due to salt content and temperature), these layers of the ocean do not mix easily. Seafloor sediments are sediments that can be found at the bottom of the seafloor that is still in contact with seawater. These sediments can still be influenced by the water around them. There are several types of sediments that make up the seafloor, and which are porous. We consider this type of sea-bed as the one for the present problem. More such practical information can be found in [99]. The surfaces of interfaces between different layers become unstable due to the variation in density gradient, and when some impulse is applied, wave-like disturbances are often generated, which are known as internal interfacial waves. For detail description on interfacial wave and its significance, one can refer to the monograph by Massel [67]. Exchange of momentum and wave energy takes place between the surface and interfacial waves. Subsequently, the effects of wave amplitudes on various marine structures can be studied which leads to full information of interfacial waves impinging upon structures.

Linton and Cadby [56] examined the trapped-mode frequencies for submerged horizontal circular cylinders in a two-layer fluid consisting of a finite layer bounded above by a free surface and below by an infinite layer of greater density. Saha and Bora [87, 88] investigated the existence of trapped modes in a two-layer fluid of finite depth bounded

TH-2746_176123008

above by a rigid lid or an ice-sheet. For a fixed geometrical configuration, they numerically computed the values of such wave frequencies for which the values of the truncated determinant became approximately zero confirming the existence of trapped modes. Manam and Sahoo [65] used Havelock's expansion for the potential function to investigate scattering and radiation of oblique water waves by a thin porous structure in a two-layer fluid for both finite and infinite depth cases. It revealed that porous structures underwent a substantial resistance by the interfacial waves. Afterward, Behera and Sahoo [8] discussed the effect of porous structures on scattering and trapping of water waves in a two-layer fluid due to a breakwater placed on a permeable sea-bed. The seepage effects by both surface and interfacial waves on the structure were found to be of the same magnitude.

It seems pertinent to discuss a few aspects of use of multi-porosity structures as breakwaters. Caisson type breakwaters usually consist of multiple layers (two or three). An enormous breakwater was constructed for the first liquefied natural gas (LNG) receiving terminal along the Pacific Coast of North and South America known as Costa Azul caisson breakwater. This project successfully demonstrated that very large caissons can be installed in relatively deep water. This is one of the prime examples that has motivated our present work. As an example of another such structure, 40 large concrete caissons were arranged in a specific manner for the Port of Piraeus, West Pier 3 expansion project, just south of Athens, Greece. The individual caisson boxes were built on a large, semi-submersible barge. Now, if we consider one caisson box and its vertical cross-section, then effectively multiple chambers will be formed which also clearly resembles our present work. Méhauté [79], while discussing wave damping, introduced high wave energy damping due to the progressive wave absorber with multiple layers and analyzed the effect of using multiple damping materials. Experiments were carried out to analyze the effects of two-layer and three-layer porous structures, that is, by using porous blocks with multiple values of porosity and friction factor. Twu et al. [103] considered a stratified porous structure and they were successful in establishing that the multi-porosity structure could be efficiently used as partial shelter to shorelines in order to avoid high wave attack. It was concluded that use of multiple porosities in the breakwater structure added more efficiency to the wave blocking. Lin et al. [54] examined the effect of a horizontal composite porous barrier in linear wave propagation. Venkateswarlu and Karmakar [107] numerically investigated reflection of water waves by multiple porous structures on leeward region. They also considered a stratified porous structure and examined its hydrodynamic performance by computing the reflection coefficient corresponding to various depths, structure width, and porosity [105]. The above works amply justify that use of stratified porous structure has immense contribution in protecting various coastal and offshore facilities by attenuating the wave height.

The sea-bed was thought to be flat and rigid in the wave-structure interaction problems as mentioned above. However, it is important to note that, when gravity waves spread

TH-2746_176123008

over the sea-bed along the coast, they undergo shear stress, strain and pressure due to the permeable and elastic nature of the sea-bed. Owing to the sea-bed permeability, elasticity and shear force, which also slow down wave motion, significant changes can be observed in wave characteristics along the coast. Due to the occurrence of high waves during storms, a mud hole in the Gulf of Mexico is found to be used as an emergency harbour where fishing boats often take shelter [36]. Similar mud beds can be found at many places, for example, on the inner shelf of the south-central Kerala coast in south-west India (see Kurian et al. [51], Narayana et al. [80] and the literature cited therein). When Mallard and Dalrymple [64] investigated wave propagation over a deformable bottom, they noticed a major shift in the wave characteristics due to the elasticity of the sea-bed. Dawson [34] extended this work in examining the wave motion by taking into account the influence of soil inertia. Utilizing linear water wave theory, Mohapatra and Sahoo [76] investigated the impact of flexible nature of the sea-bed on the propagation of the surface gravity waves. Lee and Lan [52] considered the combined effects of porosity and elasticity of the sea-bed on the propagation of the surface gravity waves and found that, in terms of pressure distribution, the elastic effect outweighed the bed permeability. Tsai et al. [102] examined the response of a poro-elastic sea-bed to waves and modelled a caisson motion using Biot consolidation theory. An analytical model was proposed by Kumagai and Foda [50] for the response of a composite type breakwater and sea-bed to sinusoidal standing waves.

1.6 Main motivation for the current work

Researchers have suggested many forms of porous breakwaters for the protection of coastal areas and building sites. Waveloads and wave run-up are reduced by porous structures. In the preceding section, we covered some of the key works. These structures are very adaptable and reusable, and they may be utilized to create low-cost wave attenuation and protection of systems. Because of its numerous uses, porous structures are often utilized in the construction of coastal and offshore structures. Floating airports, semi-submersibles, and wave power energy conversion systems are just a few examples. Oil rigs are constructed from a variety of porous materials. Porous structures are also used in sea-cage culturing, to build Very Large Floating Structures (VLFS), such as floating airports, bridges, breakwaters, piers, and docks. To construct maritime structures, a variety of atmospheric variables must be considered, as well as an accurate estimate of hydrodynamic influence on the structures. As a result, research has concentrated on improving the system in order to minimize large hydrodynamic repercussions. The idea behind using porous bodies is to lessen the impact of wave-body interaction on the body surface through the pores. Offshore wind energy, in particular, has attracted the interest of many governments seeking an alternative and stable source of energy. South Korea

TH-2746_176123008

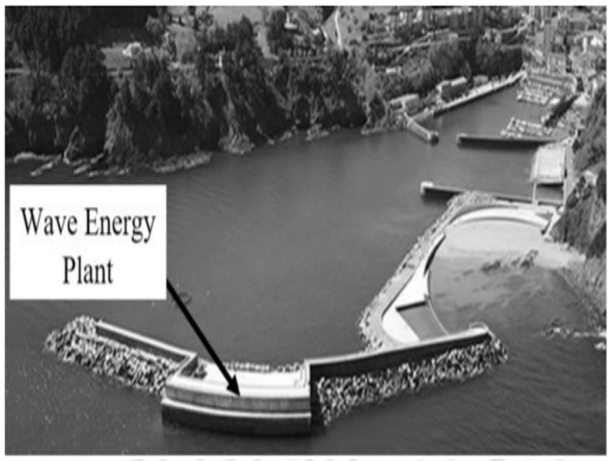

Figure 1.2: The Mutriku Wave Energy Plant (Courtesy Mustapa et al. [78])

has chosen to spend $9 billion in the construction of a 2.5 GW offshore wind farm in the country's south west sea. The foundation for a wind turbine grows in size as the tower grows in height, and the rotor nackle grows in size as gross generation grows. The wave force has a significant impact on the substructures. As a result, reducing wave stresses on substructures is an essential aim. Using a structure with a porous surface is one option.

In 1970, the whole globe experienced a worldwide oil crisis. The notion of putting renewable energy to the forefront has gained attraction since then. Parallel to this, a significant amount of effort has been put into research and emerging activities such as solar, wind, and ocean energy. This progress has aided in the research of the current gap between renewable and non-renewable energy sources. It has recently been discovered that WEC (Wave Energy Converter) systems are more expensive than standard energy generated by coal power stations. However, the WEC's charm may be boosted by combining it with other marine constructions like a breakwater pier or a jetty. The following are the results of combining a breakwater with a wave energy device over a stand-alone wave energy device (Mustapa et al., [78]):

1. Overtopping WEC-breakwater integration,
2. Oscillating water column and WEC-breakwater integration,
3. Piston-Type Porous Wave Energy Converter (PTPWEC) integration.

"The Mutriku Wave Energy Plant" (Figure 1.2), located in Mutriku on the northern coast of Spain between San Sebastian and Bilbao, and "Siadar Wave Energy Project" (Figure 1.3), located in Siadar Bay, Lewis, Scotland, are two identified current important projects in connection with breakwater integration. The semi-circular breakwater idea built in Miyazaki Port in Japan (Figure 1.4) is another porous breakwater project.

Wind farms may be installed in any large body of water, especially in the ocean on the continental shelf, to capture offshore wind power or wind energy. Wind energy may

TH-2746_176123008

Figure 1.3: Siadar Wave Energy Project (Courtesy [78])

Figure 1.4: Semi-circular breakwater concept at Miyazaki Port, Japan (Courtesy [78])

be transformed to electricity in a suitable manner. There are several wind energy power resources accessible across the globe. One such important wind energy resource is "Mar de Trafalgar" (Figure 1.4) in the sea, which runs south-west to the Gulf of Cadiz in Spain. Multiple uses of a marine site via the co-location of such complementing activities would almost certainly result in more effective use of ocean space, which is good for nature. The ideal method to investigate the economic benefits and efficient use of ocean space via multi-use and co-location is to start growing aquaculture inside the structure that serves as an ocean wind farm. The co-location of these two businesses, aquaculture and wind energy generation, will result in cost savings for both the public and commercial sectors. The public advantages are attributable to the fact that such a shared structural layout does not have a detrimental impact on ecological services received from the ocean region, which would otherwise take up and exhaust more space. Cost reductions resulting from the pooling of infrastructure, logistical operations, and systems are the private advantages. Buck and Langan [11] have discussed in great depth on such difficulties. Sarkar and Bora

TH-2746_176123008

[93] discussed the diffraction of linear water waves by a cylindrical storage tank whose inner part contained a cylindrical pile and the outer part contained a coaxial thin hollow porous cylinder in finite ocean depth.

A few features of the utilisation of multi-porosity structures as breakwaters appear important to be examined. It is a significant problem to build a breakwater that achieves optimal wave reflection, transmission, and high energy damping while using the least amount of construction material possible. Several research have been conducted on various kinds of coastal structures, and it has been shown that porous structures are the best for attenuating wave energy, which in turn regulates wave energy in the seaward and leeward open water zones. As a practical example, porous blocks were successfully used to control high wave attack in the Gudong and Zhuangxi Sea Dike in the Shengli Oilfield in China [124]. To protect against wave impact, perforated wall breakwaters were erected at Dieppe, France ([9]) and Dalian Chemical Production Terminal, China ([43]).

Furthermore, surface waves in reservoirs or lakes induced by landslides during earthquakes have been studied using the thin porous-wavemaker hypothesis, which has considerable applications in the research of surface waves in these water bodies. Landslides produce water waves by moving vertically, at an angle, or horizontally, during the part of their journey. A vertical landslide was simulated by Noda [81] by using a two-dimensional box that fell to the bottom at the end of a semi-infinite canal. A porous box or wall would be more suitable when the majority mass of a landslide comprises of rocks and soils. Another conceivable use of the current approach is in the cases when the wavemaker is subjected to some type of structural limitation on the highest permitted force, and the wavemaker's efficiency is of primary importance. As the porous-effect parameter grows, a porous wavemaker may be useful in lowering the overall load, which is followed by a drop in the wave amplitude. The thin plate inhibits the vertical motion of water oscillations so efficiently that it may significantly lower wave amplitudes. Wu et al. [112] proposed an engineering application in which a horizontal plate might be connected to an existing seawall to lessen wave reflections. A pitching plate may be designed as part of a wave controller, according to Yip and Chwang [118]. They further investigated the hydrodynamic performance of a perforated wall breakwater with an internal horizontal plate (Yip and Chwang [119]).

After reviewing the preceding studies, it is clear that further substantial effort is required to develop (i) a composite porous structure, (ii) thin porous structures, and (iii) flexible poro-elastic bodies. This sort of construction will aid in lowering the hydrodynamic effect on shoreline and structures that may be erected in the ocean for a variety of purposes. We address issues related to scattering and radiation using wave absorbing structures that also serve as wave energy devices in this context.

In this thesis, we are inspired to tackle the scattering and radiation issues in a two-layer fluid with different types of porous and flexible bodies in the presence of various types of

TH-2746_176123008

sea-bed, such as rigid, porous and elastic. The linearised water wave theory assumption underpins the mathematical methodology for tackling such situations. Because of its high precision, an eigenfunction expansion, in combination with the matching approach, is commonly utilised in the analysis of water wave interaction with thick porous objects. For thin bodies, least square approach is being utilised. The analytical solutions for the scattering problems are provided by utilising an eigenfunction expansion method, and the separation of variables technique. The influence of different factors on the wave reflection, wave force, wave run-up, and hydrodynamic coefficients of porous bodies is examined by using analytical solutions. The acquired findings are likely to offer designers of such structures with some relevant important information. We calculate the hydrodynamic coefficients related to wave interaction for various types of porous structures. It is intended that the findings would aid in the development of a suitable gadget that can accommodate a variety of aquatic activities, as indicated before. To the best of our knowledge, no one else has tried challenges of this kind before, and we have great hope that our findings will shed fresh light on these themes.

1.7 Outline of the thesis

This thesis is divided into nine chapters, the first of which discusses the fundamental principles and key equations in the linearized theory of water waves, as well as a number of past major works and our rationale for doing this research. Chapters 2–8 provide the seven problems investigated, while Chapter 9 summarises the results, and suggests future challenges that can be investigated in this field. We investigate three types of problems in this thesis: (i) water wave scattering by a single or multi-chamber thick porous structure in a two-layer fluid bounded above by a free surface and bounded below by different types of bottom surfaces, (ii) water wave interaction by a thin porous or poro-elastic barrier in a two-layer fluid with a free surface and porous bottom boundary conditions, and (iii) water wave interaction by a floating moored elastic plate along with thick porous structure in a two-layer fluid with a free surface and a rigid bottom. The eigenfunction expansion methodology, application of orthogonality in vertical matching boundaries and the least square approach are the key mathematical techniques used in this thesis.

The scattering of water waves by a thick double chamber porous structure on a step-type rigid sea-bed for the oblique incidence scenario, where the top layer has a free surface, is addressed in **Chapter 2**. The boundary value problem is reduced to a two-dimensional boundary value problem for the periodic wave assumption of the potentials. The two-dimensional velocity potentials are obtained by using the method of separation of variables and eigenfunction expansion approach. The orthogonality of the eigenfunctions are then used to calculate the associated reflection coefficients. Explicit analysis of the waveload on

TH-2746_176123008

the various parts of the structure is carried out. It is worth noting that, when an oblique wave strikes on the structure consisting of two different porous blocks, reflection as well as waveload present significant differences as compared to the hydrodynamic coefficients found by scattering by the same porous blocks. The analytical results are compared with an established result and a good agreement is found. Moreover, the porous bottom is considered for a similar kind of problem and a comparison is made.

Chapter 3 investigates the oblique water wave interaction by a double layer composite caisson type breakwater placed upon a rigid base, with a free surface and a porous sea-bed. For dealing with the trapping problem, a rigid sea-wall is considered at a finite distance from the breakwater. A structure with two different porous blocks results in better reflection, transmission as well as waveload than a single block structure. The analytical results are compared with an established result and a good agreement is observed. Periodic pattern of trapping positions is also observed. Reasonable effect on bottom porosity can be observed in the hydrodynamic coefficients. Moreover, a thin perforated wall in front of the porous structure is considered which establishes the effectiveness of the structure.

Chapter 4 deals with the water wave interaction by a single block caisson structure with a perforated front wall upon a rigid base in a two-layer fluid bounded above by a free surface and below by an elastic bottom. Different velocity potentials are explored as previously and the relevant dispersion relation is fully analysed. The mode swapping in a porous body is discussed. The matching eigenfunction expansion method and linear algebraic approach are used to get the entire analytical solution along with the unknown coefficients. The reflection and transmission coefficients, as well as the waveload, free surface and interface elevations, shear force etc. are computed numerically. The stiffness of the elastic bottom is also examined. Computed results are compared with single layer and two-layer interaction problems. The impact of bottom elasticity is discussed for hydrodynamic coefficients.

Chapter 5 deals with an identical water wave interaction by multiple block caisson structure with a perforated front wall upon a rigid base in a two-layer fluid bounded above by a free surface and below by an elastic bottom. As discussed in **Chapter 4**, the matching eigenfunction expansion method is used to get the entire analytical solution along with the unknown coefficients. The reflection coefficients, as well as the waveload, free surface and interface elevations, shear force etc., are computed numerically. The stiffness of the elastic bottom is examined. The inclusion of a perforated front wall has the following effects: (i) the percolative property of the front wall increases the effectiveness of the breakwater in generating lower waveload effective on the rigid wall, (ii) significant difference in the reflection coefficients in both cases.

Chapter 6 discusses the water wave interaction in a two-layer fluid with a thin poro-elastic structure placed upon a porous bottom. A partially reflective sea-wall is considered

TH-2746_176123008

at a distance. The dispersion relation is analysed deeply, and mode-swapping as well as other characteristics are discussed. The dead water analogue is also illustrated. The energy identity for such a complex system is also derived. Various hydrodynamic coefficients are compared with different values of parameters like the porous-effect parameter and the length of the barrier, the angle of incidence, and the porosity of the sea-bed etc. Trapping is analysed for the occurrence of wave reflection minima. Due to adequate change of structural parameters of the barrier, a significant portion of the wave energy dissipation can be observed.

An identical experiment is carried out in **Chapter 7**, but this time the poro-elastic structure is substituted with a thin porous body. Along with the other issues in **Chapter 6**, here the water wave radiation is also explored. When the propagating wave strikes the submerged vertical porous barriers, significant variations in the porous-effect parameter of the sea-bed show a significant impact. A reasonable change in the porous-effect parameters in the structure has an important impact in wave radiation. Furthermore, owing to energy absorption by such a geometry, the important energy identities are also established.

Chapter 8 studies the oblique surface wave interaction with a porous structure in front of a moored floating elastic plate in a fluid consisting of two immiscible layers. The following issues are examined: (i) incident and reflected wave scattering, (ii) structural waveload, (iii) plate elevation, bending moment and shear force, (iv) effect of mooring lines on the plate. Comparison of moored edge emphasizes that suitable edge conditions must be chosen in order to achieve optimum panel deflection and other physical quantities. An optimal structural length is proposed so that maximal wave reflection and minimal transmission can be obtained. Furthermore, the lowest waveload on the plate can be obtained from appropriate values of porous structures.

Finally, **Chapter 9** contains a concise review of the findings in this thesis, focusing on the most relevant outcomes. It also gives details on the scope of future investigations.

TH-2746_176123008

TH-2746_176123008

CHAPTER 2

Linear water wave interaction with a composite porous structure in a two-layer fluid flowing over a step-like sea-bed

2.1 Mathematical formulation

The problem of surface wave interaction with a two-block porous structure, possessing block-wise distinct porosity, placed on an impermeable multi-step bottom is considered in Cartesian coordinates. Using linear water wave theory, irrotational and simple harmonic motion are assumed in an inviscid, incompressible fluid of two layers with a free surface and a linear interface under the action of gravity. Any effect due to surface tension at the interface of the two fluids is ignored since, for such cases, the contribution of surface tension is found to be negligible. The upper layer fluid having density ρ_1 has its free surface at $z = d$ and the lower layer fluid with density ρ_2 has its lower boundary as an

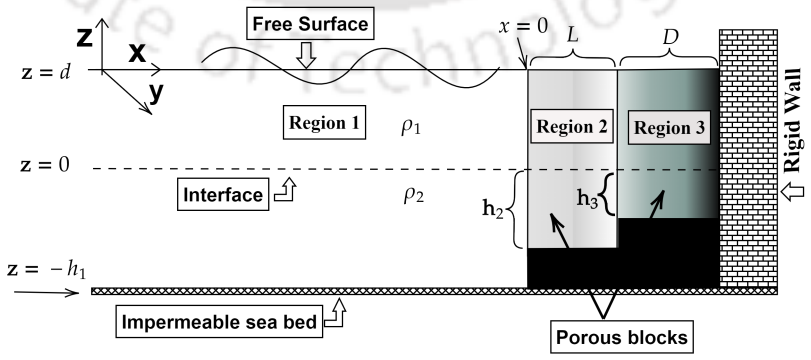

Figure 2.1: Definition sketch of wave interaction with porous blocks placed on an elevated bottom

TH-2746_176123008

impermeable step-bottom. The surface wave is obliquely incident on the porous structure, which has its upper boundary coinciding with the mean free surface, at an angle θ to the x-axis. This ensures that velocity potentials $\Phi_j,\ j = 1, 2, 3$ can be taken in the form $\Phi_j(x, y, z, t) = \mathrm{Re}\{\phi_j(x, z)e^{\mathrm{i}(k_y y-\omega t)}\}$, where ω is angular wave frequency, $k_y = k_{1,I}\sin\theta$ is the y-component of the wavenumber $k_{1,I}$ of the plane progressive wave propagating in the surface mode where the subscripts j and n in $k_{j,n}$ correspond to the j-th region and n-th wavenumber, respectively, Re denotes the real part of $\phi_j(x, z)e^{\mathrm{i}(k_y y-\omega t)}$ and $\mathrm{i} = \sqrt{-1}$ is the usual imaginary quantity. The fluid region is split into three regions as follows: Region 1 $(-\infty < x < 0,\ -h_1 < z < d)$, Region 2 $(0 < x < L,\ -h_2 < z < d)$ and Region 3 $(L < x < L + D,\ -h_3 < z < d)$. The contribution of k_y leads to Snell's law for refraction across discontinuities in the water depth which obeys the equality of k_y across all three regions. Therefore, the variation of the potential functions $\phi_j(\ j = 1, 2, 3)$ in the y-direction is the same so that we are able to match the velocity potentials along the vertical boundaries. Here, ϕ_j denotes the the velocity potential in the j-th sub-domain, $j = 1, 2, 3$, in Regions 1, 2 and 3, respectively, as shown in Figure 2.1. With all the above considerations, the boundary value problem for each potential ϕ_j is governed by the modified Helmholtz equation

$$(\nabla^2_{x,z} - k_y^2)\phi_j = 0 \qquad \text{for} \quad j = 1, 2, 3, \tag{2.1}$$

in which $\nabla^2_{x,z} = \dfrac{\partial^2}{\partial x^2} + \dfrac{\partial^2}{\partial z^2}$ is the two-dimensional Laplacian operator.

The linearized boundary condition at the mean free surface for Region 1 is

$$\frac{\partial \phi_1}{\partial z} - K\phi_1 = 0 \qquad \text{on} \quad z = d, \tag{2.2}$$

where $K = \dfrac{\omega^2}{g}$.

On the other hand, the linearized boundary condition at the mean free surface in Regions 2 and 3 are

$$\frac{\partial \phi_j}{\partial z} - K\gamma_{j-1}\phi_j = 0 \qquad \text{on} \quad z = d \quad (j = 2, 3). \tag{2.3}$$

Derivation of mean surface boundary condition (2.3) was detailed for homogeneous porosity in a homogeneous fluid by Das and Bora [33]. The impermeable step bottom has the boundary condition

$$\frac{\partial \phi_j}{\partial z} = 0 \qquad \text{on} \quad z = -h_j, \qquad \text{for} \quad j = 1, 2, 3. \tag{2.4}$$

Considering the ratio of the densities of the two fluids as ρ such that $0 < \rho = \rho_1/\rho_2 < 1$,

TH-2746_176123008

the linearized boundary conditions at the mean interface $z = 0$ are of the following forms:

$$\left.\frac{\partial \phi_j}{\partial z}\right|_{z=0^-} = \left.\frac{\partial \phi_j}{\partial z}\right|_{z=0^+} \qquad \text{for } j = 1, 2, 3, \tag{2.5}$$

$$\left(\frac{\partial \phi_1}{\partial z} - K\phi_1\right)_{z=0^-} = \rho\left(\frac{\partial \phi_1}{\partial z} - K\phi_1\right)_{z=0^+}, \tag{2.6}$$

$$\left(\frac{\partial \phi_j}{\partial z} - K\gamma_{j-1}\phi_j\right)_{z=0^-} = \rho\left(\frac{\partial \phi_j}{\partial z} - K\gamma_{j-1}\phi_j\right)_{z=0^+} \qquad \text{for } j = 2, 3. \tag{2.7}$$

Further, the continuity of mass flux and pressure across the interfaces at $x = 0$ and $x = L$ yield the matching conditions

$$\frac{\partial \phi_1}{\partial x} = \epsilon_1 \frac{\partial \phi_2}{\partial x} \quad \text{at} \quad x = 0, \quad \text{for} \quad -h_2 < z < d, \tag{2.8}$$

$$\phi_1 = \gamma_1 \phi_2 \quad \text{at} \quad x = 0, \quad \text{for} \quad -h_2 < z < d, \tag{2.9}$$

$$\frac{\partial \phi_2}{\partial x} = \imath \frac{\partial \phi_3}{\partial x} \quad \text{at} \quad x = L, \quad \text{for} \quad -h_3 < z < d, \tag{2.10}$$

$$\gamma_1 \phi_2 = \gamma_2 \phi_3 \quad \text{at} \quad x = L, \quad \text{for} \quad -h_3 < z < d, \tag{2.11}$$

where $\imath = \epsilon_2/\epsilon_1$, with ϵ_1 and ϵ_2 denoting the porosity of the second and third region, respectively.

Due to the impermeable steps, the velocity potentials ϕ_1 and ϕ_2 satisfy the following boundary conditions:

$$\frac{\partial \phi_1}{\partial x} = 0 \quad \text{at} \quad x = 0, \quad \text{for} \quad -h_1 < z < -h_2, \tag{2.12}$$

$$\frac{\partial \phi_2}{\partial x} = 0 \quad \text{at} \quad x = L, \quad \text{for} \quad -h_2 < z < -h_3. \tag{2.13}$$

The rigid wall responds to the impermeable condition

$$\frac{\partial \phi_3}{\partial x} = 0 \quad \text{at} \quad x = L + D. \tag{2.14}$$

With all these equations, we are now in a position to proceed for solving the scattering problem.

2.2 Solution procedure

In this section, the interaction of gravity waves with a porous composite structure in a two-layer fluid having a free surface and an interface, and flowing over a 2-step bottom is studied. Based on the equations from the previous section, the solutions for the potential are evaluated and the related reflection phenomenon is analyzed. The width of the first and second blocks of the porous structure are taken to be L and D, respectively, as shown

TH-2746_176123008

in Figure 2.1. Two progressive wave modes contribute in Free Surface Mode (SM) and Interface Mode (IM) in the water region. However, since all modes are complex within the porous medium, most of the progressive wave modes in both SM and IM are considered. Since the velocity potentials ϕ_j for $j = 1, 2, 3$ satisfy the governing equation (2.1) and the respective boundary conditions (2.2)-(2.7), with ϕ_3 additionally satisfying the no-flow condition (2.14), they have the following forms of infinite series corresponding to the imaginary roots:

$$\phi_1 = \sum_{n=I}^{II} \left(e^{\mathrm{i}q_{1,n}x} + R_n e^{-\mathrm{i}q_{1,n}x}\right) I_{1,n}(k_{1,n}, z) + \sum_{n=1}^{\infty} R_n e^{-\mathrm{i}q_{1,n}x} I_{1,n}(k_{1,n}, z), \tag{2.15}$$

$$\phi_2 = \sum_{n=I,II,1}^{\infty} \left(A_n e^{\mathrm{i}q_{2,n}x} + B_n e^{-\mathrm{i}q_{2,n}(x-L)}\right) I_{2,n}(k_{2,n}, z), \tag{2.16}$$

$$\phi_3 = \sum_{n=I,II,1}^{\infty} C_n \cos q_{3,n}(L + D - x) I_{3,n}(k_{3,n}, z), \tag{2.17}$$

with the eigenfunctions $I_{j,n}(k_{j,n}, z)$, for $j = 1, 2, 3$, given by

$$I_{1,n} = \begin{cases} \dfrac{\sinh k_{1,n}h_1 (K \sinh k_{1,n}(z-d) + k_{1,n} \cosh k_{1,n}(z-d))}{K \cosh k_{1,n}d - k_{1,n} \sinh k_{1,n}d}, & 0 < z < d, \\ \cosh k_{1,n}(z + h_1), & -h_1 < z < 0, \end{cases} \tag{2.18}$$

$$I_{j,n} = \begin{cases} \dfrac{\sinh k_{j,n}h_j (K\gamma_{j-1} \sinh k_{j,n}(z-d) + k_{j,n} \cosh k_{j,n}(z-d))}{K\gamma_{j-1} \cosh k_{j,n}d - k_{j,n} \sinh k_{j,n}d}, & 0 < z < d, \\ \cosh k_{j,n}(z + h_j), & -h_j < z < 0, \end{cases} \quad \text{for } j = 2,\ 3. \tag{2.19}$$

Here the unknowns R_n, A_n, B_n and C_n are to be determined with $q_{j,n} = \sqrt{k_{j,n}^2 - k_y^2}$ for $j = 1, 2, 3$ and $k_{j,n}$ satisfying the dispersion relations

$$K^2(\rho + \coth k_{1,n}d \coth k_{1,n}h_1) + k_{1,n}^2(1 - \rho) - Kk_{1,n}(\coth k_{1,n}d + \coth k_{1,n}h_1) = 0, \tag{2.20}$$

$$K^2\gamma_1^2(\rho + \coth k_{2,n}d \coth k_{2,n}h_2) + k_{2,n}^2(1 - \rho) - K\gamma_1 k_{2,n}(\coth k_{2,n}d + \coth k_{2,n}h_2) = 0, \tag{2.21}$$

$$K^2\gamma_2^2(\rho + \coth k_{3,n}d \coth k_{3,n}h_3) + k_{3,n}^2(1 - \rho) - K\gamma_2 k_{3,n}(\coth k_{3,n}d + \coth k_{3,n}h_3) = 0. \tag{2.22}$$

We show in Appendix B that dispersion relation (2.20) has two sets of real roots of the form $k_{1,n} = \pm k_{1,I}, \pm k_{1,II}$ and infinitely many purely imaginary roots $k_{1,n} = \pm k_{1,3}, \pm k_{1,4}, \ldots$ of the form $k_{1,n} = \mathrm{i}t_n$ for $n = 3, 4, \ldots$, where t_n are real. Due to the symmetry of the roots, we consider only the positive roots in the positive x-direction

TH-2746_176123008

$k_{1,n} = k_{1,I}$ (Free surface mode), $k_{1,II}$ (Interface mode) with $0 < k_{1,I} < k_{1,II}$ and an infinite number of positive purely imaginary roots $k_{1,n} = \mathrm{i}t_n$. However, complication arises in finding the roots of the dispersion relation given by equations (2.21) and (2.22) since it is connected to the porous regions. As discussed in Appendix B, dispersion relation (2.21) and (2.22) has infinitely many complex roots given by $k_{j,n} = a_{j,n} + \mathrm{i}b_{j,n}$ for $j = 2, 3$, where all $a_{j,n}$ and $b_{j,n}$ are real. A numerical algorithm based on Newton-Raphson method is implemented in Matlab to evaluate the roots of (2.20).

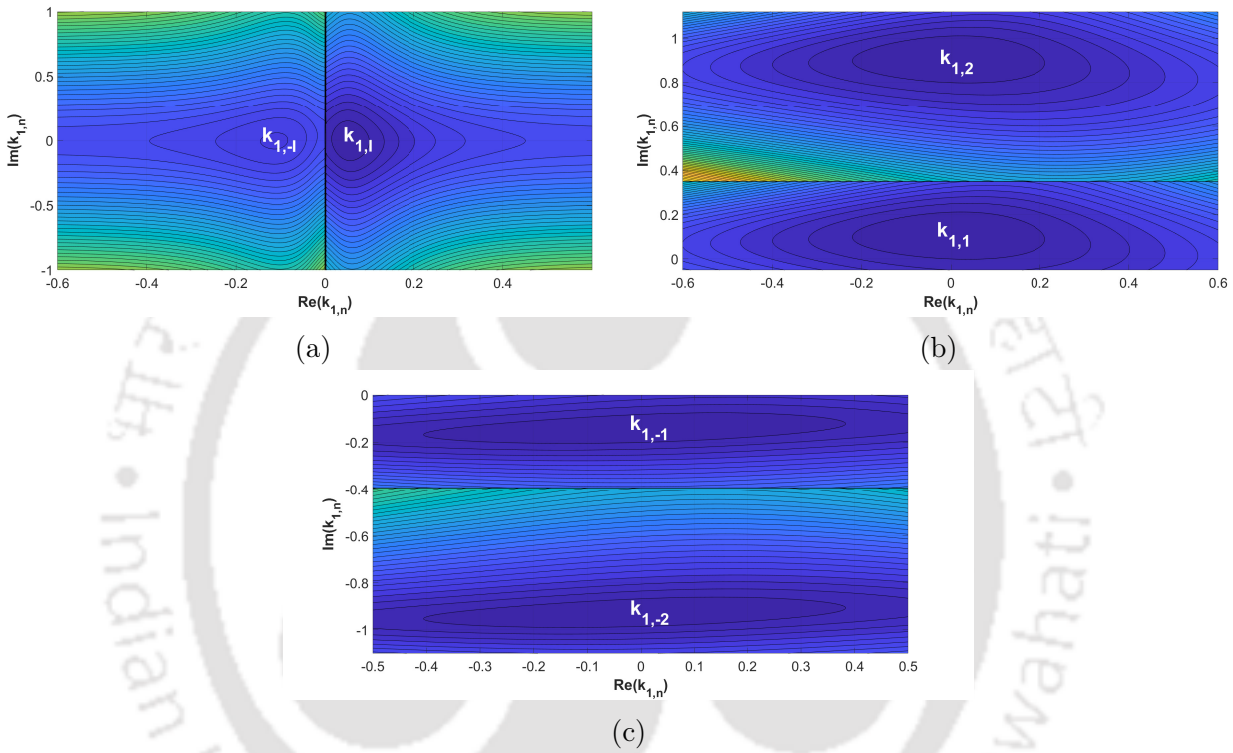

Figure 2.2: Contour plots for real and purely imaginary roots of the dispersion relation equation (2.20) with $d/h_1 = 0.5, \rho = 0.9$ and $Kh_1 = 0.3$.

In Figure 2.2(a,b,c), we present contour plots to demonstrate the roots of dispersion relation (2.20) in the water region. Among infinitely many purely imaginary roots in Region 1, here we show only the first few roots. This type of contour plot is helpful for finding a suitable initial approximation to compute the roots numerically in Matlab.

It is understood that corresponding to different types of upper surfaces, interfaces, bottom surfaces and media, different types of dispersion relations come into picture. Finding the roots of the dispersion relation related to water medium is a familiar procedure. However, the same cannot be held true with respect to porous media and therefore, here we emphasize mainly on finding the roots of the dispersion equation corresponding to porous medium only. Both the dispersion relations (2.21) and (2.22) are similar. The only difference is the bottom depth h_j. Subsequently, we illustrate the dispersion relation (2.21) only. Direct use of the Newton-Raphson based algorithm on Matlab can give us the roots

TH-2746_176123008

but there may be some complications while finding the proper initial guess. Moreover, when derivative of the dispersion equation with respect to $k_{2,n}$ becomes 0, the Newton-Raphson method also fails. The eigenfunction expansion in the porous medium similarly fails at these $k_{2,n}$ values. Therefore, in this present work, the homotopy perturbation (HP) method as devised by Chang and Liou [18] is followed to find these roots. While finding the roots, we observe that corresponding to $\gamma_1 = 1$, dispersion relation (2.21) has two pairs of real roots (positive and negative). These two modes correspond to progressive wave modes in the water region (rigid bottom). The other modes, $k_{2,n}, n = 3, 4, \ldots$, are purely imaginary for $f_1 = 0$. The influence of f_1 is to damp the wave motion by adding (only) an imaginary part to $k_{2,n}$ for $n = 1, 2$, and real parts to the $k_{2,n}$, $n > 2$. According to their algorithm, it was shown that, as the dissipation factor (here γ_1 which is 1 for plain water region) changes from real to complex, the corresponding dispersive roots of the water region also get converted to the roots of dispersion equation with complex parameter. Dispersive root for $\gamma_1 = 1$ is considered as the initial guess for obtaining the roots. Detailed analysis regarding the method of Mendez and Losada [68] can be found in Appendix C. Further, the results are compared with the roots found by adopting the approach followed by Mendez and Losada [68] (ML method) for validation. The velocity potentials in porous regions 2 and 3, that is, $\phi_2(x, z)$ and $\phi_3(x, z)$ given by (2.16) and (2.17), respectively, are found by assuming that dispersion relation given by (2.21) has distinct roots. Further, if there are repeated roots, then the expansion formulas should be appropriately adjusted as per the description in Behera and Sahoo [8].

$k_{2,n} \Downarrow, f_1 \Rightarrow$	$f_1 = 0.5$		$f_1 = 1$	
	ML Method	HP Method	ML Method	HP Method
$k_{2,I}$	$0.0612058 + 0.0150948i$	$0.0612104 + 0.0150924i$	$0.0649332 + 0.0284352i$	$0.0649444 + 0.0284233i$
Error^+	$3.5158874 \times 10^{-06}$	$2.7930691 \times 10^{-15}$	$1.2576776 \times 10^{-05}$	$4.9065389 \times 10^{-18}$
$k_{2,II}$	$0.0448815 + 0.8218551i$	$0.0448842 + 0.8218618i$	$0.0954814 + 0.8277503i$	$0.0955097 + 0.8278048i$
Error^-	$5.3651800 \times 10^{-06}$	$1.1107649 \times 10^{-17}$	$1.1308983 \times 10^{-05}$	$6.1398113 \times 10^{-14}$
$k_{2,1}$	$0.0152566 + 1.7635881i$	$0.0152570 + 1.7635871i$	$0.0307384 + 1.7626630i$	$0.0307418 + 1.7626584i$
Error^+	$7.2650844 \times 10^{-07}$	$2.4234932 \times 10^{-12}$	$3.6503180 \times 10^{-06}$	$2.5899863 \times 10^{-14}$
$k_{2,2}$	$0.0078913 + 2.6736948i$	$0.0078915 + 2.6736926i$	$0.0156237 + 2.6718085i$	$0.0156244 + 2.6717979i$
Error^+	$2.8219652 \times 10^{-06}$	$4.7590238 \times 10^{-14}$	$1.3194386 \times 10^{-05}$	$4.8266479 \times 10^{-16}$
$k_{2,3}$	$0.0091546 + 3.7496971i$	$0.0091549 + 3.7496956i$	$0.0183529 + 3.7484738i$	$0.0183551 + 3.7484672i$
Error^+	$1.5760327 \times 10^{-06}$	$4.4127166 \times 10^{-13}$	$7.3935360 \times 10^{-06}$	$1.3825648 \times 10^{-16}$

Table 2.1: Variation of $k_{2,n}(n = I, II, 1, 2, \ldots 5)$ in a porous medium against f_1 for $d/h_2 = 0.7$ and $m_1 = 1$

In Table 2.1, we compare the results of dispersion relation (2.21) for the methods of Mendez and Losada (ML Method) and Chang and Liou (HP Method) for a homogeneous porous medium. The roots in the above two methods do not show any significant difference up to the working precision level, except for the number of iterations and the prescribed error in K defined by $Error^{\pm}$, and is discussed in Appendix B (equation (B.5)). It is observed that the HP method converges more rapidly for the same number of iterations and with a very negligible error with respect to the values of the wavenumber. The

TH-2746_176123008

eigenfunctions $I_{j,n}(k_{j,n}, z)$ in (2.18) and (2.19) are integrable in corresponding domains $(-h_j, d)$ for $j = 1, 2, 3$ and they form an orthogonal set with respect to the following inner product as mentioned by Meng and Lu [70, 71]:

$$< I_{j,n}, I_{j,m} >= \sum_{k=j}^{3} \int_{-h_k}^{-h_{k+1}} I_{j,n}, I_{j,m} \mathrm{d}z + \rho \int_{0}^{d} I_{j,n}, I_{j,m} \mathrm{d}z, \text{ with } j = 1, 2, 3, \quad h_4 = 0. \quad (2.23)$$

Furthermore, it may be noted that Meng and Lu [69] defined the inner product for a region consisting of both plain water and porous structure in a homogeneous fluid where the porosity and friction both were directly incorporated in the inner product as well as in the eigenfunctions. Meanwhile, it is required to mention here that, due to the presence of the rigid steps in Regions 2 and 3, no velocity potential is considered below $z = -h_j$ for the j-th region ($j = 2, 3$). Hence, the eigenfunctions $I_{j,n}$ for $j = 2, 3$ are defined only for the porous region with respect to mean free surface condition (2.3) and impermeable bottom condition (2.4), and subsequently, the porous impedance parameter appearing in the inner product for $j = 2, 3$ are incorporated via $I_{j,n}$. As a result, the following can be easily derived [8]:

$$< I_{j,n}, I_{j,m} >= \begin{cases} 0, & \text{for} \quad m \neq n, \\ E_{j,n}, & \text{for} \quad m = n, \end{cases} \quad (2.24)$$

where the inner product is found with the help of Chamberlain and Porter [12] as

$$E_{j,n} = \frac{(\sinh 2k_{j,n}h_j + 2k_{j,n}h_j)}{4k_{j,n}} + Q_{j,n}\left(\frac{(k_{j,n}^2 - K^2\gamma_{j-1}^2)d}{2} + \frac{(k_{j,n}^2 + K^2\gamma_{j-1}^2)\sinh 2k_{j,n}d}{4k_{j,n}} - K\gamma_{j-1}\sinh^2 k_{j,n}d\right),$$

with $Q_{j,n} = \rho \sinh^2 k_{j,n}h_j/(K\gamma_{j-1}\cosh k_{j,n}d - k_{j,n}\sinh k_{j,n}d)^2$ and $\gamma_0 = 1$.

Now, by using the matching conditions (2.8)-(2.11) and the boundary conditions (2.12) and (2.13) by considering a linear combination of N terms, we obtain the following equations:

$$\sum_{n=I}^{II} q_{1,n}I_{1,n} - \sum_{n=I,II,1}^{N} R_n q_{1,n}I_{1,n} = \begin{cases} 0, \text{ for } -h_1 < z < -h_2, \\ \epsilon_1 \sum_{n=I,II,1}^{N} \left(A_n - B_n e^{\mathrm{i}q_{2,n}L}\right) q_{2,n}I_{2,n}, \text{ for } -h_2 < z < d, \end{cases} \quad (2.25)$$

$$\sum_{n=I}^{II} I_{1,n} + \sum_{n=I,II,1}^{N} R_n I_{1,n} = \gamma_1 \sum_{n=I,II,1}^{N} \left(A_n + B_n e^{\mathrm{i}q_{2,n}L}\right) I_{2,n}, \text{ for } -h_2 < z < d, \quad (2.26)$$

TH-2746_176123008

$$\sum_{n=I,II,1}^{N}\left(A_n e^{\mathrm{i}q_{2,n}L}-B_n\right)q_{2,n}I_{2,n}=\begin{cases}0,\ \text{for}\ -h_2<z<-h_3,\\ -\mathrm{i}\imath\sum\limits_{n=I,II,1}^{N}C_n\sin(q_{3,n}D)q_{3,n}I_{3,n},\ \text{for}\ -h_3<z<d,\end{cases}\tag{2.27}$$

$$\gamma_1\sum_{n=I,II,1}^{N}(A_n e^{\mathrm{i}q_{2,n}L}+B_n)I_{2,n}=\gamma_2\sum_{n=I,II,1}^{N}C_n\cos(q_{3,n}D)I_{3,n},\ \text{for}\ -h_3<z<d.\tag{2.28}$$

Thereafter, using equations (2.25)-(2.28) and applying the orthogonality of the eigenfunction $I_{2,n}$ given by equation (2.24) for $j=2$, we get

$$\sum_{n=I,II,1}^{N}R_n q_{1,n}b_{1,n,m}+\epsilon_1\left(A_m-B_m e^{\mathrm{i}q_{2,m}L}\right)q_{2,m}a_{2,m}=\sum_{n=I}^{II}q_{1,n}b_{1,n,m},\tag{2.29}$$

$$\sum_{n=I,II,1}^{N+2}R_n\hat{b}_{1,n,m}-\gamma_1\left(A_m+B_m e^{\mathrm{i}q_{2,m}L}\right)a_{2,m}=-\sum_{n=I}^{II}\hat{b}_{1,n,m},\tag{2.30}$$

$$\left(A_m e^{\mathrm{i}q_{2,m}L}-B_m\right)q_{2,m}a_{2,m}+\mathrm{i}\imath\sum_{n=I,II,1}^{N}C_n q_{3,n}\sin(q_{3,n}D)\hat{b}_{2,m,n}=0,\tag{2.31}$$

$$\gamma_1\sum_{n=I,II,1}^{N}\left(A_n e^{\mathrm{i}q_{2,n}L}+B_n\right)\hat{a}_{2,m,n}-\gamma_2\sum_{n=I,II,1}^{N}C_n\cos(q_{3,n}D)\hat{b}_{2,m,n}=0,\tag{2.32}$$

where

$$a_{j,m}=\int_{-h_j}^{0}I_{j,m}I_{j,m}\mathrm{d}z+\rho\int_{0}^{d}I_{j,m}I_{j,m}\mathrm{d}z,\ \hat{a}_{j,m,n}=\int_{-h_{j+1}}^{0}I_{j,m}I_{j,n}\mathrm{d}z+\rho\int_{0}^{d}I_{j,m}I_{j,n}\mathrm{d}z,$$
$$b_{j,m,n}=\int_{-h_j}^{0}I_{j,m}I_{j+1,n}\mathrm{d}z+\rho\int_{0}^{d}I_{j,m}I_{j+1,n}\mathrm{d}z,\ \hat{b}_{j,m,n}=\int_{-h_{j+1}}^{0}I_{j,m}I_{j+1,n}\mathrm{d}z+\rho\int_{0}^{d}I_{j,m}I_{j+1,n}\mathrm{d}z,$$

for $j=1,2$.

Now, for $m=I,II,1,\ldots,N$, equations (2.29)-(2.32) constitute a $(4N+8)\times(4N+8)$ system of equations defined by

$$AX=B,\tag{2.33}$$

where A is a square matrix of size $(4N+8)$ of the form

$$A=\begin{bmatrix}A_{1,1} & \epsilon_1 A_{1,2} & -\epsilon_1 A_{1,3} & O_{N+2}\\ A_{2,1} & -\gamma_1 A_{2,2} & -\gamma_1 A_{2,3} & O_{N+2}\\ O_{N+2} & A_{3,2} & -A_{3,3} & \mathrm{i}GA_{3,4}\\ O_{N+2} & \gamma_1 A_{4,2} & \gamma_1 A_{4,3} & -\gamma_2 A_{4,4}\end{bmatrix}$$

with O_{N+2} being the zero matrix of size $(N+2)$ and all other submatrices are square with

size $(N+2)$. Further, we have

$$B = \Bigg[\underbrace{\ldots, \sum_{n=I}^{II} q_{1,n} b_{1,n,m}, \ldots}_{m=I,II,1,\ldots,N}, \ldots, \underbrace{\sum_{n=I}^{II} \hat{b}_{1,n,m}, \ldots}_{m=I,II,1,\ldots,N}, \overbrace{\ldots, 0, \ldots, 0}^{(2N+4)\text{ zeros}} \Bigg]$$

and the unknown vector is

$$X = [R_I, R_{II}, R_1, \ldots, R_N, A_I, \ldots, A_N, B_I, \ldots, B_N, C_I, \ldots, C_N]^T.$$

The reflection coefficients for both free surface and interface modes are computed by taking $R_{SM} = |R_I|, R_{IM} = |R_{II}|$. Further, the unit horizontal wave forces acting on the front and back walls of the porous blocks, denoted by $\mathcal{F}_{f,j}$ for $j = 1, 2$ and $\mathcal{F}_{b,1}$, respectively, can be computed by using the formulas

$$\mathcal{F}_{f,1} = \mathrm{i}\omega\gamma_1 \left[\rho_2 \int_{-h_2}^{0} \phi_2(0,z)\,\mathrm{d}z + \rho_1 \int_{0}^{d} \phi_2(0,z)\,\mathrm{d}z \right], \tag{2.34}$$

$$\mathcal{F}_{f,2} = \mathrm{i}\omega\gamma_2 \left[\rho_2 \int_{-h_3}^{0} \phi_3(L,z)\,\mathrm{d}z + \rho_1 \int_{0}^{d} \phi_3(L,z)\,\mathrm{d}z \right], \tag{2.35}$$

$$\mathcal{F}_{b,1} = \mathrm{i}\omega\gamma_1 \left[\rho_2 \int_{-h_2}^{0} \phi_2(L,z)\,\mathrm{d}z + \rho_1 \int_{0}^{d} \phi_2(L,z)\,\mathrm{d}z \right]. \tag{2.36}$$

Similarly, the unit horizontal wave force on the rigid wall, denoted by $\mathcal{F}_w$, has the form

$$\mathcal{F}_w = \mathrm{i}\omega\gamma_2 \left[\rho_2 \int_{-h_3}^{0} \phi_3(x,z)\,\mathrm{d}z + \rho_1 \int_{0}^{d} \phi_3(x,z)\,\mathrm{d}z \right] \text{ at } x = L + D. \tag{2.37}$$

Further, the non-dimensional hydrodynamic forces, denoted by $F_{f,1}, F_{f,2}, F_{b,1}$ and F_w, can be evaluated from

$$F_{f,j} = \frac{|\mathcal{F}_{f,j}|}{\rho_2 g d h_1}, \text{ for } j = 1, 2,$$
$$F_{b,1} = \frac{|\mathcal{F}_{b,1}|}{\rho_2 g d h_1} \text{ and } F_w = \frac{|\mathcal{F}_w|}{\rho_2 g d h_1}.$$

Due to the presence of the step-type bottom, there is a reduction of wave force, denoted

TH-2746_176123008

by F_{RW}, locally at $x = L$, which has the non-dimensional form

$$F_{RW} = \frac{(\mathcal{F}_{b,1} - \mathcal{F}_{f,2})}{\rho_2 g d h_1}. \tag{2.38}$$

We consider free surface and interfacial elevations in the form $\zeta_i = \mathrm{Re}(\eta_i e^{-\mathrm{i}\omega t})$ for $i = 1, 2$, respectively. The amplitude of elevation η_i can be obtained from

$$\frac{\partial \zeta_i}{\partial t} = \frac{\partial \Phi_j}{\partial z} \Rightarrow \eta_i = \frac{\mathrm{i}}{\omega}\frac{\partial \phi_j}{\partial z}, \text{ where } j \text{ corresponds to the } j\text{-th region.} \tag{2.39}$$

Once the unknowns are determined, the reflection taking place within the porous structure can be examined. Section 2.4 deals with the numerical computation of various quantities and the associated results and observations.

2.3 Validation

We compare our results with those of Behera and Sahoo [8] by plotting the reflection coefficients against non-dimensional D/λ ($\lambda = 2\pi/k_{1,I}$) (Figures 2.3(a) and 2.3(b)). For a proper comparison, we consider the following parameter values: $N = 10$, $(d + h_1) = 5$ m, $h_1 = h_2 = h_3 = d$, $T = 8$ s, $m_1 = m_2 = 1$, $f_1 = 0.5$, $\epsilon_1 = 0.5$, $\rho = 0.9$, $f_2 = 0$, $\epsilon_2 = 1$, $g = 9.81$ m/s^2 in order to convert our model to that of Behera and Sahoo [8].

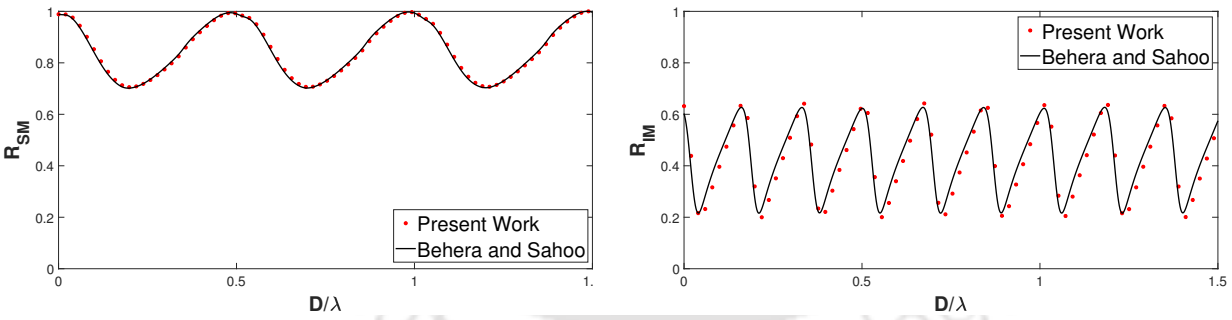

(a) (b)

Figure 2.3: R_{SM} and R_{IM} against D/λ at (a) free surface and (b) interface corresponding to two different results with $L/h_1 = 0.5$ and $f_2 = 0$.

An excellent agreement in the results follows. We present a table which gives a comparison between the computed values with respect to both works. Further, we calculate the error in $\mathbf{L}_2$ norm by the method

$$\text{Relative Error} = \left\| R_{PM} - R_{BS} \right\|_2 / \left\| R_{BS} \right\|_2,$$

and find that the overall relative error in SM is 7.68×10^{-3} while in IM, it is 8.7×10^{-2}. The

TH-2746_176123008

D/λ	0	0.1	0.2	0.3	0.4	0.5	0.6	0.7	0.8	0.9	1
R_{SM}(PM)	0.99	0.84	0.71	0.78	0.93	0.99	0.85	0.71	0.78	0.93	0.99
R_{SM}(BS)	0.99	0.84	0.70	0.78	0.93	0.99	0.84	0.70	0.78	0.93	0.99
R_{IM}(PM)	0.63	0.40	0.28	0.53	0.24	0.63	0.36	0.44	0.48	0.21	0.60
R_{IM}(BS)	0.61	0.45	0.27	0.55	0.28	0.62	0.38	0.41	0.51	0.24	0.61

Table 2.2: Difference between reflection coefficients computed for the present model and Behera and Sahoo Model [8]

relative error shows a good approximation. This comparison confirms that our model can be considered efficient for formulating and solving various problems of wave interaction by porous structures which may contain block-wise different porosity.

2.4 Results and discussion

The in-built program Matlab R2019a is used to solve the system of equations given by equation (2.33). For computational purpose, the following fixed values of some parameters are considered: $d/h_1 = 5/8$; $m_1 = m_2 = 1$, $\rho = 0.9$; $h_1 - h_2 = h_2 - h_3 = h_1/8$; $\theta = [0°, 90°]$ with a range of values of f_j and ϵ_j as $f_j = [0.25, 1.5]$; $\epsilon_j = [0.5, 0.9]$. For such problems, in order to carry out the numerical experiments, it is very important that physically meaningful parameter values are chosen. The parameter values considered above have been chosen very carefully through an elaborate study of various works. It is felt pertinent to give an in-depth idea about such selection and subsequently, in order to justify and also for the convenience of readers, a detailed discussion is placed in Appendix D. Throughout the present work, these values are maintained unless otherwise stated.

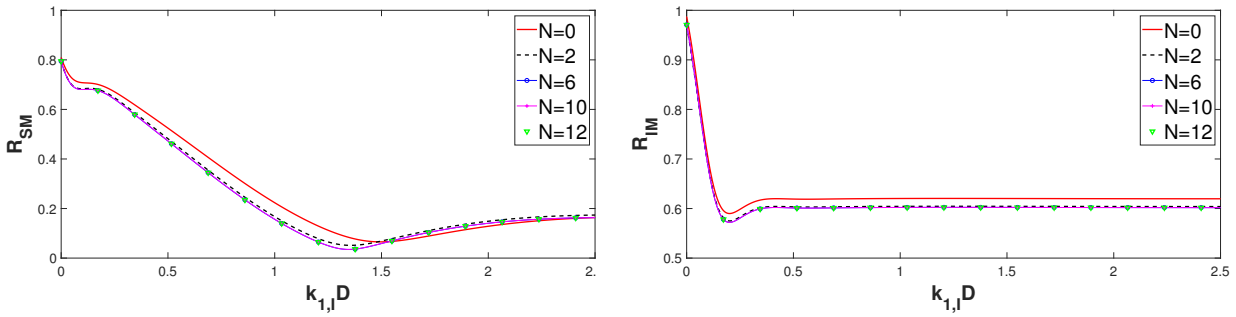

(a) (b)

Figure 2.4: Variation of (a) R_{SM} and (b) R_{IM} against $k_{1,I}D$ corresponding to different number of evanescent modes N with $L/h_1 = 1/4, f_1 = 1, f_2 = 1.25$, $\theta = 40°$ and $\epsilon_1 = 0.9, \epsilon_2 = 0.8$.

At the outset, we investigate the variation of reflection coefficient against the non-dimensional width of the second porous block corresponding to different numbers of

TH-2746_176123008

evanescent modes. From Figure 2.4(a,b), it can be clearly observed that, for very small values of $k_{1,I}D$, reflection can be described by the propagating mode corresponding to the value $N = 2$ alone. When an increase in the structural width takes place, it is clear that consideration of different numbers of evanescent modes affects R_{SM} and R_{IM}. However, when higher number of evanescent modes is considered, the reflection coefficients converge to a fixed value. For our further investigations, as suggested by Figure 2.4(a,b), we can assume the number of evanescent modes given by $N = 10$ to be sufficient which clearly ensures the convergence of the results.

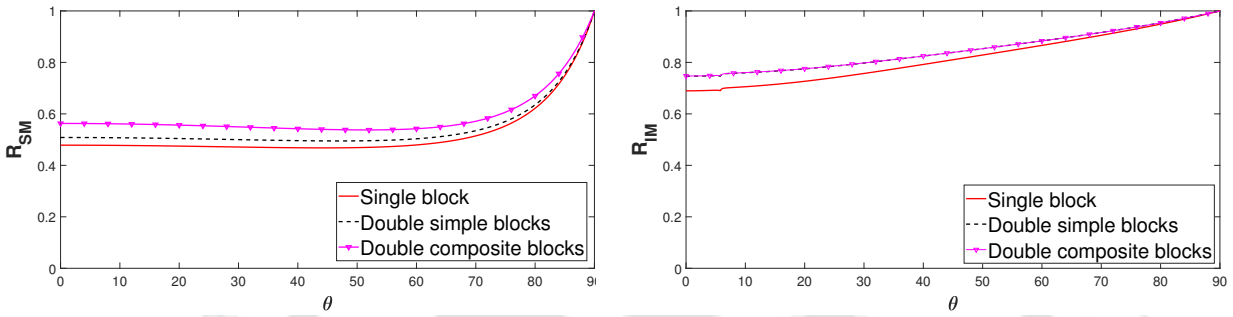

(a) (b)

Figure 2.5: Variation of (a) R_{SM} and (b) R_{IM} against incident angle θ with $d/h_1 = 1$ and $(i)L/h_1 = 2, f_1 = 0.75, \epsilon_1 = 0.5, (ii)L/h_1 = D/h_1 = 1, f_1 = f_2 = 0.75,\ \epsilon_1 = \epsilon_2 = 0.5, (iii)L/h_1 = D/h_1 = 1, f_1 = 0.75, f_2 = 1,\ \epsilon_1 = 0.5, \epsilon_2 = 0.6$.

At first, we show the comparison between a one-block structure and a two-block structure. We consider $D = 0$ which converts the model into a single block structure. In Figure 2.5(a,b), we plot the reflection coefficients for different structural configurations: (i) a single block, (ii) double blocks of equal width with the same porosity and friction and (iii) double blocks of equal width with different porosity and friction. The total structural width is assumed fixed, i.e., $(L + D)/h_1 = 2$, for all three cases. It clearly shows that the double block structure of length $(L + D)/h_1 = 2$ returns higher reflection in both propagating modes than for the single block (Case (i)). Furthermore, the double composite blocks (Case (iii)) show the highest value of reflection in SM. However, no major difference is observed for IM between double simple blocks and double composite blocks. In support of our comparison, we also provide the variation of waveload on the wall for various structural configurations.

Also from Figure 2.6, we can observe the visible difference of waveload on the wall. The double composite block structure on the 2-step bottom shows the lowest impact on the rigid wall while the single block structure shows the highest impact. Therefore, the double block structure shows better energy dissipation and better reflection than the single block structure.

TH-2746_176123008

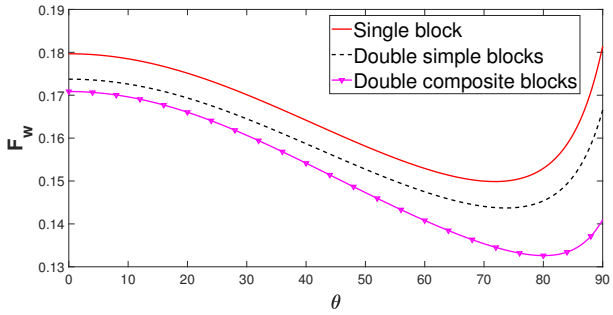

Figure 2.6: Variation of F_w against incident angle θ with $d/h_1 = 1$ and $(i)L/h_1 = 2, f_1 = 0.75, \epsilon_1 = 0.5, (ii)L/h_1 = D/h_1 = 1, f_1 = f_2 = 0.75,\ \epsilon_1 = \epsilon_2 = 0.5, (iii)L/h_1 = D/h_1 = 1, f_1 = 0.75, f_2 = 1,\ \epsilon_1 = 0.5, \epsilon_2 = 0.6$.

2.4.1 Blocks having the same porosity and friction

Initially we assume that both blocks of the porous structure have the same friction parameter, i.e., $f_1 = f_2$ corresponding to the same porosity, i.e., $\epsilon_1 = \epsilon_2$ for our results.

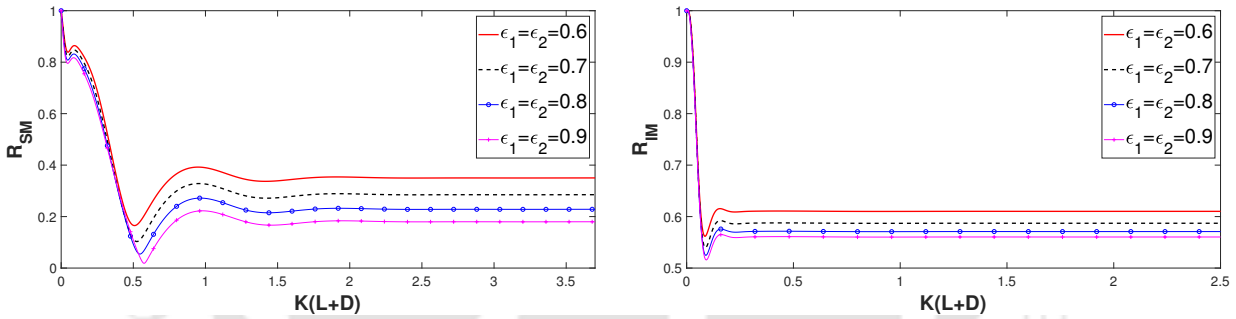

(a) (b)

Figure 2.7: Variation of (a) R_{SM} and (b) R_{IM} against non-dimensional total width of the porous blocks corresponding to various porosity values ϵ_j for $j = 1, 2$ with $f_1 = f_2 = 1$ and $\theta = 0°$.

In Figures 2.7(a,b) and 2.8(a,b), the reflection coefficients in SM and IM, respectively, are plotted against the total non-dimensional width $K(L+D)$ of the structure corresponding to values of porosity coefficient ϵ_j and friction parameter f_j where $\epsilon_1 = \epsilon_2,\ f_1 = f_2$. It is observed that, as the porosity increases, coefficients R_{SM} and R_{IM} take considerably lower values. Consideration of higher porosity and lower width of the porous blocks results in higher values of reflection coefficients, but with the width increasing, the value of the reflection coefficient reduces sharply and remains almost constant after some specific width. The same trend is observed for both propagating modes. On the contrary, an opposite pattern is visible with the coefficients R_{SM} and R_{IM} taking considerably higher values corresponding to an increase in the value of the friction parameter. Though it is found that the reflection coefficients behave similarly for both cases corresponding to

TH-2746_176123008

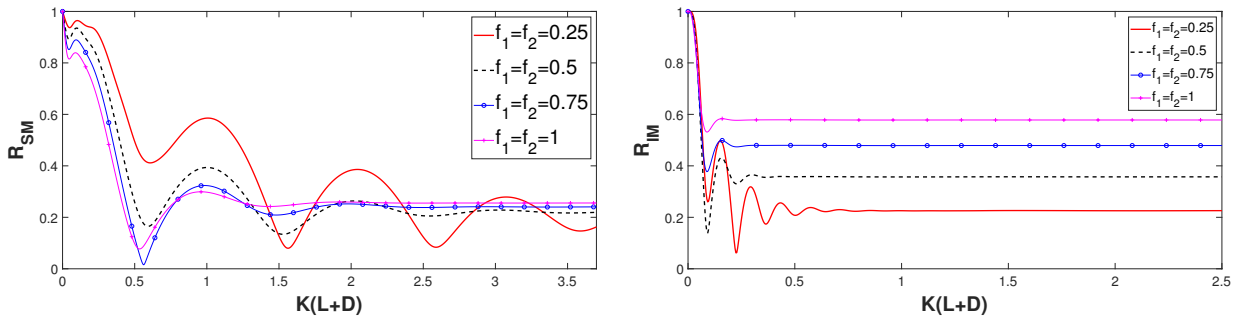

(a) (b)

Figure 2.8: Variation of (a) R_{SM} and (b) R_{IM} against non-dimensional total width of the porous blocks corresponding to various friction parameter values f_j for $j = 1, 2$ with $\epsilon_1 = \epsilon_2 = 0.75$ and $\theta = 0°$.

lower structural width, but an increase in width changes the behaviour as is evident from Figure 2.8(a,b) where both (a) and (b) exhibit oscillating behaviours of R_{SM} and R_{IM} for lower structural width for which oscillation is higher corresponding to the lower values of the friction factors. From Figures 2.7(a,b) and 2.8(a,b), we observe minimal changes in the values of reflection coefficients in both SM and IM corresponding to higher values of $K(L+D)$. This establishes the fact that, after a certain width of the structure, reflection attains a steady state for both modes.

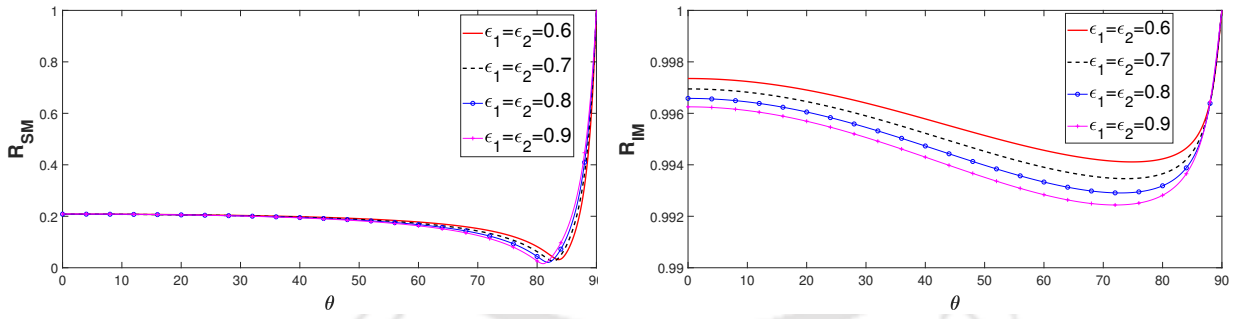

(a) (b)

Figure 2.9: Variation of (a) R_{SM} and (b) R_{IM} against incident angle θ corresponding to various porous coefficients ϵ_j for $j = 1, 2$ with $f_1 = f_2 = 1$ and $(L + D)/h_1 = 1/4$.

Figures 2.9(a,b) and 2.10(a,b) illustrate the effect of porosity and friction parameter on the reflection coefficients against angle of incidence θ in surface mode and interface mode, respectively. By varying the porosity and keeping friction the same, the reflection coefficients are seen reaching their minimum values in the ranges 80°-90° in SM and 75°-85° in IM. Further, for lower porosity values, less reflection is observed for higher incident angles in SM with no such occurrence for IM. Again for IM, no significant changes are observed for the coefficients obtaining optima value, but they reduce corresponding to an

TH-2746_176123008

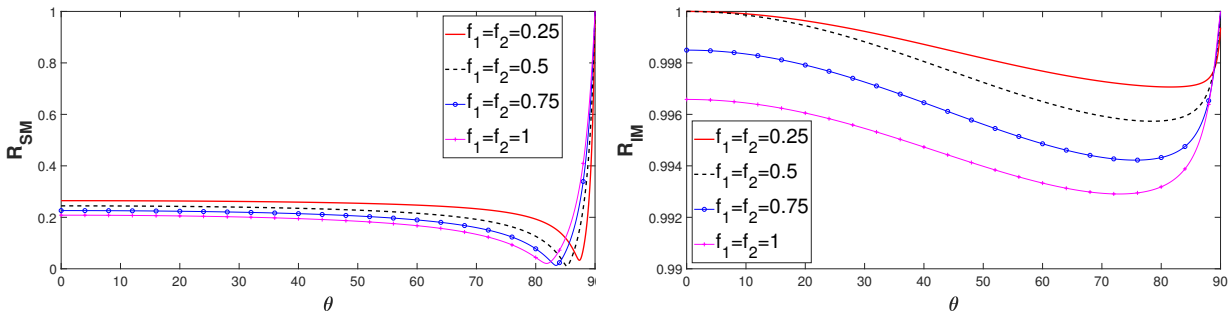

(a) (b)

Figure 2.10: Variation of (a) R_{SM} and (b) R_{IM} against incident angle θ corresponding to various friction parameters f_j for $j = 1, 2$ with $\epsilon_1 = \epsilon_2 = 0.75$ and $(L + D)/h_1 = 1/4$.

increase in porosity.

In Figure 2.10(a,b), where the porosity is fixed but the friction parameter varies, the reflection coefficients are found to reach their minimum values in the range 70°-90° for both propagating modes. As in the case for porosity, increasing friction also results in lower reflection corresponding to smaller incident angles and the variations in R_{SM} and R_{IM} alter similarly after obtaining minimum value. Therefore, it can be inferred that the porosity and the friction parameter behave in a similar manner for both modes against the incident angle, and that for obtaining minimum reflection, visible difference is observed in incident angle for SM, but for IM, no significant difference of the incident angle is required, for both cases of varying porosity and varying friction. Further, it can be observed in both cases that the deviation is not very high for waves in IM. This may be due to the impermeable step of increasing height whilst a reasonable portion of the wave energy concentrated near the interface gets dissipated by the step closer to the interface. Thus, studying the wave pattern, porous structures can be designed as breakwaters by appropriately adjusting structure width, step height and friction factor in order to achieve maximum wave reflection which will in turn protect the marine facilities.

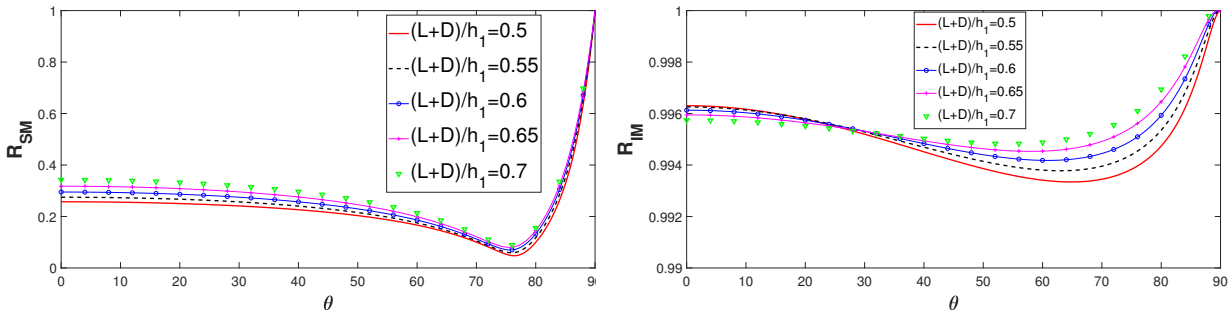

(a) (b)

Figure 2.11: Variation of (a) R_{SM} and (b) R_{IM} against incident angle θ corresponding to various values of $(L + D)/h_1$ with $f_1 = f_2 = 1$ and $\epsilon_1 = \epsilon_2 = 0.9$.

TH-2746_176123008

In Figure 2.11(a,b), the reflection coefficients are plotted against incident angle θ for SM and IM, respectively, corresponding to different values of structure width $(L+D)/h_1$. Unlike the variations observed in the minimum values in R_{SM} and R_{IM}, corresponding to different values of the parameters f and ϵ, change in width $(L+D)/h_1$ for fixed f and fixed ϵ does not bring any change in the minimum values of the reflection coefficients. This confirms that the minimum values for R_{SM} and R_{IM} do not depend on the structural width but they are totally dependent on the friction factor f and porosity ϵ only. For the waves in SM, the difference in the values of the reflection coefficients corresponding to various values of $(L+D)/h_1$ gradually reduces. This means that greater structural width gives higher reflection. However, when structural width is increased, waves in IM experience a similar wave-like nature but the effect of various structural width can be noticed corresponding to higher values of incident angle. While attaining the minimum value in wave reflection, significant difference can be observed.

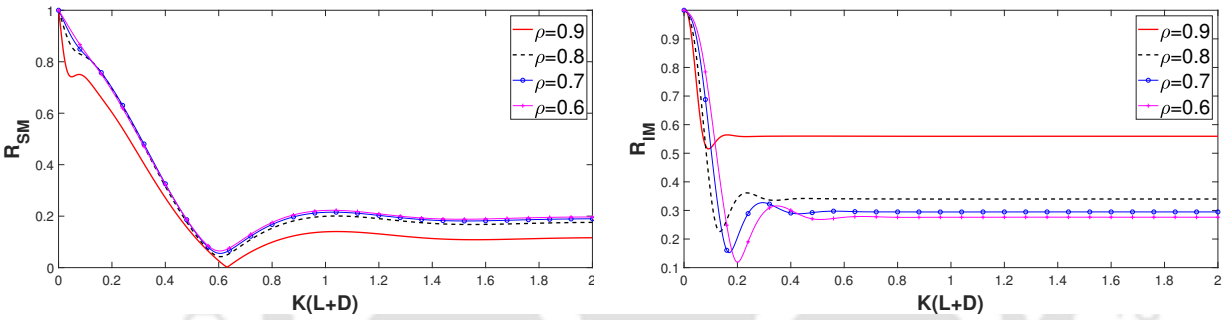

(a) (b)

Figure 2.12: Variation of (a) R_{SM} and (b) R_{IM} against non-dimensional width of the blocks $K(L+D)$ corresponding to various values of ρ with $f_1 = f_2 = 1$, $\epsilon_1 = \epsilon_2 = 0.9$ and $\theta = 30°$.

In Figure 2.12(a,b), reflection coefficients are plotted against width $K(L+D)$ corresponding to various values of density ratio ρ. In SM, a lower density ratio gives higher reflection and on the other hand, for IM, higher density ratio gives higher reflection. It is observed that, after some specific value of density ratio, the change in the ratio does not affect wave reflection for both modes. However, corresponding to higher values of structural width $K(L+D)$, both the reflection modes converge to a steady value. In SM, the optimum wave reflection is also obtained for nearly the same structural width for any density ratio. On the other hand, a visible difference is observed while obtaining optima in IM, i.e., the structural width needs to be increased when a fall in the values of density ratio occurs. It may be noted that, for waves in interface modes (IM), as the density ratio ρ approaches 1, the reflection coefficient which also approaches 1 is higher corresponding to higher values of $K(L+D)$. This is highly desired since, as ρ approaches unity, wave concentration in IM near the interface increases significantly for deep-water waves. This

TH-2746_176123008

increase in the interface elevation establishes the fact that there are more waves in IM. It is important to note that as $\rho \approx 1$ in real ocean, the preceding observation suggests that the structure is subjected to a large waveload in the case of a two-layer fluid when the interface is closer to the free surface. Thus, the effect of the wave motion in IM remains significant as $\rho \approx 1$.

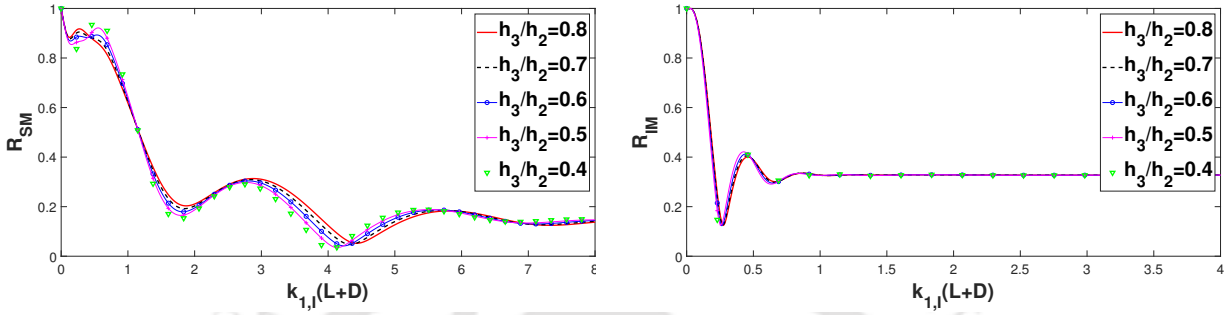

(a) (b)

Figure 2.13: Variation of (a) R_{SM} and (b) R_{IM} against $k_{1,I}(L+D)$ corresponding to different values of h_3/h_2 with $\theta = 0°$, $f_1 = f_2 = 0.5$ and $\epsilon_1 = \epsilon_2 = 0.9$.

In Figure 2.13(a,b), reflection coefficients R_{SM} and R_{IM} are plotted against $k_{1,I}(L+D)$ in SM and IM, respectively, corresponding to various values of depth ratio h_3/h_2. No significant difference is observed for IM, but there are visible differences in wave reflection occurring for SM. For the waves in SM, there are oscillatory patterns in reflection, and overall, the reflection is higher corresponding to lower structural width, whereas it gradually reduces as the width increases. As the step ratio $(h_2 - h_3)/h_2$ increases, a small amount of higher wave reflection can be observed in SM. With an increase in the structural width, the reflection modes attain a steady state. However, for a wider structure, the depth ratio does not affect wave reflection in any propagating mode.

In Figure 2.14(a,b), wave forces $F_{f,1}$ and F_w, respectively, are plotted against $k_{1,I}(L+D)$ corresponding to different values of friction parameter where $f_1 = f_2$. Both the figures show that wave forces generally reduce for an increase of the friction parameter. This may have happened due to the dissipation of a large amount of wave force by the structure. Further, from Figure 2.14(c), it can be observed that energy loss occurs due to the presence of the step bottom and the second porous block. Figure 2.14(b) clearly shows that, for lower friction $f_1 = f_2 = 0.5$, higher waveload on the wall results and increasing friction can result in reduction of waveload. Although the waveload $F_{f,1}$ shows a negligible difference for different friction values but Figure 2.14(c) clearly shows that the waveload impact for lower friction is pretty much higher and the loss of waveload also decreases sharply along with the increase of friction. Figure 2.14 clearly establishes that appropriate friction parameter should be chosen to get the lowest impact on the rigid wall. When the structural width is increased, F_{RW} at $x = L$ also reduces while lower friction

TH-2746_176123008

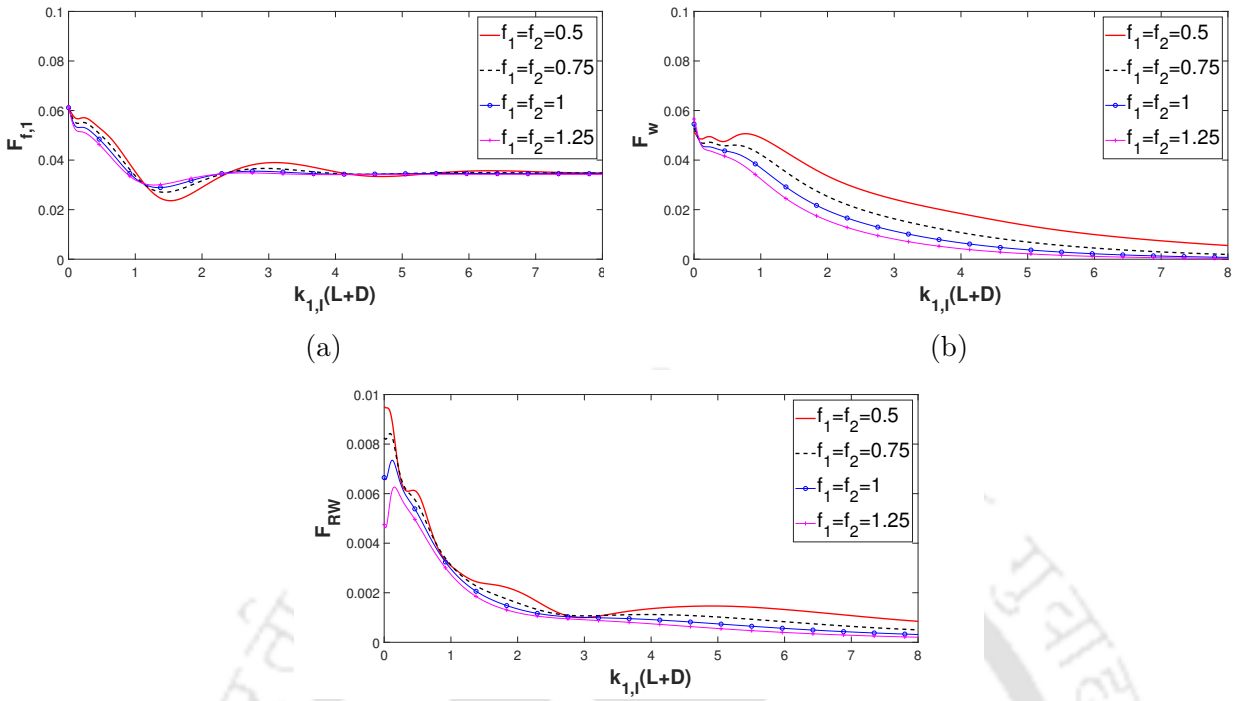

Figure 2.14: Variation of wave force (a) $F_{f,1}$, (b) F_w and (c) F_{RW} at $x = L$ against $k_{1,I}(L + D)$ corresponding to different values of f_j with $\epsilon_1 = \epsilon_2 = 0.8$ and $\theta = 30°$.

and lower width are found to be responsible for higher reduction of waveload. This limited reduction of wave force (for higher $k_{1,I}(L + D)$) is observed due to the insignificant effect of the step bottom for the case of wide structures, for which the waveloads $F_{f,2}$ and $F_{b,1}$ are nearly the same. Another reason for this limited reduction is the steadiness of the wave forces corresponding to higher values of $k_{1,I}(L + D)$. This happens because wave reflection remains steady beyond a specific structural width.

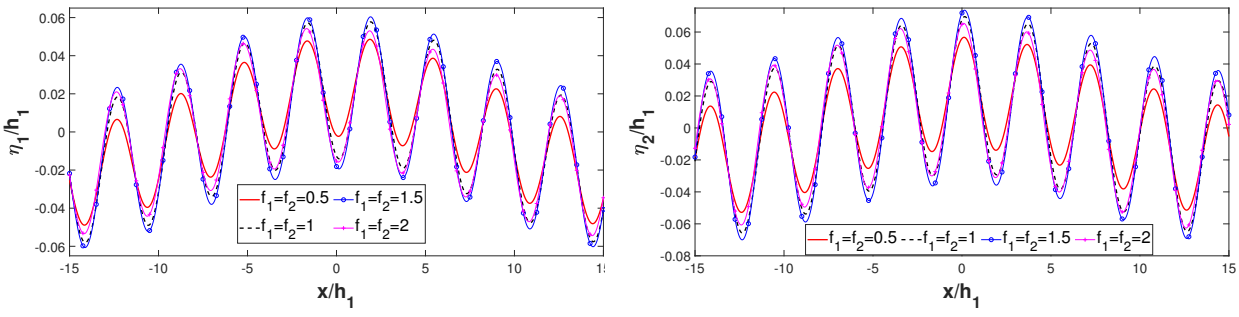

Figure 2.15: Variation of the non-dimensional elevation amplitude for (a) free surface and (b) interface against x/h_1 corresponding to various values of f_j with $L/h_1 = D/h_1 = 0.5$, $\theta = 30°$ and $\epsilon_1 = \epsilon_2 = 0.5$.

TH-2746_176123008

Figure 2.15(a,b) presents the elevations η_1/h_1 at the free surface and η_2/h_1 at the interface, respectively, plotted against the non-dimensional distance x/h_1 corresponding to different values of friction coefficients for $f_1 = f_2$, where x is the distance in the horizontal direction measured from $x = 0$. Both the figures show that the elevation at the interface becomes higher than the elevation at the free surface. We can assume that this difference between the elevations of these two modes is observed due to the resonating interaction between the free surface waves and interfacial waves. The elevations in both propagating modes increase when the friction f_j takes higher values. However, for both modes, we can observe a significant reduction of elevations in the second porous region.

2.4.2 Porous blocks with different porosity and friction

Now we consider different porosity and friction parameters for each of the blocks. In other words, we examine interaction of waves with a composite type of structure for which also, as in the earlier case, we examine the effect of porosity and friction on the reflection characteristics.

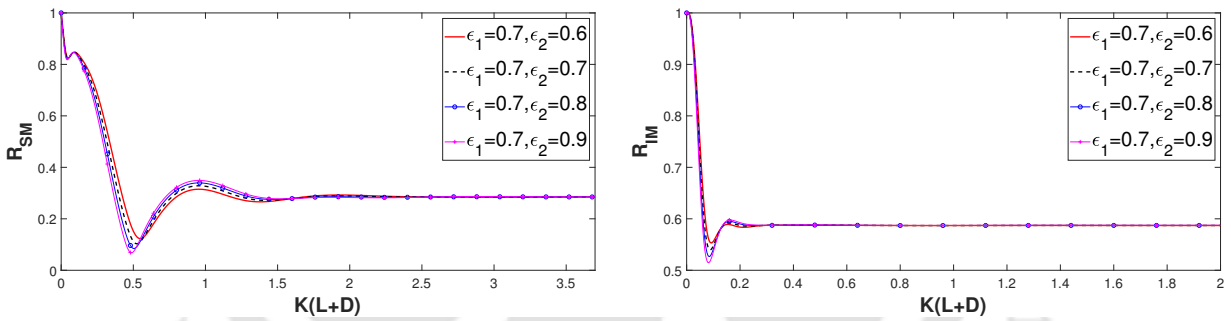

(a) (b)

Figure 2.16: Variation of (a) R_{SM} and (b) R_{IM} against $K(L+D)$ corresponding to various porosity of the second block with ϵ_1 fixed, $f_1 = f_2 = 1$ and $\theta = 0°$.

In Figures 2.16(a,b) and 2.17(a,b), the variation in reflection coefficients is plotted against $K(L+D)$ respectively, corresponding to various values of the porosity and friction. In Figure 2.16, negligible difference between the coefficients is observed in SM as well as in IM. However, Figure 2.16 shows that the same trend is observed for both propagating modes and after a certain value, the changed porosity has no significant effect on the width of the blocks. As seen in the case for the blocks with the same porosity in Figure 2.8(a,b), here also, lower friction and lower width give rise to higher values of reflection coefficients in both SM and IM (Figure 2.17). Although keeping the porosity $\epsilon_1 = \epsilon_2$ fixed and varying friction parameter f_1 of the first block (in Figure 2.17) give different coefficients in SM, they become convergent after certain width. In any case, the coefficients in SM or IM keep their minimum value approximately at the same width as the one observed

TH-2746_176123008

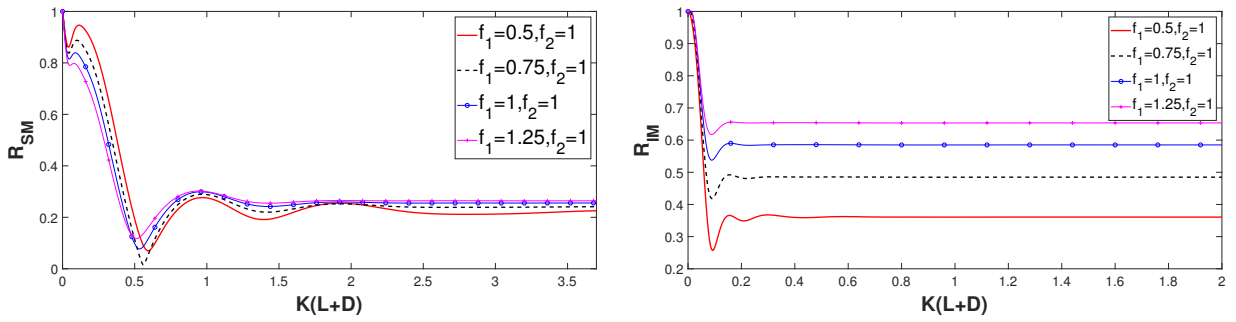

(a) (b)

Figure 2.17: Variation of (a) R_{SM} and (b) R_{IM} against non-dimensional width $K(L+D)$ corresponding to various values of friction parameter f_1 with f_2 fixed, $\epsilon_1 = \epsilon_2 = 0.75$ and $\theta = 0°$.

in Figures 2.7 and 2.8. The changes in the reflection coefficients in SM and IM establish that, after a certain width of the structure, the reflection in both modes reach steady states and therefore, there is an effect of ϵ_j and f_j which is, however, not significant for wider structures. Although different porosity ($\epsilon_1 \neq \epsilon_2$, Figure 2.16(a,b)) has no significant effect on total non-dimensional width but keeping the porosity lower for the first block results in lower reflection compared to the second one, and consequently, suitable width of the block should be chosen to prevent higher reflection in both modes. Alongside, the varying friction parameter also results in (i) lower reflection for $f_1 > f_2$ and (ii) higher reflection for $f_1 < f_2$ than those for the case $f_1 = f_2$. On the basis of our graphical results, if we make a comparison between a simple structure ($\epsilon_1 = \epsilon_2, f_1 = f_2$) and a composite structure ($\epsilon_1 \neq \epsilon_2, f_1 \neq f_2$), we observe that using a composite structure can have, on an average, a 18% higher reflection than that for the simple structure in SM. On the other hand, in IM, the composite structure can have nearly 12% higher reflection than that for the simple structure.

Figures 2.18(a) to 2.18(d) illustrate the effect of oblique angle θ on the reflection coefficient in surface mode and interface mode, respectively, for various porosity ϵ_j and friction parameter f_j keeping the porosity or friction of one of the blocks fixed. In Figure 2.18(a), the change of porosity does not affect the reflection in a significant way in SM, although in IM, all curves for different ϵ_j and f_j maintain a similar nature for all the cases (Figure 2.18(b)). Both R_{SM} and R_{IM} attain their minimum values in the ranges 80°-90° and 70°-90° in surface mode and interfacial mode, respectively, for θ (for both cases). As seen in Figures 2.9(a,b)-2.10(a,b), in SM, the incident angle for obtaining minimum differs to some extent for different porosity or friction but it is meanwhile the same in IM. Therefore, porosity and friction parameter behave in a similar manner against the angle of incidence for both cases. It can be concluded that it is advisable to use composite blocks to construct barriers to get minimum wave reflection.

TH-2746_176123008

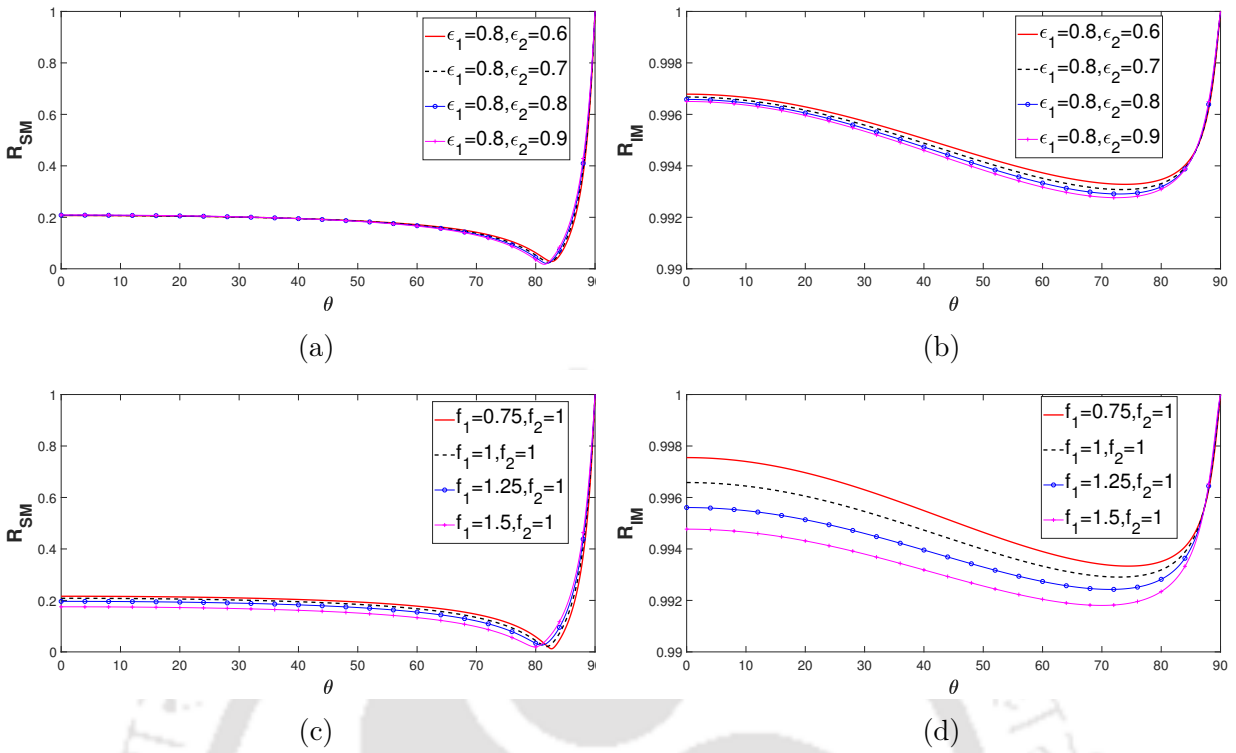

Figure 2.18: Variation of R_{SM} and R_{IM} against incident angle θ corresponding to various values of porosity and friction parameter keeping one of the parameter fixed, $f_1 = f_2 = 1$ (for (a,b)), $\epsilon_1 = \epsilon_2 = 0.8$ (for (c,d)) and $(L + D)/h_1 = 1/4$.

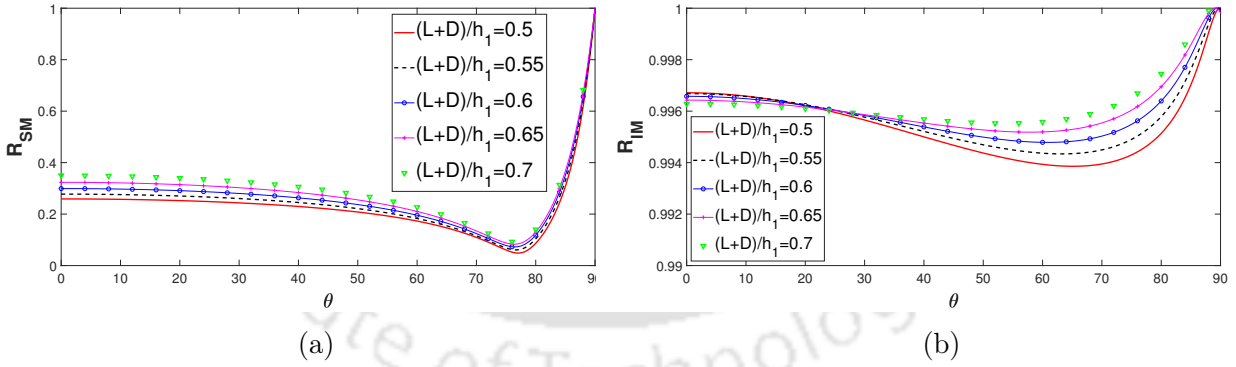

Figure 2.19: Variation of (a) R_{SM} and (b) R_{IM} against incident angle θ corresponding to various values of $(L + D)/h_1$ with $f_1 = f_2 = 1$ and $\epsilon_1 = 0.8$,$\epsilon_2 = 0.9$.

Figure 2.19(a,b) presents the reflection coefficients R_{SM} and R_{IM} plotted against incident angle θ in SM and IM corresponding to various values of $(L + D)/h_1$. The minimum in reflection for various values of $(L + D)/h_1$ occurs for the same incident angle in any mode. As in Figure 2.11(a,b), here also we observe a similar nature of the reflection coefficients. Even the minimum of reflection also occurs for the same range of angles in both modes as seen in Figure 2.11(a,b). Higher values of $(L + D)/h_1$ results in higher reflection

TH-2746_176123008

for SM. On the other hand, for initial incident angles, we observe an opposite nature for IM but as the incident angle increases, a similar nature is observed.

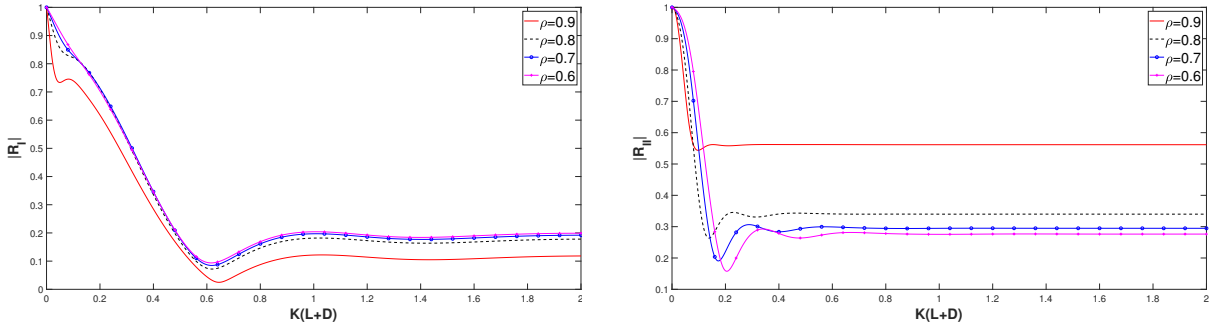

(a) (b)

Figure 2.20: Variation of (a) R_{SM} and (b) R_{IM} against non-dimensional total width of the structure $K(L+D)$ corresponding to various values of ρ with $f_1 = 1, f_2 = 1.2$, $\epsilon_1 = 0.9, \epsilon_2 = 0.8$ and $\theta = 30°$.

Figure 2.20(a,b) shows reflection coefficients plotted against the non-dimensional total width of the blocks corresponding to different values of density ratio ρ. A similar pattern is observed here also, as in Figure 2.12, for both propagating modes. In SM, a lower density ratio gives higher reflection and vice versa for IM. The same explanation provided for higher reflection in interface mode as in Figure 2.12(b) holds good for the case of Figure 2.20(b). For both propagating modes, the reduction of density ratio exhibits a convergent behaviour in wave reflection.

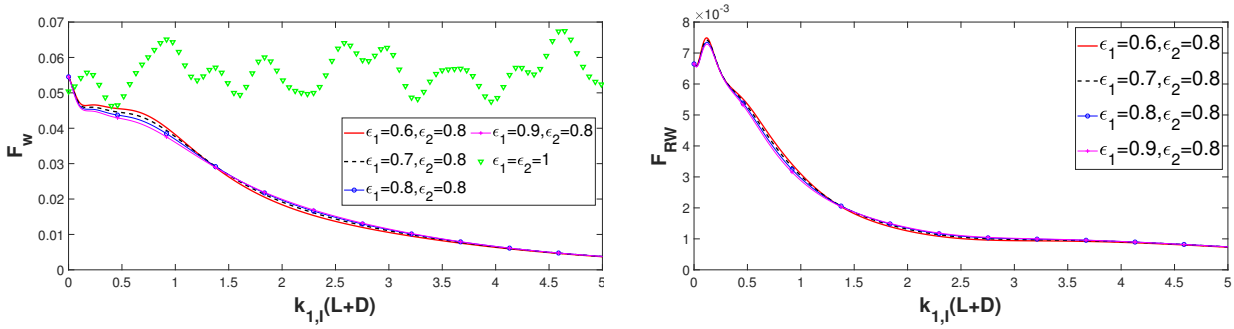

(a) (b)

Figure 2.21: Variation of wave force (a) F_w and (b) F_{RW} against $k_{1,I}(L+D)$ corresponding to various values of porosity with $f_1 = f_2 = 1$ and $\theta = 30°$.

Figures 2.21(a,b) and 2.22(a,b) look into the behaviour of the wave force F_w and force reduction F_{RW} against $k_{1,I}(L+D)$ corresponding to different values of porosity and friction. The patterns of wave force F_w on the rigid wall is similar in general in comparison to those seen in Figure 2.14. In both cases, the reduction of wave force is very high for

TH-2746_176123008

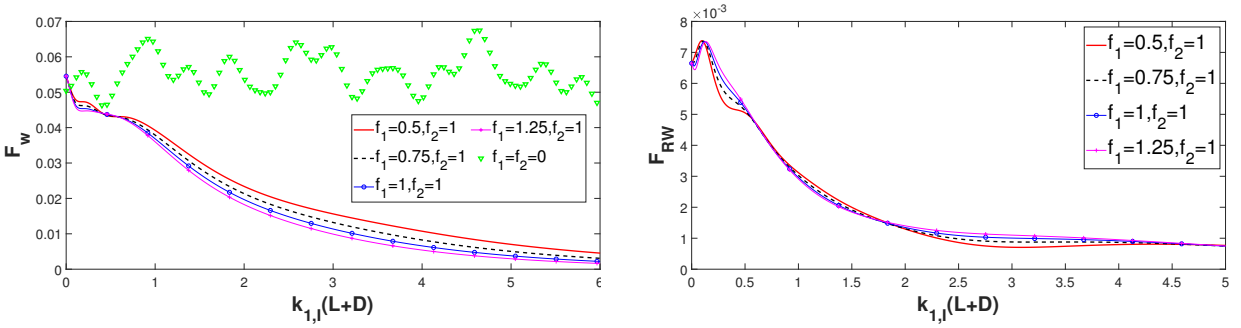

(a) (b)

Figure 2.22: Variation of wave force (a) F_w and (a) F_{RW} against $k_{1,I}(L+D)$ corresponding to various values of friction parameter with $\theta = 30°$ and $\epsilon_1 = \epsilon_2 = 0.8$.

lower structural width, although at some particular width, the reduction of force assumes a steady rate. The effect of the presence of the porous structure is also clearly observed by plotting for the numerical data $f_1 = f_2 = 0$ and $\epsilon_1 = \epsilon_2 = 1$ which converts the porous region into a plain water one. It can be clearly observed that, without the presence of the structure, the waveload is much higher. It also signifies the effect of wave dissipation due to the presence of porous structure. From Figures 2.21(b) and 2.22(b), we can observe that using a composite structure ($\epsilon_1 \neq \epsilon_2, f_1 \neq f_2$) can result in a better reduction of wave force at $x = L$ compared to that for a simple structure ($\epsilon_1 = \epsilon_2, f_1 = f_2$). Also, Figures 2.21(a) and 2.22(a), respectively, show that approximately 2% and 7% lower wave impact is made possible by using a composite structure rather than a simple structure. Even though this comparison is solely on the basis of the results found for some sample parameters, we are confident that it can support our conclusion to use composite structures as wave-absorbers. Moreover, we observe that the waveload F_w is lower for lower ϵ_2 ($\epsilon_1 \geq \epsilon_2$) and lower f_2 ($f_1 \geq f_2$). Reduction of wave force is also observed to be lower under the same consideration at the vertical boundary between the blocks.

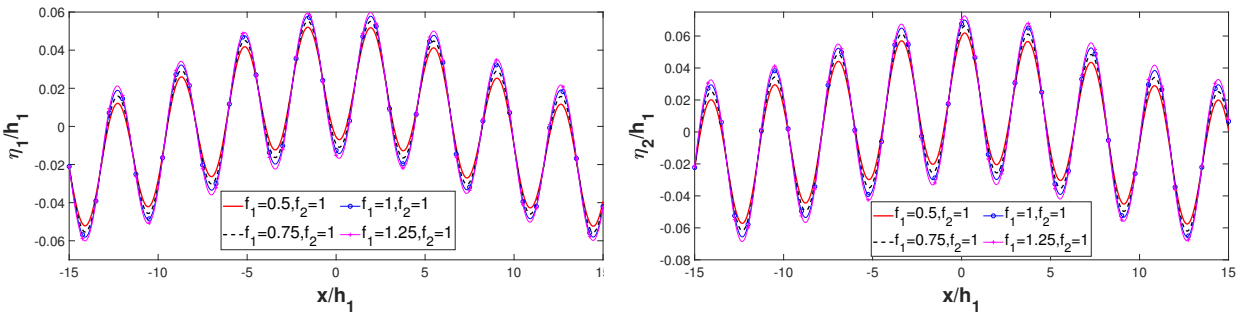

(a) (b)

Figure 2.23: Variation of non-dimensional elevation against x/h_1 at (a) free surface and (b) interface corresponding to various values of ϵ_1 with $L/h_1 = D/h_1 = 0.5$ and $\epsilon_1 = 0.6, \epsilon_2 = 0.8$ and $\theta = 30°$.

TH-2746_176123008

Figure 2.23(a,b) presents free surface and interface elevations against x/h_1 corresponding to values of friction parameter f_1 of the first porous region. Similar to Figure 2.15, here also, the interface elevations are comparatively higher than the free surface elevation. Effect of the porous blocks brings a reduction in the elevations between the porous regions in front of the rigid wall. Therefore, the case $f_1 \leq f_2$ results in lower elevation compared to the case $f_1 > f_2$. It also justifies our conclusion to take lower friction in the first block along with other geometrical configurations to construct an efficient breakwater.

Subsequently, by an appropriate selection of physical parameters for a composite type structure interacting with waves, a tranquillity zone can be created which will reduce waveload on the rigid wall and the porous structure to a large extent.

2.5 Special case: Wave interaction with vertically composite caisson-type breakwaters

Multiple-porosity objects are mainly used to construct various kinds of shoreline protectors, e.g., breakwaters. The vertically composed caisson-type breakwater is one of the familiar examples. The structure under consideration here is placed on a common elevated bottom of height $(h_1 - h_2)$. Due to this, equation (2.13) in the earlier problem is of no consequence.

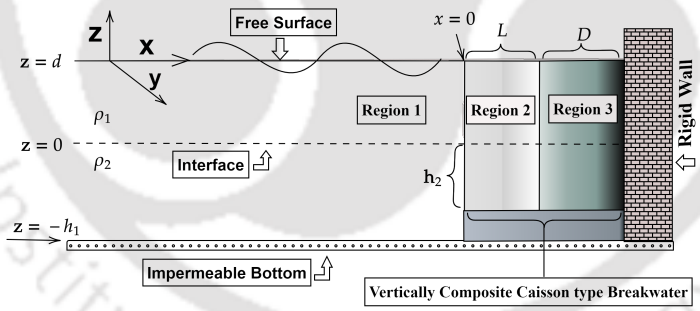

Figure 2.24: Schematic diagram of wave interaction by caisson-type breakwater

Except for the first equation of (2.27), equations (2.25)-(2.28) remain unchanged for the governing matrix equations system with $h_2 = h_1$. Now, using the orthogonality of $I_{2,n}$ gives us

$$\left(A_m e^{\mathrm{i}q_{2,m}L} - B_m\right) q_{2,m} a_{2,m} + \mathrm{i}\varkappa \sum_{n=I,II,1}^{N} C_n q_{3,n} \sin(q_{3,n}D)\hat{b}_{2,m,n} = 0, \tag{2.40}$$

$$\gamma_1\left(A_m e^{\mathrm{i}q_{2,m}L} + B_m\right) a_{2,m} - \gamma_2 \sum_{n=I,II,1}^{N} C_n \cos(q_{3,n}D)\hat{b}_{2,m,n} = 0. \tag{2.41}$$

TH-2746_176123008

Using (2.40) and (2.41) along with (2.29) and (2.30), a system of equations of the form $\tilde{A}\tilde{X} = \tilde{B}$ is obtained from which we can evaluate the unknown coefficients in a similar manner as was adopted in the earlier case.

2.5.1 Results

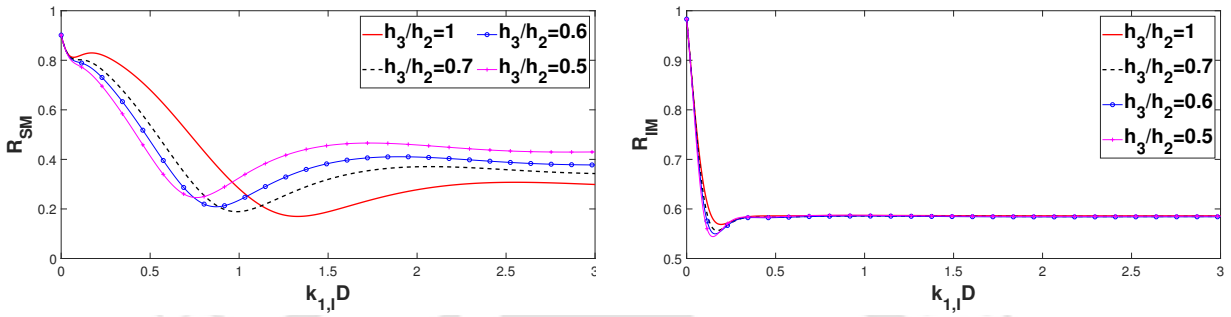

(a) (b)

Figure 2.25: Variation of (a) R_{SM} and (b) R_{IM} against non-dimensional width of the second block $k_{1,I}D$ corresponding to various values of h_3/h_2 with $L/h_1 = 1/4$; $f_1 = 1$, $f_2 = 1.5$, $\epsilon_1 = 0.6, \epsilon_2 = 0.8$ and and $\theta = 0°$.

Comparison of results for step-type breakwater and vertically composite caisson-type breakwater are shown in Figures 2.25(a,b) and Figures 2.26(a,b,c). From the comparison of reflection coefficients plotted against non-dimensional $k_{1,I}D$, we can observe the impact of different step ratios (h_3/h_2), and no step effect in both modes. A similar wave-like nature in SM is observed for all step ratios. It is observed from Figure 2.25 that different depth ratios alter the values of reflection coefficients appreciably in SM whilst for waves in IM, the coefficients do not exhibit any major difference for any case except the reflecting mode of caisson type breakwater. On an average, a maximum of 15% higher reflection in SM can be attained by using a step-type structure (for $h_3/h_2 \neq 1$) compared to that due to a common elevated structure ($h_3/h_2 = 1$). But, in IM, the difference between those two types of structures is very negligible ($\leq 0.5\%$).

Further, in Figures 2.26(a) to 2.26(c), the wave forces $F_{f,1}, F_w$ and the reduction of wave force at $x = L$ (F_{RW}) are examined. The wave force $F_{f,1}$ shows negligible effect due to the change of structure width in Region 3, but a reasonable difference is observed for the wave impact F_w on the wall and that for F_{RW}. For the caisson-type breakwater, the reduction of wave force is nearly zero. On the other hand, it is clear that the step-type structure produces a reasonable amount of energy loss due to the steps. On an average, 21% lower waveload on the wall can be attained by using a step-type structure (for $h_3/h_2 = 0.7$) instead of a common elevated structure. But the average wave force $F_{f,1}$ does not show any difference (nearly 0%) between these two kinds of structures. Also,

TH-2746_176123008

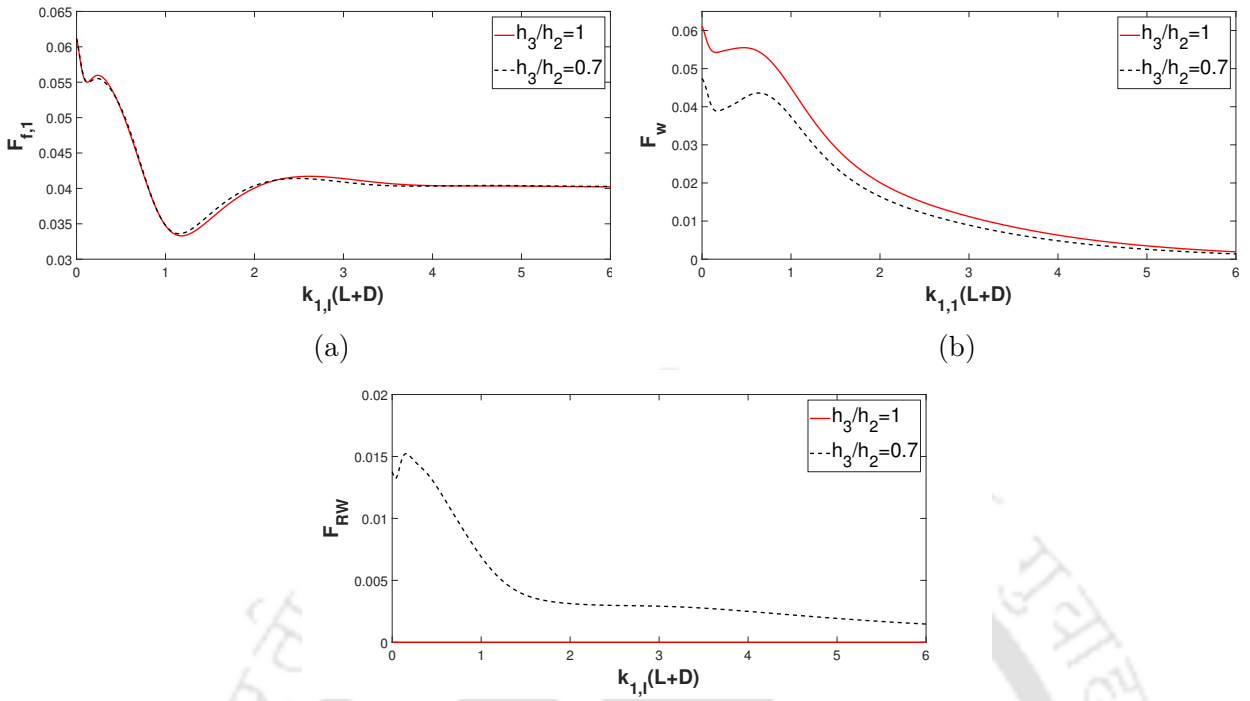

Figure 2.26: Variation of (a) $F_{f,1}$, (b) F_w (c) F_{RW} against non-dimensional total width of the structure $k_{1,I}(L+D)$ corresponding to various values of h_3/h_2 with $f_1 = 1, f_2 = 1.5$, $\epsilon_1 = 0.6, \epsilon_2 = 0.8$ and $\theta = 0°$

the average F_{RW} is very much higher for the case $h_3/h_2 \neq 1$ which establishes a better dissipating nature of the step-type structure than a structure without steps. It is to be noted that waveloads and reflection coefficients are being compared corresponding to our tested results only.

2.6 Porous bottom effects on composite structure

In any practical situation, the sea-bed is not impermeable and it is composed of some absorbent which makes the bed percolative. Due to the percolative property, there may be some effect of the sea-bed on the wave reflection and energy. In this section, we consider the sea-bed for the portion $-\infty < x < 0$ to be porous and subsequently, we examine the effect of this bottom on reflection phenomenon.

2.6.1 Mathematical formulation and solution

We consider a porous sea-bed and the composite structure is placed within the same bathymetry. Then bottom boundary condition (2.2) for Region 1 ($j = 1$) gets converted

TH-2746_176123008

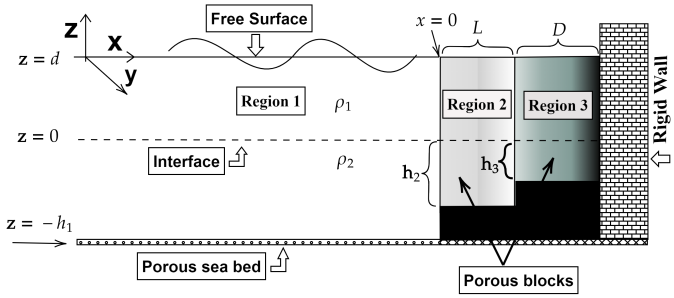

Figure 2.27: Definition sketch of wave interaction of the porous structure placed on a step following a porous sea-bed

into

$$\frac{\partial \phi_1}{\partial z} + G_1 \phi_1 = 0 \qquad \text{at} \qquad z = -h_1, \tag{2.42}$$

where G_1 is the real porous-effect parameter of the sea-bed (See Section 1.4).

Therefore, the velocity potential ϕ_1 satisfying (2.42) takes a similar form like (2.15):

$$\phi_1 = \sum_{n=I}^{II} \left(e^{\mathrm{i}q_{1,n}x} + R_n e^{-\mathrm{i}q_{1,n}x} \right) I_{1,n}(p_n, z) + \sum_{n=1}^{\infty} R_n e^{-\mathrm{i}q_{1,n}x} I_{1,n}(p_n, z), \tag{2.43}$$

where $n = 1, 2$, respectively, denote the two propagating modes - surface mode and interface mode - corresponding to a real G_1 and $n = 3, 4, \ldots$, denote the evanescent modes, $q_{1,n} = \sqrt{p_n^2 - k_y^2}$ and the eigenfunctions are given by

$$I_{1,n} = \begin{cases} \dfrac{g(p_n)\big(K \sinh p_n(z-d) + p_n \cosh p_n(z-d)\big)}{K \cosh p_n d - p_n \sinh p_n d}, & 0 < z < d, \\ \left(\cosh p_n(z+h_1) - \dfrac{G_1}{p_n} \sinh p_n(z+h_1) \right), & -h_1 < z < 0, \end{cases} \tag{2.44}$$

where $g(p_n) = \left(\sinh p_n h_1 - \dfrac{G_1}{p_n} \cosh p_n h_1 \right)$.

The wavenumber p_n satisfies the dispersion relation

$$\begin{aligned} &K^2(\rho + \coth p_n d \coth p_n h_1) - K p_n(\coth p_n d + \coth p_n h_1) + p_n^2(1-\rho) \\ &+ \frac{G_1}{p_n}\left[(\rho-1)p_n^2 \coth p_n h_1 - K^2(\rho \coth p_n h_1 + \coth p_n d)\right. \\ &\left. + p_n K(1 + \coth p_n h_1 \coth p_n d)\right] = 0. \end{aligned} \tag{2.45}$$

Equation (2.45) has two sets of positive and symmetrically negative real roots and infinitely many purely imaginary roots for real G_1, which is associated with the special percolated porous bottom. Applying the procedure adopted in Section 2.2, we solve the system of equations (2.33), with different eigenfunction $I_{1,n}$ as given by (2.44), to find the

TH-2746_176123008

unknown coefficients.

2.6.2 Results

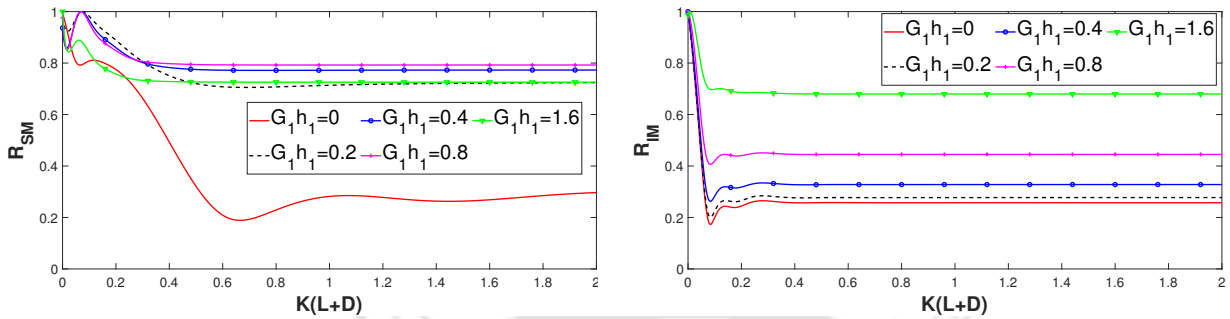

(a) (b)

Figure 2.28: Variation of reflection coefficients against $K(L+D)$ at (a) free surface and (b) interface corresponding to various values of G_1h_1 with $\epsilon_1 = 0.5, \epsilon_2 = 0.7$ and $f_1 = 0.75, f_2 = 1$.

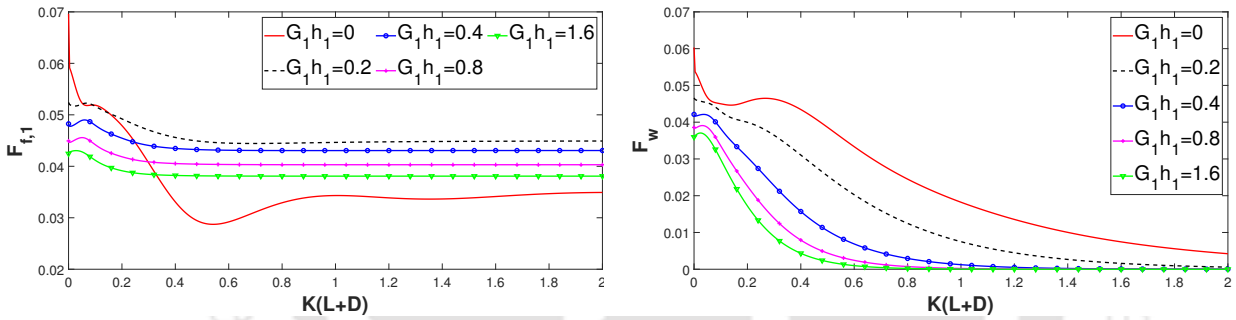

(a) (b)

Figure 2.29: Variation of (a) $F_{f,1}$ and (b) F_w against non-dimensional $K(L+D)$ corresponding to various values of G_1h_1 with $f_1 = 0.75, f_2 = 1$ and $\epsilon_1 = 0.5, \epsilon_2 = 0.7$.

Porous bottom effect on a porous structure placed on a step-like bottom is examined in Figures 2.28(a,b) and 2.29(a,b) where $G_1h_1 = 0$ refers to the impermeable sea-bed. In Figure 2.28, reflection coefficients are plotted in both propagating modes for various bottom porosity. The effect of porous sea-bed can easily be observed in reflection coefficients for both SM and IM. In both propagating modes, lower reflection values are observed for zero G_1 (impermeable bed). Due to the consideration of porosity of the sea-bed, higher reflection is observed in both propagating modes, as also was observed by Chanda and Bora [14]. Similarly, the porous bed impact for wave forces $F_{f,1}$ and F_w is clearly visible in Figure 2.29(a,b). In this case, wave force $F_{f,1}$ maintains a steady state corresponding to an increasing width but F_w gradually reduces to very low values. Different values of G_1h_1 produce a major difference for $F_{f,1}$ which clearly shows that, for thin structures ($K(L+D) < 0.2$), higher waveload $F_{f,1}$ is observed due to the bed impermeability but

TH-2746_176123008

this decays with the increase of the structure width. Furthermore, regarding the waveload on the wall, visible difference is observed in the model with the incorporation of the sea-bed porosity in which case, a lower waveload F_w on the wall occurs, contrary to the case for an impermeable sea-bed for which a higher waveload F_w is observed on the wall. It is worthwhile mentioning that a major portion of the wave energy gets dissipated through the porous sea-bed which may have resulted in the lower impact of waveload on the rigid sea-wall compared to the case when the sea-bed is impermeable. Even higher G_1h_1 results in a negligible wave impact on the sea-wall for wide structures ($K(L+D) > 1.2$).

2.7 Conclusion

This work studies oblique water wave interaction by a simple porous structure and a composite porous structure, with different block-wise porosity, of finite width in a two-layer fluid flowing over a multi-step bottom where the structures pierce the linear interface. Linear water wave theory and eigenfunction expansion are utilized to find the solution of the corresponding scattering problem. The structure is placed on the multi-step bottom in water of finite depth. By using the given equations and conditions, a system of linear algebraic equations is obtained and solved which in turn gives the potentials and the reflection coefficients. The roots of the dispersion relations are computed and analysed. Thereafter, a number of numerical results are obtained and analyzed. The reflected waves, along with the elevations on the free surface and interface, exist due to wave interaction with the porous structure. We observe a greater waveload on both porous regions and on the vertical rigid wall due to the mutual interactions of the both surface and interfacial wave modes. This study also leads us to find the optimum width with suitable structural configuration, which makes a porous structure more efficient to possess both reflective and dissipative characteristics. Consideration of moderate values of the angle of incidence allows to achieve minimum wave reflection through the utilization of a porous composite structure as a breakwater. By an appropriate selection of structural height, width, porosity and porous impedance parameter, one can find (i) the minimum wave reflection by the structure, (ii) the minimum values of the waveload on the porous structure and the wall. Further, the maximum wave reflection can be achieved by the interface-piercing structures with suitable positioning of the interface. A composite porous structure produces a better desired result compared to a simple structure. The wave forces acting on the wall and porous structure are found to be higher in the case of the composite structure corresponding to higher porosity of the first block. Further, as a special case, the sea-bed preceding the step bottom is considered to be porous, and it is observed that the porosity of the bed has a reasonable impact on reflection phenomenon.

As a summary, the study of water wave interaction with such structures presents a

TH-2746_176123008

clear understanding of the effect of the porous structures that have the capability to create a tranquillity zone. It also demonstrates that there is some sort of relation among the optimum wave reflection by the porous structures, the optimum waveload on the rigid wall and the maximum waveload on the porous structure. Thus, using a composite porous structure with suitable geometric characteristics is a more viable option in creating a tranquillity zone to protect the coastal facilities appropriately. Validation of present result with an available result shows a very good agreement which points toward the appropriateness of the present model.

TH-2746_176123008

CHAPTER 3

Scattering and trapping of water waves by a composite breakwater placed on an elevated bottom in a two-layer fluid flowing over a porous sea-bed

3.1 Mathematical formulation

The problem of surface wave interaction with a composite porous breakwater, consisting of two vertical portions with different porosity and placed on an impermeable stony block bottom, in a two-layer fluid over a porous sea-bed is considered in Cartesian coordinates by using linear water wave theory. Irrotational and simple harmonic motion is assumed in this two-layer fluid, which is inviscid and incompressible, with a free surface and a linear interface under the action of gravity.

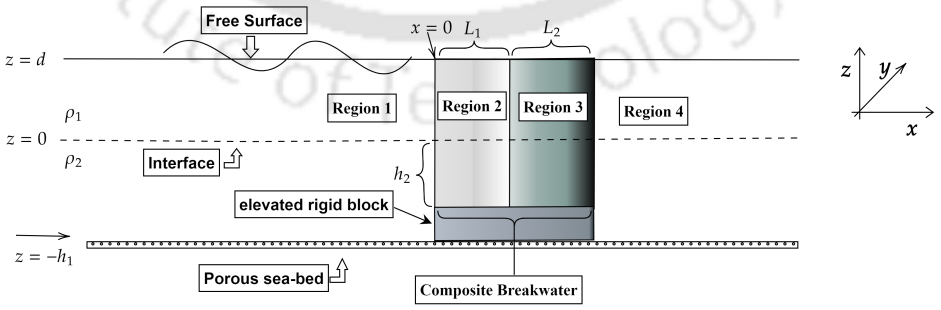

Figure 3.1: Sketch definition of scattering model

The coordinate system is chosen such that $z = 0$ is the interface of the fluid layers and the z-axis is considered positive in upward direction. The upper layer fluid having density

TH-2746_176123008

ρ_1 has its mean free surface at $z = d$ and the lower layer fluid with density ρ_2 has its bottom in the form of a porous sea-bed at the mean bottom $z = -h_1$ followed by an elevated rigid block of height $(h_1 - h_2)$ from $x = 0$ to $x = (L_1 + L_2)$. The obliquely incident surface wave strikes the porous structure at an angle θ to the x-axis. It ensures that velocity potentials Φ_j for $j = 1, 2, 3, 4$ can be expressed as $\Phi_j(x, y, z, t) = \mathrm{Re}[\phi_j(x, z)e^{\mathrm{i}(k_y y - \omega t)}]$ in Regions 1, 2, 3 and 4, respectively, as shown in Figure 3.1. The variation of the potentials $\Phi_j (j = 1, 2, 3, 4)$ in the y-direction is taken to be the same so that we can match the velocity potentials along the vertical boundaries (by Snell's Law). For layer-wise clear understanding, the potentials $\phi_j(x, z)$ for $j = 1, 2, 3, 4$ are split along the z-direction as follows:

$$\phi_j = \left\{ \begin{array}{ll} \psi_j^{(1)}, & 0 < z < d, \\ \psi_j^{(2)}, & -h_1 < z < 0, \end{array} \right\} \text{ for } j = 1, 4, \tag{3.1}$$

$$\phi_j = \left\{ \begin{array}{ll} \psi_j^{(1)}, & 0 < z < d, \\ \psi_j^{(2)}, & -h_2 < z < 0, \end{array} \right\} \text{ for } j = 2, 3, \tag{3.2}$$

where the superscripts $^{(1)}$ and $^{(2)}$ denote potentials for the specific layers.

With all above considerations, the boundary value problems involving these potentials $\phi_j, j = 1, 2, 3, 4$ are governed by modified Helmholtz equation as follows:

$$(\nabla^2_{x,z} - k_y^2)\phi_j = 0 \quad \text{for } j = 1, 2, 3, 4. \tag{3.3}$$

For clear understanding, equation (3.3), with the expressions from (3.1) and (3.2), is split into the following:

$$(\nabla^2_{x,z} - k_y^2)\psi_j^{(1)} = 0, \quad 0 < z < d, \text{ for } j = 1, 2, 3, 4, \tag{3.4}$$

$$(\nabla^2_{x,z} - k_y^2)\psi_j^{(2)} = 0, \quad -h_1 < z < 0, \text{ for } j = 1, 4, \tag{3.5}$$

$$(\nabla^2_{x,z} - k_y^2)\psi_j^{(2)} = 0, \quad -h_2 < z < 0, \text{ for } j = 2, 3. \tag{3.6}$$

The linearized mean free surface condition for Regions 1 and 4 is given by

$$\frac{\partial \psi_j^{(1)}}{\partial z} - K\psi_j^{(1)} = 0 \text{ on } z = d \ (j = 1, 4). \tag{3.7}$$

On the other hand, the linearized mean free surface condition in Regions 2 and 3 is

$$\frac{\partial \psi_j^{(1)}}{\partial z} - K\gamma_j\psi_j^{(1)} = 0 \text{ on } z = d \ (j = 2, 3), \tag{3.8}$$

where $\gamma_j = m_j + \mathrm{i}f_j$ for $j = 1, \ldots, 4$, is the porous impedance parameter (See Appendix A). We assume $f_1 = f_4 = 0, m_1 = m_4 = 1$, and hence $\gamma_1 = \gamma_4 = 1$ which corresponds to

the situation in Regions 1 and 4 containing only water. Further, Regions 2 and 3 have porosity $\epsilon_j,\ j = 2, 3$ with the assumption of $\epsilon_j = 1$ for $j = 1, 4$.

The velocity potential $\psi_j^{(2)}$ satisfies the following bottom boundary condition:

$$\frac{\partial \psi_j^{(2)}}{\partial z} + G\psi_j^{(2)} = 0 \text{ on } z = -h_1, \text{ for } j = 1, 4, \tag{3.9}$$

where G is the real porous-effect parameter of the sea-bed (See Section 1.4).

Due to the impermeable step bottom, the porous regions have the bottom boundary condition as follows:

$$\frac{\partial \psi_j^{(2)}}{\partial z} = 0 \text{ on } z = -h_2, \text{ for } j = 2, 3. \tag{3.10}$$

The linearized matching conditions at the mean interface $z = 0$ can be written in the following forms:

$$\frac{\partial \psi_j^{(1)}}{\partial z} = \frac{\partial \psi_j^{(2)}}{\partial z} \quad \text{for } j = 1, 2, 3, 4, \tag{3.11}$$

$$\rho\left(\frac{\partial \psi_j^{(1)}}{\partial z} - K\psi_j^{(1)}\right) = \left(\frac{\partial \psi_j^{(2)}}{\partial z} - K\psi_j^{(2)}\right) \quad \text{for } j = 1, 4, \tag{3.12}$$

$$\rho\left(\frac{\partial \psi_j^{(1)}}{\partial z} - K\gamma_j\psi_j^{(1)}\right) = \left(\frac{\partial \psi_j^{(2)}}{\partial z} - K\gamma_j\psi_j^{(2)}\right) \quad \text{for } j = 2, 3, \tag{3.13}$$

where $\rho = \rho_1/\rho_2 < 1$.

Further, combining the potentials $\psi_j^{(1)}$ and $\psi_j^{(2)}$ into ϕ_j as given in (3.1) and (3.2) for $j = 1, 2, 3, 4$, the continuity of mass flux and pressure across the interfaces $x = 0, L_1, (L_1 + L_2)$ gives the following matching conditions:

$$\phi_1 = \gamma_2\phi_2, \quad \frac{\partial \phi_1}{\partial x} = \epsilon_2\frac{\partial \phi_2}{\partial x}, \quad \text{at } x = 0 \quad \text{for } -h_2 < z < d, \tag{3.14}$$

$$\gamma_2\phi_2 = \gamma_3\phi_3, \quad \epsilon_2\frac{\partial \phi_2}{\partial x} = \epsilon_3\frac{\partial \phi_3}{\partial x}, \quad \text{at } x = L_1 \quad \text{for } -h_2 < z < d, \tag{3.15}$$

$$\gamma_3\phi_3 = \phi_4, \quad \epsilon_3\frac{\partial \phi_3}{\partial x} = \frac{\partial \phi_4}{\partial x}, \quad \text{at } x = (L_1 + L_2) \quad \text{for } -h_2 < z < d. \tag{3.16}$$

Due to the rigid step, the velocity potentials $\psi_1^{(2)}$ and $\psi_4^{(2)}$ satisfy the following boundary conditions:

$$\frac{\partial \psi_1^{(2)}}{\partial x} = 0 \quad \text{at } x = 0 \text{ for } -h_1 < z < -h_2, \tag{3.17}$$

$$\frac{\partial \psi_4^{(2)}}{\partial x} = 0 \quad \text{at } x = (L_1 + L_2) \text{ for } -h_1 < z < -h_2. \tag{3.18}$$

TH-2746_176123008

3.2 Scattering problem

In this section, the scattering of waves by a composite porous structure placed on a rigid elevated bottom in a two-layer fluid flowing over a porous sea-bed is studied. At first, we derive the expansion formula for the velocity potential associated with surface wave interaction with a porous sea-bed of finite depth.

3.2.1 Plane wave approximation

Based on the equations from the previous section, solutions for the potential are evaluated. The width of the first and second blocks of the porous structure are taken to be L_1 and L_2, respectively, as shown in Figure 3.1. The velocity potentials $\psi_j^{(1)}$ and $\psi_j^{(2)}$ for $j = 1, 2, 3, 4$ satisfying the governing equations (3.4)-(3.6) and the respective boundary conditions (3.7)-(3.11) have the following forms:

$$\phi_j = \left\{ \begin{array}{ll} \psi_j^{(1)} & = \exp(\pm \mathrm{i}xq_1) I_1^{(1)}(k_1, z), \quad 0 < z < d, \\ \psi_j^{(2)} & = \exp(\pm \mathrm{i}xq_1) I_1^{(2)}(k_1, z), \quad -h_1 < z < 0, \end{array} \right\} \text{ for } j = 1, 4, \tag{3.19}$$

$$\phi_j = \left\{ \begin{array}{ll} \psi_j^{(1)} & = \exp(\pm \mathrm{i}xq_j) I_j^{(1)}(k_j, z), \quad 0 < z < d, \\ \psi_j^{(2)} & = \exp(\pm \mathrm{i}xq_j) I_j^{(2)}(k_j, z), \quad -h_2 < z < 0, \end{array} \right\} \text{ for } j = 2, 3, \tag{3.20}$$

with $q_j = \sqrt{k_j^2 - k_y^2}$ for $j = 1, 2, 3$, and $I_j(k_j, z)$ given by

$$I_1 = \left\{ \begin{array}{ll} I_1^{(1)} & = \dfrac{g(k_n)(K \sinh k_1(z-d) + k_1 \cosh k_1(z-d))}{K \cosh k_1 d - k_1 \sinh k_1 d}, \quad 0 < z < d, \\ I_1^{(2)} & = \left(\cosh k_1(z+h_1) - \dfrac{G}{k_1} \sinh k_1(z+h_1) \right), \qquad -h_1 < z < 0, \end{array} \right. \tag{3.21}$$

$$I_j = \left\{ \begin{array}{ll} I_j^{(1)} & = \dfrac{\sinh k_j h_2 (K\gamma_j \sinh k_j(z-d) + k_j \cosh k_j(z-d))}{K\gamma_j \cosh k_j d - k_j \sinh k_j d}, \quad 0 < z < d, \\ I_j^{(2)} & = \cosh k_j(z+h_2), \qquad -h_2 < z < 0, \end{array} \right. \tag{3.22}$$

where $g(k_n) = \left(\sinh k_1 h_1 - \dfrac{G}{k_1} \cosh k_1 h_1 \right)$.

All k_j appearing above can be found from the dispersion relations, constructed by using (3.12) and (3.13), through

$$K^2(\rho + \coth k_1 d \coth k_1 h_1) - K k_1(\coth k_1 d + \coth k_1 h_1) + k_1^2(1-\rho) + G\left[(\rho-1)k_1 \coth k_1 h_1 - \frac{K^2}{k_1}(\rho \coth k_1 h_1 + \coth k_1 d) + K(1 + \coth k_1 h_1 \coth k_1 d)\right] = 0. \tag{3.23}$$

$$K^2\gamma_j^2(\rho + \coth k_j d \coth k_j h_2) - K\gamma_j k_j(\coth k_j d + \coth k_j h_2) + k_j^2(1-\rho) = 0, \text{ for } j = 2, 3. \tag{3.24}$$

TH-2746_176123008

3.2.2 Analysis of the dispersion relations

Now, if we put $G = 0$, then dispersion relation (3.23) implies the dispersion relation of a two-layer fluid flowing over an impermeable bottom. Also, $\rho \to 1$ and $d \to 0$ in both relations (3.23) and (3.24) give the dispersion relations in a homogeneous fluid with the similar bottom characteristics as defined in corresponding regions. For real G, dispersion relation (3.23) has two pairs of real roots $k_1 = \pm k_{1,1}, \pm k_{1,2}$, corresponding to the two propagating modes (free surface and interface) and an infinite number of purely imaginary roots given by $k_1 = \pm k_{1,n}$ for $n = 3, 4, 5, \ldots$ where $k_{1,n} = \mathrm{i}t_n$, t_n being the real number. It is very routine to find the roots of dispersion relation (3.23) by applying Newton-Raphson Method. Equation (3.24) has infinitely many complex roots given by $k_j = k_{j,n} = \pm a_{j,n} \pm \mathrm{i}b_{j,n}$ for $j = 2, 3$, and $n = 1, 2, 3, \ldots$, where all $a_{j,n}$ and $b_{j,n}$ are real [8]. Recall that Section 2.2 contains a detailed discussion regarding these roots. For verification of the roots in a porous medium, Table 2.1 may be referred to.

In this regard, we mention that, if $\gamma_2 = \gamma_3$ and $\epsilon_2 = \epsilon_3$, then Regions 2 and 3 merge into a single one and then the formulation becomes totally different. Therefore, we assume two cases: either $\gamma_2 \neq \gamma_3$ or $\gamma_2 = \gamma_3$. For the latter case, we assume $\epsilon_2 \neq \epsilon_3$ so that the two blocks in the structure remain distinct.

3.2.3 Full wave approximation and method of solution

The real roots of dispersion relation (3.23) contribute two progressive propagating wave modes in the water region: Free Surface Mode (SM) and Interface Mode (IM); the infinitely purely imaginary roots correspond to the evanescent modes. Now, to solve by eigenfunction expansion method, we express ϕ_j for $j = 1, 2, 3, 4$ by combining $\psi_j^{(1)}$ and $\psi_j^{(2)}$ as

$$\phi_1 = \sum_{n=1}^{2} e^{\mathrm{i}q_{1,n}x} I_{1,n}(k_{1,n}, z) + \sum_{n=1}^{\infty} R_n e^{-\mathrm{i}q_{1,n}x} I_{1,n}(k_{1,n}, z), \tag{3.25}$$

$$\phi_2 = \sum_{n=1}^{\infty} (A_n e^{\mathrm{i}q_{2,n}x} + B_n e^{-\mathrm{i}q_{2,n}(x-L_1)}) I_{2,n}(k_{2,n}, z), \tag{3.26}$$

$$\phi_3 = \sum_{n=1}^{\infty} (C_n e^{\mathrm{i}q_{3,n}(x-L_1)} + D_n e^{-\mathrm{i}q_{3,n}(x-L_1-L_2)}) I_{3,n}(k_{3,n}, z), \tag{3.27}$$

$$\phi_4 = \sum_{n=1}^{\infty} T_n e^{\mathrm{i}q_{1,n}(x-L_1-L_2)} I_{1,n}(k_{1,n}, z), \tag{3.28}$$

where R_n, A_n, B_n, C_n and T_n are the unknowns to be determined. The unknowns R_n and T_n are, respectively, the associated reflection and transmission coefficients which are going to be analyzed in the next section. The velocity potentials in (porous) Regions 2

TH-2746_176123008

and 3, that is, $\phi_2(x,z)$ and $\phi_3(x,z)$, given by equations (3.26) and (3.27), respectively, are found by assuming that dispersion relation (3.24) has distinct roots. Further, if there are repeated roots, then the expansion formulas need to be appropriately adjusted as per the description in Behera and Sahoo [8].

The eigenfunctions $I_{j,n}(k_{j,n},z)$ for $j=1,2,3$ in equations (3.21) and (3.22) are integrable in corresponding domains $(-h_1,d)$ for $j=1$ and $(-h_2,d)$ for $j=2,3$, respectively, and they form an orthogonal set with respect to the following inner product:

$$\langle \varphi_n, \Psi_m \rangle = \int_{-h_j}^{0} \varphi_n \Psi_m \mathrm{d}z + \rho \int_{0}^{d} \varphi_n \Psi_m \mathrm{d}z. \tag{3.29}$$

Subsequently, the following can be easily derived:

$$\langle I_{j,n}, I_{j,m} \rangle = \left\{ \begin{array}{ll} 0, & m \neq n, \\ W_{j,n}, & m = n, \end{array} \right\} \text{ for } j = 1,2,3, \tag{3.30}$$

where

$$\begin{aligned} W_{1,n} &= \frac{h_1 k_{1,n}^2 - G^2 h_1 + G}{2k_{1,n}^2} - \frac{2Gk_{1,n}\cosh\left(2h_1k_{1,n}\right) - \left(k_{1,n}^2 + G^2\right)\sin 2k_{1,n}h_1}{4k_{1,n}^3} \\ &\quad + q_{1,n}\left(\frac{(k_{1,n}^2 - K^2)d}{2} + \frac{(k_{1,n}^2 + K^2)\sinh 2k_{1,n}d}{4k_{1,n}} - K\sinh^2 k_{1,n}d\right), \\ W_{j,n} &= \frac{2h_2k_{j,n} + \sinh 2h_2k_{j,n}}{4k_{j,n}} + Q_{j,n}\left(\frac{(k_{j,n}^2 - K^2\gamma_j^2)d}{2}\right. \\ &\quad \left. + \frac{(k_{j,n}^2 + K^2\gamma_j^2)\sinh 2k_{j,n}d}{4k_{j,n}} - K\gamma_j\sinh^2 k_{j,n}d\right), \text{ for } j = 2,3, \end{aligned}$$

with

$$\begin{aligned} Q_{1,n} &= \frac{\rho\left(\sinh k_{1,n}h_1 - G/k_{1,n}\sinh k_{1,n}h_1\right)^2}{(K\cosh k_{1,n}d - k_{1,n}\sinh k_{1,n}d)^2}, \\ Q_{j,n} &= \frac{\rho\sinh^2 k_{j,n}h_2}{(K\gamma_j\cosh k_{j,n}d - k_{j,n}\sinh k_{j,n}d)^2} \quad \text{for } j = 2,3. \end{aligned}$$

From equations (3.14) to (3.16) and boundary conditions (3.17)-(3.18), with consideration of N evanescent modes, we get the following equations:

$$\sum_{n=1}^{2} q_{1,n}I_{1,n} - \sum_{n=1}^{N+2} R_n q_{1,n} I_{1,n} = \left\{ \begin{array}{ll} 0, & \text{for } -h_1 < z < -h_2, \\ \epsilon_2 \displaystyle\sum_{n=1}^{N+2}(A_n - B_n e^{\mathrm{i}q_{2,n}L_1})q_{2,n}I_{2,n}, & \text{for } -h_2 < z < d, \end{array} \right. \tag{3.31}$$

TH-2746_176123008

$$\left.\begin{aligned}\sum_{n=1}^{2} I_{1,n} + \sum_{n=1}^{N+2} R_n I_{1,n} &= \gamma_2 \sum_{n=1}^{N+2} (A_n + B_n e^{\mathrm{i}q_{2,n}L_1}) I_{2,n},\\ \epsilon_2 \sum_{n=1}^{N+2} (A_n e^{\mathrm{i}q_{2,n}L_1} - B_n) q_{2,n} I_{2,n} &= \epsilon_3 \sum_{n=1}^{N+2} (C_n - D_n e^{\mathrm{i}q_{3,n}L_2}) q_{3,n} I_{3,n},\end{aligned}\right\} \text{ for } -h_2 < z < d, \tag{3.32}$$

$$\gamma_2 \sum_{n=1}^{N+2} (A_n e^{\mathrm{i}q_{2,n}L_1} + B_n) I_{2,n} = \gamma_3 \sum_{n=1}^{N+2} (C_n + D_n e^{\mathrm{i}q_{3,n}L_2}) I_{3,n}, \text{ for } -h_2 < z < d, \tag{3.33}$$

$$\sum_{n=1}^{N+2} T_n q_{1,n} I_{1,n} = \begin{cases} 0, & \text{for } -h_1 < z < -h_2,\\ \epsilon_3 \sum_{n=1}^{N+2} (C_n e^{\mathrm{i}q_{3,n}L_2} - D_n) q_{3,n} I_{3,n}, & \text{for } -h_2 < z < d, \end{cases} \tag{3.34}$$

$$\sum_{n=1}^{N+2} T_n I_{1,n} = \gamma_3 \sum_{n=1}^{N+2} (C_n e^{\mathrm{i}q_{3,n}L_2} + D_n) I_{3,n}, \text{ for } -h_2 < z < d. \tag{3.35}$$

Now, applying the orthogonality of eigenfunctions $I_{1,n}$ and $I_{2,n}$ (equation (3.30)), we get

$$R_m q_{1,m} a_{1,m} + \epsilon_2 \sum_{n=1}^{N+2} (A_n - B_n e^{\mathrm{i}q_{2,n}L_1}) q_{2,n} b_{n,m} = \sum_{j=1}^{2} \delta_{j,m} Q_m a_{1,m}, \tag{3.36}$$

$$\sum_{n=1}^{N+2} R_n \hat{a}_{1,m,n} - \gamma_2 \sum_{n=1}^{N+2} (A_n + B_n e^{\mathrm{i}q_{2,n}L_1}) b_{n,m} = -\sum_{n=1}^{2} \hat{a}_{1,m,n}, \tag{3.37}$$

$$\epsilon_2 (A_m e^{\mathrm{i}q_{2,m}L_1} - B_m) q_{2,m} a_{2,m} - \epsilon_3 \sum_{n=1}^{N+2} (C_n - D_n e^{\mathrm{i}q_{3,n}L_2}) q_{3,n} b_{1,n,m} = 0, \tag{3.38}$$

$$\gamma_2 (A_m e^{\mathrm{i}q_{2,m}L_1} + B_m) a_{2,m} - \gamma_3 \sum_{n=1}^{N+2} (C_n + D_n e^{\mathrm{i}q_{3,n}L_2}) b_{1,n,m} = 0, \tag{3.39}$$

$$\epsilon_3 \sum_{n=1}^{N+2} (C_n e^{\mathrm{i}q_{3,n}L_2} - D_n) q_{3,n} \hat{b}_{n,m} - T_m q_{1,m} a_{1,m} = 0, \tag{3.40}$$

$$\gamma_3 \sum_{n=1}^{N+2} (C_n e^{\mathrm{i}q_{3,n}L_2} + D_n) \hat{b}_{n,m} - \sum_{n=1}^{N+2} T_n \hat{a}_{1,m,n} = 0, \tag{3.41}$$

where

$$a_{1,m} = \int_{-h_1}^{0} I_{1,m} I_{1,m} \mathrm{d}z + \rho \int_{0}^{d} I_{1,m} I_{1,m} \mathrm{d}z, \quad \hat{a}_{1,m,n} = \int_{-h_1}^{0} I_{1,m} I_{1,n} \mathrm{d}z + \rho \int_{0}^{d} I_{1,m} I_{1,n} \mathrm{d}z,$$

$$a_{2,m} = \int_{-h_2}^{0} I_{2,m} I_{2,m} \mathrm{d}z + \rho \int_{0}^{d} I_{2,m} I_{2,m} \mathrm{d}z, \quad b_{n,m} = \int_{-h_1}^{0} I_{1,m} I_{2,n} \mathrm{d}z + \rho \int_{0}^{d} I_{1,m} I_{2,n} \mathrm{d}z,$$

TH-2746_176123008

$$\hat{b}_{n,m} = \int_{-h_1}^{0} I_{1,m} I_{3,n} \mathrm{d}z + \rho \int_{0}^{d} I_{1,m} I_{3,n} \mathrm{d}z, \quad b_{1,n,m} = \int_{-h_2}^{0} I_{2,m} I_{3,n} \mathrm{d}z + \rho \int_{0}^{d} I_{2,m} I_{3,n} \mathrm{d}z.$$

Therefore, the system (3.36)-(3.41) consists of $(6N + 12)$ linear equations (for $m = 1, \ldots, (N + 2)$) with $(6N + 12)$ unknowns through
$X = [R_1, ..., R_{N+2}, A_1, ..., A_{N+2}, B_1, ..., B_{N+2}, C_1, ..., C_{N+2}, D_1, ..., D_{N+2}, T_1, ..., T_{N+2}]^T$.

Thus it yields a linear system of size $(6N + 12)$ of the form

$$\hat{A}X = \hat{B}. \tag{3.42}$$

Once the unknown X is determined, the reflection and transmission taking place within the porous structure can be examined.

If $\gamma_2 = \gamma_3$, then $I_{2,n} = I_{3,n}$ and $k_{2,n} = k_{3,n}$. Accordingly, after using the orthogonality of $I_{2,n}$, the system of equations becomes different due to equations (3.38) and (3.39) getting replaced by

$$\epsilon_2(A_m e^{\mathrm{i}q_{2,m}L_1} - B_m)q_{2,m} - \epsilon_3(C_m - D_m e^{\mathrm{i}q_{2,m}L_2})q_{2,m} = 0, \tag{3.43}$$

$$(A_m e^{\mathrm{i}q_{2,m}L_1} + B_m) - (C_m + D_m e^{\mathrm{i}q_{2,m}L_2}) = 0. \tag{3.44}$$

The consideration of the same porosity in both blocks ($\epsilon_2 = \epsilon_3$) leads to $A_m = C_m e^{-\mathrm{i}q_{2,m}L_1}$ and $B_m = D_m e^{\mathrm{i}q_{2,m}L_2}$, which merges Regions 2 and 3 into a single one.

The reflection and transmission coefficients for both free surface and interface modes ($N = 1, 2$) are computed by taking $R_{SM} = |R_1|, R_{IM} = |R_2|$ and $T_{SM} = |T_1|, T_{IM} = |T_2|$, respectively. Further, the unit horizontal wave forces acting on the front and back faces of the porous blocks, denoted by $C_{f,j}$ and $C_{b,j}$ for $j = 2, 3$, respectively, can be computed by using the following formulas:

$$C_{f,2} = \mathrm{i}\omega\gamma_2 \left[\rho_2 \int_{-h_2}^{0} \phi_2(0, z)\mathrm{d}z + \rho_1 \int_{0}^{d} \phi_2(0, z)\mathrm{d}z\right], \tag{3.45}$$

$$C_{f,3} = C_{b,2} = \mathrm{i}\omega\gamma_3 \left[\rho_2 \int_{-h_2}^{0} \phi_3(L_1, z)\mathrm{d}z + \rho_1 \int_{0}^{d} \phi_3(L_1, z)\mathrm{d}z\right], \tag{3.46}$$

$$C_{b,3} = \mathrm{i}\omega\gamma_3 \left[\rho_2 \int_{-h_2}^{0} \phi_3(L_1 + L_2, z)\mathrm{d}z + \rho_1 \int_{0}^{d} \phi_3(L_1 + L_2, z)\mathrm{d}z\right]. \tag{3.47}$$

Further, the non-dimensional hydrodynamic forces, denoted by $K_{f,j}$ and $K_{b,j}$, can be

TH-2746_176123008

evaluated from the following:

$$K_{f,j} = \frac{|C_{f,j}|}{\rho_2 g d h_1}, \text{ and } K_{b,j} = \frac{|C_{b,j}|}{\rho_2 g d h_1} \text{ for } j = 2, 3. \tag{3.48}$$

Following the same procedure as in Section 2.2, amplitude of elevation at the free surface and interface, i.e., η_i for $i = 1, 2$, can be obtained as

$$\eta_1 = \frac{\partial \phi_j}{\partial z}, \text{ at } z = d, \text{ and } \eta_2 = \frac{\partial \phi_j}{\partial z}, \text{ at } z = 0. \tag{3.49}$$

3.2.4 Numerical results and discussion

The in-built program Matlab R2019a is used to solve the system of equations given by (3.42). For computational purpose, the following fixed values of some parameters are considered: $d/h_1 = 1$; $m_2 = m_3 = 1$; $\rho = 0.9$; $(h_1 - h_2) = h_1/20$; $Kh_1 = 0.16$; $Gh_1 = 0.1$, $\theta = 30^\circ$ with a range of values of f_j and ϵ_j, $j = 2, 3$ as $f_j = [0, 2]$; $\epsilon_j = [0.25, 1]$, respectively. For convenience, a detailed discussion regarding the appropriateness of the parameter values is placed in Appendix D.

At the outset, we examine the effect of different numbers of evanescent modes on reflection and transmission coefficients.

	$N \Rightarrow$ / R_{SM} $R_{IM} \Downarrow$	0	4	8	10	12
$Kh_1 = 0.16,\ f_2 = 0.8$	R_{SM}	0.2023	0.3178	0.3208	0.3196	0.3197
	T_{SM}	0.6448	0.6962	0.6996	0.6997	0.6997
$Kh_1 = 0.16,\ f_2 = 1.2$	R_{SM}	0.1758	0.3028	0.3083	0.3075	0.3076
	T_{SM}	0.5858	0.6164	0.6236	0.6237	0.6237
$Kh_1 = 0.1,\ f_2 = 0.8$	R_{SM}	0.2679	0.3027	0.3035	0.3034	0.3034
	T_{SM}	0.7293	0.7532	0.7537	0.7537	0.7537
$Kh_1 = 0.1,\ f_2 = 1.2$	R_{SM}	0.2270	0.3103	0.3123	0.3121	0.3121
	T_{SM}	0.6510	0.7037	0.7054	0.7054	0.7054

Table 3.1: Convergence study of R_{SM} and T_{SM} for different Kh_1 and f_2 with $L_1/h_1 = L_2/h_1 = 0.8$; $f_3 = 1$; $\epsilon_2 = 0.7, \epsilon_3 = 0.9$ and $\theta = 30^\circ$.

From Table 3.1, it can be clearly observed that there is a major contribution of the evanescent modes in reflection and transmission coefficients compared to the situation of no consideration of evanescent modes, i.e., $N = 0$, and we also verify the convergence of the results. It is easily visible that the difference between two successive reflection coefficients converges to 0 with an increase in the number of evanescent modes. Therefore, for our further investigations, as suggested by Table 3.1, we assume the number of evanescent modes given by $N = 12$ to be sufficient which clearly ensures the convergence of the results.

TH-2746_176123008

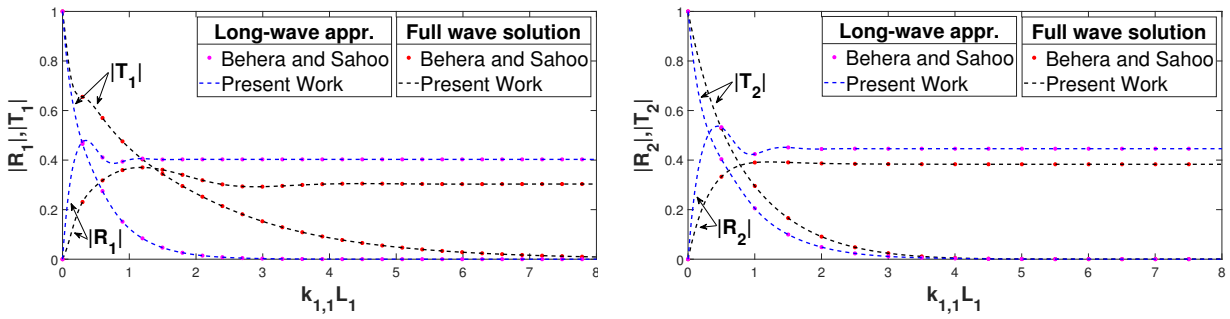

(a) (b)

Figure 3.2: Reflection and transmission coefficients against $k_{1,1}L_1$ at (a) free surface and (b) interface corresponding to present result and [8].

To validate our model, we compare one result with the corresponding result of Behera and Sahoo [8] in which they had examined water wave interaction with a porous block for a two-layer fluid flow over an impermeable sea-bed. As in Venkateswarlu et al. [108], two different cases (full wave solution and long-wave approximation) are compared to ascertain the complete efficiency of the model. Therefore, in order to have a proper comparison by converting our model to their model, we consider $G = 0$ so that the porous sea-bed becomes an impermeable one and assume the following parameter values: $h_1 = h_2 = d = 2.5$ meter, $T = 8$ sec, $g = 9.81$ m/s^2, $\epsilon_2 = 0.5$, $f_2 = 1$, $L_2 = 0$. An excellent agreement in the results follows when the reflection and transmission coefficients are plotted against non-dimensional $k_{1,1}L_1$ (Figure 3.2(a,b)). In other words, the successful validation confirms that our model can be considered as an efficient one for formulating and solving various problems of wave interaction by porous structures containing block-wise different porosity for a two-layer fluid flow.

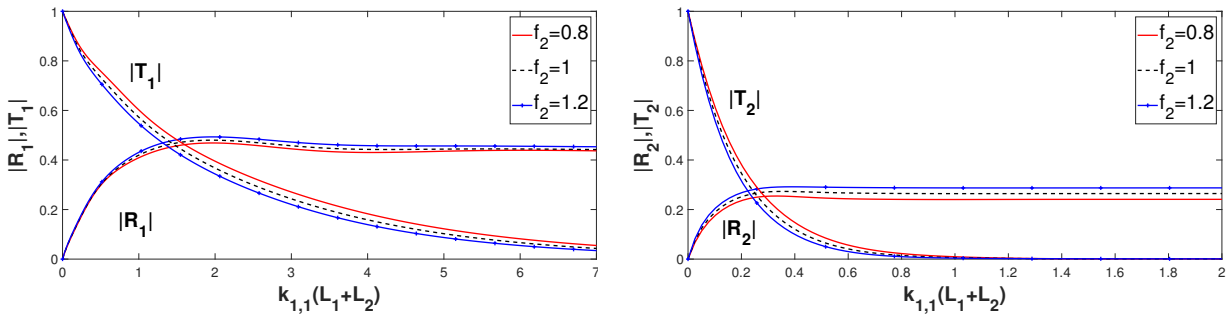

(a) (b)

Figure 3.3: Variation of reflection and transmission coefficients against non-dimensional width $k_{1,1}(L_1 + L_2)$ corresponding to various friction values f_2 with $f_3 = 1$ and $\epsilon_2 = 0.7, \epsilon_3 = 0.8$

In Figures 3.3(a) and 3.3(b) and Figures 3.4(a) and 3.4(b), the reflection and transmis-

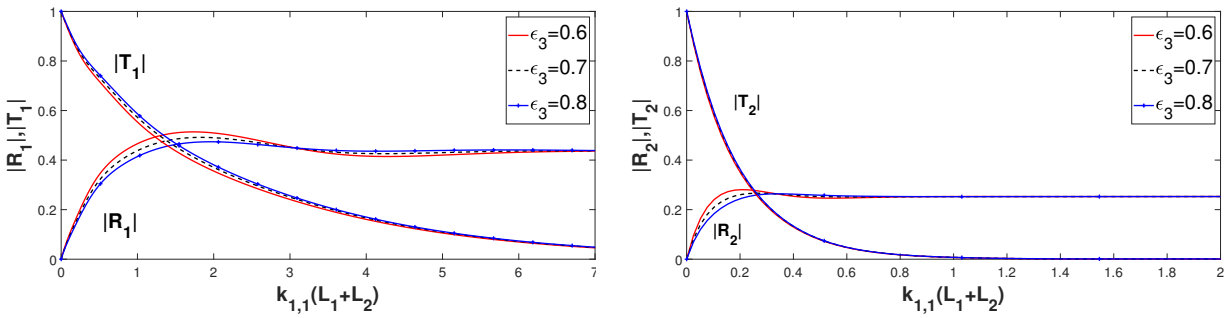

(a) (b)

Figure 3.4: Variation of reflection and transmission coefficients against non-dimensional length $k_{1,1}(L_1+L_2)$ corresponding to various porosity ϵ_3 with $\epsilon_2 = 0.7$ and $f_2 = 0.9$, $f_3 = 1$.

sion coefficients in SM and IM, respectively, are plotted against non-dimensional width $k_{1,1}(L_1 + L_2)$ of the structure corresponding to various values of porosity ϵ_3 and friction parameter f_2. Similar patterns are visible for both modes in Figure 3.3(a,b) while changing friction parameter f_2. Further, reflection and transmission coefficients both remain almost constant after some specific width. However, transmission in both modes reduces sharply with increasing $(L_1 + L_2)$ while the interfacial transmission vanishes after $k_{1,1}(L_1 + L_2) \geq 1$. Consideration of different values of friction factor f_2 results in difference in the values of the reflection and transmission coefficients, where higher value of friction factor $(f_2 > f_3)$ results in higher reflection and lower transmission while lower value $(f_2 \leq f_3)$ results in lower reflection and higher transmission in both propagating modes. In Figure 3.4, it is observed that change of porosity ϵ_3 does not lead to a major impact in the coefficients T_{SM} and T_{IM}. However, differences are observed for reflection coefficients in both modes where the lower values of ϵ_3 (i.e., $\epsilon_2 > \epsilon_3$) results in higher reflection and higher values of ϵ_3 (i.e., $\epsilon_2 \leq \epsilon_3$) results in lower reflection. The same trend is observed for both cases of varying porosity and varying friction. It can be concluded that it is advisable to use a composite structure of appropriate structural length to obtain higher reflection and lower transmission. Both cases result in the convergence of reflecting modes after some structural width and the propagating modes also attain the optimum at nearly the same structural width. But both the propagating modes maintain a steady behaviour with respect to the structural width which establishes the fact that, after a certain value, higher structural width has no impact on reflection and transmission.

Figure 3.5(a,b) illustrates the effect of friction parameter on the reflection coefficients with respect to angle of incidence θ in surface mode and interface mode, respectively. By varying the friction factor, the reflection coefficients are observed to start from their minimum values, and keep increasing to the maximum in both modes while transmission follows an opposite trend. In both propagating modes, maximum reflection and minimum transmission are obtained at the angle 90°. However, change of friction does not contribute

TH-2746_176123008

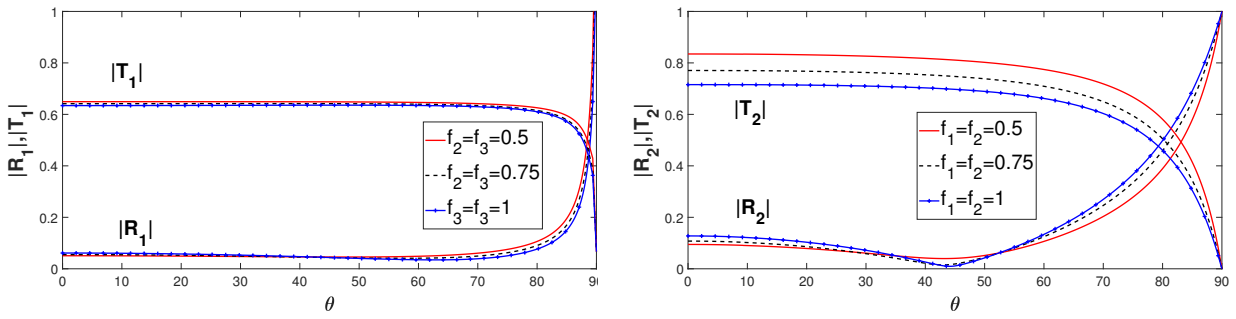

(a) (b)

Figure 3.5: Variation of reflection and transmission coefficients against incident angle θ corresponding to various friction parameter f_j for $j = 2, 3$ with $f_2 = f_3$, $\epsilon_2 = 0.7, \epsilon_3 = 0.9$ and $(L_1 + L_2)/h_1 = 0.5$.

to any difference in the angle of incidence for obtaining its optimum in SM but differences are observed for attaining minimum in IM. Therefore, the optimum values depend on the friction parameter also. In both modes, lower friction results in lower reflection and higher transmission. Thus, by studying the wave pattern, porous structures can be designed as breakwaters by appropriately incorporating structure width, step height and friction factor in order to achieve maximum wave reflection and minimum transmission which will in turn protect the marine facilities.

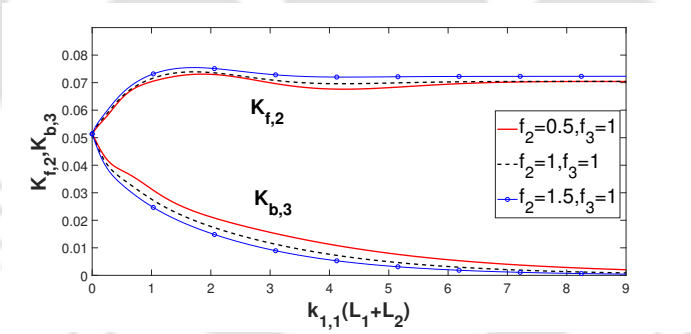

Figure 3.6: Variation wave forces $K_{f,2}$ and $K_{b,3}$ against non-dimensional length $k_{1,1}(L_1 + L_2)$ corresponding to various values of f_j with $\epsilon_2 = 0.9, \epsilon_3 = 0.8$.

In Figure 3.6, waveloads $K_{f,2}$ and $K_{b,3}$ are, respectively, plotted against $k_{1,1}(L_1 + L_2)$ corresponding to different values of friction parameter. The figure shows that wave force $K_{f,2}$ does not show any major difference due to the increase of the structure width but $K_{b,3}$ starts from its highest value and generally reduces with an increase in the width. This may have happened due to the dissipation of a large amount of wave energy by the porous structure. Wave force $K_{f,1}$ produces a higher impact for higher friction f_2 with $f_2 \leq f_3$ but wave force $K_{b,3}$ exhibits the opposite. As observed earlier, the steady nature of the reflection and transmission modes for higher structural width is one of the

TH-2746_176123008

reasons for the fixed wave forces. Different friction does not produce any difference for attaining optimum value of waveload. The steady nature of waveload also justifies that the dissipation of energy is fixed up to some structural width beyond which the energy loss is independent of the structure length. Therefore, by using an efficient dissipative structure as a breakwater, higher wave energy can be absorbed to provide safety to various structures in ocean.

3.3 Trapping Problem

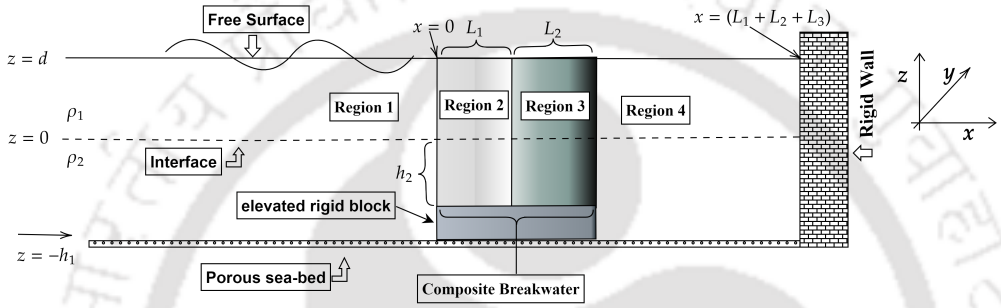

Figure 3.7: Sketch definition of trapping model

A rigid sea-wall is considered in Figure 3.7, placed at distance $x = (L_1 + L_2 + L_3)$ from the far end of the porous structure to model it as an effective breakwater-seawall wave-trapping system [109]. The wave gets partially reflected by the porous structure and the rest gets transmitted to the fourth region where the wave again gets reflected back due to the rigid vertical wall. An occurrence of wave trapping is observed and studied.

Due to the rigid wall, potential ϕ_4 (i.e., $\psi_4^{(1)}$ and $\psi_4^{(2)}$ from (3.1) for $j = 4$) additionally satisfies the no flow condition at $x = L_1 + L_2 + L_3$ as follows:

$$\frac{\partial \phi_4}{\partial x} = 0. \tag{3.50}$$

3.3.1 Method of solution

The expressions for velocity potentials ϕ_j for $j = 1, 2, 3$ remain unchanged here (equations (3.25) to (3.27)). Only potential ϕ_4 has a different expression since it satisfies an extra rigid wall boundary condition (3.50). Therefore, considering contribution of N number of evanescent modes, ϕ_4 has the following form:

$$\phi_4 = \sum_{n=1}^{N+2} \hat{D}_n \cos(q_{1,n}(x - L_1 - L_2 - L_3)) I_{1,n}(k_{1,n}, z). \tag{3.51}$$

TH-2746_176123008

After using ϕ_4 in the matching conditions (3.16) and in boundary condition (3.18), the differences appear only in equations (3.34) to (3.35) while the others remain unchanged. Those have the following forms:

$$\sum_{n=1}^{N+2} \hat{D}_n q_{1,n} \sin(q_{1,n} L_3) I_{1,n} = 0, \text{ for } -h_1 < z < -h_2, \tag{3.52}$$

$$\sum_{n=1}^{N+2} \hat{D}_n q_{1,n} \sin(q_{1,n} L_3) I_{1,n} = \mathrm{i}\epsilon_3 \sum_{n=1}^{N+2} (C_n e^{\mathrm{i}q_{3,n} L_2} - D_n) q_{3,n} I_{3,n}, \text{ for } -h_2 < z < d, \tag{3.53}$$

$$\sum_{n=1}^{N+2} \hat{D}_n \cos(q_{1,n} L_3) I_{1,n} = \gamma_3 \sum_{n=1}^{N+2} (C_n e^{\mathrm{i}q_{3,n} L_2} + D_n) I_{3,n}, \text{ for } -h_2 < z < d. \tag{3.54}$$

Now, upon applying the orthogonality of eigenfunction $I_{1,n}$ in equations (3.52) to (3.54), we obtain

$$\mathrm{i}\epsilon_3 \sum_{n=1}^{N+2} (C_n e^{\mathrm{i}q_{3,n} L_2} - D_n) q_{3,n} \hat{b}_{n,m} - \hat{D}_m q_{1,m} \sin(q_{1,m} L_3) a_{1,m} = 0, \tag{3.55}$$

$$\gamma_3 \sum_{n=1}^{N+2} (C_n e^{\mathrm{i}q_{3,n} L_2} + D_n) \hat{b}_{n,m} - \sum_{n=1}^{N+2} \hat{D}_n \cos(q_{1,n} L_3) \hat{a}_{1,m,n} = 0. \tag{3.56}$$

Therefore, equations (3.55) to (3.56), along with equations (3.36) to (3.39), constitute a system of $(6N + 12)$ linear equations (for $m = 1, \ldots, (N + 2)$) with $(6N + 12)$ unknowns as

$X = [R_1, ..., R_{N+2}, A_1, ..., A_{N+2}, B_1, ..., B_{N+2}, C_1, ..., C_{N+2}, D_1, ..., D_{N+2}, \hat{D}_1, ..., \hat{D}_{N+2}]^T$.

This yields a modified linear system of size $(6N + 12)$, similar to (3.42), as follows:

$$\hat{A}_1 X = \hat{B}_1. \tag{3.57}$$

Similarly, the unknown X is determined to study the reflection phenomenon within the porous structure. For the case $\gamma_2 = \gamma_3$, the same procedure as followed in the previous section is to be applied.

3.3.2 Numerical results and discussion

C_w, the horizontal wave force per unit length at the rigid sea-wall, is given by

$$C_w = \mathrm{i}\omega \left[\rho_2 \int_{-h_1}^{0} \phi_4(x, z) \mathrm{d}z + \rho_1 \int_{0}^{d} \phi_4(x, z) \mathrm{d}z \right] \text{ at } x = (L_1 + L_2 + L_3), \tag{3.58}$$

TH-2746_176123008

and the non-dimensional form of the hydrodynamic force coefficient, denoted by K_w, is evaluated from

$$K_w = \frac{|C_w|}{\rho_2 g d h_1}. \tag{3.59}$$

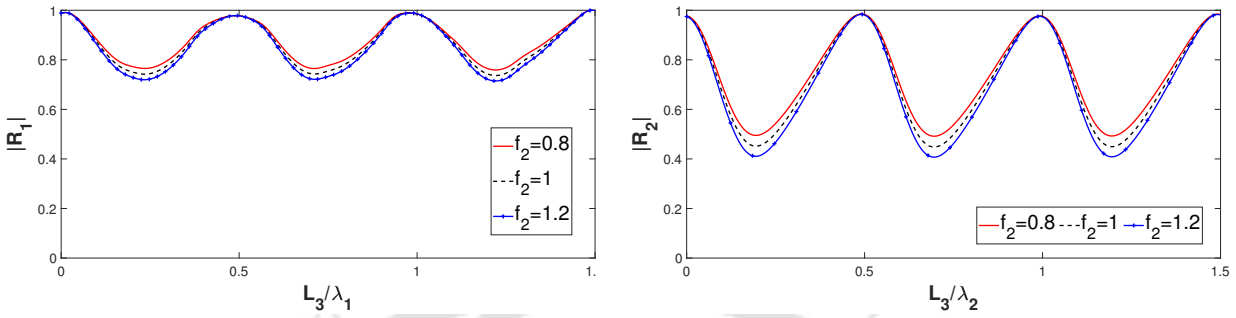

(a) (b)

Figure 3.8: Variation of (a) R_{SM} and (b) R_{IM} against L_3/λ_j for $j = 1, 2$ corresponding to different values of f_2 with $\rho = 0.7,\ \theta = 0°,\ (L_1 + L_2)/h_1 = 0.2,\ (h_1 - h_2) = h_1/25,\ f_3 = 1$ and $\epsilon_2 = 0.45, \epsilon_3 = 0.5$.

In Figure 3.8(a,b), reflection coefficients are plotted versus normalized distance between the breakwater and the rigid wall L_3/λ_j for $j = 1, 2$ ($\lambda_j = 2\pi/k_{1,j}$) in both propagating modes for various values of friction parameter f_2. In both propagating waves, the same oscillating behaviour is observed, and lower friction of $f_2 (\leq f_3)$ results in higher reflection. For both modes, due to the composite thick breakwater, resonating pattern of reflection is observed in almost periodic intervals within the range $(2n-1)\lambda_j/4 < L_3 < (2n+1)\lambda_j/4$ for each integer value n. Furthermore, minimum reflection in both modes is achieved in the region $(m-1)\lambda_j/2 < L_3 < m\lambda_j/2$ for $j = 1, 2,\ m = 1, 2, \ldots$. However, the minimum value depends on the friction factor of the structure. These minimum values in wave reflection are referred as wave trapping in the confined zone between the barrier and the sea-wall. Further, it is observed that the optima are obtained for the same normalized distance L_3 for any friction factor f_2. Therefore, to protect the shoreline and coastal areas, the use of block-wise composite breakwater is considered ideal for obtaining higher or lower reflection in both modes.

Figure 3.9(a,b) shows the impact of changing structural width $(L_1 + L_2)$ on reflection coefficients in which differences are observed for overall reflection in both propagating modes. Lower values of structural width result in higher reflection for both modes. Comparing with Figure 3.8(a,b), we observe the similarity in obtaining the optimum values for certain L_3/λ_j. Furthermore, the optimum value of wave reflection is dependent upon the structural width for both cases. As the width of the structure increases, more amount of wave energy gets reflected. The minimum value of reflection for a certain structural width is comparatively higher for SM than that for IM. For both propagating modes, certain

TH-2746_176123008

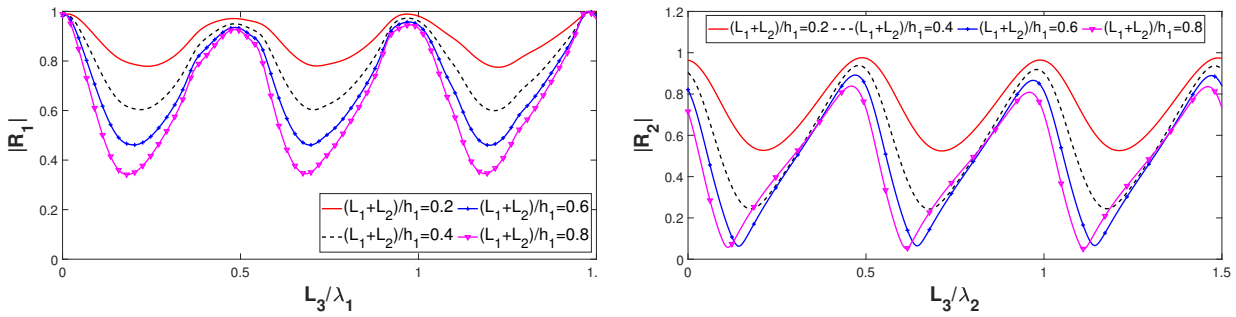

(a) (b)

Figure 3.9: Variation of (a) R_{SM} and (b) R_{IM} against normalized distance L_3/λ_j for $j = 1, 2$ corresponding to different values of $(L_1 + L_2)/h_1$ with $L_3/h_1 = 0.6$, $f_2 = 1.25$, $f_3 = 1$ and $\epsilon_2 = 0.7, \epsilon_3 = 0.6$.

shift toward left in the minimum value is observed with increasing values of $(L_1 + L_2)/h_1$ which may be due to the phase shift of the incoming and outgoing waves in surface mode and interface mode. Therefore, the overall reflection achieved due to the interface-piercing breakwater is mainly dependent on the physical properties of the structure.

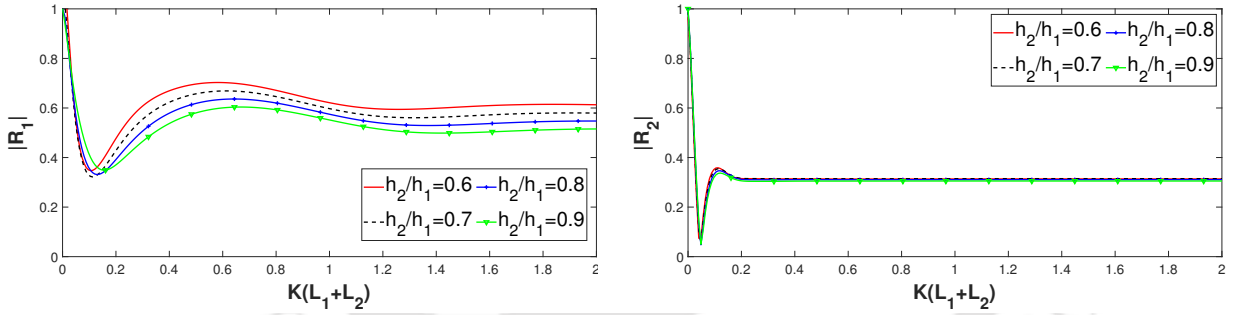

(a) (b)

Figure 3.10: Variation of (a) R_{SM} and (b) R_{IM} against $K(L_1 + L_2)$ corresponding to different values of h_2/h_1 with $L_3/h_1 = 16$, $f_2 = 0.75$, $f_3 = 1$ and $\epsilon_2 = 0.6, \epsilon_3 = 0.7$.

Figure 3.10(a,b) describes the effect of various values of depth ratio h_2/h_1 on reflection coefficients with depth h_1 fixed. If we observe the patterns, lower depth ratio causes maximum reflection although the difference in h_2/h_1 brings negligible difference in reflection for IM. An increase in the length of the rigid block implies a reduction of the size of the porous structure and therefore, relatively less amount of wave passes through the porous structure. This reduces the dissipation of energy by the porous block which may be the reason for occurrence of higher reflection in both modes for lower h_2/h_1. It is also observed that higher step ratio $(h_1 - h_2)/h_1$ results in higher wave reflection in SM. Simillar result is observed at subsection 2.5.1.

TH-2746_176123008

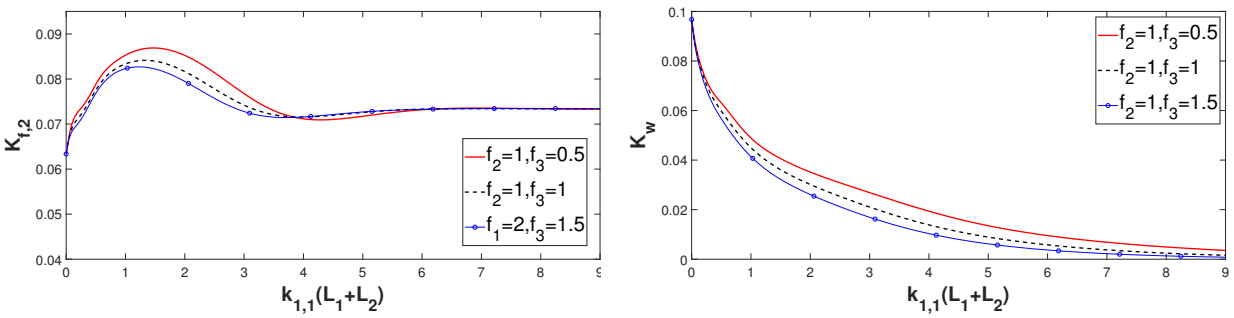

(a) (b)

Figure 3.11: Variation wave forces (a) $K_{f,2}$ and (b) K_w against non-dimensional length $k_{1,1}(L_1 + L_2)$ corresponding to various values of f_3 with $f_2 = 1$, $L_3/\lambda_1 = 1$, and $\epsilon_2 = 0.7, \epsilon_3 = 0.6$.

Figure 3.11(a,b) describes the effect of waveloads $K_{f,2}$ and K_w, respectively, corresponding to different values of friction parameter. Comparing Figures 3.11(a) and 3.11(b), we observe that the wave force K_w reduces sharply with an increase in the width and tends to negligible waveload for higher breakwater width. This amply justifies the dissipation of a large amount of wave energy by the porous structure. However, both the wave forces converge to a steady state after some width which is also justified by the occurrence of steady reflection for higher structural width which we observed earlier. Both wave forces produce a higher impact for lower friction f_3 with $f_2 \geq f_3$. Further, the wave forces on the first porous block initially show a difference due to the impact of different friction values but later on, all the graphs converge to one. But the steady nature of waveload also justifies that the dissipation by the structure is fixed up to some structural length beyond which the energy loss is independent of the structure length.

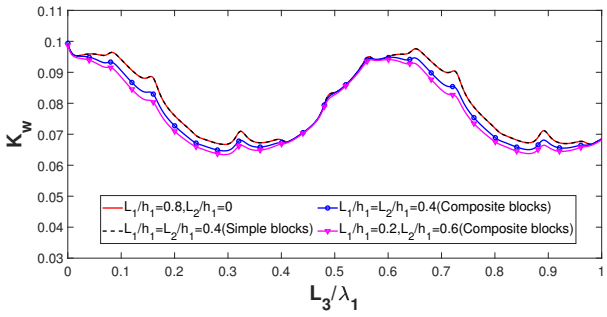

Figure 3.12: Variation wave force K_w against normalized distance L_3/λ_1 corresponding to various values of L_2/h_1 with the cases (i) $f_2 = 1$ and $\epsilon_2 = 0.6$,(ii) $f_2 = f_3 = 1$ and $\epsilon_2 = \epsilon_3 = 0.6$,(iii) $f_2 = 1, f_3 = 1.5$ and $\epsilon_2 = 0.6, \epsilon_3 = 0.7$,(iv) $f_2 = 1, f_3 = 1.5$ and $\epsilon_2 = 0.6, \epsilon_3 = 0.7$.

In Figure 3.12, the impact of a fixed width breakwater ($(L_1 + L_2)/h_1 = 0.8$) with various structural configurations is examined on the basis of the influence of waveload on

TH-2746_176123008

the sea-wall. Varying the normalized length, we can easily observe that the waveload is much higher in the case of a single block breakwater. As already explained in Section 3.2.2, the equal porosity and equal friction (i.e., $\epsilon_2 = \epsilon_3, \gamma_2 = \gamma_3$) merge Regions 2 and 3 into a single one due to which the two-block structure gets converted into a single block. Therefore, the cases of a single block ($L_1/h_1 = 0.8, L_2/h_1 = 0$) and two blocks ($L_1/h_1 = L_2/h_1 = 0.4$) with same porosity and friction produce the same results. Moreover, it clearly shows that the two-block structure with different porosity and friction (in cases (iii) and (iv) in Figure 3.12) result in higher dissipation of energy and among them, the structure with unequal block widths (case (iv) $(L_1 + L_2)/h_1 = 0.8$, but $L_1/h_1 \neq L_2/h_1$) results in the lowest waveload among all the cases. For a fixed set of parameters in the confined zone between the breakwater and the sea-wall, if the overall waveload is evaluated in $\mathbf{L}_2$ norm, then case (iii) results in nearly 2% less waveload compared to the cases (i) and (ii). For a composite structure with unequal block widths (case (iv)), nearly a 4% lower waveload is observed than cases (i) and (ii). Therefore, composite structures are found to be comparatively more efficient as a wave-absorber than a single block structure, and an adjustment in the attributes of the composite structure results in better depletion.

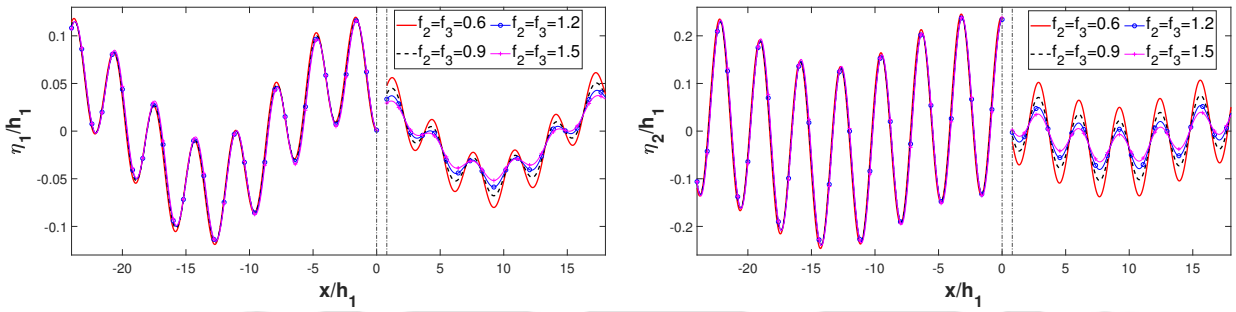

(a) (b)

Figure 3.13: Variation of the non-dimensional elevation amplitude for (a) free surface and (b) interface against x/h_1 corresponding to various values of $f_2 = f_3$ with $(L_1 + L_2)/h_1 = 0.8$, $L_3/\lambda_1 = 1$ and $\epsilon_2 = 0.7, \epsilon_3 = 0.9$.

Figure 3.13(a,b) presents the elevations η_1/h_1 at the free surface and η_2/h_1 at the interface, respectively, plotted against the non-dimensional distance x/h_1 corresponding to different values of friction coefficients, where x is the distance in the horizontal direction measured from $x = 0$. It shows that the elevation at the interface becomes higher than the elevation at the free surface. However, there is a significant reduction of elevation at both propagating modes in the confined zone between the porous structure and the wall. On both sides of the breakwater, each propagating mode shows that lower friction results in higher oscillation. Before the penetration of the wave into the structure, the elevations exhibit a negligible difference between them but an appropriate dissipation effect on the elevation is clearly visible in the confined zone between the breakwater and the sea-wall.

TH-2746_176123008

Subsequently, by an appropriate selection of physical parameters for a composite type structure interacting with waves, a tranquillity zone can be created which will reduce waveload to a large extent on the porous structure as well as the rigid wall.

3.4 Composite breakwater with a perforated front wall

In recent times, it has been observed that an enormous number of breakwaters have been designed and used with a perforated front wall. In this section, we assume a composite breakwater with a perforated front wall and subsequently discuss its scattering and trapping effects.

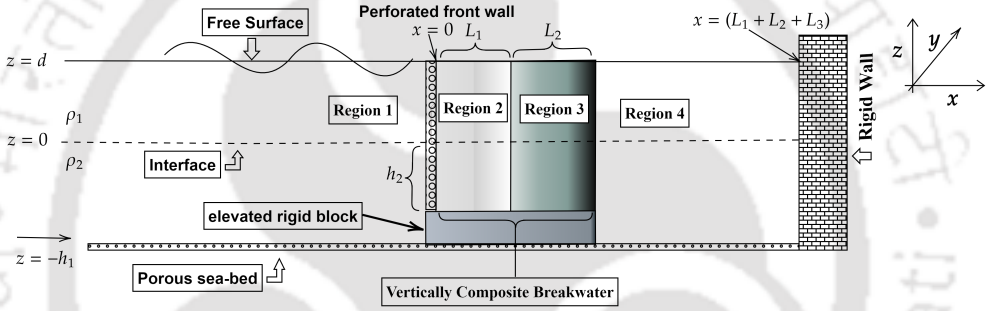

Figure 3.14: Definition sketch of wave interaction with perforated front wall

All the velocity potentials and conditions remain the same as per the formulation of the previous problem except the matching conditions (3.14). Now, the matching conditions due to the continuity of velocity and the pressure drop across the perforated front wall (as in Isaacson et al. [44]) at $x = 0,\ -h_2 < z < d$ yield

$$\frac{\partial \phi_1}{\partial x} = \epsilon_2 \frac{\partial \phi_2}{\partial x}, \tag{3.60}$$

$$\frac{\partial \phi_1}{\partial x} = \mathrm{i} k_{1,1} G_1 (\phi_1 - \gamma_2 \phi_2), \tag{3.61}$$

where G_1 is the porous-effect parameter given by $G_1 = \dfrac{\epsilon_W}{k_{1,1} b_W (f_W - \mathrm{i} m_W)}$, where the subscript W refers to various parameters associated with the perforated front wall, which is also treated as a porous medium, and b_W refers to the thickness of the front wall. The condition given by equation (3.60) is the same as (3.14) and so the only difference that occurs in the system of equations (3.57) is due to equation (3.61). Now, using the velocity potentials from (3.25)-(3.26) in matching conditions (3.61), we obtain the

TH-2746_176123008

following equation for $-h_2 < z < d$:

$$\sum_{n=1}^{N+2} R_n(q_{1,n} + k_{1,1}G_1)I_{1,n} - k_{1,1}G_1\gamma_2 \sum_{n=1}^{N+2}(A_n + B_n e^{\mathrm{i}q_{2,n}L_1})I_{2,n} = \sum_{n=1}^{2}(q_{1,n} - k_{1,1}G_1)I_{1,n}. \tag{3.62}$$

Now, using the orthogonality of $I_{1,n}$ in equation (3.62) and combining with (3.31), we obtain

$$R_m q_{1,m} a_{1,m} + k_{1,1}G_1 \sum_{n=1}^{N+2} R_n \hat{a}_{1,m,n} - k_{1,1}G_1\gamma_2 \sum_{n=1}^{N+2}(A_n + B_n e^{\mathrm{i}q_{2,n}L_1})b_{n,m} = \sum_{j=1}^{2} \delta_{j,m} q_{1,m} a_{1,m} - k_{1,1}G_1 \sum_{n=1}^{2} \hat{a}_{1,m,n}. \tag{3.63}$$

Along with the remaining $(5N + 10)$ equations from (3.36), (3.38)-(3.41), we obtain a system of $(6N + 12) \times (6N + 12)$ equations from which we can solve for the unknown coefficients.

3.4.1 Results

In this subsection, we present the comparison between two various geometric configurations as defined by Figures 3.7 and 3.14 on the basis of reflection coefficients and waveload K_w on the wall.

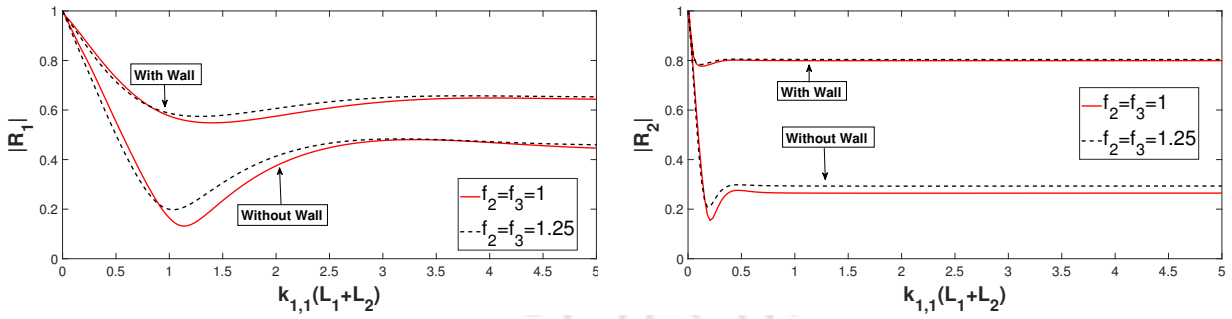

(a) (b)

Figure 3.15: Variation of (a) R_{SM} and (b) R_{IM} against $k_{1,1}(L_1 + L_2)$ corresponding to various values of f_j, for $j = 2, 3$ with perforated wall and without perforated wall configuration with $G_1 = 1 + \mathrm{i}$, $\epsilon_2 = 0.7, \epsilon_3 = 0.8$ and $L_3 = \lambda_1$.

From Figure 3.15 (a,b), it is clearly visible that the structure with a perforated front wall attains a higher reflection than for the case without a front wall in both propagating modes. Further, we also observe that the minimum reflection is obtained for certain values of non-dimensional width $k_{1,1}(L_1 + L_2)$. We can assume that this may have happened due

TH-2746_176123008

to the destructive interference of the incident and reflective waves near the breakwater and the loss of wave energy due to the friction while the wave passes through the breakwater. It may be noted that a pair of waves experience interference when they pass each other. The individual waves add together (superposition) so that a new wavefront is created. Destructive interference occurs when a positive displacement of one wave is cancelled exactly by a negative displacement of the other wave. Basically, if a crest of one wave meets a trough of another wave, then the amplitude is equal to the difference in the individual amplitudes.

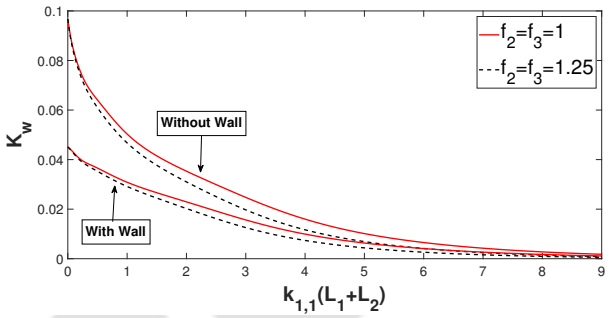

Figure 3.16: Variation of K_w against non-dimensional length $k_{1,1}(L_1 + L_2)$ corresponding to various values of f_j, for $j = 2, 3$ with perforated wall and without perforated wall configuration with $G_1 = 1 + \mathrm{i}$, $\epsilon_1 = 0.7, \epsilon_2 = 0.8$ and $L_3 = \lambda_1$.

From Figure 3.16, we observe that the variation of waveload K_w differs to some extent between these two types of structures. Without the perforated wall, the structure exerts higher waveload on the sea-wall as compared to the structure with the perforated wall. But with an increase in the structural width, the dissipating nature of the porous object reduces the energy of the wave and therefore, the waveload converges to 0 for both structures. From a practical point of view, we can assume that the perforated wall slows down the wave motion due to its inertial resistance which is associated with an increase in the energy dissipation within the breakwater. Subsequently, in order to protect the shore, a perforated front wall helps a structure to achieve better reflection and lesser waveloads exhibiting suitable dissipating properties. Therefore, a composite structure with a perforated front is more appropriate for the creation of a breakwater.

3.5 Effect of sea-bed porosity

In practical situations, the sea-bed usually exhibits some amount of porosity, however small it may be. A number of researchers have also dealt with interaction of water waves with porous structures by idealizing the sea-bed to be an impermeable one, which is accepted as a reasonable idealization for many problems. However, it is felt that consideration of the porosity of the sea-bed may have some influence on matters related

TH-2746_176123008

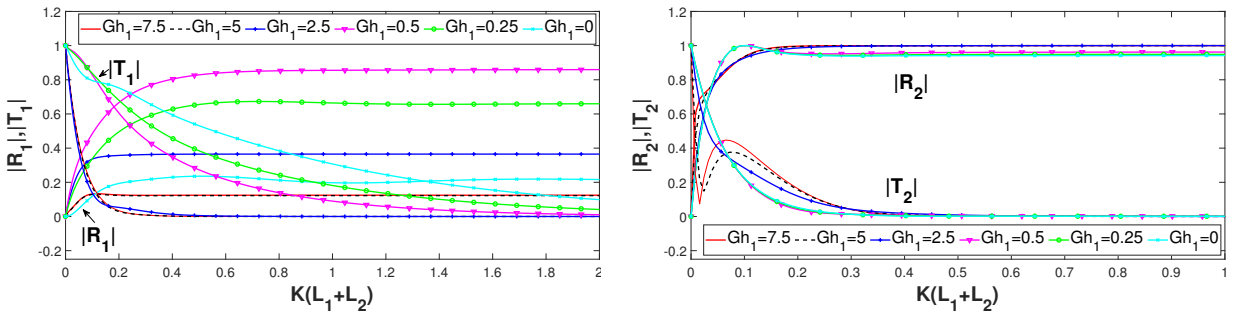

(a) (b)

Figure 3.17: Variation of reflection and transmission against $K(L_1 + L_2)$ on the scattering model as defined in Figure 3.7, corresponding to different non-dimensional values of porous-effecr parameter Gh_1 with $\epsilon_2 = 0.7, \epsilon_3 = 0.8$ and $f_2 = 0.75, f_3 = 1$

to scattering and trapping of waves. Therefore, in this direction, this section examines the (porous) sea-bed effects on the scattering model. We assume two types of bottom profiles, e.g., (i) a porous one with non-dimensional porous-effect parameter $Gh_1 = 0.5, 0.25, 0.05$ and (ii) an impermeable one where $Gh_1 = 0$. Subsequently, the effects of the sea-bed on reflection and transmission coefficients and waveload (K_w) are compared and discussed.

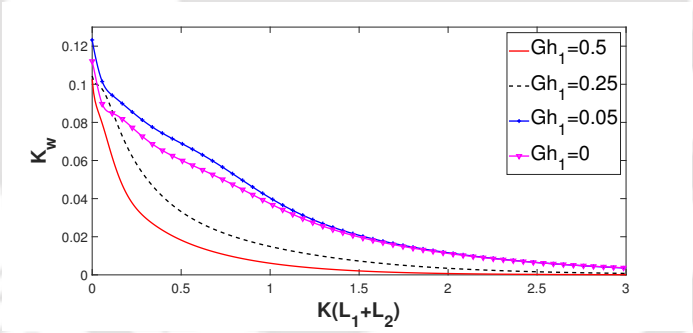

Figure 3.18: Variation of K_w against non-dimensional length $K(L_1 + L_2)$ on the trapping model as defined in Figure 3.7, corresponding to different values of Gh_1, with $\epsilon_2 = 0.7, \epsilon_3 = 0.8$ and $L_3 = \lambda_1$.

The effect of porous-effect parameter G of the sea-bed is examined against non-dimensional width $K(L_1+L_2)$ in Figure 3.17(a,b) and Figure 3.18. Here, Figure 3.17(a,b) describes the effect of the porous sea-bed on reflection and transmission coefficients in the scattering model while Figure 3.18 describes the effect of waveload K_w in the trapping model. We observe that different values of porous-effect parameter G produces a major contribution to reflection and transmission in both propagating modes due to oblique wave interaction with structures. In free surface mode, increase of sea-bed porous-effect parameter up to $Gh_1 \leq 0.5$ results in the enhancement of reflection but when much higher bed porous-effect parameter is considered ($Gh_1 \geq 5$), it brings down both reflection and

TH-2746_176123008

transmission. In other words, reflection and transmission coefficients both can get attenuated for higher porous-effect parameter values of the sea-bed. Meanwhile, transmission decreases gradually with the increase of bed porous-effect parameter in free surface mode. Although negligible difference is noticed for reflection and transmission coefficients for IM, but for $|R_2|$, a difference is observed between higher and lower bed porous-effect parameter values. The structural width presents a major contribution in the variation of reflection and transmission but after some width, the structural width does not make impact anymore as observed earlier. Therefore, a porous sea-bed dissipates the incident wave energy, and increasing values of porosity realizes higher dissipation, which may be a reason for this variation. Furthermore, the physical properties of the structure also produce a significant contribution regarding both reflection and transmission phenomena.

Furthermore, with respect to the waveload on the wall, visible difference is observed in the trapping model with the incorporation of the sea-bed porosity in which case a lower waveload K_w on the wall occurs, contrary to the case for an impermeable sea-bed for which a higher waveload is observed on the wall. It is worthwhile mentioning that a major portion of the wave energy gets dissipated through the porous sea-bed which may have resulted in the lower impact of waveload on the rigid sea-wall compared to the case when the sea-bed is impermeable.

3.6 Conclusion

This work studies oblique water wave interaction by a composite porous structure, with different block-wise porosity, in a two-layer fluid flowing over a porous sea-bed followed by an elevated rigid bottom on which the structure is placed and where the structure pierces the linear interface. Moreover, a similar geometrical configuration with a perforated front wall on the porous structure is also considered to examine the wave interaction. Linear water wave theory and eigenfunction expansion are utilized to find the solution of the corresponding scattering and trapping problems. The region is divided into a number of sub-regions, and by using the given equations and matching conditions, a system of linear algebraic equations is obtained and solved which in turn give the potentials and the reflection and transmission coefficients. Upon comparing a present result with an available result, an excellent agreement between them can be noticed which validates the usefulness of the present model which confirms that the investigation could be carried forward. Thereafter, a number of numerical results are obtained and analyzed. The incident, reflected and transmitted waves for the scattering problem and elevations in the free surface and interface exist due to wave interaction with the porous structure. Due to the mutual interaction of the waves in both propagating modes, we observe a greater waveload on the porous structure which reduces sharply at the end of the structure.

TH-2746_176123008

For the trapping problem, less waveload on the vertical rigid wall is also observed due to the dissipation of the breakwater. This study also leads us to find the optimum width with a suitable structural configuration, which produces a more efficient porous structure possessing both reflective and dissipative characteristics. Consideration of moderate values of the angle of incidence allows one to achieve minimum wave reflection through the utilization of a porous composite structure as a breakwater. By an appropriate selection of structural height, width, porosity and porous impedance parameter, one can find (i) the maximum wave reflection by the structure, (ii) the maximum dissipation of energy by the porous body, and (iii) the minimum value of the waveload on the wall. Also, maximum wave reflection by the interface-piercing structures can be achieved with the consideration of an appropriate size of the elevated bottom upon which the structure is placed. We also find that a composite porous structure is more efficient in producing higher reflection and lower waveload compared to a simple kind of structure. In comparison, for the structure with a perforated front wall, our observations are as follows: (i) the percolative property of the front wall makes the breakwater more effective in producing higher reflection in both propagating modes, and (ii) better dissipation of the energy reflects lower waveload acting on the rigid wall.

Further, due to the consideration of the sea-bed to be porous, it is observed that the porosity of the sea-bed has a reasonable impact on reflection and transmission characteristics and the waveload due to oblique wave interaction with the porous structure under consideration. The comparison between the porous and impermeable sea-bed shows that a significant effect of porosity on the waveload as well as in the reflection and transmission phenomena is visible due to the bed characteristics. Therefore, study of water wave interaction with such structures presents a clear understanding of the effects of the porous structures and the porous sea-bed that together help in creating a tranquillity zone. It also demonstrates that there is some kind of relation among the optimum wave reflection by the porous structures, the optimum waveload on the rigid wall and the maximum wave load on the porous structure and vice-versa. It can be clearly observed that use of a composite porous structure with suitable geometrical configuration along with appropriate characteristics of the sea-bed is a more viable option in creating a tranquillity zone to protect the coastal facilities appropriately.

TH-2746_176123008

CHAPTER 4

Interaction of oblique water waves with a single chamber caisson type breakwater for a two-layer fluid flow over an elastic bottom

4.0.1 Mathematical formulation

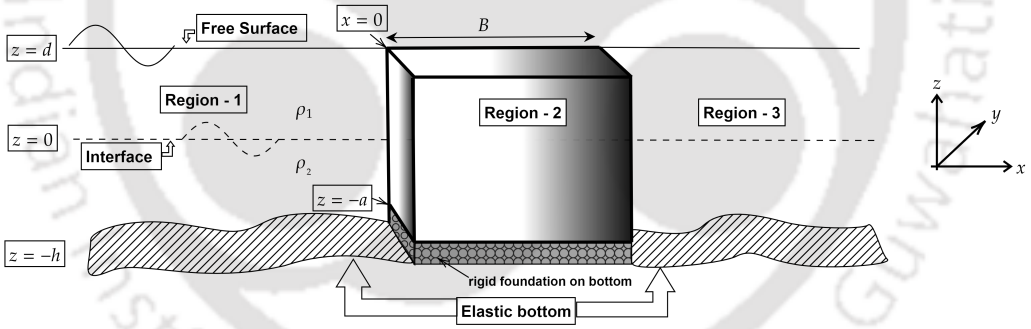

Figure 4.1: Definition sketch of wave scattering due to interface piercing structure

An interface-piercing porous breakwater is considered in a two-layer fluid flowing over an elastic sea bottom. Linear water wave theory and small amplitude bottom deflection in finite ocean water depth are taken into consideration to discuss the oblique surface wave interaction with the breakwater. By assuming large length of the bottom, the thin elastic plate theory can be employed for the elastic bottom, as being considered extensively for problems on wave-structure/ice-sheet interaction problems. The elastic sea bottom is considered as only a boundary in this analysis, and the fluid motion beneath it is not investigated. The flexible nature of the elastic plate renders the condition at the bottom to a fifth order condition which is different from the usual Neumann condition applicable for a rigid bottom. The motion is assumed to be irrotational and simple harmonic, and the

TH-2746_176123008

fluid to be inviscid and incompressible consisting of two layers under the action of gravity. The interface between the layers is taken to be linear. A right-handed coordinate system is employed in such a way that $z = 0$ represents the interface of the layers with the z-axis pointing upwards. Further, the mean free surface of the upper fluid layer of density ρ_1 is located at $z = d$ whereas the lower fluid layer of density ρ_2 is bounded below by an elastic bottom $-\infty < x < \infty$ with the mean depth $z = -h$. Based on the previous studies, it can be inferred that the wave force acting on the shoreline is a recurring phenomenon, and placing a porous structure is one of the ways to reduce the wave force on the shoreline. The present study elaborates the importance of the porous structure standing upon a rigid foundation in protecting the shoreline. The porous structure is used as a caisson type breakwater above a rock bottom foundation located in $0 \leq x \leq B$. We consider an incident wave obliquely incident at an inclination θ to the x-axis on the structure. Subsequently, $\Phi_j,\ j = 1, 2, 3$, which denote the velocity potentials in Regions 1, 2 and 3, respectively, can be written as $\Phi_j(x, y, z, t) = \mathrm{Re}[\phi_j(x, z)e^{\mathrm{i}(k_y y - \omega t)}]$. The schematic diagram of the problem is depicted in Figure 4.1. The variation of each potential Φ_j $(j = 1, 2, 3)$ in the y-direction is considered to be identical in order that all Φ_j along the vertical boundaries can be matched according to Snell's Law. A rock foundation is considered on which the caisson type breakwater is placed. Assuming this, we consider an impermeable bottom for porous Region 2 and consequently, elastic bottom effect exists for Regions 1 and 3 only. Furthermore, the effect of the bottom underneath the rigid block is ignored. In order that this specific arrangement is physically viable and can be used for practical problems, justification is provided in Appendix E.

In order that the problem can be clearly understood layer-wise, $\phi_j(x, z)$ are split in the following manner:

$$\phi_j = \begin{cases} \psi_j^{(1)}, & 0 < z < d, \\ \psi_j^{(2)}, & -h < z < 0, \end{cases} \quad \text{for } j = 1, 3, \text{ and } \phi_2 = \begin{cases} \psi_2^{(1)}, & 0 < z < d, \\ \psi_2^{(2)}, & -a < z < 0, \end{cases} \tag{4.1}$$

with the superscripts denoting the specific layer.

By taking into account all information, the boundary value problems for $\phi_j, j = 1, 2, 3$ are found to satisfy modified Helmholtz equation

$$(\nabla_{x,z}^2 - {k_y}^2)\phi_j = 0. \tag{4.2}$$

With the help of equations (4.1), (4.2) can be written as follows:

$$\left.\begin{aligned} (\nabla_{x,z}^2 - {k_y}^2)\psi_j^{(1)} &= 0, \quad 0 < z < d, \\ (\nabla_{x,z}^2 - {k_y}^2)\psi_j^{(2)} &= 0, \quad -h < z < 0, \end{aligned}\right\} \text{ for } j = 1, 3, \tag{4.3}$$

$$\left.\begin{aligned}(\nabla_{x,z}^2 - {k_y}^2)\psi_2^{(1)} = 0, \quad 0 < z < d,\\ (\nabla_{x,z}^2 - {k_y}^2)\psi_2^{(2)} = 0, \quad -a < z < 0.\end{aligned}\right\} \tag{4.4}$$

For Regions 1 and 3, the linearized mean free surface condition has the following form:

$$\frac{\partial \psi_j^{(1)}}{\partial z} - K\psi_j^{(1)} = 0 \ \text{ on } z = d \ \ (j = 1, 3). \tag{4.5}$$

However, the linearized mean free surface condition for Region 2 differs since the region is porous and is given by

$$\frac{\partial \psi_2^{(1)}}{\partial z} - K\gamma\psi_2^{(1)} = 0 \ \text{ on } z = d, \tag{4.6}$$

where $\gamma = m + \mathrm{i}f$ denotes the complex porous impedance parameter. In Appendix A, the details are provided for equations in a porous medium, as found in Dalrymple et al. [25]. Further, Region 2 is assumed to have a porosity ϵ.

It is assumed that there exists no cavitation between the elastic bottom and the lower layer water surface. We obtain the linearized boundary condition on the mean elastic bottom for $\phi_j, j = 1, 3$ as

$$\left[\hat{E}\mathrm{I}\frac{\partial^4}{\partial z^4} - \rho_p\hbar\omega^2 + \rho_2 g\right]\frac{\partial \phi_j}{\partial z} - \rho_2\omega^2\phi_j = 0 \ \text{ on } z = -h. \tag{4.7}$$

This can also be written explicitly as

$$E\frac{\partial^5 \psi_j^{(2)}}{\partial z^5} + (1 - \delta K)\frac{\partial \psi_j^{(2)}}{\partial z} - K\psi_j^{(2)} = 0, \tag{4.8}$$

where $E = \hat{E}\mathrm{I}/\rho_2 g$ with $\hat{E}\mathrm{I}$ being the flexural rigidity of the elastic plate, where $\hat{E}$ is the Young's modulus, $\mathrm{I} = \hbar^3/(12(1-\nu))$ and ν, $\hbar$ and ρ_p are, respectively, the Poisson's ratio, the thickness and the density of the elastic plate, g is the usual gravitational constant and $\delta = \rho_p\hbar/\rho_2$.

Due to the rigid foundation, the impermeable bottom condition in Region 2 yields

$$\frac{\partial \psi_2^{(2)}}{\partial z} = 0 \text{ at } z = -a. \tag{4.9}$$

Let us denote by $\rho = \rho_1/\rho_2$ the ratio of the densities of the two fluids. Subsequently, the linearized conditions at $z = 0$ take the following forms:

$$\frac{\partial \psi_j^{(1)}}{\partial z} = \frac{\partial \psi_j^{(2)}}{\partial z} \quad \text{for } j = 1, 2, 3, \tag{4.10}$$

TH-2746_176123008

$$\rho\left(\frac{\partial\psi_j^{(1)}}{\partial z}-K\psi_j^{(1)}\right)=\left(\frac{\partial\psi_j^{(2)}}{\partial z}-K\psi_j^{(2)}\right)\quad\text{for } j=1,3, \tag{4.11}$$

$$\rho\left(\frac{\partial\psi_2^{(1)}}{\partial z}-K\gamma\psi_2^{(1)}\right)=\left(\frac{\partial\psi_2^{(2)}}{\partial z}-K\gamma\psi_2^{(2)}\right). \tag{4.12}$$

Thereafter, combining the potentials $\psi_j^{(1)}$ and $\psi_j^{(2)}$ into ϕ_j as given in (4.1), the matching conditions across the wall yield

$$\left.\begin{aligned}&\phi_1=\gamma\phi_2,\\&\frac{\partial\phi_1}{\partial x}=\epsilon\frac{\partial\phi_2}{\partial x},\end{aligned}\right\}\ \text{at } x=0, \tag{4.13}$$

$$\left.\begin{aligned}&\phi_3=\gamma\phi_2,\\&\frac{\partial\phi_3}{\partial x}=\epsilon\frac{\partial\phi_2}{\partial x},\end{aligned}\right\}\ \text{at } x=B. \tag{4.14}$$

The above conditions arise due to the continuity of vertical velocity component and the pressure at $x=0$ and $x=B$.

Due to the rigid step, the velocity potentials $\psi_1^{(2)}$ and $\psi_3^{(2)}$ satisfy the following boundary condition:

$$\frac{\partial\psi_j^{(2)}}{\partial x}=0\ \text{ at } x=0\ \text{ for }\ -h<z<-a,\ \text{for } j=1,3. \tag{4.15}$$

Some additional constraints are required to be imposed at the edges of the elastic bottom. Practically, the rigid base of the structure is being constructed upon the bottom and that is why the clamped edge condition is justified to be assumed with respect to the bottom as an elastic plate. Furthermore, the edge conditions are also helpful in view of the need for stable creation of such structures. Under the physical considerations of our model, it is assumed that the elastic plate edges satisfy the clamped-edge boundary conditions at $(x,z)=(0,-h),(B,-h)$ which are as follows:

$$\frac{\partial^2\psi_j^{(2)}}{\partial x\partial z}=0,\ \frac{\partial\psi_j^{(2)}}{\partial z}=0\quad\text{for } j=1,3. \tag{4.16}$$

There exist some more standard edge conditions which can be applied separately at the edge, e.g., the simply supported edge boundary conditions which are given by

$$\frac{\partial^3\psi_j^{(2)}}{\partial x^2\partial z}=0,\ \frac{\partial\psi_j^{(2)}}{\partial z}=0\quad\text{for } j=1,3. \tag{4.17}$$

It can be added here that some more complicated boundary conditions may be taken into account. However, in the present context, such a situation does not arise because of

TH-2746_176123008

the simple physical conditions considered here and therefore, such boundary conditions are not required to be discussed. The choice of such edge conditions can be found in more details in Appendix E.

4.1 Scattering by the porous structure

Here, the scattering of oblique ocean waves by the porous structure in a two-layer fluid flowing over an elastic bottom is formulated and solved analytically. At the outset, the velocity potentials associated with surface wave interaction under the present situation are derived.

4.1.1 Approximation of the plane waves

The velocity potentials $\psi_j^{(1)}$ and $\psi_j^{(2)}$, $j = 1, 2, 3$ satisfying the governing equations (4.3) and (4.4), respectively, subject to the respective boundary conditions (4.5)-(4.10) have the following forms:

$$\phi_1 = \left\{ \begin{array}{l} \psi_1^{(1)} = \exp(\pm \mathrm{i}xq_1) I_1^{(1)}(k_1, z), \quad 0 < z < d, \\ \psi_1^{(2)} = \exp(\pm \mathrm{i}xq_1) I_1^{(2)}(k_1, z), \quad -h < z < 0, \end{array} \right\} \text{ for } x < 0, \tag{4.18}$$

$$\phi_2 = \left\{ \begin{array}{l} \psi_2^{(1)} = \exp(\pm \mathrm{i}xq_2) I_2^{(1)}(k_2, z), \quad 0 < z < d, \\ \psi_2^{(2)} = \exp(\pm \mathrm{i}xq_2) I_2^{(2)}(k_2, z), \quad -a < z < 0, \end{array} \right\} \text{ for } 0 < x < B, \tag{4.19}$$

$$\phi_3 = \left\{ \begin{array}{l} \psi_3^{(1)} = \exp(\pm \mathrm{i}xq_1) I_1^{(1)}(k_1, z), \quad 0 < z < d, \\ \psi_3^{(2)} = \exp(\pm \mathrm{i}xq_1) I_1^{(2)}(k_1, z), \quad -h < z < 0, \end{array} \right\} \text{ for } B < x < \infty, \tag{4.20}$$

with $q_j = \sqrt{k_j^2 - {k_y}^2}$ for $j = 1, 2$ and the eigenfunctions given by

$$I_1 = \left\{ \begin{array}{ll} I_1^{(1)} = \dfrac{g_1(k_1)(K \sinh k_1(z-d) + k_1 \cosh k_1(z-d))}{K \cosh k_1 d - k_1 \sinh k_1 d}, & 0 < z < d, \\ I_1^{(2)} = \left(\cosh k_1(z+h) + \dfrac{K}{F(k_1)} \sinh k_1(z+h) \right), & -h < z < 0, \end{array} \right. \tag{4.21}$$

$$I_2 = \left\{ \begin{array}{ll} I_2^{(1)} = \dfrac{\sinh k_2 a(K\gamma \sinh k_2(z-d) + k_2 \cosh k_2(z-d))}{K\gamma \cosh k_2 d - k_2 \sinh k_2 d}, & 0 < z < d, \\ I_2^{(2)} = \cosh k_2(z+a), & -a < z < 0, \end{array} \right. \tag{4.22}$$

where $g_1(k_1) = \left(\sinh k_1 h + \dfrac{K}{F(k_1)} \cosh k_1 h \right)$ and $F(k_1) = (Ek_1^4 + 1 - \delta K)k_1$.

All k_j's appearing above are computed from the dispersion relations which can be found as follows by using (4.11) and (4.12):

$$D_W(k_1) \equiv k_1^2(1-\rho) \tanh k_1 d \tanh k_1 h - k_1 K(\tanh k_1 d + \tanh k_1 h)$$

TH-2746_176123008

$$+K^2(\rho\tanh k_1d\tanh k_1h+1)+\frac{K}{F(k_1)}\left[k_1^2(1-\rho)\tanh k_1d-k_1K(1+\tanh k_1d\tanh k_1h)\right.$$
$$\left.+K^2(\tanh k_1h+\rho\tanh k_1d)\right]=0, \tag{4.23}$$
$$D_P(k_2)\equiv k_2^2(1-\rho)\tanh k_2d\tanh k_2a-k_2\gamma K(\tanh k_2d+\tanh k_2a)$$
$$+K^2\gamma^2(\rho\tanh k_2d\tanh k_2a+1)=0. \tag{4.24}$$

4.1.2 Discussion on the roots of the dispersion relations

The cases $\rho\to 1$ and $d\to 0$, respectively, in (4.23) and (4.24) yield the dispersion relation for a homogeneous fluid for a similar geometrical configuration. It is obvious that $k_1=0$ is a root of equation (4.23). Consideration of a very thin elastic plate with respect to the wavelength ($\delta K\ll 1$), adopting Euler-Bernoulli beam equation, results in dispersion relation (4.23) having two positive real roots, say, $k_{1,1}$ and $k_{1,2}$ where $0<k_{1,1}<k_{1,2}$ and these correspond to the propagating modes; two pairs of complex conjugate roots, say $k_{1,\pm I}=\pm P+\mathrm{i}Q$ and $k_{1,\pm II}=\pm P-\mathrm{i}Q$ and these correspond to the non-propagating modes; and also an infinite number of purely imaginary roots given by $k_{1,n}=\mathrm{i}t_n$ for $n=3,4,5,\ldots$ and real t_n, and these correspond to the evanescent modes. The existence of exactly two positive zeros, as also observed in [16, 17, 89, 62], implies that there exist two wave modes (wavenumbers) which propagate at the free surface (say, SM) and at the interface (say, IM), respectively, along the positive x-direction. The study of the wave characteristics corresponding to $x\geq 0$ is sufficient due to the symmetry about $x=0$. The negative values of real and purely imaginary roots represent waves travelling in the negative direction. In Newton-Raphson numerical solution procedure, the roots are found by using Matlab. The initial choice is always considered to be crucial for finding the roots. This does not always result in success. It is important that suitable starting values are chosen. This is particularly true when the wavenumbers of two different modes are close to each other (or when they coincide).

$E/h^4\Downarrow$	$k_{1,1}h$	$k_{1,2}h$	$k_{1,3}h$	$k_{1,4}h$	$k_{1,5}h$	$k_{1,I}h$
$E/h^4=10^1$	0.10082	6.60658	1.81108i	3.12540i	5.38720i	$0.4170+0.3889$i
$E/h^4=10^2$	0.10289	6.60658	1.81080i	3.12538i	5.38720i	$0.2477+0.1986$i
$E/h^4=10^3$	0.17687	6.60658	1.81078i	3.12538i	5.38720i	$0.1225+0.0594$i
$E/h^4=10^4$	0.22937	6.60658	1.81077i	3.12538i	5.38720i	$0.0516+0.0430$i
$E/h^4=10^5$	0.23255	6.60658	1.81077i	3.12538i	5.38720i	$0.0273+0.0258$i
$E/h^4=10^6$	0.23286	6.60658	1.81077i	3.12538i	5.38720i	$0.0150+0.0148$i
$E/h^4=10^7$	0.23289	6.60658	1.81077i	3.12538i	5.38720i	$0.0084+0.0083$i

Table 4.1: Variation of $k_{1,n}h$ $(n=1,2,\ldots,5,I)$ against the flexural rigidity E/h^4 for $\rho=0.97,\ Kh=0.1,\ d/h=1$ and $\delta/h=0.0001$.

Now we examine the roots $k_{1,n}h, n=1,2,\ldots,I$, against the flexural rigidity and

TH-2746_176123008

structure width and subsequently present the results through two tables. From Table 4.1, one may observe that the wavenumbers in SM attain increasing values corresponding to higher elastic parameter E/h^4 of the bottom but no difference is observed for the IM. The strength of the evanescent modes faces a negligible decay when the elastic parameter increases. However, it is known that such waves have no role in changing the asymptotic behaviour of the resultant reflected and transmitted waves. The impact of flexural rigidity can be easily observed for the complex root $k_{1,I}h$. The non-dimensional modulus value of the complex root can be observed to reduce sharply and tend to 0 with an increase of flexural rigidity E/h^4. Physically, the higher the flexural rigidity, the stiffer the bottom, and the harder for it to bend. Therefore, higher flexural rigidity will render the bottom to a rigid one, and as already observed, wave scattering in a two-layer fluid for an impermeable bottom results in two pairs of real roots. Moreover, the stiffness depends not only on the flexural rigidity but also on the length of the plate and its end conditions as well.

$\frac{\delta}{h} \Downarrow$	$k_{1,1}h$	$k_{1,2}h$	$k_{1,3}h$	$k_{1,4}h$	$k_{1,5}h$	$k_{1,I}h$
$\frac{\delta}{h} = 1$	0.07528	6.60658	1.81080i	3.12538i	5.38720i	$0.2460 + 0.1901$i
$\frac{\delta}{h} = 0.1$	0.10065	6.60658	1.81080i	3.12538i	5.38720i	$0.2475 + 0.1978$i
$\frac{\delta}{h} = 0.01$	0.10265	6.60658	1.81080i	3.12538i	5.38720i	$0.2476 + 0.1985$i
$\frac{\delta}{h} = 0.001$	0.10285	6.60658	1.81080i	3.12538i	5.38720i	$0.2477 + 0.1986$i
$\frac{\delta}{h} = 0.0001$	0.10287	6.60658	1.81080i	3.12538i	5.38720i	$0.2477 + 0.1986$i

Table 4.2: Variation of $k_{1,n}h$ $(n = 1, 2, \ldots, 5, I)$ against $\hbar$ in non-dimensional δ/h for $\rho = 0.97,\ Kh = 0.1,\ d/h = 1$ and $E/h^4 = 10^2$.

While changing δ/h, we can observe from Table 4.2 that reducing δ can result in an increase of the mode $k_{1,1}h$ whereas $k_{1,2}h$ remains unchanged as observed for E/h^4. No difference is observed for evanescent modes while changing δ. Furthermore, the complex root gets changed by a negligible amount. Due to the consideration of a thin elastic plate, it is already mentioned that δK is very small and moreover, we can conclude that after some value of $\delta/h \leq 0.1$, reduction of δ will not affect our result to a large extent.

A detailed analysis can be found in Section 2.2 regarding the roots in porous region. It is to be noted that if $\epsilon = 0, \gamma = 0$, then Region 2 becomes a rigid block. However, for shallow water waves (for both layers), $\tanh k_j d \approx k_j d$ for $j = 1, 2$ and $\tanh k_1 h \approx k_1 h,\ \tanh k_2 a \approx k_2 a$ which yield, from (4.23) and (4.24),

$$k_1^4 dh(1-\rho) - k_1^2 K\left(d + h + \rho K dh\right) + K^2 + \frac{K k_1}{F(k_1)}\left[k_1^2 d\left\{1 - \rho - Kh\right\} - K + K^2(h + \rho d)\right] = 0, \tag{4.25}$$

$$k_2^4 da(1-\rho) - k_2^2 K\left\{\gamma(d+a) + \rho K \gamma^2 da\right\} + K^2\gamma^2 = 0. \tag{4.26}$$

TH-2746_176123008

Equation (4.25) can be rewritten in the form $k_1\mathfrak{F}(k_1) = 0$ where

$$\mathfrak{F}(k_1) = a_1k_1^8 + b_1k_1^6 + c_1k_1^4 + d_1k_1^2 + e_1.$$

Consideration of $k_1^2 = x$ results in a quartic function $f_1(x)$ such that

$$f_1(x) = a_1x^4 + b_1x^3 + c_1x^2 + d_1x + e_1.$$

$f_1(x) = 0$ gives us the required roots k_1. If we calculate the discriminant of $f_1(x) = \mathfrak{D}$ numerically, it can be observed that $\mathfrak{D} < 0$ which results in two distinct real roots and two complex conjugate roots. Hence, equation (4.25) results in two pairs of real roots, four complex conjugate roots and one zero root. Similar observation has been made by Chanda [13]. Equation (4.26) can also be written in the form

$$a_2k_2^4 - b_2k_2^2 + c_2 = 0.$$

The roots of the above equation are given by

$$k_2 = \pm\sqrt{\frac{b_2 \pm \sqrt{b_2^2 - 4a_2c_2}}{2a_2}}.$$

Therefore, it can be clearly observed that (4.26) has two symmetric pairs of roots which depend upon the parameter γ. We use inbuilt "*ROOTS*" function in Matlab to easily obtain these polynomial roots.

In Figures 4.2(a), 4.2(c) and 4.2(e), dimensionless real propagating modes are plotted corresponding to various parameters. The real roots tend to 0 as $h, K \to 0$. For shallow water waves, the difference between the propagating modes is minimum and as the wave tends to be deeper, the mode difference increases. The interfacial mode increases monotonically over Kh. For phase velocity, they maintain a steady state while varying h, and the interfacial mode has a lower phase velocity. As the time duration of gravity waves is $T = [0, 20]$ s, while varying K, the similar characteristics in wave modes can be observed as seen in Figure 4.2(a). Phase velocity is also lower for the interfacial mode. The free surface mode attains the maximum value for lower frequency and decreases over Kh. For varying ρ, the interfacial mode blows out as $\rho \to 1$. Further, $\rho = 1$ results in a single layer fluid propagation and that is why $\rho \to 0$ results in zero phase velocity for the interfacial mode. Further, the free surface mode attains a steady state of phase velocity over varying ρ. Between the propagating modes, the free surface one is found to be lower for all cases and it attains higher phase velocity.

Figure 4.3 illustrates the behaviour of the dispersion relationship with dimensionless depth and we examine if there exists any situation where the eigenfunction solution

TH-2746_176123008

fails. The plots show the complex wavenumber for the first five non-dimensional modes $(k_{2,n}h,\ n = 1, \ldots, 5)$ for the values of f in the range $[0, 20]$ and a given value of Kh.

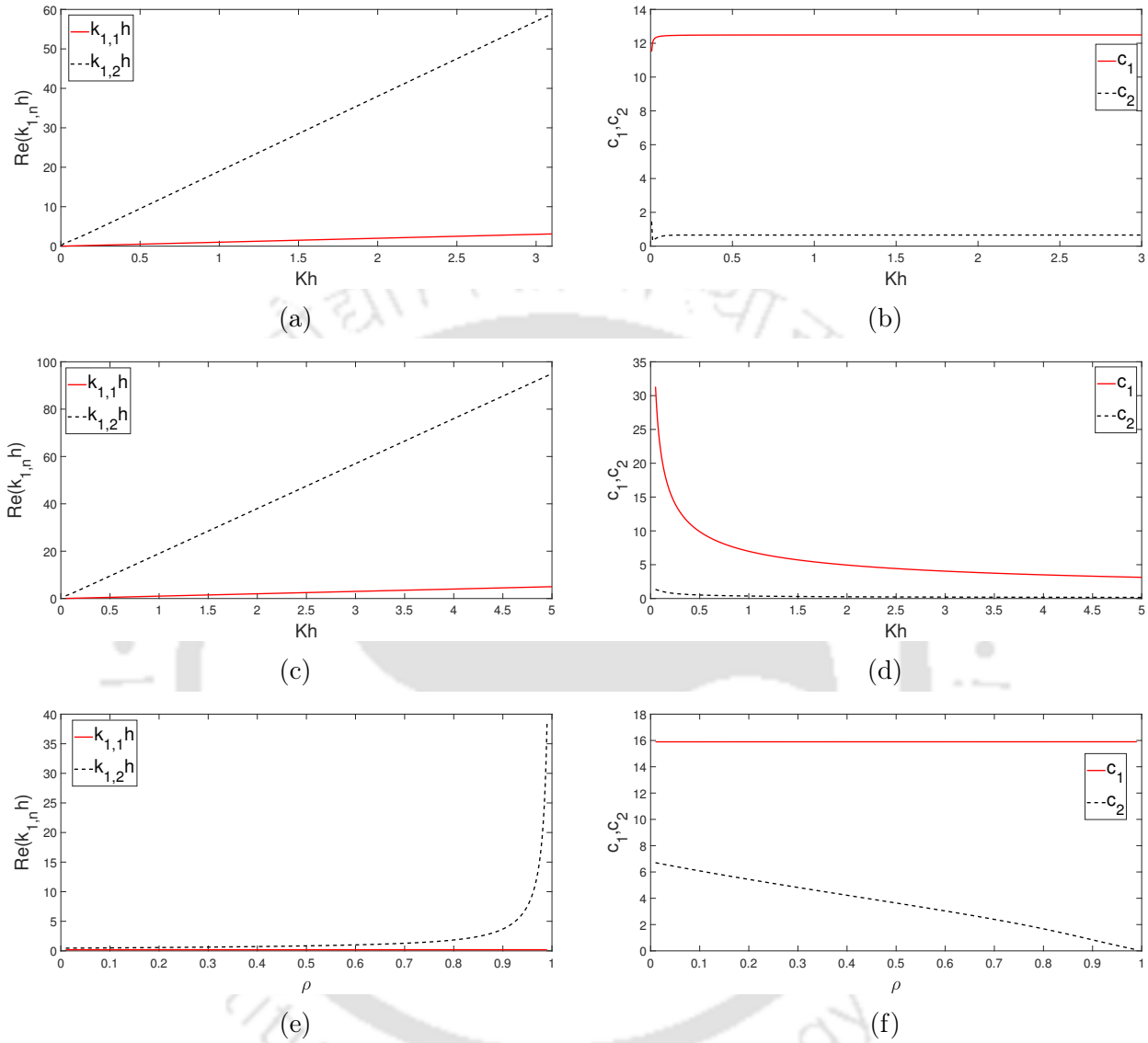

Figure 4.2: Real propagating modes and their phase velocity correponding to (a,b) varying h, (c,d) varying K and (e,f) varying ρ of dispersion relation (4.23) with $d/h = 1$ and $\rho = 0.9$.

For shallow water case, $Kh = 0.1886$, Figure 4.3(a) shows the dimensionless wavenumbers in the porous medium as f varies from 0 to 20. For this case, $k_{2,1}h$ and $\mathrm{Im}(k_{2,n}h)$ first increase and then decrease with higher f but $k_{2,2}h$ rises sharply where increasing f causes higher oscillation. No mode swapping appears for shallow water. In Figures 4.3(b) to 4.3(f), a value of $Kh \in [0.8602 - 2.0122]$ is used and the real parts in evanescent modes show a decreasing nature for increasing f. In Figures 4.3(a) to 4.3(d), the real part of the evanescent mode exceeds $\mathrm{Re}(k_{2,1}h)$ for higher $f > 11$, which means that the plane-wave

TH-2746_176123008

approximation is not valid for large values of f for such Kh.

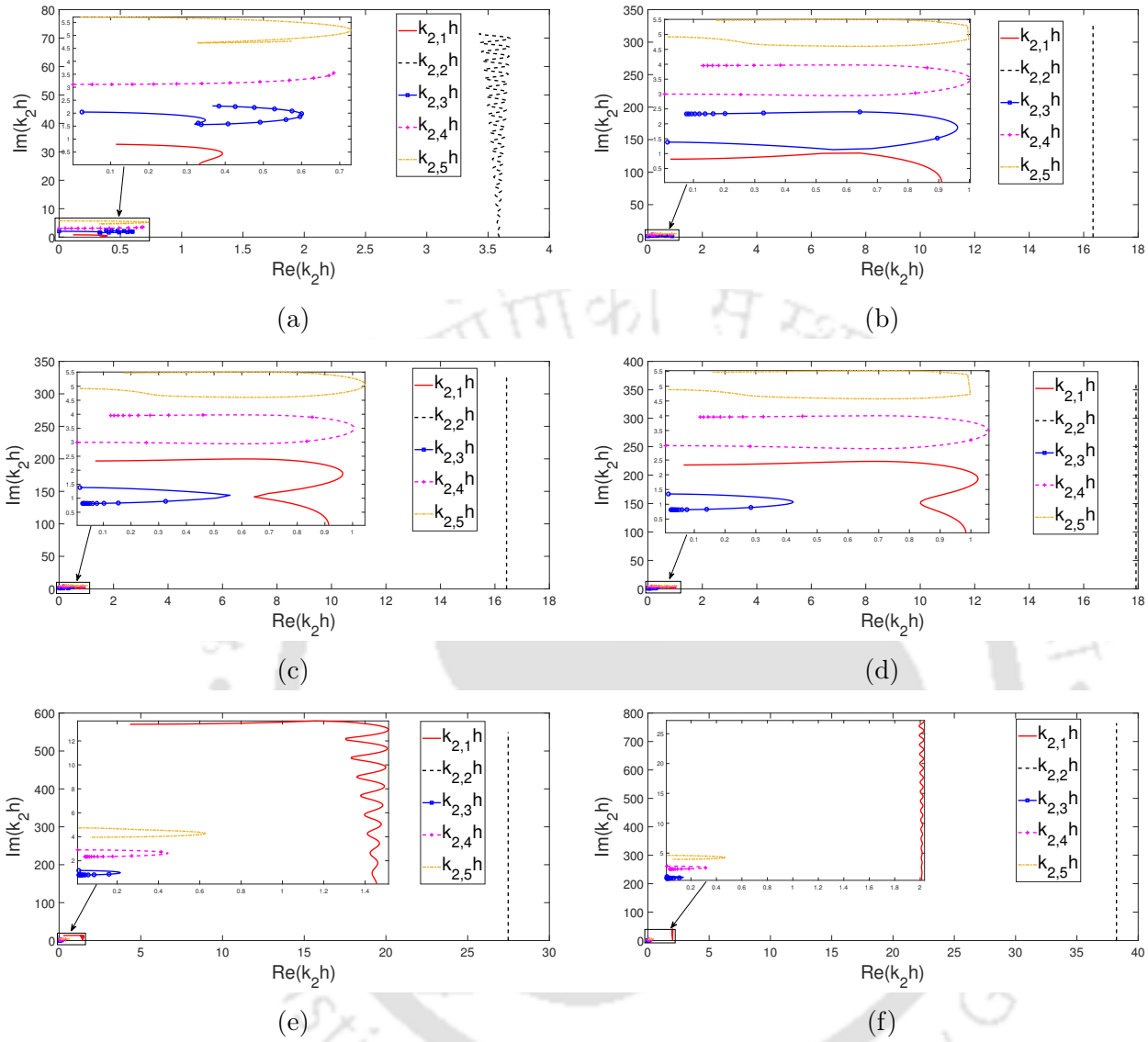

Figure 4.3: Roots of dispersion relation (4.24) corresponding to varying f in the range of $[0, 20]$ for (a) $Kh = 0.1886$, (b) $Kh = 0.8602$, (c) $Kh = 0.8646$, (d) $Kh = 0.9432$, (e) $Kh = 1.4462$ and (f) $Kh = 2.0122$ with $d/h = 1$.

For the values of $Kh \in [0, 0.8602]$, the curve corresponding to $k_{2,1}h$ passes below the dimensionless evanescent curves whereas for $Kh \in [0.8646, 2.0122]$, it passes above the non-dimensional evanescent curves. In fact, the trajectory followed by each curve is the same as that followed by the other mode at the higher value of f. If there is any intersection between two curves, then it is referred to as mode swapping (e.g., [22]). As Kh increases towards deeper water conditions, the curve corresponding to dimensionless $k_{2,1}$ moves further away from the evanescent modes. In the intermediate region, our main concern is to check for mode swapping. From all the curves, it is clear that the value $k_{1,n}h$

oscillates about the vertical line $\mathrm{Re}(k_{2,1}h) = Kh$.

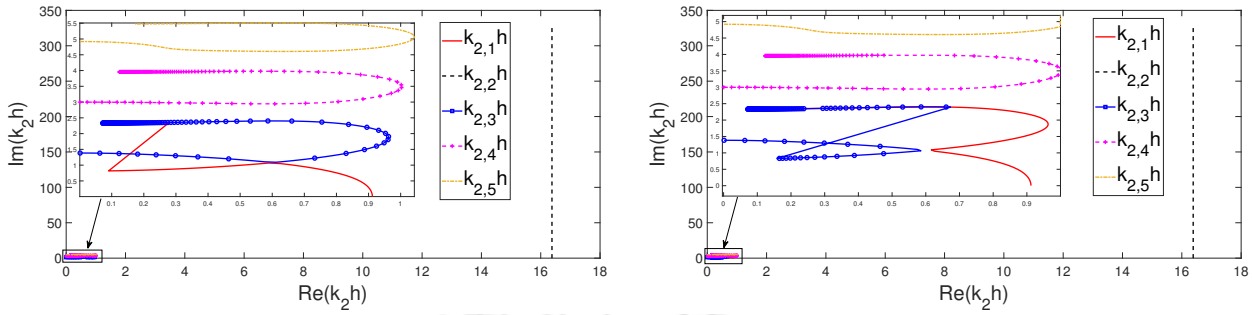

(a) (b)

Figure 4.4: Roots of dispersion relation (4.24) corresponding to varying f in the range of $[0, 20]$ for (a) $Kh = 0.8620$, (b) $Kh = 0.8623$, with $d/h = 1$.

For the values of $Kh = 0.8620$ and 0.8623, corresponding to intermediate water depth, the curve of $k_{2,1}h$ versus f oscillates with that of $k_{2,3}h$, as shown in Figure 4.4. In Figure 4.4(a), the curve corresponding to $k_{2,1}h$ intersects once at $f = 14.2749$, and after $f = 15.055$, it leaves a negligible distance with $k_{2,3}h$ in the form $|k_{2,1}h - k_{2,3}h| < O(10^{-6})$. In Figure 4.4(b), corresponding to a f-value of 17.6875, the curve corresponding to $k_{2,1}h$ shows a negligible distance of $O(10^{-5})$ with $k_{2,3}h$. As Kh increases towards deeper water conditions, the dimensionless $k_{2,n}$ curve may not intersect other $k_{2,n}$ modes. The coalescence of the two modes implies that another new mode must be present in a similar way when double roots are obtained in the characteristic equation while solving an ordinary differential equation with constant coefficients. As defined by Dalrymple et al. [25], the Green's function technique could be used to overcome the situation. For our choice of parameters along with the value of $f \in [0, 2]$, the mode swapping does not happen.

4.1.3 Method of solution

By using the method of eigenfunction expansion, the velocity potentials $\phi_j(x, z)$ for each subdomain $j = 1, 2, 3$ can be written as

$$\phi_1 = \sum_{n=1}^{2} e^{\mathrm{i}q_{1,n}x} I_{1,n}(k_{1,n}, z) + \sum_{n=I,II,1}^{\infty} R_n e^{-\mathrm{i}q_{1,n}x} I_{1,n}(k_{1,n}, z), \tag{4.27}$$

$$\phi_2 = \sum_{n=1}^{\infty} (\mathrm{A}_n e^{\mathrm{i}q_{2,n}x} + \mathrm{B}_n e^{-\mathrm{i}q_{2,n}(x-B)}) I_{2,n}(k_{2,n}, z), \tag{4.28}$$

$$\phi_3 = \sum_{n=I,II,1}^{\infty} T_n e^{\mathrm{i}q_{1,n}(x-B)} I_{1,n}(k_{1,n}, z), \tag{4.29}$$

TH-2746_176123008

where R_n and T_n, $n = 1, 2, \ldots$ are, respectively, the reflection and transmission coefficients. In accordance with the realistic physical problems in wave-structure interactions, we take the contribution of the complex wavenumbers in Regions 1 and 3 with $k_{1,n}$ $(n = I, II)$ being complex conjugates having positive real parts.

It is assumed that the wavenumbers take distinct values in water and porous regions or otherwise the alternative approach as mentioned by Behera and Sahoo [8] may be considered. The eigenfunctions $I_{2,n}(k_{2,n}, z)$ in (4.22) are integrable in $(-a, d)$, and they are orthogonal with respect to the following inner product:

$$\langle \varphi_n, \Psi_m \rangle = \int_{-a}^{0} \varphi_n \Psi_m \mathrm{d}z + \rho \int_{0}^{d} \varphi_n \Psi_m \mathrm{d}z, \tag{4.30}$$

and this gives

$$\langle I_{2,n}, I_{2,m} \rangle = \begin{cases} 0, & m \neq n, \\ W_n, & m = n, \end{cases} \tag{4.31}$$

where

$$W_n = \frac{2ak_{2,n} + \sinh 2ak_{2,n}}{4k_{2,n}} + Q_n \left(\frac{(k_{2,n}^2 - K^2\gamma^2)d}{2} + \frac{(k_{2,n}^2 + K^2\gamma^2)\sinh 2k_{2,n}d}{4k_{2,n}} - K\gamma \sinh^2 k_{2,n}d \right),$$

with

$$Q_n = \frac{\rho \sinh^2 k_{2,n}a}{(K\gamma \cosh k_{2,n}d - k_{2,n} \sinh k_{2,n}d)^2}.$$

The vertical eigenfunctions $I_{1,n}$ in Regions 1 and 3 are found to be not orthogonal in the usual way. They form an orthogonal mode-coupling relation as follows:

$$\langle \varphi_n, \Psi_m \rangle = \left[\int_{-h}^{0} \varphi_n \Psi_m \mathrm{d}z + \rho \int_{0}^{d} \varphi_n \Psi_m \mathrm{d}z \right] - \frac{E}{K} \left[\varphi_n'(-h)\Psi_m'''(-h) + \varphi_n'''(-h)\Psi_m'(-h) \right], \tag{4.32}$$

which is similar to the one in the work of Mohapatra and Sahoo [76]. Furthermore, in the present study, orthogonality of the eigenfunction $I_{2,n}$ in the porous region is utilized to solve the boundary value problem.

Now, using the matching conditions (4.13)-(4.15) by considering N evanescent modes,

TH-2746_176123008

we get the following:

$$\sum_{n=1}^{2} I_{1,n} + \sum_{n=I,II,1}^{N+2} R_n I_{1,n} = \gamma \sum_{n=1}^{N+2} (\mathrm{A}_n + \mathrm{B}_n e^{\mathrm{i}q_{2,n}B}) I_{2,n}, \quad \text{for } -a < z < d, \tag{4.33}$$

$$\sum_{n=1}^{2} q_{1,n} I_{1,n} - \sum_{n=I,II,1}^{N+2} R_n q_{1,n} I_{1,n} = \begin{cases} 0, & \text{for } -h < z < -a, \\ \epsilon \sum_{n=1}^{N+2} (\mathrm{A}_n - \mathrm{B}_n e^{\mathrm{i}q_{2,n}B}) q_{2,n} I_{2,n}, & \text{for } -a < z < d, \end{cases} \tag{4.34}$$

$$\sum_{n=I,II,1}^{N+2} T_n I_{1,n} = \gamma \sum_{n=1}^{N+2} (\mathrm{A}_n e^{\mathrm{i}q_{2,n}B} + \mathrm{B}_n) I_{2,n}, \quad \text{for } -a < z < d, \tag{4.35}$$

$$\sum_{n=I,II,1}^{N+2} T_n q_{1,n} I_{1,n} = \begin{cases} 0, & \text{for } -h < z < -a, \\ \epsilon \sum_{n=1}^{N+2} (\mathrm{A}_n e^{\mathrm{i}q_{2,n}B} - \mathrm{B}_n) q_{2,n} I_{2,n}, & \text{for } -a < z < d. \end{cases} \tag{4.36}$$

Thereafter, applying the orthogonality of the eigenfunction $I_{2,n}$ (equation (4.31)), we get

$$\sum_{n=I,II,1}^{N+2} R_n \hat{b}_{n,m} - \gamma(\mathrm{A}_m + \mathrm{B}_m e^{\mathrm{i}q_{2,m}B}) a_m = -\sum_{n=1}^{2} \hat{b}_{n,m}, \tag{4.37}$$

$$\sum_{n=I,II,1}^{N+2} R_n q_{1,n} b_{n,m} + \epsilon(\mathrm{A}_m - \mathrm{B}_m e^{\mathrm{i}q_{2,m}B}) q_{2,m} a_m = \sum_{n=1}^{2} q_{1,n} b_{n,m}, \tag{4.38}$$

$$\gamma(\mathrm{A}_m e^{\mathrm{i}q_{2,m}B} + \mathrm{B}_m) a_m - \sum_{n=I,II,1}^{N+2} T_n b_{n,m} = 0, \tag{4.39}$$

$$\epsilon(\mathrm{A}_m e^{\mathrm{i}q_{2,m}B} - \mathrm{B}_m) q_{2,m} a_m - \sum_{n=I,II,1}^{N+2} T_n q_{1,n} b_{n,m} = 0, \tag{4.40}$$

where

$$a_m = \int_{-a}^{0} I_{2,m} I_{2,m} \mathrm{d}z + \rho \int_{0}^{d} I_{2,m} I_{2,m} \mathrm{d}z, \quad b_{n,m} = \int_{-h}^{0} I_{1,n} I_{2,m} \mathrm{d}z + \rho \int_{0}^{d} I_{1,n} I_{2,m} \mathrm{d}z,$$

$$\hat{b}_{n,m} = \int_{-a}^{0} I_{1,n} I_{2,m} \mathrm{d}z + \rho \int_{0}^{d} I_{1,n} I_{2,m} \mathrm{d}z.$$

Therefore, the system (4.37)-(4.40) consists of $(4N + 8)$ linear equations with $(4N + 12)$

TH-2746_176123008

unknowns where the unknown vector is

$$X = [R_I, R_{II}, R_1, R_2, \ldots, R_{N+2}, \mathrm{A}_1, \ldots, \mathrm{A}_{N+2}, B_1, \ldots, \mathrm{B}_{N+2}, T_I, T_{II}, T_1, \ldots, T_{N+2}]^T. \tag{4.41}$$

It leaves us with the requirement of four more conditions which can be obtained from the edge conditions (4.16). Subsequently, it yields a linear system of size $(4N+12)$ as follows:

$$\mathbb{A}X = \mathbb{B}. \tag{4.42}$$

Determination of X allows us to discuss the reflection within the porous structure. The computation of various quantities along with the relevant results and discussions take place in the next section. R_n, T_n $(n = 1, 2)$, respectively, represent the reflection and transmission coefficients for both SM and IM, and they are evaluated by considering $R_{SM} = |R_1|$, $R_{IM} = |R_2|$, $|T_{SM}| = |T_1|$, $T_{IM} = |T_2|$. Furthermore, F_f and F_b, the unit horizontal wave forces acting on the front and back faces, respectively, of the porous structure can be evaluated from the following:

$$F_f = \mathrm{i}\omega\gamma \left[\rho_2 \int_{-a}^{0} \phi_2(0,z)dz + \rho_1 \int_{0}^{d} \phi_2(0,z)dz \right],$$

$$F_b = \mathrm{i}\omega\gamma \left[\rho_2 \int_{-a}^{0} \phi_2(B,z)dz + \rho_1 \int_{0}^{d} \phi_2(B,z)dz \right].$$

$\mathbb{F}_f$ and $\mathbb{F}_b$ are, respectively, the non-dimensional form of F_f and F_b, and are given by

$$\mathbb{F}_f = \frac{|F_f|}{\rho_2 g a d}, \text{ and } \mathbb{F}_b = \frac{|F_b|}{\rho_2 g a d}. \tag{4.43}$$

Assuming that the progressive waves in the surface and interfacial modes are of the forms $\zeta_i = \mathrm{Re}(\eta_i e^{-\mathrm{i}\omega t})$ for $i = 1, 2$, respectively, the amplitude is obtained from the kinematic conditions in the open water as

$$\eta_1 = \frac{\mathrm{i}}{\omega}\frac{\partial \phi_j}{\partial z} \text{ for } j = 1, 3, \text{ at } z = d, \tag{4.44}$$

$$\eta_2 = \frac{\mathrm{i}}{\omega}\frac{\partial \phi_j}{\partial z} \text{ for } j = 1, 3, \text{ at } z = 0. \tag{4.45}$$

Similarly, the amplitude of bottom deflection $\xi = \mathrm{Re}(\varsigma e^{-\mathrm{i}\omega t})$ is given by the formula

$$\varsigma = \frac{\mathrm{i}}{\omega}\frac{\partial \phi_j}{\partial z} \text{ for } j = 1, 3, \text{ at } z = -h. \tag{4.46}$$

TH-2746_176123008

The shear force $\mathbb{S}_F$ on the elastic bottom is obtained by using the formula

$$\mathbb{S}_F = \left| \frac{E}{Kh}\frac{\partial}{\partial x}\left\{\left(\frac{\partial^2}{\partial x^2} - (2-\nu){k_y}^2\right)\right\}\frac{\partial \phi_j}{\partial z}\right| \text{ at } z=-h \text{ for } j=1,3. \tag{4.47}$$

4.1.4 Linear algebraic approach

Our initial aim is to verify our computational results by comparing solutions obtained via another method. However, depending on the boundary conditions in a boundary value problem, the orthogonality of eigenfunctions may be an issue while trying to solve the problem by using the matched eigenfunction expansion method. When the complex dispersive roots in region 1 or 3 are in a close range with the complex dispersive roots of region 2, then the inner product value $b_{n,m}$ or $\hat{b}_{n,m}$ will give rise to singularity. This may result in ill-conditioned matrices in the system of equations (4.42). Therefore, in addition to using the orthogonality of eigenfunctions, the solution of the set of equations equations (4.33) to (4.36) can be approximated by applying the algebraic least squares (LS) method. There are $(4N+12)$ unknowns in X, where N is the number of evanescent modes in velocity potentials. In order to apply the algebraic least squares method, infinite number of discrete points are considered as follows: $z_{1,1}, z_{1,2}, \ldots$ in $(d,0)$, $z_{2,1}, z_{2,2}, \ldots$ in $(0,-a)$ and $z_{3,1}, z_{3,2}, \ldots$ in $(-a,-h)$. This consideration leads to an over-determined system (ODS) consisting of an infinite number of equations and finite unknowns given by

$$A_1 X_1 = B_1, \tag{4.48}$$

where X_1 is the same unknown vector as X and A_1 is the coefficient matrix.

For numerical implementation of this algorithm, we consider N_1 number of points in $(d,0)$, N_2 number of points in $(0,-a)$ and N_3 number of points in $(-a,-h)$, which gives us the ODS of size $M \times (4N+12)$, where $M=(N_1+N_2+N_3)$ and $4N+12<M$. By using the algebraic least squares method, this ODS can be solved to get the values of the unknowns. Furthermore, minimization of the error gives

$$Err = \frac{\|B_1 - A_1 X_1\|_2}{\|B_1\|_2}, \tag{4.49}$$

where $\|.\|_2$ is the Euclidean norm. The unique LS solution X_1 of equation (4.48) is (Miller [72])

$$X_1 = (A_1^* A_1)^{-1} A_1^* B_1, \tag{4.50}$$

where A_1^* represents the conjugate transpose of A_1. Further, the unique solution exists provided A_1 has linearly independent columns.

TH-2746_176123008

4.1.5 Plane wave solution

In the plane wave assumptions, only the most progressive modes (least damped) of all regions are considered while employing the matching conditions. The velocity potentials ϕ_j for $j = 1, 2, 3$ have the following forms:

$$\phi_1 = \sum_{n=1}^{2} e^{\mathrm{i}q_{1,n}x} I_{1,n}(k_{1,n}, z) + \sum_{n=1}^{2} R_n e^{-\mathrm{i}q_{1,n}x} I_{1,n}(k_{1,n}, z), \tag{4.51}$$

$$\phi_2 = \sum_{n=1}^{2} (\mathrm{A}_n e^{\mathrm{i}q_{2,n}x} + \mathrm{B}_n e^{-\mathrm{i}q_{2,n}(x-L)}) I_{2,n}(k_{2,n}, z), \tag{4.52}$$

$$\phi_3 = \sum_{n=1}^{2} T_n e^{\mathrm{i}q_{1,n}(x-B)} I_{1,n}(k_{1,n}, z). \tag{4.53}$$

Applying a similar procedure, we obtain a system of equations from which we can easily obtain the solution by employing any of the methods. For shallow water approximation, no evanescent modes are needed in order to match the solutions. The system of equations for shallow wave approximation remains the same as like in plane waves. Furthermore, to obtain normal incidence solution, k_y should be 0.

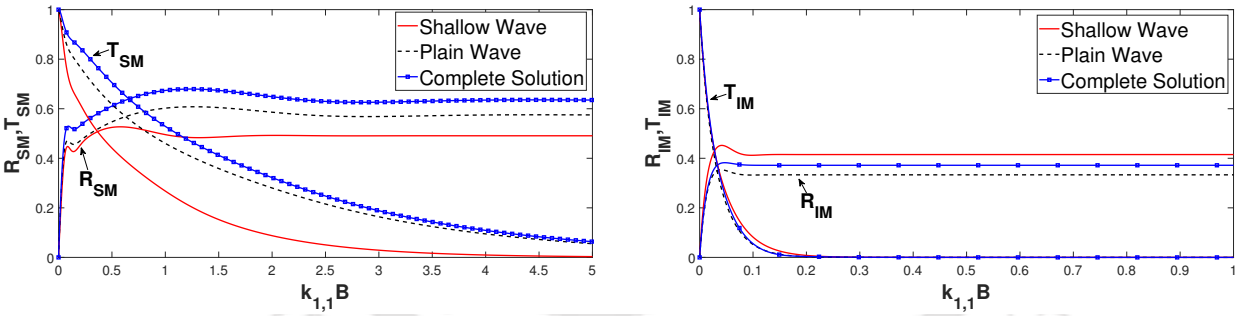

(a) (b)

Figure 4.5: Reflection and transmission coefficients in (a) free surface mode and (b) interfacial mode against non-dimensional width $k_{1,1}B$ for various different wave approximation with $f = 1, \epsilon = 0.5$.

From Figure 4.5(a,b), it can be clearly observed that the consideration of different numbers of evanescent modes affects reflection and transmission coefficients. Shallow wave approximation also shows a similar pattern but the difference is easily visible.

4.1.6 Results and discussion

The system of equations given by (4.42) is solved by using the in-built program Matlab R2019a. It is to be noted that, in order to utilize the algebraic approach and analytical

TH-2746_176123008

approach, the occurrence of ill-conditioned matrices must be avoided. In this context, it is very important to choose the appropriate value of the parameters so as to avoid such an occurrence. Since A and A_1 are $m \times n$ $(m \leq n)$ complex matrices and $B, B_1 \in \mathbb{C}$, therefore the solutions $X, X_1 \in \mathbb{C}$. Therefore, finding an appropriate algorithm to obtain the inverse may be one of the key aspects in numerical approach. In both the methods, we finally have to solve a large-scale linear square system and hence we choose the in-built function algorithm which uses LU factorization with partial pivoting. Proper care must be taken for ill-conditioned systems since it may give some inaccurate solution.

To carry out the computation, some parameter values are fixed as follows: $(h-a)/h = \frac{1}{25}$, $d/h = 1$; $m = 1$; $\rho = 0.97$; $E/h^4 = 10^5, \delta/h = 10^{-4}$, $\theta = 30^\circ$, $Kh = 0.1$, $\nu = 0.3$ along with values of f and ϵ in $[0.25, 2]$ and $[0.3, 0.9]$, respectively. A detailed justification for consideration of these parameter values can be found in Appendix D.

	$Kh = 0.28$		$Kh = 0.16$		$Kh = 0.10$		$Kh = 0.07$	
	R_{SM}	T_{SM}	R_{SM}	T_{SM}	R_{SM}	T_{SM}	R_{SM}	T_{SM}
$N = 0$	0.866	0.516	0.958	0.671	0.849	0.655	0.660	0.548
$N = 2$	0.650	0.478	0.712	0.574	0.607	0.520	0.455	0.407
$N = 4$	0.636	0.457	0.680	0.542	0.573	0.489	0.432	0.387
$N = 6$	0.609	0.444	0.644	0.518	0.546	0.469	0.417	0.374
$N = 8$	0.594	0.432	0.630	0.506	0.540	0.463	0.415	0.373
$N = 10$	0.578	0.422	0.615	0.496	0.532	0.457	0.411	0.369
$N = 12$	0.568	0.415	0.610	0.492	0.530	0.456	0.410	0.369
$N = 14$	0.559	0.409	0.603	0.486	0.526	0.453	0.409	0.367
$N = 16$	0.558	0.408	0.603	0.486	0.526	0.453	0.409	0.367

Table 4.3: Convergence study of R_{SM} and T_{SM} for different Kh with $B/(d+h) = 0.75$, $E/h^4 = 10^5$, $\epsilon = 0.8$ and $\gamma = 1 + \mathrm{i}$.

At the outset, we perform the convergence study of the reflection coefficient and transmission coefficient against the non-dimensional depth Kh corresponding to different values of evanescent modes N. An analytical approach is considered to find these values. Table 4.3 shows that the evanescent modes contribute significantly since zero evanescent mode $(N = 0)$ produces a significant difference when compared with other propagating modes. Further, when the number of evanescent modes increases, a very good numerical convergence is attained for $N = 16$. Therefore, Table 4.3 suggests the consideration of the number of evanescent modes $N = 16$ to be appropriate for all further computations.

Convergence of N_1, N_2 and N_3 (the number of points in different intervals) is verified by calculating the reflection and transmission coefficients in both propagating modes. In Table 4.4, values of R_{SM}, R_{IM}, T_{SM} and T_{IM} are calculated for different values of N_1, N_2 and N_3 by the algebraic least squares method. Table 4.4 suggests that the convergence of the coefficients up to four decimal places are obtained after $N_1 = N_2 = N_3 = 1900$.

TH-2746_176123008

$N_1 \Rightarrow$	100	400	700	1000	1300	1600	1900	2100
R_{SM}	0.1838	0.1717	0.1693	0.1683	0.1678	0.1674	0.1671	0.1671
R_{IM}	0.7932	0.7958	0.7963	0.7965	0.79656	0.7967	0.7967	0.7967
T_{SM}	0.1149	0.1106	0.1098	0.1095	0.1094	0.1092	0.1092	0.10913
T_{IM}	0.0195	0.0193	0.0193	0.0192	0.0192	0.0192	0.0192	0.0192

Table 4.4: Convergence study of $N_1 = N_2 = N_3$ with respect to R_{SM}, R_{IM}, T_{SM} and T_{IM} with $N = 16,\ B/(d+h) = 1,\ E/h^4 = 10^5,\ \epsilon = 0.5$ and $f = 0.75$.

Consequently, for calculation by this approach, we consider $N_1 = N_2 = N_3 = 1900$ throughout this study unless otherwise stated.

Methods	Analytical Approach⇓			Linear Algebraic Approach⇓		
$KB \Rightarrow$	KB=0.02	KB=0.03	KB=0.05	KB=0.02	KB=0.03	KB=0.05
$R_{SM} =$	0.44234	0.52568	0.51768	0.46933	0.51006	0.52551
$T_{SM} =$	0.07652	0.04793	0.03337	0.07928	0.04872	0.03164
$R_{IM} =$	0.38299	0.37429	0.37283	0.36715	0.37002	0.37115
$T_{IM} =$	0.25926	0.09052	0.02830	0.18534	0.10637	0.06920
$Err =$	$4.83e{-16}$	$4.69e{-16}$	$1.13e{-16}$	$2.7e{-3}$	$2.58e{-3}$	$2.53e{-3}$

Table 4.5: Comparison of analytical and linear algebraic approaches with respect to various reflection, transmission coefficients and error Err as defined in (4.49) with $B/(d+h) = 1,\ \epsilon = 0.5$ and $\gamma = 1 + \mathrm{i}$.

Before analyzing the effect of various parameters, the key question that arises is whether these two approaches lead to a correct result or not. Moreover, complications of badly scaled parameters is one of the drawbacks of linear algebraic procedure. The numerical values of the reflection and transmission coefficients and error Err as defined in (4.49) obtained by the present methods are compared for different values of KB in Table 4.5 from which it is observed that the results match up to two decimal places. This fact provides another check on the correctness of the present results. The error given by relation (4.49) is also computed for these different approaches in Table 4.5. However, it is noticed that a significant difference in error is observed and for both the methods, the error decreases as KB increases. Therefore, the method giving an analytic solution based on the eigenfunction approach provides a better solution than the least squares method based on the concepts of linear algebra of over-determined system of equations arising from the scattering of water waves by a porous structure. Therefore, the analytic approach can be used in all numerical works here. However, this kind of comparison may add an extra support in checking the accuracy while obtaining numerical results.

In Figure 4.6(a,b)-Figure 4.7(a,b), the reflection and transmission coefficients are plotted against non-dimensional width $k_{1,1}B$ in SM and IM corresponding to various values of friction and porosity, respectively. In Figure 4.6(a,b), similar patterns can be observed for

TH-2746_176123008

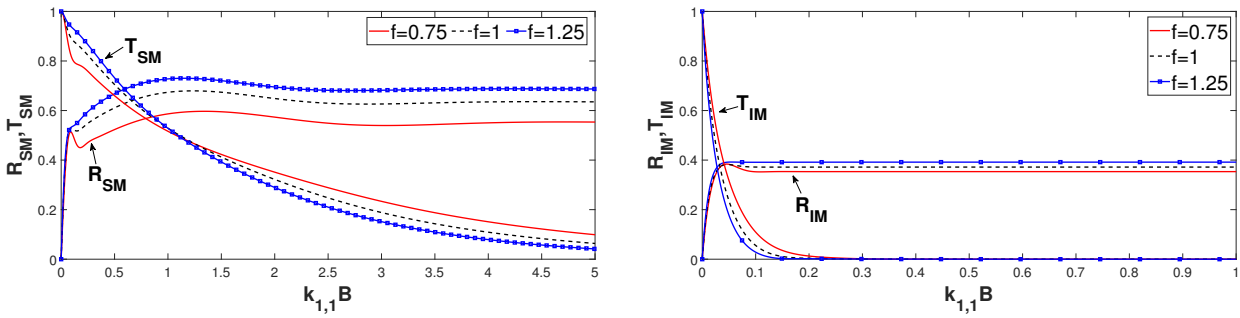

(a) (b)

Figure 4.6: Reflection and transmission coefficients in (a) free surface mode and (b) interfacial mode against non-dimensional width $k_{1,1}B$ for various friction f with $\epsilon = 0.5$.

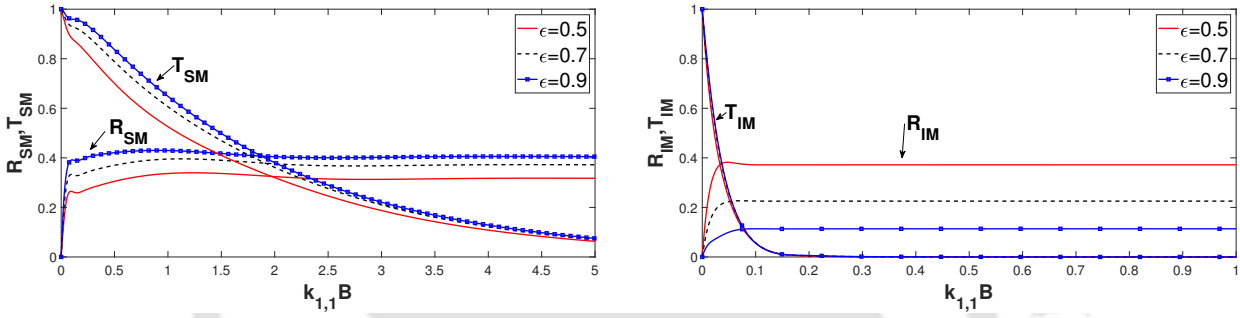

(a) (b)

Figure 4.7: Reflection and transmission coefficients in (a) free surface mode and (b) interfacial mode against non-dimensional length $k_{1,1}B$ corresponding to various porosity parameter ϵ with $f = 1$.

both propagating modes. Higher friction gives rise to higher reflection and lower transmission. But T_{SM} attains higher values for the lower values of f only in $k_{1,1}B < 1.5$ whereas the patterns are the opposite for $k_{1,1}B \geq 1.5$. Consideration of different values of porosity ϵ brings a difference in the behaviour of the reflection and transmission coefficients between two propagating modes. We observe that higher porosity leads to higher reflection and higher transmission for SM whereas lower reflection is observed for IM. However, no major effect can be observed in T_{IM} for different porosity values. Therefore, higher reflection and lower transmission can be achieved by choosing appropriate porosity and friction values.

It is observed that, after a specific width, the reflection and transmission coefficients change sharply and remain almost constant. The same trend follows for the cases of varying porosity and varying friction. For both cases, the convergence of reflection and transmission modes is attained after some structural width. It is also observed that the propagating modes have an optimum for almost the same structural width. An important observation is that a steady behaviour is noticed for both the propagating modes corresponding to the structural width and subsequently, it may be concluded that,

TH-2746_176123008

beyond a specific value, an increase in the width of the structure cannot influence either reflection or transmission.

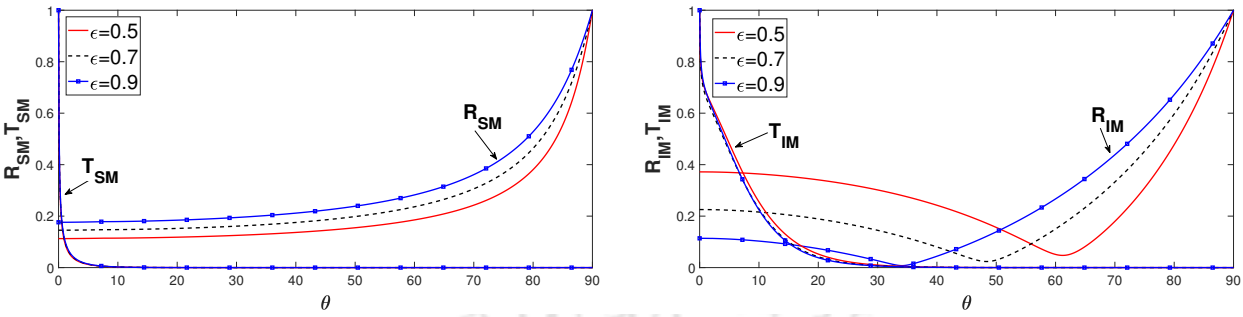

(a) (b)

Figure 4.8: Reflection and transmission coefficients in (a) free surface mode and (b) interfacial mode versus angle of incidence for different porosity parameters ϵ with $f = 1$ and $B/(d+h) = 1$.

Figure 4.8(a,b) shows the effect of porosity on the reflection coefficient and transmission coefficient against θ in surface mode and interfacial mode, respectively. When the porosity is varied, the reflection coefficient begins from the minimum value to the maximum value in both propagating modes. An opposite behaviour is observed for transmission coefficients. With a change in porosity, a negligible difference in transmission coefficients for both SM and IM is observed. Moreover, all transmission graphs tend to 0 with rising θ (T_{SM} for $\theta > 5°$ and T_{IM} for $\theta > 25°$). However, in the case of the reflection coefficients, a significant difference is observed in all graphs and they obtain their maximum corresponding to the angle 90°. But a change in porosity does not take into account the difference in the incident angle in order to obtain its optimum. For the surface mode, lower porosity values give rise to lower reflection but for the interfacial mode, R_{IM} initially exhibits the opposite nature and after attaining the minimum value, they follow the similar behaviour as SM. Subsequently, a study of the wave pattern allows the design of efficient breakwaters with an appropriate selection of the width, step height and friction factor of the structure so as to get the maximum wave reflection which can help in protecting the offshore structures.

Figure 4.9(a,b) shows waveloads $\mathbb{F}_f$ and $\mathbb{F}_b$, respectively, versus $k_{1,1}B$ for various values of friction. For the initial non-dimensional width ($k_{1,1}B \approx 0$), the wave forces on both walls $x = 0$ and $x = B$ are the same and very much close to 0. But when the structural width is increased, $\mathbb{F}_f$ increases and attains its maximum value. Figure 4.9(b) shows that wave force $\mathbb{F}_b$ also increases and achieves its highest value but a sharp reduction is observed when the width is increased. This may be attributed to a substantial amount of wave energy getting dissipated by the porous structure. Moreover, the wave forces initially show the highest impact for the lower structural width, and different values of γ

TH-2746_176123008

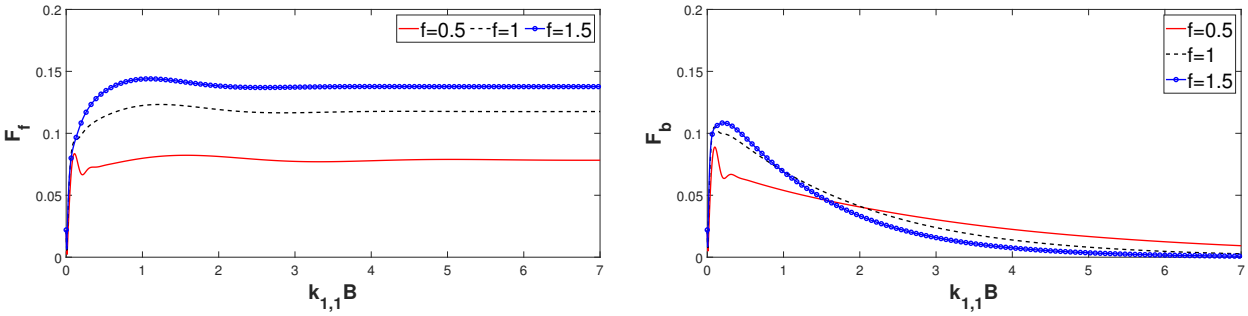

(a) (b)

Figure 4.9: Wave forces (a) $\mathbb{F}_f$ and (b) $\mathbb{F}_b$ against non-dimensional length corresponding to various values of f with $\epsilon = 0.8$.

do not introduce any difference in attaining optimum value of the waveload. However, it is observed that both the wave forces exhibit a steady behaviour after a specific width. $\mathbb{F}_f$ is observed to have a higher impact corresponding to higher friction f but $\mathbb{F}_b$ follows this pattern only for the initial width, and after $k_{1,1}B > 1.5$, the pattern is altered. Moreover, the steady waveload justifies that the energy dissipation is fixed up to a specific structural width beyond which the energy loss does not depend on the structural width.

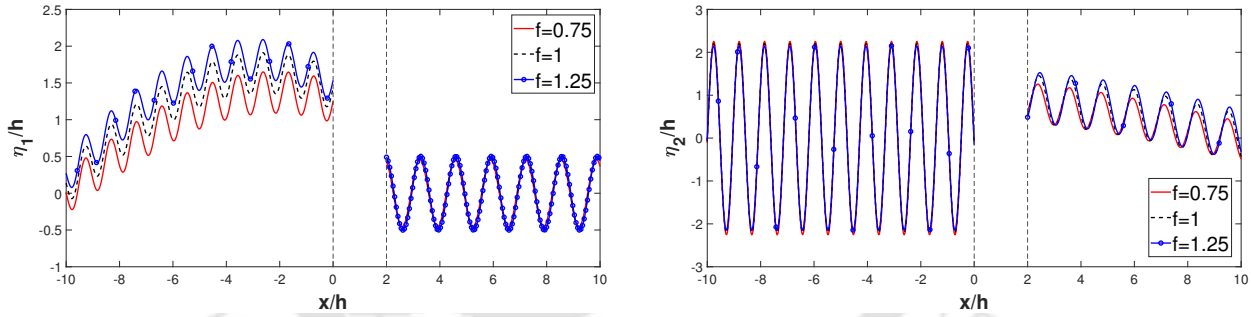

(a) (b)

Figure 4.10: Non-dimensional elevation amplitude for (a) free surface and (b) interfacial modes versus x/h corresponding to different values of f for $B/(d+h) = 2$, $\epsilon_1 = 0.8$.

Figure 4.10(a,b) shows the free surface elevations η_1/h and interface elevation η_2/h versus the non-dimensional distance x/h for various values of friction with x denoting the horizontal distance measured from $x = 0$. It shows that η_2/h becomes higher than η_1/h. We can assume that this difference between the elevations of these two modes arises due to the resonating interaction between the free surface waves and interfacial waves. The elevation reduces significantly due to the presence of the porous structure. The oscillations in both propagating modes increase when the friction coefficient f takes higher values. However, for the interface, a negligible difference in elevations is observed corresponding to different f.

TH-2746_176123008

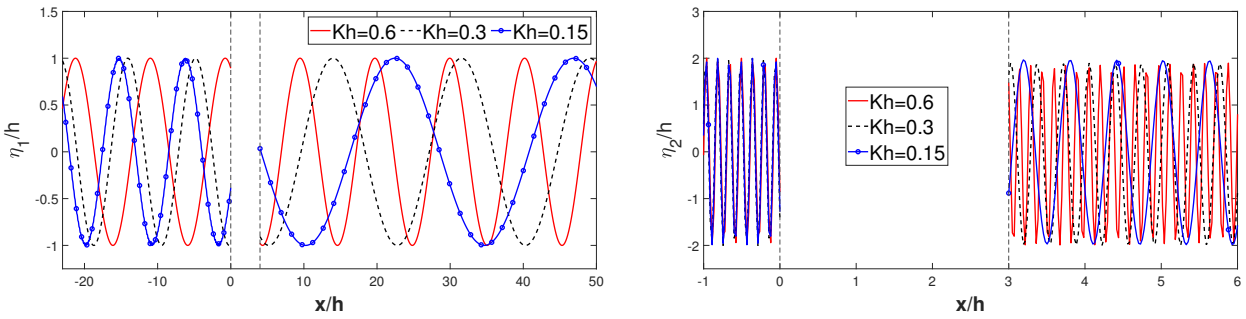

(a) (b)

Figure 4.11: Non-dimensional elevation amplitude for (a) free surface and (b) interfacial modes versus x/h corresponding to different values of f for $B/(d+h) = 2,\ \epsilon_1 = 0.8$.

Non-dimensional elevation with respect to x is plotted in Figure 4.11(a,b) for various values of Kh. We can easily observe the phase shift that occurs in the elevations in both propagating modes due to the presence of the structure. For the interface, it is observed that the number of oscillations is higher corresponding to the same x distance on the free surface. There is a continuous phase lag in the vertical displacement response for the free surface, but in the interfacial mode, it is highly dependent on the structure.

Based on the outcome, a suitable choice of parameters pertaining to a porous structure interacting with waves will allow the creation of a tranquillity zone by reducing the waveload on the rigid wall and the porous structure.

$E/h^4 \Downarrow$	$f = 1$				$f = 1.5$			
	R_{SM}	T_{SM}	R_{IM}	T_{IM}	R_{SM}	T_{SM}	R_{IM}	T_{IM}
10^1	0.9043	0.7683	0.3719	0.2723	0.8658	0.6588	0.4117	0.2778
10^2	0.8729	0.7683	0.3719	0.2707	0.8369	0.65923	0.41167	0.2762
10^3	0.8493	0.9931	0.3718	0.2985	0.7671	0.8653	0.4116	0.3032
10^4	0.9007	0.5353	0.3718	0.2225	0.8592	0.4522	0.4115	0.2342
10^5	0.6227	0.4126	0.3718	0.2209	0.5971	0.3470	0.4115	0.2331
10^6	0.6045	0.3995	0.3718	0.2204	0.5795	0.3357	0.4115	0.2329
10^7	0.6028	0.3981	0.3718	0.2204	0.5779	0.3345	0.4115	0.2329

Table 4.6: Reflection and transmission coefficients against different f corresponding to different values of E with $B/(d+h) = 1,\ \epsilon = 0.8$ and $f = 1$.

The effect of flexural rigidity E of the elastic bottom is examined against different f in Table 4.6. A difference is observed only for the values of $E/h^4 = 10^1$ to $E/h^4 = 10^5$, otherwise, all the reflection and transmission coefficients converge to a fixed value in both propagating modes for higher E. Different rigidity E does not contribute to any major difference for reflection and transmission coefficients in interfacial mode. It was also observed in Table 4.1 that the change of flexural rigidity did not contribute any

TH-2746_176123008

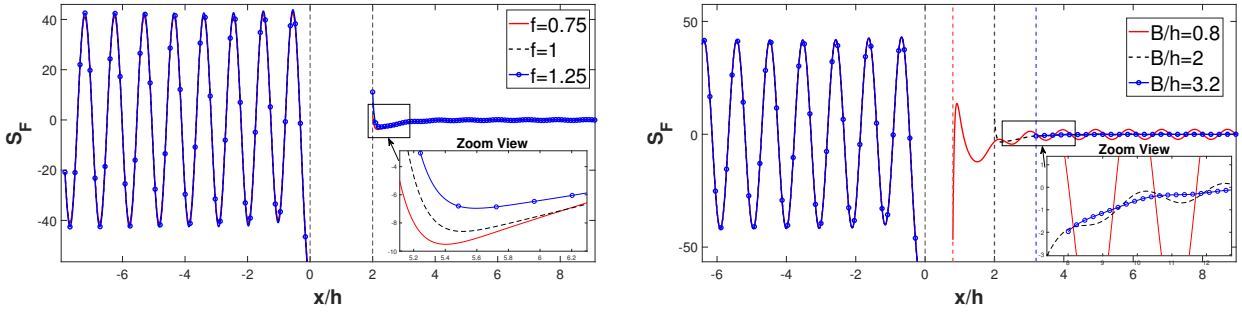

(a) (b)

Figure 4.13: Shear force against non-dimensional x/h for (a) different values of friction f, (b) different values of non-dimensional structural width with $\epsilon = 0.8, E/h^4 = 10^7$ and (a) $B/(d+h) = 1$, (b) $f = 1$.

major difference in the dispersive roots in interfacial propagation. This may be one of the reasons for such behaviour of R_{IM} and T_{IM}.

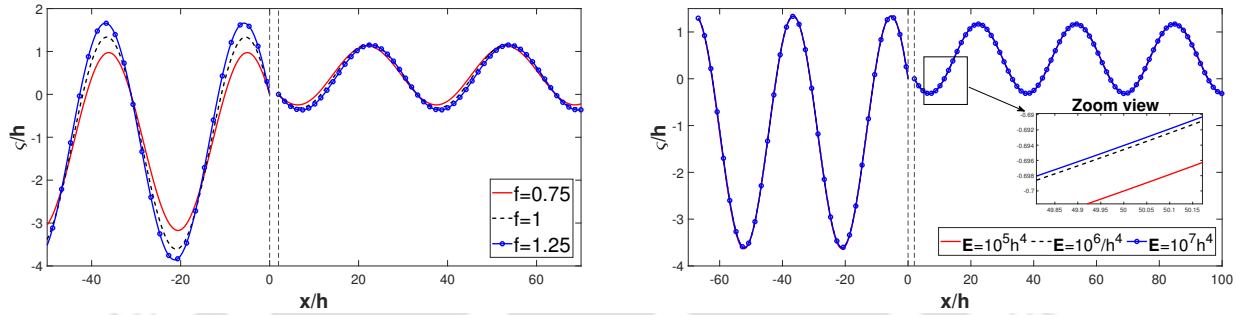

(a) (b)

Figure 4.12: Non-dimensional bottom deflection amplitude against non-dimensional x/h for (a) various values of friction f, (b) various values of non-dimensional flexural rigidity with $B/(d+h) = 2$, $\epsilon = 0.8$ and (a) $E/h^4 = 10^7$, (b) $f = 1$.

Furthermore, the impact of the friction parameter as well as of the flexural rigidity upon the elastic bottom deflection is also plotted against the non-dimensional distance in Figure 4.12(a,b). It can be observed that the elastic bottom attains the lowest amplitude of deflection corresponding to the lowest value of f. Further, ζ attains 0 value at both the edges of the elastic bottom plate which also satisfies the clamped edge conditions. Moreover, a major reduction in the amplitude can be observed clearly for the bottom deflection due to the structure. Deflection for various E maintains the same value which clearly shows that, after some value of the elastic rigidity, the bottom does not have any impact for such a wave interaction system.

Figure 4.13(a,b) presents the shear force on the elastic bottom for different values of the friction and different values of structural length. It reveals that the shear force

TH-2746_176123008

achieves the lowest value near the edge $(0, -h)$. Further, the forces exhibit an oscillatory behaviour similar to the deflection pattern of the elastic bottom. Figure 4.13(a) shows the variation in the shear force acting on the elastic bottom for different values of the friction f. For the interaction of the waves with the structure after $x > B/h$, the amplitude of the shear force decreases corresponding to an increase in f. Lower f results in lower $\mathbb{S}_F$ and the oscillation reduces to the one with increasing x. Furthermore, Figure 4.13(b) shows that, for an increase in B/h - the width of the porous structure, the amplitude of shear force on the elastic bottom decreases. This fact can be understood clearly from the argument that a porous structure of larger width can cause greater dissipation of energy, which is responsible for lesser shear force acting on the bottom. The fact that an increase in the width B/h of the porous breakwater gives rise to a greater reflection and dissipation of wave energy, as observed in Figure 4.6(a,b) and Figure 4.9(b), supports this observation.

4.2 Comparison of results for elastic and rigid bottom

Comparing our interaction method to the rigid sea bottom case seems very interesting because it simplifies the study while keeping the formulation applicable to wave attenuation applications. In view of this, it would be very useful to equate the rigid sea-bed with a stiff elastic sea bottom, i.e., a case of increased stiffness. In a similar way to the justification of our schematic model as shown in Appendix E, comparison of the impermeable bottom with an elastic bottom with increased stiffness can provide a fair validation of the Euler-Bernoulli beam equations concept for the sea-bed as those two should converge asymptotically.

$k_{1,1}h$	$k_{1,2}h$	$k_{1,3}h$	$k_{1,4}h$	$k_{1,5}h$
0.23290	6.60659	1.81077i	3.12538i	5.38720i

Table 4.7: Roots $k_{1,n}h$ $(n = 1, 2, \ldots, 5)$ of the dispersion relation (4.24) with $\gamma = 1$ for $\rho = 0.97$, $Kh = 0.1$ and $d/h = 1$.

Dispersion relation (4.23) does not directly give our desired dispersion relation for a rigid bottom but (4.24) gives us that for $\gamma = 1$. Upon comparing Table 4.7 with Table 4.1, it can be observed that, as the flexural rigidity increases, the roots more or less become the same. Furthermore, the complex root tends to 0 with rising rigidity in Table 4.1. If we obtain the same wave interaction system for an impermeable bottom, then the system of equations becomes of order $(4N + 8) \times (4N + 8)$ and the vanishing edge conditions also match due to the impermeability of the bottom. The advantage is that, by using the orthogonality of the eigenfunctions in both regions and using the similar orthogonality of eigenfunction $I_{2,n}$, we solve the system.

TH-2746_176123008

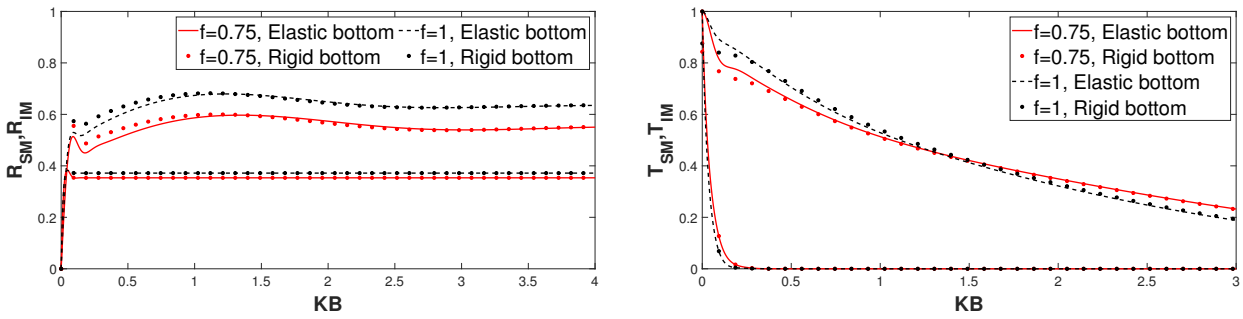

(a) (b)

Figure 4.14: Variation of (a) reflection coefficients and (b) transmission coefficients versus non-dimensional length KL corresponding to elastic and rigid bottom with $\epsilon = 0.5$ and $E/h^4 = 10^7$.

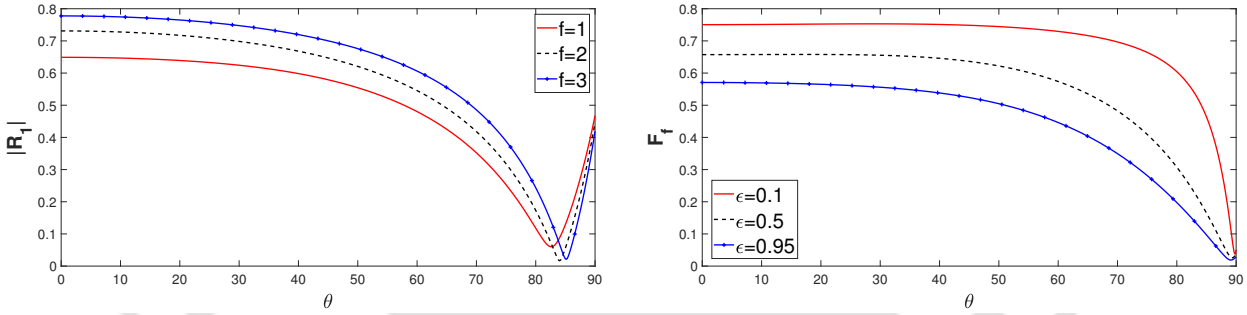

(a) (b)

Figure 4.15: Variation of (a) reflection coefficients and (b) waveload on the structure versus incident angle θ corresponding to elastic bottom with $\rho = 0.99$ and $E/h^4 = 10^8$.

It can be seen from the graphs in Figure 4.14(a,b) that the reflection and transmission coefficients converge to a single graph for both forms of bottom characteristics (elastic and rigid). For narrower width structures, minor variations can be seen. We may conclude that the bottom characteristics correspond to a thin long elastic plate with a very high flexural stiffness and it is more difficult to bend it. As a result, we come to the realization that the stiff elastic sea bottom behaves asymptotically like a rigid bottom. This will provide a fair level of model validity for the bottom.

Figure 4.15(a) demonstrates that the reflection coefficient is generally larger for higher friction coefficients. Maxima occur at the same initial angle and minima occur at slightly different angles of incidence as f changes. Similar characteristics of the reflection curve in the free surface mode are observed in Figure 5 of Losada et al. [59] for incident angle θ. For comparing with a homogeneous fluid model, we consider $\rho = 0.99, d/h = 1/25$ and some other parameters as $\epsilon = 0.45, (h-a)/h = 0.25, d/h = 1$ which result in similar graphs as can be found in a homogeneous fluid. Small difference can be observed due to the density differences in two layers for the upper layer portion and frequency differences. Furthermore, the dimensionless vertical force coefficient $\mathbb{F}_f$ is plotted in Figure 4.15(b)

TH-2746_176123008

showing a favourable comparison between the present theory and Figure 7 of Losada et al. [59]. The result demonstrates that an increase in the porosity induces a reduction of the vertical force. The characteristics as well as graphs are same here for the homogeneous case.

4.3 Validation

Validation of such a wave interaction system is very much difficult due to the lack of literature in this direction. The most straightforward way to establish validation is to compare our results when the thickness of the bed as well as elasticity are excluded from the equation. When the values of both elastic parameters E and δ are taken as 0, then the bottom configuration turns into a rigid one as in Chanda and Bora [15] although that depends on the schematic configuration as well as on the physical considerations of the model. But a similar procedure is used in this work so that bottom boundary condition can be converted to the one used by Behera and Sahoo [8].

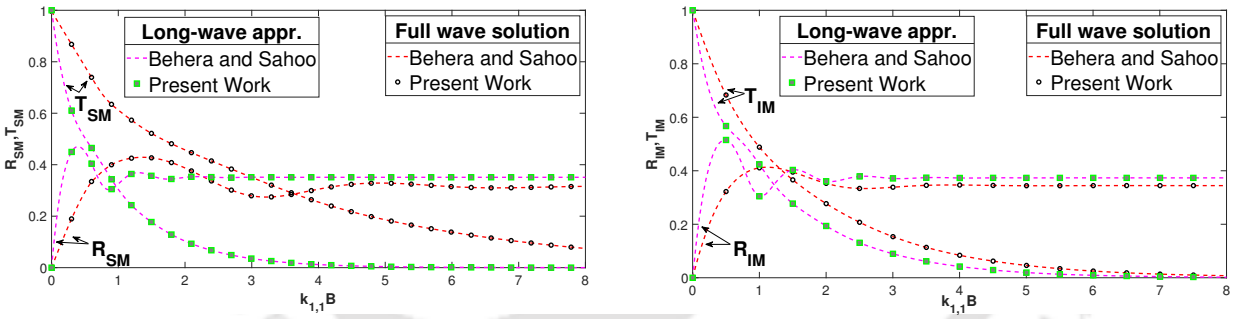

(a) (b)

Figure 4.16: Reflection and transmission coefficients against $k_{1,1}B$ at (a) free surface and (b) interface corresponding to present result and [8].

The complete utility of the model is assessed by comparing two separate cases (full wave solution and long-wave approximation). To form a correct relation by translating our model to that of Behera and Sahoo [8], we use $E = 0, \delta = 0$ to transform the elastic bottom to an impermeable one and also the following parameter values: $d = h = a = 2.5$ meter, $T = 8$ sec, $g = 9.81; \mathrm{m/s^2}, \epsilon = 0.5, f = 0.5$. Figure 4.16(a,b) shows the plots of the reflection and transmission coefficients versus $k_{1,1}B$ and study of both the works indicate a high level of consensus of the work of Behera and Sahoo [8] with the current work. This means that the current model is reasonably accurate and can be applied to a variety of coastal and offshore infrastructure issues.

TH-2746_176123008

4.4 Breakwater with a perforated front wall

Within the same bathymetry as in Figure. 4.1, a perforated front wall is considered at $x = 0$. Now, combining the potentials $\psi_j^{(1)}$ and $\psi_j^{(2)}$ into ϕ_j (for $j = 1, 2$), the matching conditions at $x = 0$ yield (as in Isaacson et al. [44])

$$\frac{\partial \phi_1}{\partial x} = \epsilon \frac{\partial \phi_2}{\partial x}, \quad \text{for} \quad -a < z < d, \tag{4.54}$$

$$\frac{\partial \phi_1}{\partial x} = \mathrm{i} k_{1,1} G(\phi_1 - \gamma \phi_2), \quad \text{for} \quad -a < z < d, \tag{4.55}$$

with $G = \dfrac{\epsilon_{_P}}{k_{1,1} b_{_P} (f_{_P} - \mathrm{i} m_{_P})}$ as the porous-effect parameter, where the quantities with the subscript P, except for b_P, denote various parameters associated with the perforated front-wall and b_P refers to the thickness of the front-wall. As particular cases, $G = 0$ for a solid wall and $G = \infty$ when the perforated wall is entirely transparent. It is to be noted that, although the thickness of the perforated wall is considered as zero when the wave interaction with the whole breakwater is considered, the thickness of the wall is taken into account for the flow within the perforated wall.

The velocity potentials take similar forms like equations (4.27) to (4.29). Now, applying the conditions (4.54) and (4.55) to the potentials and using a similar procedure as carried out earlier, the following equations arise:

$$\sum_{n=I,II,1}^{N+2} R_n q_{1,n} b_{n,m} + \epsilon (A_m - B_m e^{\mathrm{i} q_{2,m} L}) q_{2,m} a_m = \sum_{n=1}^{2} q_{1,n} b_{n,m}, \tag{4.56}$$

$$\sum_{n=I,II,1}^{N+2} R_n Q_n \hat{b}_{n,m} - k_{1,1} G \gamma (A_m + B_m e^{\mathrm{i} q_{2,m} L}) a_m = \sum_{n=1}^{2} (q_{1,n} - k_{1,1} G) \hat{b}_{n,m}, \tag{4.57}$$

where $\hat{b}_{n,m} = \int_{-a}^{0} I_{1,n} I_{2,m} \mathrm{d}z + \rho \int_{0}^{d} I_{1,n} I_{2,m} \mathrm{d}z$ and $Q_n = (q_{1,n} + k_{1,1} G)$.

Now, solving the system of equations consisting of equations (4.56),(4.57),(4.45) and(4.46), and the clamped edge conditions, the required unknown coefficients can be evaluated.

In Figure 4.17(a,b), the impact of the perforated wall on the reflection and transmission coefficients is examined against the non-dimensional structure width. It can be observed that, due to the presence of the thin perforated wall, the reflection and transmission coefficients do not vary much for either of the propagating modes. Further, the impact of waveloads is observed to be the lowest for the porous structure with a perforated wall. In general, we clearly observe a major impact of the perforated wall on both waveloads. Practically, it can be assumed that the perforated wall is instrumental in retarding the wave motion due to its inertial resistance associated with the increase in the energy dissipation within the structure. As a result, it can be concluded that, in order to protect

TH-2746_176123008

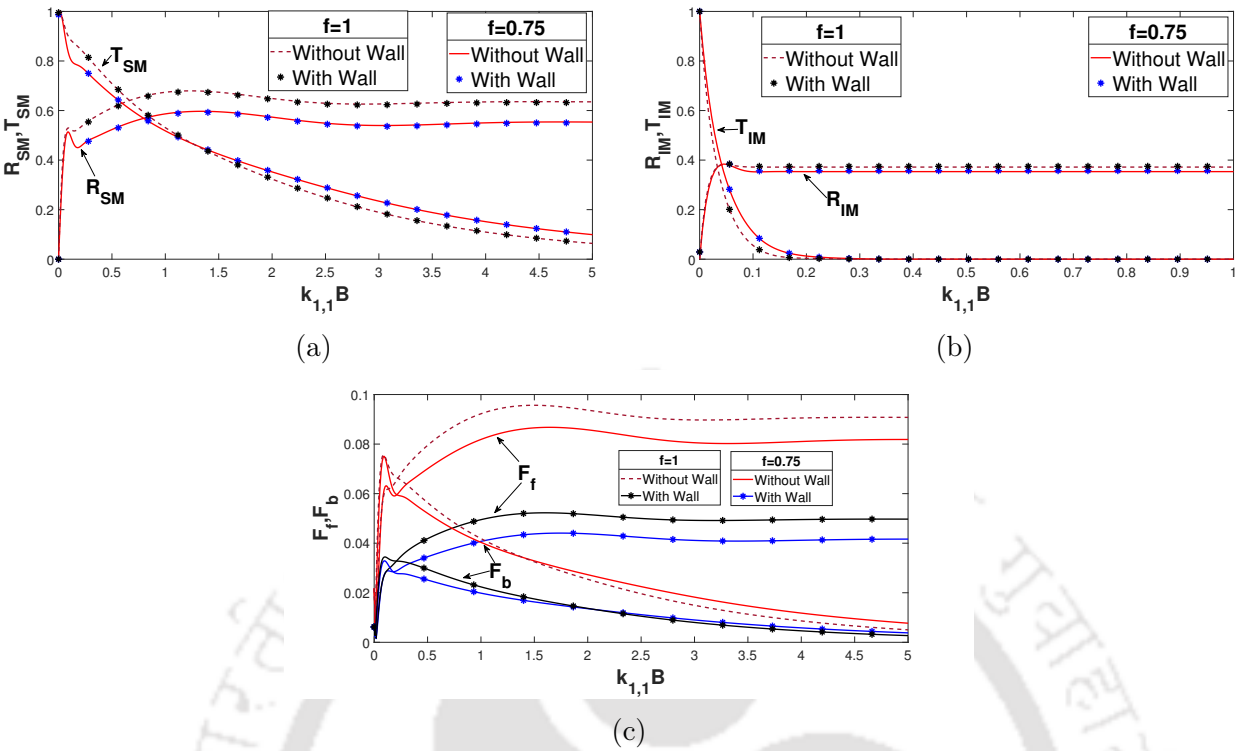

Figure 4.17: Reflection and transmission coefficients versus $k_{1,1}B$ for (a) free surface mode and (b) interfacial mode and (c) waveloads $\mathbb{F}_f$ and $\mathbb{F}_b$ against non-dimensional structural length $k_{1,1}B$ in the presence and absence of perforated wall with $G = 2 + 4\mathrm{i}$ and $\epsilon = 0.5$.

the shoreline, adding a perforated front wall to a structure will lead to lesser waveloads due to better dissipating properties. In this direction, in order to construct a porous structure, insertion of a perforated front is deemed more effective.

4.5 Conclusion

This work attempts to throw light on the interaction of oblique water waves with a specific porous structure in a two-layer fluid flowing over an elastic bottom. The linear interface-piercing structure is placed on a rigid bottom which follows the elastic bottom. Additionally, the problem is also considered by attaching a perforated front wall to the porous structure. The associated scattering problems are solved by utilizing linear water wave theory and eigenfunction expansion method. By considering the contribution of complex conjugate wavenumbers, the effect of the elastic bottom is also accounted for while finding the potentials. Thereafter, a number of results are obtained and analyzed with respect to various parameters. Another method known as the linear algebraic approach is adopted to provide an additional mean to support the accuracy of our evaluated results. Less amount of waveload is observed on the back face of the porous region and less elevation is observed in the water region following the structure due to the wave

TH-2746_176123008

dissipation by the structure. It also allows one to find the optimum width for a suitable structural configuration possessing both reflective and dissipative characteristics. In order to attain higher wave reflection and lower transmission for a porous breakwater, moderate value of the angle of incidence is helpful. Choosing the height, width, porosity and porous impedance parameter of the structure appropriately, the following can be achieved: (i) maximum wave reflection and minimum transmission, (ii) maximum dissipation of energy, (iii) minimum elevation in the confined zone. Moreover, the characteristics of the bottom also affect the waveload as well as the reflection and transmission coefficients. The shear force and bottom deflection are analyzed for various elastic parameters. A suitable agreement in shear force is observed while placing such a structure at the bottom with elastic characteristics. When the porous structure is considered with a perforated front wall, one can observe the following: (i) the percolative property of the front wall adds more efficiency to the breakwater in producing lower waveload on both faces of the structure compared to the case without any front wall, (ii) no major difference exists with respect to the reflection and transmission coefficients in both cases. By matching a current outcome with an available result, an excellent consensus is reached, confirming the utility of the current model and that the inquiry can go forward.

To sum it up, the study of water wave interaction with such type of structures allows one to clearly understand the effect of the porous structures that can create a tranquillity zone. It can be concluded that the consideration of a porous structure with suitable geometrical configuration along with appropriate characteristics of the bottom is a very important aspect to be taken into account in order to provide safety to the coastal facilities.

TH-2746_176123008

TH-2746_176123008

CHAPTER 5

Elastic bottom effects on ocean water wave scattering by a composite caisson type breakwater placed upon a rock foundation in a two-layer fluid

5.1 Mathematical formulation

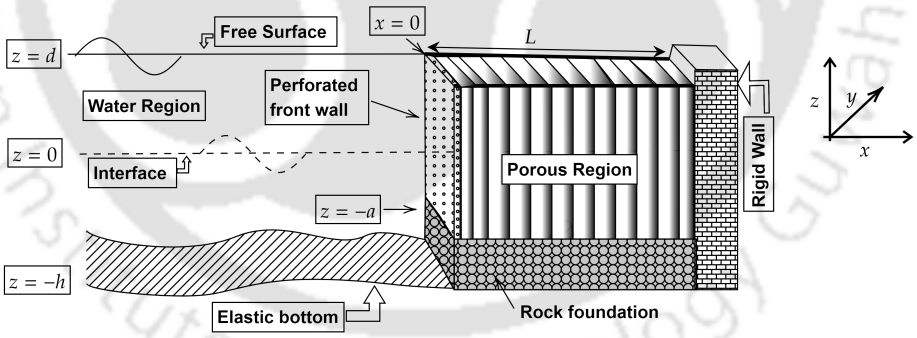

Figure 5.1: Definition sketch of wave scattering due to interface piercing structure

An interface-piercing caisson type composite porous breakwater (porous blocks) is considered in a two-layer fluid flowing over an elastic bottom. The breakwater is placed upon a rock rigid foundation. Linear water wave theory and small amplitude bottom deflection in finite ocean water depth are taken into consideration to discuss the oblique surface wave interaction with the breakwater. By assuming large length of the bottom, the thin elastic plate theory can be employed for the elastic bottom, as being considered extensively for such problems on wave-structure/ice-sheet interaction. The flexible nature of the elastic plate renders the condition at the bottom to a fifth order condition which is different from

TH-2746_176123008

the usual Neumann condition applicable for a rigid bottom. The motion is assumed to be irrotational and simple harmonic, and the fluid an inviscid and incompressible consisting of two layers under the action of gravity. The interface between the layers is taken to be linear. The surface tension effect at the interface of the two layers is not taken into account since, for such type of water wave problems, the surface tension does not have any consequential contribution. A right-handed coordinate system is employed in such a way that $z = 0$ represents the interface of the layers with the z-axis pointing upwards. Further, the mean free surface of upper fluid layer of density ρ_1 is located at $z = d$ whereas the lower fluid layer of density ρ_2 is bounded below by an elastic bottom $-\infty < x < 0$ with the mean depth $z = -h$ followed by a rigid foundation of height $h - a$ from $x = 0$ to $x = L$. The present study elaborates the significance of the composite porous structure having a perforated front wall in reducing the wave force acting on the seawall. The thin perforated front-wall is considered at $x = 0$ in front of the porous structure, and a rigid sea-wall is considered at $x = L$. The porous structure is to be utilized as a composite breakwater. Moreover, the structure is divided into p number of vertical subregions from $x = L_1 = 0$ to $x = L_{p+1} = L$ with each strip in (x_j, x_{j+1}) having the width $l_j = (L_{j+1} - L_j)$ for $j = 1, 2, 3, \ldots, p$ and $\sum_{j=1}^{p} l_j = L$. Each region contains different porosity and porous impedance parameters, and the porous structure is compact in nature. We consider an incident wave obliquely incident at an inclination θ to the x-axis on the structure. Subsequently, velocity potential Φ_1 for pure water region and $\Phi_j,\ j = 2, \ldots, p+1$ for the j-th porous region, $j = 1,\ 2, \ldots, p+1$, can be written as $\Phi_j(x, y, z, t) = \mathrm{Re}[\phi_j(x, z)e^{\mathrm{i}(k_y y - \omega t)}]$. The schematic diagram of the problem is depicted in Figure 5.1. The variation of each of the potentials Φ_j $(j = 1, 2, \ldots, p+1)$ in the y-direction is considered to be identical in order that all the potentials along the vertical boundaries can be matched according to Snell's Law. Due to the rigid foundation, an impermeable bottom is considered for the porous regions and consequently, the elastic bottom effect is observed to exist for Region 1 only. In order that this specific arrangement is physically viable and can be used for practical problems, justification is provided in Appendix E.

To clearly understand the problem layer-wise, $\phi_j(x, z)$ are split in the following manner:

$$\phi_1 = \begin{cases} \psi_1^{(1)}, & 0 < z < d, \\ \psi_1^{(2)}, & -h < z < 0, \end{cases} \text{ and } \phi_j = \begin{cases} \psi_j^{(1)}, & 0 < z < d, \\ \psi_j^{(2)}, & -a < z < 0, \end{cases} \text{ for } j = 2, \ldots, p+1, \quad (5.1)$$

with the superscripts denoting the specific layer.

By taking into account all information, the boundary value problems for $\phi_j, j = 1, 2, \ldots, p+1$ are found to satisfy modified Helmholtz equation

$$(\nabla_{x,z}^2 - k_y^2)\phi_j = 0. \quad (5.2)$$

TH-2746_176123008

With the help of (5.1), equation (5.2) can be written as follows:

$$\left.\begin{aligned}(\nabla^2_{x,z} - k_y^2)\psi_1^{(1)} &= 0, \quad 0 < z < d,\\ (\nabla^2_{x,z} - k_y^2)\psi_1^{(2)} &= 0, \quad -h < z < 0,\end{aligned}\right\} \tag{5.3}$$

$$\left.\begin{aligned}(\nabla^2_{x,z} - k_y^2)\psi_j^{(1)} &= 0, \quad 0 < z < d,\\ (\nabla^2_{x,z} - k_y^2)\psi_j^{(2)} &= 0, \quad -a < z < 0,\end{aligned}\right\} \text{ for } j = 2, 3, \ldots, p+1. \tag{5.4}$$

For Region 1, the linearized mean free surface condition has the following form:

$$\frac{\partial \psi_1^{(1)}}{\partial z} - K\psi_1^{(1)} = 0 \text{ on } z = d, \text{ for } x \in (-\infty, L_1)\,. \tag{5.5}$$

However, the linearized mean free surface condition for Regions $2, 3, \ldots, p+1$ differs since these regions are porous and it is given by

$$\frac{\partial \psi_j^{(1)}}{\partial z} - K\gamma_j\psi_j^{(1)} = 0 \text{ on } z = d, \text{ for } x \in (L_{j-1}, L_j)\,. \tag{5.6}$$

where $\gamma_j = m_j + \mathrm{i}f_j$ denotes the complex porous impedance parameter. For more information on m_j and f_j, one can refer to Appendix A. Further, each j-th region, $j = 1, 2, \ldots, p$, has porosity ϵ_j. Meanwhile, for plain water region, i.e., in Region 1, $m_1 = 1, f_1 = 0$ ($\gamma_1 = 1$) and $\epsilon_1 = 1$.

We obtain the linearized boundary condition on the mean elastic bottom for ϕ_1 as

$$\left\{E\left(\frac{\partial^2}{\partial x^2} - k_y^2\right)^2 + 1 - \delta K\right\}\frac{\partial \psi_1^{(2)}}{\partial z} - K\psi_1^{(2)} = 0, \text{ for } x \in (-\infty, L_1)\,. \tag{5.7}$$

Due to the rigid foundation, the impermeable bottom condition in Regions $2, 3, \ldots, p+1$ yields

$$\frac{\partial \psi_j^{(2)}}{\partial z} = 0 \text{ at } z = -a, \text{ for } x \in (L_{j-1}, L_j)\,. \tag{5.8}$$

Linearized conditions at $z = 0$ take the following forms:

$$\left.\begin{aligned}\frac{\partial \psi_1^{(1)}}{\partial z} &= \frac{\partial \psi_1^{(2)}}{\partial z},\\ \rho\left(\frac{\partial \psi_1^{(1)}}{\partial z} - K\psi_1^{(1)}\right) &= \left(\frac{\partial \psi_1^{(2)}}{\partial z} - K\psi_1^{(2)}\right),\end{aligned}\right\} \text{ for } x \in (-\infty, L_1)\,, \tag{5.9}$$

$$\left.\begin{aligned}\frac{\partial \psi_j^{(1)}}{\partial z} &= \frac{\partial \psi_j^{(2)}}{\partial z},\\ \rho\left(\frac{\partial \psi_j^{(1)}}{\partial z} - K\gamma_j\psi_j^{(1)}\right) &= \left(\frac{\partial \psi_j^{(2)}}{\partial z} - K\gamma_j\psi_j^{(2)}\right)\end{aligned}\right\} \text{ for } x \in (L_{j-1}, L_j)\,, \tag{5.10}$$

TH-2746_176123008

where equation (5.10) is valid for $j = 2, 3, \ldots, p+1$.

Now, combining the potentials $\psi_j^{(1)}$ and $\psi_j^{(2)}$ into ϕ_j as given in (5.1) for $j = 1, 2$, the matching conditions across the perforated front-wall (as in Isaacson et al. [44]) at $x = 0$ yield

$$\left.\begin{aligned} \frac{\partial \phi_1}{\partial x} &= \epsilon_2 \frac{\partial \phi_2}{\partial x}, \\ \frac{\partial \phi_1}{\partial x} &= \mathrm{i}k_{1,1} G(\phi_1 - \gamma_2 \phi_2), \end{aligned}\right\} \quad \text{for} \quad -a < z < d. \tag{5.11}$$

Equation (5.11) arises due to the continuity of the vertical velocity component and the pressure drop across the perforated front-wall and $G = \dfrac{\epsilon_{PW}}{k_{1,1} b_{PW} (f_{PW} - \mathrm{i}m_{PW})}$ is the porous-effect parameter of the perforated wall where quantities with the subscript PW (except for b_{PW}) denote various parameters associated with the perforated front-wall and b_{PW} refers to the thickness of the front-wall.

Boundary conditions arising due to the continuity of mass flux and pressure at $x = L_j$ for $j = 2, \ldots, p$, are

$$\left.\begin{aligned} \gamma_j \phi_j &= \gamma_{j+1} \phi_{j+1}, \\ \epsilon_j \frac{\partial \phi_j}{\partial x} &= \epsilon_{j+1} \frac{\partial \phi_{j+1}}{\partial x}, \end{aligned}\right\} \quad \text{for} \quad -a < z < d. \tag{5.12}$$

Due to the rigid wall, ϕ_{p+1} satisfies

$$\frac{\partial \phi_{p+1}}{\partial x} = 0 \ \text{ at } \ x = L. \tag{5.13}$$

The velocity potential $\psi_1^{(2)}$ satisfies the following boundary condition due to the rigid step:

$$\frac{\partial \psi_1^{(2)}}{\partial x} = 0 \ \text{ at } x = 0 \text{ for } \ -h < z < -a. \tag{5.14}$$

Some additional constraints are required to be satisfied at the edge of the elastic bottom due to the presence of the rigid foundation. Under the physical considerations of our model, it is assumed that the elastic plate edge satisfies the clamped-edge boundary conditions at $(x, z) = (0, -h)$ which are as follows:

$$\frac{\partial^2 \psi_1^{(2)}}{\partial x \partial z} = 0, \ \frac{\partial \psi_1^{(2)}}{\partial z} = 0. \tag{5.15}$$

There exist some more standard edge conditions which can be applied separately at the edge and those correspond to free, simply supported and sliding situations. However, in the present context, such situation does not arise because of the simple physical condition considered here and therefore, such boundary conditions are not required to be discussed.

TH-2746_176123008

5.2 Scattering by the composite porous structure

Here, the interaction of oblique ocean waves by the composite porous structure upon rigid foundation in a two-layer fluid flowing over an elastic bottom is formulated mathematically and solved analytically. At the outset, the velocity potentials associated with surface wave interaction under the considered situation are derived.

5.2.1 Approximation of the plane waves

The velocity potentials satisfying the governing equations (5.3) and (5.4), respectively, subject to the respective boundary conditions (5.5)-(5.9) have the following forms:

$$\phi_1 = \left\{ \begin{array}{ll} \psi_1^{(1)} = \exp(\pm \mathrm{i}xq_1) I_1^{(1)}(k_1, z), & 0 < z < d, \\ \psi_1^{(2)} = \exp(\pm \mathrm{i}xq_1) I_1^{(2)}(k_1, z), & -h < z < 0, \end{array} \right\} \text{for } x < 0, \tag{5.16}$$

$$\phi_j = \left\{ \begin{array}{ll} \psi_j^{(1)} = \exp(\pm \mathrm{i}xq_j) I_j^{(1)}(k_j, z), & 0 < z < d, \\ \psi_j^{(2)} = \exp(\pm \mathrm{i}xq_j) I_j^{(2)}(k_j, z), & -a < z < 0, \end{array} \right\} \text{for } L_{j-1} < x < L_j,\ j = 2, \ldots, p+1, \tag{5.17}$$

with $q_j = \sqrt{k_j^2 - k_y^2}$ for $j = 1, 2, \ldots, p+1$ and the eigenfunctions $I_j,\ j = 1, 2, \ldots, p+1$, given by

$$I_1 = \left\{ \begin{array}{ll} I_1^{(1)} = \dfrac{g_1(k_1)(K \sinh k_1(z-d) + k_1 \cosh k_1(z-d))}{K \cosh k_1 d - k_1 \sinh k_1 d}, & 0 < z < d, \\ I_1^{(2)} = (F(k_1) \cosh k_1(z+h) + K \sinh k_1(z+h)), & -h < z < 0, \end{array} \right. \tag{5.18}$$

$$I_j = \left\{ \begin{array}{ll} I_j^{(1)} = \dfrac{\sinh k_j a(K\gamma_j \sinh k_j(z-d) + k_j \cosh k_j(z-d))}{K\gamma_j \cosh k_j d - k_j \sinh k_j d}, & 0 < z < d, \\ I_j^{(2)} = \cosh k_j(z+a), & -a < z < 0, \end{array} \right. \text{for } j = 2, \ldots, p+1, \tag{5.19}$$

where $g_1(k_1) = (F(k_1) \sinh k_1 h + K \cosh k_1 h)$ and $F(k_1) = (Ek_1^4 + 1 - \delta K)k_1$.

All k_j's appearing above are computed from the dispersion relations which can be found as follows by using the second equation of (5.9) and (5.10):

$$\begin{aligned} & F(k_1)\left[k_1^2(1-\rho)\tanh k_1 d \tanh k_1 h - k_1 K(\tanh k_1 d + \tanh k_1 h)\right. \\ & \left. + K^2(\rho \tanh k_1 d \tanh k_1 h + 1)\right] + K\left[k_1^2(1-\rho)\tanh k_1 d\right. \\ & \left. -k_1 K(1 + \tanh k_1 d \tanh k_1 h) + K^2(\tanh k_1 h + \rho \tanh k_1 d)\right] = 0, \end{aligned} \tag{5.20}$$

$$\begin{aligned} & k_j^2(1-\rho)\tanh k_j d \tanh k_j a - k_j \gamma_j K(\tanh k_j d + \tanh k_j a) \\ & + K^2\gamma^2(\rho \tanh k_j d \tanh k_j a + 1) = 0, \quad \text{for } j = 2, 3, \ldots, p+1. \end{aligned} \tag{5.21}$$

TH-2746_176123008

5.2.2 Discussion on the roots of the dispersion relations

Consideration of a very thin elastic plate with respect to the wavelength, i.e., $\delta K \ll 1$ (adopting Euler-Bernoulli beam equation) results in dispersion relation (5.21) having two positive real roots, say, $k_{1,1}$ and $k_{1,2}$ where $0 < k_{1,1} < k_{1,2}$ and these correspond to the propagating modes; two pairs of complex conjugate roots, say, $k_{1,\pm I} = \pm\alpha_1 + \mathrm{i}\beta_1$ and $k_{1,\pm II} = \pm\alpha_1 - \mathrm{i}\beta_1$ corresponding to the non-propagating modes; and also an infinite number of purely imaginary roots given by $k_{1,n} = \mathrm{i}t_n$ corresponding to the evanescent modes. Further, the detailed analysis regarding the roots in pure water and porous region is already available in Subsection 4.1.2.

5.2.3 Method of solution

By using the method of eigenfunction expansion, the velocity potentials $\phi_j(x,z)$ for each subdomain $j = 1, 2, \ldots, p+1$ can be written as

$$\phi_1 = \sum_{n=1}^{2} e^{\mathrm{i}q_{1,n}x} I_{1,n}(k_{1,n}, z) + \sum_{n=I,II,1}^{\infty} R_n e^{-\mathrm{i}q_{1,n}x} I_{1,n}(k_{1,n}, z), \tag{5.22}$$

$$\phi_j = \sum_{n=1}^{\infty} (A_{j,n} e^{\mathrm{i}q_{j,n}(x-L_{j-1})} + B_{j,n} e^{-\mathrm{i}q_{j,n}(x-L_j)}) I_{j,n}(k_{j,n}, z), \text{ for } j = 2, 3, \ldots, p, \tag{5.23}$$

$$\phi_{p+1} = \sum_{n=1}^{\infty} C_n \cos q_{p+1,n}(L_{p+1} - x) I_{p+1,n}(k_{p+1,n}, z), \tag{5.24}$$

where R_n, $n = 1, 2, \ldots$ are the reflection coefficients. In accordance with the realistic physical problems in wave-structure interactions, we account for the contribution of the complex wavenumbers in Region 1 with $k_{1,n}$ $(n = I, II)$ as complex conjugates having positive real parts.

It is assumed that the wavenumbers take distinct values in water and porous regions, or otherwise, the alternative approach as mentioned by Behera and Sahoo [8] may be considered. The eigenfunctions $I_{j,n}(k_{j,n}, z)$ in (5.19) are integrable in $(-a, d)$, and they are orthogonal with respect to the following inner product (See Section 4.1.3):

$$\langle \varphi_n, \Psi_m \rangle = \int_{-h}^{0} \varphi_n \Psi_m \mathrm{d}z + \rho \int_{0}^{d} \varphi_n \Psi_m \mathrm{d}z, \tag{5.25}$$

and this gives

$$\langle I_{j,n}, I_{j,m} \rangle = \begin{cases} 0, & m \neq n, \\ W_{j,n}, & m = n. \end{cases} \tag{5.26}$$

Now, using the matching conditions (5.11)-(5.14) by considering N evanescent modes, the following are obtained:

$$\sum_{n=1}^{2} q_{1,n} I_{1,n} - \sum_{n=I,II,1}^{N+2} R_n q_{1,n} I_{1,n} = \begin{cases} 0, \\ \epsilon_2 \sum_{n=1}^{N+2} (A_{2,n} - B_{2,n} e^{\mathrm{i}q_{2,n} l_1}) q_{2,n} I_{2,n}, \end{cases} \tag{5.27}$$

$$\sum_{n=I,II,1}^{N+2} R_n \mathrm{Q}_n I_{1,n} - k_{1,1} G \gamma_2 \sum_{n=1}^{N+2} (A_{2,n} + B_{2,n} e^{\mathrm{i}q_{2,n} l_1}) I_{2,n} = \sum_{n=1}^{2} (q_{1,n} - k_{1,1} G) I_{1,n}, \tag{5.28}$$

$$\left.\begin{aligned} \epsilon_j \sum_{n=1}^{N+2} (A_{j,n} e^{\mathrm{i}q_{j,n} l_{j-1}} - B_{j,n}) q_{j,n} I_{j,n} = \epsilon_{j+1} \sum_{n=1}^{N+2} (A_{j+1,n} - B_{j+1,n} e^{\mathrm{i}q_{j+1,n} l_j}) q_{j+1,n} I_{j+1,n}, \\ \gamma_j \sum_{n=1}^{N+2} (A_{j,n} e^{\mathrm{i}q_{j,n} l_{j-1}} + B_{j,n}) I_{j,n} = \gamma_{j+1} \sum_{n=1}^{N+2} (A_{j+1,n} + B_{j+1,n} e^{\mathrm{i}q_{j+1,n} l_j}) I_{j+1,n}, \end{aligned}\right\}$$
$$\text{for } j = 2, 3, \ldots, p-1, \tag{5.29}$$

$$\mathrm{i}\epsilon_p \sum_{n=1}^{N+2} (A_{p,n} e^{\mathrm{i}q_{p,n} l_{p-1}} - B_{p,n}) q_{p,n} I_{p,n} = \epsilon_{p+1} \sum_{n=1}^{N+2} C_n \sin(q_{p+1,n} l_p) q_{p+1,n} I_{p+1,n}, \tag{5.30}$$

$$\gamma_p \sum_{n=1}^{N+2} (A_{p,n} e^{\mathrm{i}q_{p,n} l_{p-1}} + B_{p,n}) I_{p,n} = \gamma_{p+1} \sum_{n=1}^{N+2} C_n \cos(q_{p+1,n} l_p) I_{p+1,n}, \tag{5.31}$$

where $\mathrm{Q}_n = (q_{1,n} + k_{1,1} G)$.

Thereafter, utilization of the orthogonality of the eigenfunctions $I_{j+1,n}$ between the equations consisting of the eigenfunctions $I_{j,n}$ and $I_{j+1,n}$ for $j = 1, 2, \ldots, p$ yields

$$\sum_{n=I,II,1}^{N+2} R_n q_{1,n} \hat{b}_{n,m}^2 + \epsilon_2 (A_{2,m} - B_{2,m} e^{\mathrm{i}q_{2,m} l_1}) q_{2,m} a_m^2 = \sum_{n=1}^{2} q_{1,n} \hat{b}_{n,m}^2, \tag{5.32}$$

$$\sum_{n=I,II,1}^{N+2} R_n \mathrm{Q}_n b_{n,m}^2 - k_{1,1} G \gamma_2 (A_{2,m} + B_{2,m} e^{\mathrm{i}q_{2,m} l_1}) a_m^2 = \sum_{n=1}^{2} (q_{1,n} - k_{1,1} G) b_{n,m}^2, \tag{5.33}$$

$$\left.\begin{aligned} \epsilon_j \sum_{n=1}^{N+2} (A_{j,n} e^{\mathrm{i}q_{j,n} l_{j-1}} - B_{j,n}) q_{j,n} b_{n,m}^{j+1} - \epsilon_{j+1} (A_{j+1,m} - B_{j+1,m} e^{\mathrm{i}q_{j+1,m} l_j}) q_{j+1,m} a_m^{j+1} = 0, \\ \gamma_j \sum_{n=1}^{N+2} (A_{j,n} e^{\mathrm{i}q_{j,n} l_{j-1}} + B_{j,n}) b_{n,m}^{j+1} - \gamma_{j+1} (A_{j+1,m} + B_{j+1,m} e^{\mathrm{i}q_{j+1,m} l_j}) a_m^{j+1} = 0, \end{aligned}\right\}$$
$$\text{for } j = 2, 3, \ldots, p-1, \tag{5.34}$$

$$\mathrm{i}\epsilon_p \sum_{n=1}^{N+2} (A_{p,n} e^{\mathrm{i}q_{p,n} l_{p-1}} - B_{p,n}) q_{p,n} b_{n,m}^{p+1} - \epsilon_{p+1} C_m \sin(q_{p+1,m} l_p) q_{p+1,m} a_m^{p+1} = 0, \tag{5.35}$$

$$\gamma_p \sum_{n=1}^{N+2} (A_{p,n} e^{\mathrm{i}q_{p,n} l_{p-1}} + B_{p,n}) b_{n,m}^{p+1} - \gamma_{p+1} C_m \cos(q_{p+1,m} l_p) a_m^{p+1} = 0, \tag{5.36}$$

TH-2746_176123008

where

$$\left.\begin{aligned}
\hat{b}^2_{n,m} &= \int_{-h}^{0} I_{1,n}I_{2,m}\mathrm{d}z + \rho\int_{0}^{d} I_{1,n}I_{2,m}\mathrm{d}z,\\
a^{j+1}_{m} &= \int_{-a}^{0} I_{j+1,m}I_{j+1,m}\mathrm{d}z + \rho\int_{0}^{d} I_{j+1,m}I_{j+1,m}\mathrm{d}z,\\
b^{j+1}_{n,m} &= \int_{-a}^{0} I_{j,n}I_{j+1,m}\mathrm{d}z + \rho\int_{0}^{d} I_{j,n}I_{j+1,m}\mathrm{d}z,
\end{aligned}\right\} \text{ for } j = 1, 2, \ldots, p.$$

Therefore, the system (5.32)-(5.36) consists of $(2pN + 4p)$ linear equations with $(2pN + 4p + 2)$ unknowns where the unknown vector is

$$X = [R_I, R_{II}, R_1, , \ldots, R_{N+2}, A_{2,1}, \ldots, A_{2,N+2}, B_{2,1}, \ldots, B_{2,N+2}, \ldots \\ A_{p,1} \ldots, A_{p,N+2}, B_{p,1}, \ldots, B_{p,N+2}, C_1, \ldots, C_{N+2}]^T.$$

It leaves us with the requirement of two more conditions which can be obtained from the clamped edge conditions (equation (5.15)). Subsequently, it yields a linear system of size $(2pN + 4p + 2)$ as follows:

$$\mathbb{A}X = \mathbb{B}. \tag{5.37}$$

Details of the entries for the matrices $\mathbb{A}$ and $\mathbb{B}$ can be found in Appendix F. Determination of X allows us to discuss the reflection within the porous structure. The computation of various quantities along with the relevant results and discussions take place in the next section. $R_n (n = 1, 2)$ represent the reflection coefficients for both free surface mode (SM) and interfacial mode (IM), and they are evaluated by considering $R_{SM} = |R_1|$, $R_{IM} = |R_2|$. Furthermore, F_f and F_b, the unit horizontal wave forces acting on the front face of the composite porous structure and on the rigid wall, respectively, can be evaluated from the following:

$$F_f = \mathrm{i}\omega\gamma_2 \left[\rho_2 \int_{-a}^{0} \phi_2(0, z)dz + \rho_1 \int_{0}^{d} \phi_2(0, z)dz\right],$$

$$F_w = \mathrm{i}\omega\gamma_{p+1} \left[\rho_2 \int_{-a}^{0} \phi_{p+1}(L, z)dz + \rho_1 \int_{0}^{d} \phi_{p+1}(L, z)dz\right].$$

$\mathbb{F}_f$ and $\mathbb{F}_w$ are, respectively, the non-dimensional form of F_f and F_w, and are given by

$$\mathbb{F}_f = \frac{|F_f|}{\rho_2 g d h}, \quad \text{and} \quad \mathbb{F}_w = \frac{|F_w|}{\rho_2 g d h}. \tag{5.38}$$

Assuming that the progressive waves in the surface and interface modes are of the forms

TH-2746_176123008

$\zeta_j = \mathrm{Re}(\eta_j e^{-\mathrm{i}\omega t})$ for $j = 1, 2$, respectively, the amplitude is obtained from the kinematic conditions in open water as

$$\eta_1 = \frac{\mathrm{i}}{\omega}\frac{\partial \phi_1}{\partial z} \text{ at } z = d, \tag{5.39}$$

$$\eta_2 = \frac{\mathrm{i}}{\omega}\frac{\partial \phi_1}{\partial z} \text{ at } z = 0. \tag{5.40}$$

Similarly, the amplitude of bottom deflection $\zeta_3 = \mathrm{Re}(\eta_3 e^{-\mathrm{i}\omega t})$ is given by the formula

$$\eta_3 = \frac{\mathrm{i}}{\omega}\frac{\partial \phi_1}{\partial z} \text{ at } z = -h. \tag{5.41}$$

The shear force $\mathbb{S}_F$ on the elastic bottom is obtained by using the formula

$$\mathbb{S}_F = \left| \frac{E}{Kh}\frac{\partial}{\partial x}\left\{\left(\frac{\partial^2}{\partial x^2} - (2-\nu)k_y^2\right)\right\}\frac{\partial \phi_1}{\partial z}\right| \text{ at } z = -h. \tag{5.42}$$

5.3 Results and discussion

Matlab R2019a is used for solving the system of equations (5.37). It should be remembered that the presence of ill-conditioned matrices must be avoided in order to use the theoretical approach. In this case, it is important to choose the right parameter values to avoid such an occurrence. Finding the right algorithm to get the accurate solution may be one of the most important requirements. Finally, we must solve a large-scale linear square scheme and therefore, we use the built-in function algorithm which employs LU factorization and partial pivoting. Ill-conditioned systems must be treated with caution since they can have misleading results.

To carry out the computation, some parameter values are fixed as follows: $p = 2$, $(h - a) = h/20$, $d/h = 1$; $m = 1$; $\rho = 0.97$; $E/h^4 = 10^5, \delta/h = 10^{-4}$, $\theta = 30°$, $Kh = 0.1$, $\nu = 0.3$, $G = 6 + 4\mathrm{i}$ along with values of f_j and ϵ_j in $[0.25, 2]$ and $[0.3, 0.9]$, respectively. Regarding the choice of the values of the elastic parameters (E, ν), porosity (ϵ_j), friction (f_j) as well as those of the basic physical parameters (ρ, K etc.), one can refer to Appendix B. It may, however, be noted that, although the mathematical formulation is derived for p porous regions in this work, the computational part deals with only two porous regions for $j = 2, 3$.

To begin with, we look at how different numbers of evanescent modes affect the reflection coefficients. Table 5.1 shows that the evanescent modes have a significant contribution to the reflection coefficients as compared to the case where the evanescent modes are not considered, i.e., for $N = 0$, and the convergence of the results is checked. When the number of evanescent modes is increased, the discrepancy between two consecutive reflection coefficients converges to zero. As a result, the number of evanescent modes given by

TH-2746_176123008

Kh	N	0	2	4	6	8	10	12
$Kh = 0.28$	R_{SM}	0.818	0.824	0.631	0.628	0.747	0.759	0.759
	R_{IM}	0.961	0.961	0.957	0.957	0.963	0.963	0.963
$Kh = 0.16$	R_{SM}	0.355	0.360	0.308	0.304	0.331	0.331	0.331
	R_{IM}	0.968	0.968	0.988	0.997	1.00	1.00	1.00
$Kh = 0.10$	R_{SM}	0.265	0.271	0.262	0.260	0.262	0.267	0.267
	R_{IM}	0.951	0.952	0.965	0.967	0.970	0.977	0.977

Table 5.1: Convergence study of R_{SM} and R_{IM} for different Kh with $L_2/h = L_3/h = 0.2$.

$N = 12$ can be considered to be adequate for our further investigations, as indicated by Table 5.1.

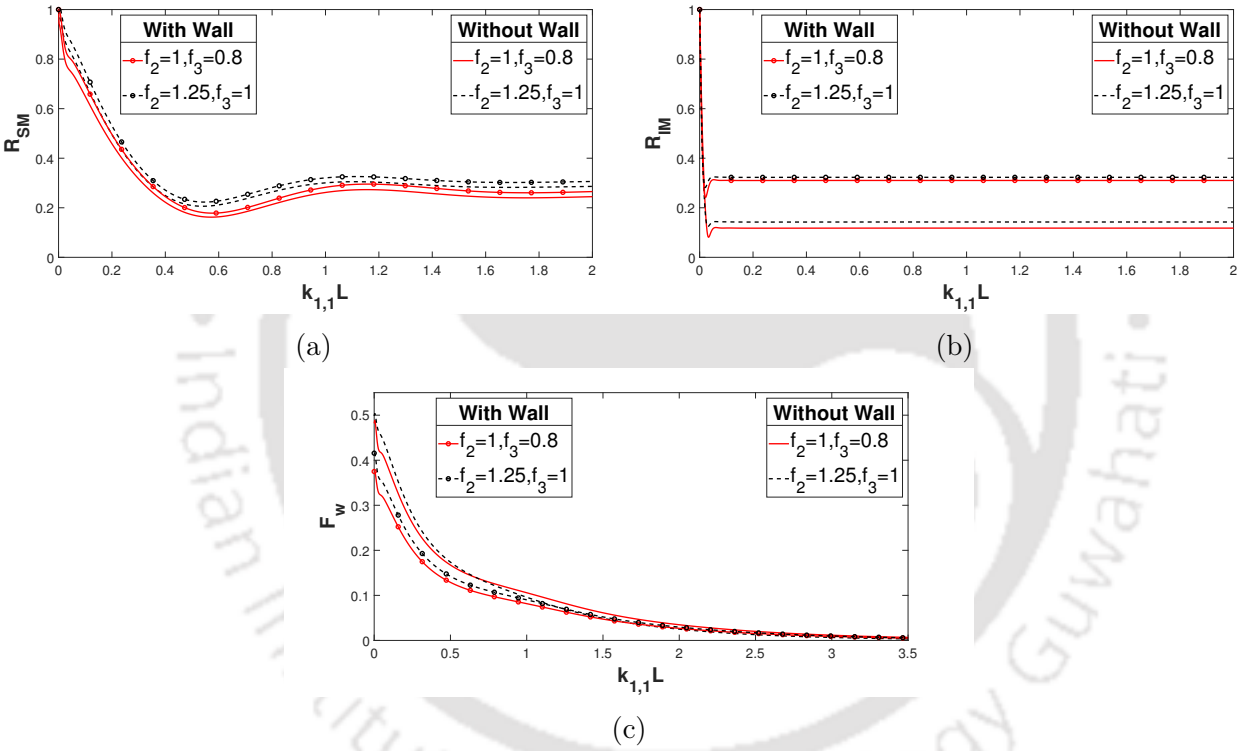

Figure 5.2: Variation of (a) R_{SM}, (b) R_{IM} and (c) $\mathbb{F}_w$ against non-dimensional length $k_{1,1}L$ corresponding to with wall and without wall configuration with $\frac{E}{h^4} = 1$, $\frac{\delta}{h} = 0.1$ and $\epsilon_2 = 0.9, \epsilon_3 = 0.8$.

For both propagating modes, it is obvious from Figure 5.2(a,b) that the structure with a perforated front wall achieves a higher reflection compared to the case without the wall. In both propagating modes, the reflection coefficients for these two types of schematic structures behave in a similar manner. For these two kinds of schematic systems, the non-dimensional waveload at the rigid wall also supports this behaviour while changing the friction values. The dissipating nature of the porous body reduces more energy of the wave as the structural width increases. We may presume that the presence of the

perforated wall delays wave motion due to its inertial resistance, which can be correlated with an improvement of energy dissipation inside the breakwater from a realistic standpoint. As a result, a perforated front wall lets the structure gain greater reflection, lower waveloads and better dissipating properties. Subsequently, for constructing a breakwater, a composite frame with a perforated front wall is usually preferable.

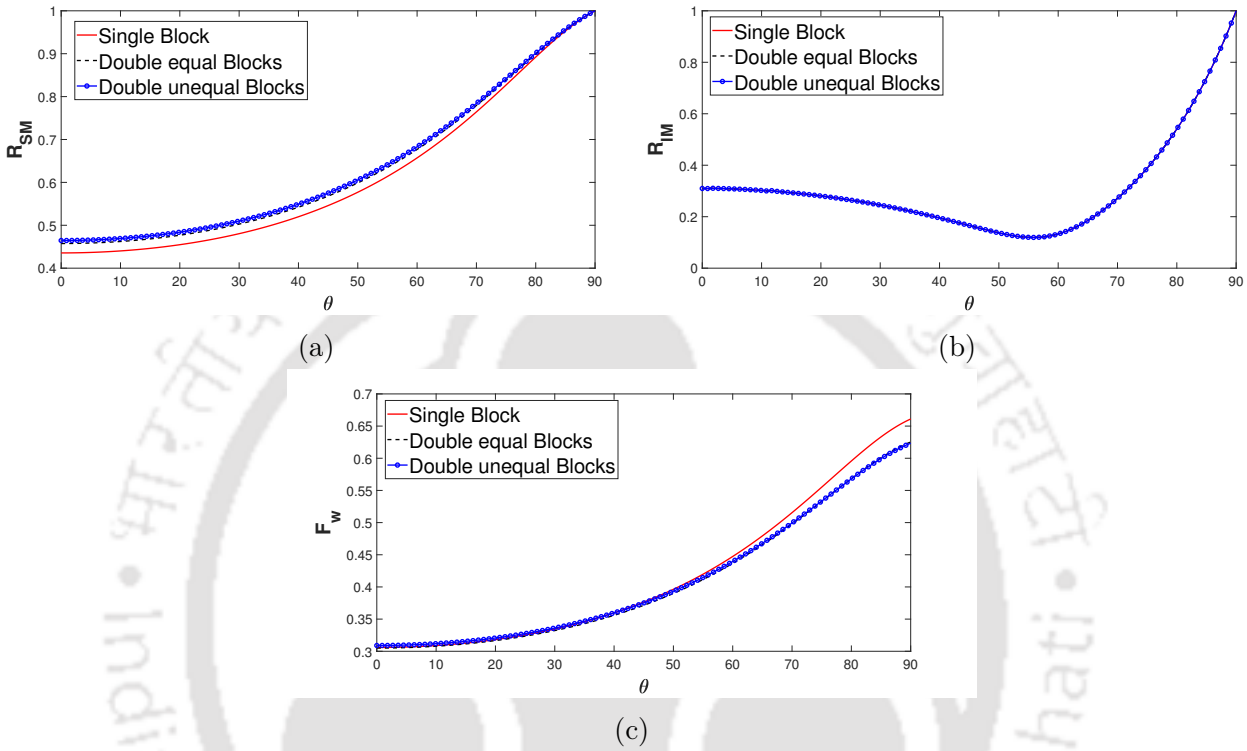

Figure 5.3: Variation of (a) R_{SM} (b) R_{IM} and (c) $\mathbb{F}_w$ against incident angle θ with (i) Single block, $l_1/h = 1, f_2 = 1.25, \epsilon_2 = 0.8$, (ii) Double equal blocks, $l_1/h = l_2/h = 0.6, f_2 = 1.25, f_3 = 1.5, \epsilon_2 = 0.8, \epsilon_3 = 0.9$, (iii) Double unequal blocks $l_1/h = 0.4, l_2/h = 0.8, f_2 = 1.25, f_3 = 1.5, \epsilon_2 = 0.8, \epsilon_3 = 0.9$.

The reflection coefficients for different configurations of the structure are plotted in Figure 5.3(a,b): (i) a single block, (ii) double blocks of equal width, and (iii) double blocks of unequal width. For all three configurations, the overall structural width is considered to be fixed: $L/h = 1$. It is obvious that the double block structure returns higher reflection in both propagating modes as compared to the single block (Case (i)). However, in the case of interfacial mode, there is no significant distinction. It may be due to the transmitted wave from the first block getting reflected back by the second block toward the open water region. We also show the difference of waveload on the wall in Figure 5.3(c) for different structural configurations to substantiate our analogy. The visible variation in waveload on the wall can also be observed in this figure. The effect of the double block framework on the rigid wall is the least while the impact of the single block structure is the maximum. As a result, the double block structure dissipates more energy and reflects

TH-2746_176123008

more wave than the single block structure.

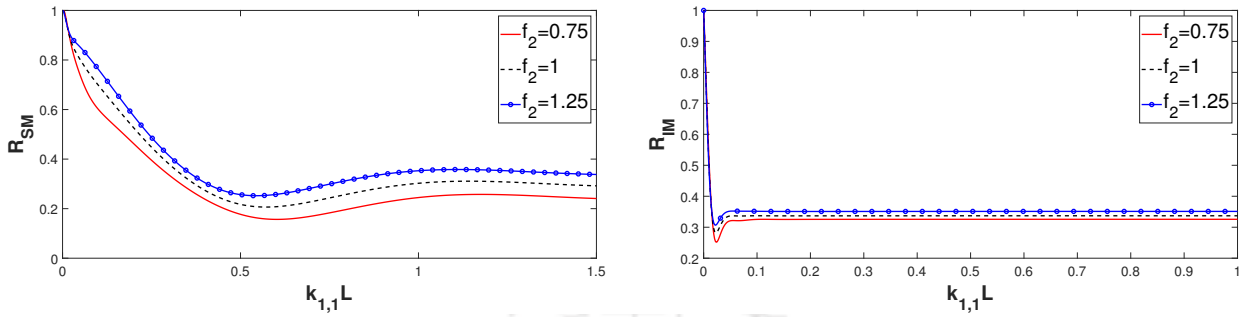

(a) (b)

Figure 5.4: Reflection coefficients against non-dimensional length $k_{1,1}L$ corresponding to various friction parameter f_2 with $f_3 = 1, \epsilon_2 = 0.7, \epsilon_3 = 0.6$.

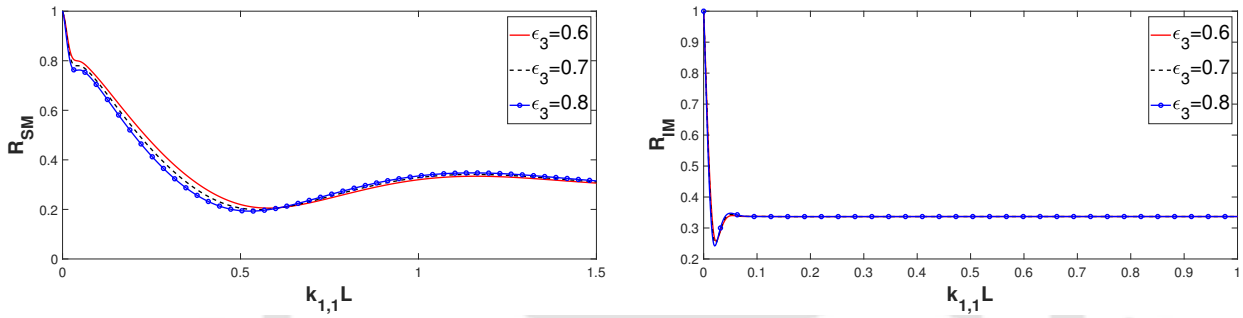

(a) (b)

Figure 5.5: Reflection coefficients against non-dimensional length $k_{1,1}L$ corresponding to various friction parameter ϵ_3 with $f_2 = 1, f_3 = 1.75, \epsilon_2 = 0.7$.

The reflection coefficients in surface and interfacial modes are plotted against the non-dimensional width $k_{1,1}L$ of the system in Figure 5.4(a,b) and Figure 5.5(a,b) for different values of friction parameter f_2 and porosity ϵ_3. When the friction parameter f_2 is varied, similar trend appears in both modes in Figure 5.4(a,b). In addition, after a certain width, the coefficients of reflection and propagation are nearly constant. However, as the width increases, reflection in both modes decreases sharply. In all propagating modes, different values of the friction factor f_2 result in different values of the reflection coefficients, with higher values of the friction factor ($f_2 > f_3$) resulting in lower reflection and lower values ($f_2 \leq f_3$) resulting in higher reflection. Changes in porosity ϵ_3 do not produce a significant effect on the coefficients, as observed in Figure 5.5. In the free surface mode, however, there are variations in reflection coefficients, with lower values of ϵ_3 (i.e., $\epsilon_2 > \epsilon_3$) resulting in higher reflection up to a certain structural width $k_{1,1}L$, and higher values of ϵ_3 (i.e., $\epsilon_2 \leq \epsilon_3$) resulting in lower reflection. Both cases of differing porosity and varying friction show the same pattern. To achieve higher reflection, it is recommended to use composite structures with acceptable structural widths. Both cases show that the

TH-2746_176123008

reflecting modes converge after a certain structural size, and propagating modes converge at approximately the same structural width. However, both propagating modes sustain a constant behaviour with respect to the structural width, demonstrating that a higher structural width does not have much effect on reflection after a certain value.

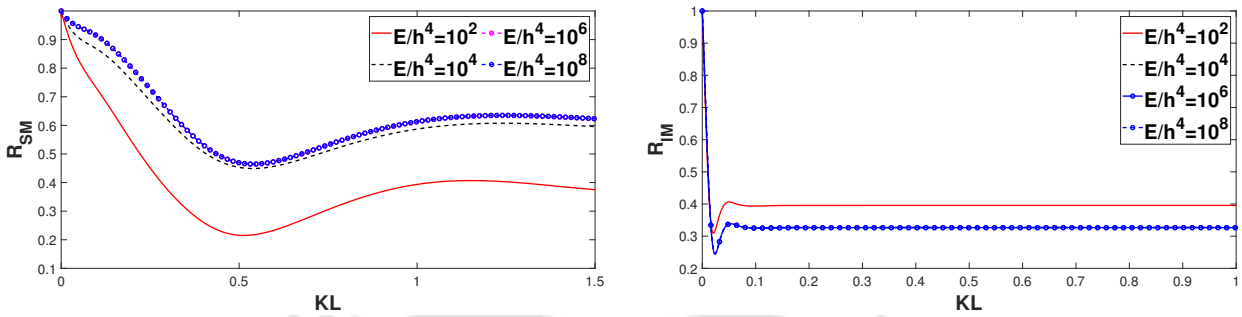

(a) (b)

Figure 5.6: Variation of (a) R_{SM} and (b) R_{IM} against KL corresponding to different values of dimensionless flexural rigidity E/h^4 with $\epsilon_2 = 0.6, \epsilon_3 = 0.7$, $f_2 = 0.75, f_3 = 1$, $\delta/h = 0.1$ and $G = 1 + \mathrm{i}$.

In Figure 5.6(a,b), the effect of the flexural rigidity E of the elastic bottom is studied against the non-dimensional width KL. The plotted reflection coefficients in both modes show a discrepancy which can be attributed to different elastic rigidity E for the comparatively smaller values ($E/h^4 = 10^2$) only. Subsequently, corresponding to higher flexural rigidity, all reflection coefficients converge to a fixed value in both propagating modes. As a result, we come to the realization that the stiff elastic sea bottom behaves asymptotically like a rigid bottom. This will provide a fair level of model validity for the bottom.

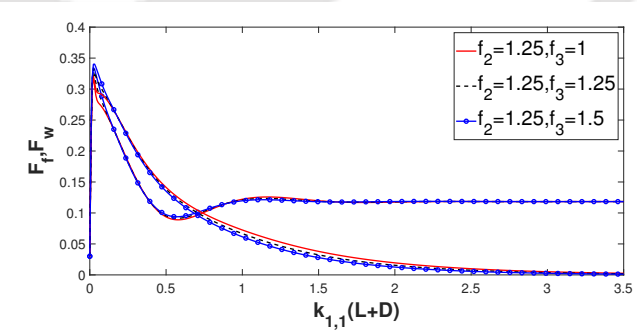

Figure 5.7: Variation of $\mathbb{F}_f, \mathbb{F}_w$ against non-dimensional length $k_{1,1}L$ corresponding to various values of f_3 with $f_1 = 1.25$ and $\epsilon_2 = \epsilon_3 = 0.6$.

Figure 5.7 shows waveloads $\mathbb{F}_f$ and $\mathbb{F}_w$ plotted against $k_{1,1}L$ corresponding to different friction parameter values. The figure reveals that wave force $\mathbb{F}_f$ does not change significantly as the structure width increases but $\mathbb{F}_w$ starts at its peak value and gradually

TH-2746_176123008

decreases as the width increases. This may have been as a result of the porous structure dissipating a significant amount of wave energy. With $f_2 \geq f_3$, the wave force $\mathbb{F}_w$ produces a greater effect, i.e., with higher friction f_2. One of the explanations for the fixed wave forces is the consistent existence of the reflection modes for larger structural widths, as previously mentioned. When it comes to achieving the best waveload performance, different friction makes no difference. The constant essence of waveload also explains why energy dissipation is fixed up to a certain structural width. After this width, the energy loss no more depends on the structure width. As a result, higher wave energy can be absorbed to provide protection to different structures in the ocean by having an appropriate dissipative system as a breakwater.

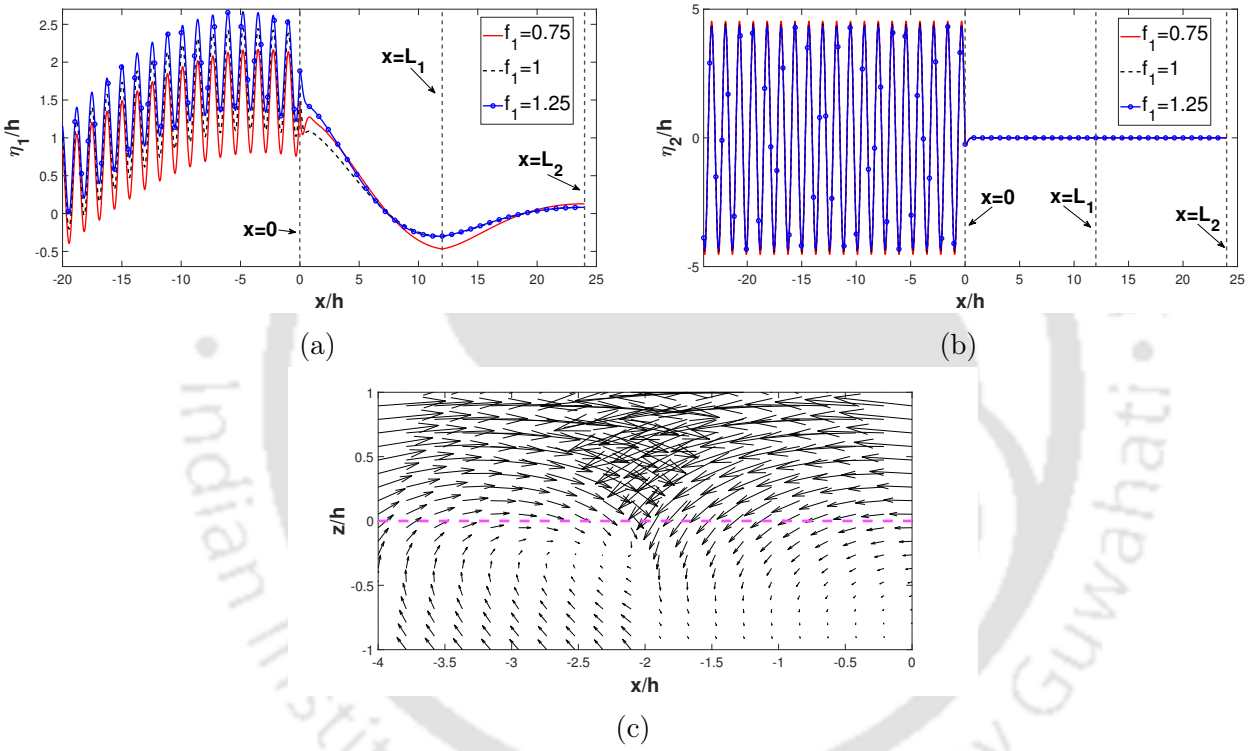

Figure 5.8: Non-dimensional elevation amplitude for (a) free surface mode, (b) interfacial mode, and (c) non-dimensional flow field versus x/h corresponding to different values of f_2 for $\epsilon_2 = 0.9$, $\epsilon_3 = 0.8$ and $f_3 = 1.5$.

Figure 5.8(a,b) shows the free surface elevation η_1/h and interface elevation η_2/h versus the non-dimensional distance x/h for various values of friction with x denoting the horizontal distance measured from $x = 0$. Figure 5.8 shows that η_2/h becomes higher than η_1/h. We can assume that this difference between the elevations of these two modes arises due to the resonating interaction between the free surface waves and interfacial waves. The elevation reduces significantly due to the presence of the porous structure. The oscillations in SM increase when the friction f_1 takes higher values. However, for the interface, a negligible difference in elevations is observed corresponding to different f_1.

TH-2746_176123008

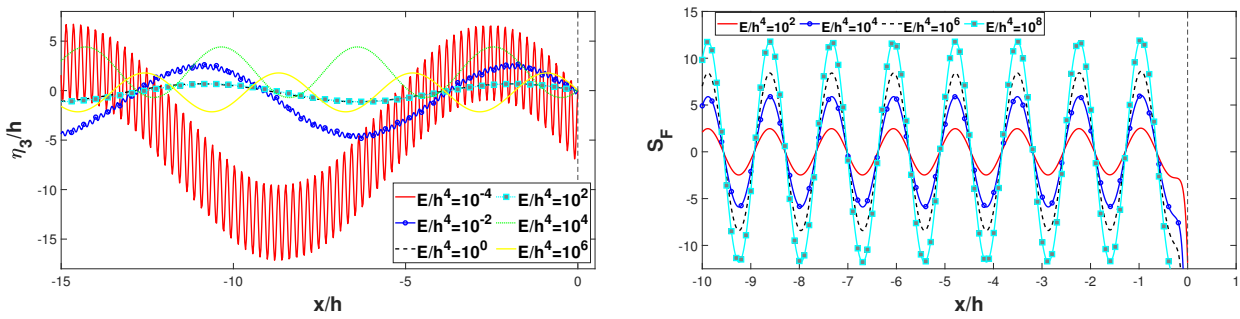

(a) (b)

Figure 5.9: (a) Non-dimensional bottom deflection amplitude and (b) Shear force against non-dimensional x/h for different values of flexural rigidity with $\epsilon_2 = 0.6, \epsilon_3 = 0.7$ and $f_2 = 0.75, f_3 = 1$.

The impact of the flexural rigidity upon the elastic bottom deflection is examined against the non-dimensional distance in Figure 5.9(a). It shows that the amplitude of the bottom elevation is maximum for lower values of the flexural rigidity but it alters the pattern after $E/h^4 = 1$. Further, η_3 attains zero value at the edge of the elastic bottom plate which also satisfies the clamped edge condition. Deflection for higher E maintains the same value which clearly shows that, after some value of the elastic rigidity, the bottom does not have any impact for such a wave interaction system. Figure 5.9(b) presents the shear force on the elastic bottom for different values of friction and different values of flexural rigidity. It is revealed that the shear achieves the lowest value near the edge $(0, -h)$. Further, the forces exhibit oscillatory behaviour similar to the deflection pattern of the elastic bottom. Furthermore, for an increase in E/h^4, the amplitude of shear force on the elastic bottom increases. Analyzing the results with respect to the seafloor helps to reduce the waveload on the structure which consequently protects the shore.

5.4 Validation

Validation of such wave interaction system is very much difficult to be produced due to the lack of literature in this direction. The most straightforward way to establish validation is to compare our results when the thickness as well as elasticity of the sea-bed are excluded from the formulation. When the values of elastic parameters E and δ are taken as 0, then the bottom configuration can be turned into a rigid one, according to Chanda and Bora [15]. However, this depends on the schematic configuration as well as on the physical considerations of the model. A similar procedure is used in this work so that the bottom boundary condition can be converted to the one used by Behera and Sahoo [8].

The complete utility of the model is assessed by comparing the results for two friction

TH-2746_176123008

parameters. To form a correct relation by translating our model to that of Behera and Sahoo [8], we use $E = 0, \delta = 0$ to transform the elastic bottom to an impermeable bottom in addition to consideration of the values $d = h = a = 2.5$ meter, $T = 8$ sec, $\theta = 0°, g = 9.81\ m/s^2, \epsilon_2 = 0.5, \epsilon_3 = 1, f_2 = 0.5, f_3 = 0$. By considering both the porosity (ϵ_3) and the porous impedance parameter value (γ_3) as unity, Region 3 is transformed to a plain water one.

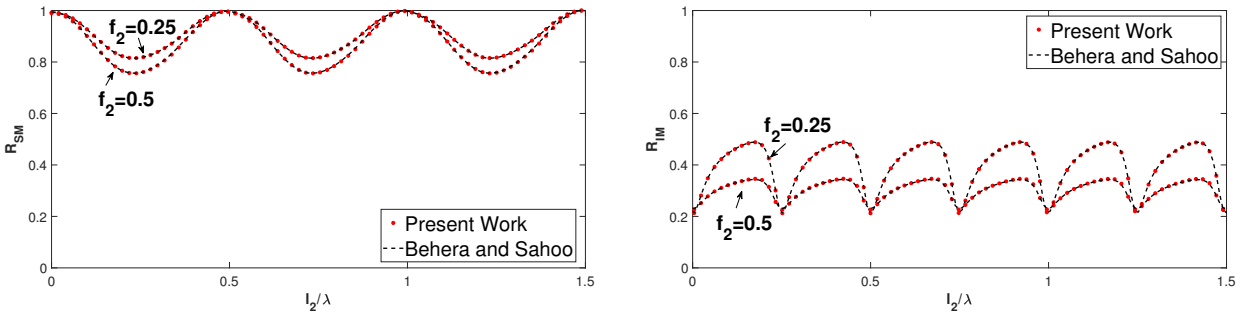

Figure 5.10: Reflection coefficients against l_2/λ for different friction parameters (f_2) at (a) free surface and (b) interface corresponding to present result and Behera and Sahoo [8].

Figure 5.10(a,b) shows the plots of the reflection coefficients versus l_2/λ (dimensionless width of Region 3 where $\lambda = 2\pi/k_{1,1}$) and it indicates a high level of consensus of that of Behera and Sahoo [8] with the current work. This implies that the current model is reasonably accurate and can be applied to a variety of coastal and offshore infrastructure issues.

5.5 Conclusion

This work attempts to throw light on the interaction of oblique water waves with a composite caisson type structure in a two-layer fluid flowing over an elastic bottom. The linear interface-piercing structure fitted with a perforated front wall is placed on a rigid bottom which follows the elastic bottom. The associated scattering problems are solved by utilizing linear water wave theory and eigenfunction expansion method. By considering the contribution of complex conjugate wavenumbers, the effect of the elastic bottom is also accounted for while finding the potentials. Thereafter, some results are obtained which are analyzed with respect to various parameters. Less amount of waveload is observed on the rigid wall and less elevation is observed in the porous region due to the wave dissipation by the structure. By comparing the reflective and dissipative properties of simple and composite structures, it is clear that the composite structure is superior. The inclusion of a perforated front wall has the following effects: (i) the percolative property of the front

TH-2746_176123008

wall increases the effectiveness of the breakwater in generating lower waveload effective on the rigid wall, (ii) significant difference in the reflection coefficients in both cases. It also allows one to find the optimum width for a suitable structural configuration possessing both reflective and dissipative characteristics. In order to attain higher wave reflection for a porous breakwater, moderate value of the angle of incidence is helpful. Choosing the height, width, porosity and porous impedance parameter of the structure appropriately, the following can be achieved: (i) maximum wave reflection, (ii) maximum dissipation of energy, (iii) minimum elevation in the porous region. Moreover, the characteristics of the bottom also affect the waveload as well as the reflection coefficients. The shear force and bottom deflection are analyzed for various elastic parameters. A suitable agreement in bottom deflection is observed while placing such a structure on the bottom with elastic characteristics. By matching a current outcome to an available result, an excellent consensus is reached, confirming the utility of the current model and that the investigation can go forward.

To sum it up, the study of linear water wave interaction with such type of structures allows one to clearly understand the effect of the porous structures that can create a tranquillity zone. It is thus concluded that the consideration of a composite porous structure of suitable geometrical configuration along with feasible characteristics of the bottom is a very important aspect which should be given importance for providing safety to the coastal facilities.

TH-2746_176123008

TH-2746_176123008

CHAPTER 6

Analysis of wave reflection, waveload and pressure distribution due to a poro-elastic structure in a two-layer fluid over a porous sea-bed

6.1 Problem statement and formulation

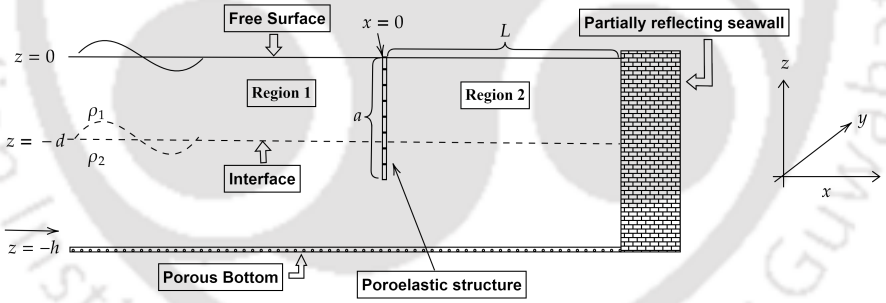

Figure 6.1: Definition sketch of wave interaction with a poro-elastic structure and a partially reflecting sea-wall.

6.1.1 Geometry of the problem

In this work, surface wave interaction with a vertically standing poro-elastic thin body, followed by a partially reflecting sea-wall placed at a distance from it, over a porous sea-bed is analysed in the context of a right-handed Cartesian coordinate system. With the z-axis considered positive in the upward direction, $z = -d$ represents the fluid layer interface. The upper layer fluid with density ρ_1 has its mean free surface at $z = 0$ while the lower layer fluid with density ρ_2 has its mean bottom surface at $z = -h$. The thin poro-elastic structure is considered at $x = 0$ while $x = L$ indicates the position of the

TH-2746_176123008

sea-wall. The surface wave strikes the structure obliquely at an angle θ to the x-axis. It guarantees that velocity potentials $\Phi_j,\ j = 1, 2$ in Regions 1 and 2 (Figure 6.1) can be expressed as $\Phi_j(x, y, z, t) = Re[\phi_j(x, z)e^{\mathrm{i}(k_y y - \omega t)}]$. Moreover, the porous sea-bed is simply considered as a boundary surface in this analysis, and fluid motion within it is not taken into account.

6.1.2 Formulation of the boundary value problem (BVP)

The velocity potentials $\phi_j(x, z)$, $j = 1, 2$ are divided along the z-direction in the following form for layer-wise clarity:

$$\phi_j = \begin{Bmatrix} \psi_j^{(1)}, & -d < z < 0, \\ \psi_j^{(2)}, & -h < z < -d, \end{Bmatrix} \text{ for } j = 1, 2, \tag{6.1}$$

with the superscripts $^{(1)}$ and $^{(2)}$ representing the potentials corresponding to the upper layer and lower layer, respectively.

With all above considerations in mind, boundary value problems involving $\phi_j, j = 1, 2$ can now be formulated using the modified Helmholtz equation

$$(\nabla^2_{x,z} - k_y^2)\phi_j = 0, \quad \text{for } j = 1, 2. \tag{6.2}$$

The linearized condition at the free surface $z = 0$ is

$$\frac{\partial \psi_j^{(1)}}{\partial z} - K\psi_j^{(1)} = 0, \quad j = 1, 2. \tag{6.3}$$

The boundary condition at the bottom $z = -h$ for the velocity potential $\psi_j^{(2)}$ is as follows:

$$\frac{\partial \psi_j^{(2)}}{\partial z} + G\psi_j^{(2)} = 0, \quad j = 1, 2, \tag{6.4}$$

where G is the porous-effect parameter of the sea-bed (See Section 1.4).
The linearized matching conditions at the mean interface $z = -d$ have the following forms:

$$\begin{aligned} \frac{\partial \psi_j^{(1)}}{\partial z} &= \frac{\partial \psi_j^{(2)}}{\partial z}, \\ \rho\left(\frac{\partial \psi_j^{(1)}}{\partial z} - K\psi_j^{(1)}\right) &= \left(\frac{\partial \psi_j^{(2)}}{\partial z} - K\psi_j^{(2)}\right), \end{aligned} \quad \text{for } j = 1, 2, \tag{6.5}$$

where $\rho = \rho_1/\rho_2 < 1$.
Potential ϕ_2 satisfies the boundary condition at $x = L$ due to the partially reflecting

sea-wall (Isaacson and Qu [45]) as follows:

$$\frac{\partial \phi_2}{\partial x} = G_w \phi_2, \tag{6.6}$$

where $G_w = \mathrm{i}k_1 \left(\frac{1-R_w}{1+R_w}\right)$ with R_w as the wall reflection coefficient. When $R_w = 1$, full reflection occurs, and when $R_w = 0$, full absorption occurs. In other words, $R_w = 1$ causes a zero flow situation near the vertical wall, causing it to become stiff.

6.1.3 Barrier deflection and related conditions

The horizontal deflection of the flexible barrier is considered to be of the type $\varsigma(y,z,t) = \mathrm{Re}\{\zeta(z)e^{\mathrm{i}(k_y y - \omega t)}\}$, where $\zeta(z)$ is the complex deflection amplitude. Combining the potentials $\psi_j^{(1)}$ and $\psi_j^{(2)}$ into ϕ_j as provided in equation (6.1) for $j = 1, 2$, the matching conditions over the poro-elastic barrier at $x = 0$ yield

$$\frac{\partial \phi_1}{\partial x} = \frac{\partial \phi_2}{\partial x} = \mathrm{i}k_1 G_1(\phi_1 - \phi_2) - \mathrm{i}\omega\zeta \quad \text{for} \quad -a < z < 0, \tag{6.7}$$

where $G_1 = \dfrac{\epsilon(f + \mathrm{i}m)}{k_1 b_p (f^2 + m^2)}$ (See Sahoo et. al. [91]) is the porous-effect parameter of the barrier where ϵ is the porosity of the barrier; f the resistance force coefficient; m the inertial force coefficient and b_p the thickness of the barrier. The homogeneous barrier is assumed to contain many fine pores. In addition to the above equation, the dynamic boundary condition on the flexible structure is

$$\hat{E}\left(\frac{\partial^2}{\partial z^2} - k_y^2\right)^2 \zeta + \hat{Q}\left(\frac{\partial^2}{\partial z^2} - k_y^2\right)\zeta - \delta\omega^2\zeta = \mathrm{i}\omega\Upsilon(\phi_1 - \phi_2), \text{ on } x = 0, \ -a < z < 0, \tag{6.8}$$

where $\hat{E} = \dfrac{E b_p^3}{12\rho_2(1-\nu^2)}$ is the flexural rigidity with E as the Young's modulus, ν as the Poisson's ratio, $\hat{Q} = Q/\rho_2$, Q the uniform compressive force; $\delta = \rho_p b_p/\rho_2$, ρ_p the density of the elastic plate and

$$\Upsilon = \begin{cases} \rho, & \text{for } -d < z < 0, \\ 1, & \text{for } -a < z < -d. \end{cases}$$

There are four main types of edge conditions that may be utilized to maintain the barrier in place and to solve the boundary value problem uniquely:

(a) Clamped-free: The barrier is supposed to be clamped at its higher end $(0, 0)$ and free at its lower end $(-a, 0)$.

TH-2746_176123008

(b) Clamped-moored: The barrier is supposed to be clamped at the higher end $(0, 0)$ and moored at the lower end $(-a, 0)$.

(c) Moored-free: The barrier is supposed to be moored at the higher end $(0, 0)$ and free at its lower end $(-a, 0)$.

(d) Moored-moored: The barrier is supposed to be moored at the higher and lower ends at $(0, 0)$ and $(-a, 0)$, respectively.

Barrier deflection and the slope of the barrier deflection disappear with respect to the clamped edge as follows:

$$\zeta(z) = 0 = \zeta'(z), \tag{6.9}$$

while the bending moment vanishes with respect to the moored edge. The horizontal components of the dynamic mooring line tensions link the restoring forces owing to the axial load to the shearing forces, which are expressed as

$$\left(\frac{d^2}{dz^2} - \nu k_y^2\right)\zeta(z) = 0, \tag{6.10}$$

$$\left[\hat{E}\left\{\frac{d^2}{dz^2} - (2-\nu)k_y^2\right\}\frac{d}{dz} + \hat{Q}\frac{d}{dz}\right]\zeta(z) = \mathcal{S}_M \sin^2(\Theta)\zeta(z), \tag{6.11}$$

where $\mathcal{S}_M = 2S_{\text{moor}}/\rho_2$ is the stiffness of the mooring line and Θ is the static mooring line angle at the static position. It could be observed that, when $\Theta = 0$, equation (6.11) is the free edge condition where the bending moment as well as the shear force will both be 0. It should be noted that, if the spring connection is examined, certain more sophisticated boundary conditions can be taken into account. However, such a situation does not arise in the current context due to the basic physical conditions under consideration and hence such boundary conditions are not deemed necessary to be analysed.

Finally, the continuity of the barrier deflection, slope of deflection, bending moment, and shear force acting on the barrier at the contact yield the following in the case of interface-piercing barriers:

$$\left.\begin{array}{l}\zeta(z),\ \zeta'(z),\ \left(\dfrac{d^2}{dz^2} - \nu k_y^2\right)\zeta(z) \text{ and} \\ \left(\hat{E}\left\{\dfrac{d^2}{dz^2} - (2-\nu)k_y^2\right\}\dfrac{d}{dz} + \hat{Q}\dfrac{d}{dz}\right)\zeta(z)\end{array}\right\} \text{ are continuous at } z = -d. \tag{6.12}$$

Along the virtual boundary between Regions 1 and 2, the potentials satisfy the continuity of velocity and pressure which yield the conditions

$$\phi_1 = \phi_2, \quad \frac{\partial\phi_1}{\partial x} = \frac{\partial\phi_2}{\partial x} \text{ at } x = 0 \text{ for } -h < z < -a. \tag{6.13}$$

We are now in a position to solve the scattering problem by utilizing all available information.

6.2 Plane wave approximation

In this part, we look at how a floating poro-elastic structure scatters linear ocean waves propagating in a two-layer fluid over a porous sea-bed. To begin with, it is essential to develop the equations for the velocity potentials associated with surface wave interaction for a finite depth elastic sea-bed.

6.2.1 Approximation of spatial velocity potentials

Solutions for the potential are approached by using the equations from the preceding section. As illustrated in Figure 6.1, the distance between the structure and the wall is assumed to be L. For $j = 1, 2$, the velocity potentials $\psi_j^{(1)}$ and $\psi_j^{(2)}$ that satisfy (6.2) and the respective boundary conditions (6.3)-(6.5) can be written as follows:

$$\phi_j = \begin{cases} \psi_j^{(1)} = \exp(\pm \mathrm{i}xq) I^{(1)}(k,z), & -d < z < 0, \\ \psi_j^{(2)} = \exp(\pm \mathrm{i}xq) I^{(2)}(k,z), & -h < z < -d, \end{cases} \tag{6.14}$$

with $q = \sqrt{k^2 - k_y^2}$, and $I^{(1)}(k,z)$ and $I^{(2)}(k,z)$ given by

$$I(k,z) = \begin{cases} I^{(1)} & = \dfrac{g_2(k)(K \sinh kz + k \cosh kz)}{K \cosh kd - k \sinh kd}, & \text{for } -d < z < 0, \\ I^{(2)} & = \left(\cosh k(z+h) - \dfrac{G}{k} \sinh k(z+h) \right), & \text{for } -h < z < -d. \end{cases} \tag{6.15}$$

where $g_2(k) = (\sinh k(h-d) - \dfrac{G}{k} \cosh k(h-d))$.

k in (6.15) can be computed from the dispersion relation which can be derived by using the second equation of (6.5) through

$$\begin{aligned} \mathcal{D} \equiv & k \left[K^2(\rho \tanh kd \tanh k(h-d) + 1) - kK(\tanh kd + \tanh k(h-d)) \right. \\ & \left. + k^2(1-\rho) \tanh kd \tanh k(h-d) \right] + G \left[(\rho - 1)k^2 \tanh kd \right. \\ & \left. - K^2(\rho \tanh kd + \tanh k(h-d)) + kK(\tanh kd \tanh k(h-d) + 1) \right] = 0, \end{aligned} \tag{6.16}$$

where k is assumed to be non-zero since zero propagating mode is not required to be considered.

TH-2746_176123008

6.2.2 Dead water analogue in permeable bottom

The dead water phenomenon, which causes excessive wave resistance in ships, is one of the more intriguing aspects of two-layer fluids. Sailors are well aware of this occurrence. A linear explanation for the dead water phenomenon in a two-layer fluid of limited depth was established by Miloh et al. [73]. We now attempt to demonstrate the dead water analogue in the presence of bottom porosity.

In the previous subsection, we have shown the form of the spatial velocity potentials. Now, considering one-dimensional plane progressive waves in the surface and interfacial modes in the forms $\chi_j = \mathrm{Re}\left\{\eta_j e^{-\mathrm{i}\omega t}\right\}$ for $j = 1, 2$, the time-dependent velocity potential in combination of the elevation amplitude can be written as

$$\Phi(x,z,t) = \begin{cases} \dfrac{\mathrm{i}\omega}{k}\left(\Lambda\cosh kz - \sinh kz\right)\chi_1, \text{ for } -d < z < 0, \\ \dfrac{\mathrm{i}\omega\left(k\cosh k(z+h) - G\sinh k(z+h)\right)}{k(G\cosh k(h-d) - k\sinh k(h-d))}\chi_2, \text{ for } -h < z < -d, \end{cases} \tag{6.17}$$

where

$$\Lambda = -\left[\coth kd - \frac{\rho(k - G\coth k(h-d))(1-\coth^2 kd)}{(k - G\coth k(h-h))(\frac{gk(1-\rho)}{\omega^2} - \rho\coth kd) - k\coth k(h-d) + G}\right].$$

The ratio of amplitudes can be written as

$$\vartheta = \frac{\eta_2}{\eta_1} = \frac{\rho(k - G\coth k(h-d))}{F_1 + (k\coth k(h-d) - G)\sinh kd}, \tag{6.18}$$

where $F_1 = (k - G\coth k(h-d))(\rho\cosh kd - \dfrac{gk(1-\rho)}{\omega^2}\sinh kd)$. It can be clearly observed that, for $k = k_c$, we have $\vartheta = 0$. Theoretically, we observe that as $\rho \to 1$ both $\omega_{_2} \to 0$ and $c_{_2} \to 0$. Hence,

$$\lim_{\rho\to 1}\vartheta \to \infty \quad \text{for } \omega = \omega_{_2}, \tag{6.19}$$

which demonstrates that the amplitude of the internal wave increases significantly as the densities of the two fluids become very close to each other.

Figures 6.2(a) and 6.2(b) illustrate the situation of dead water analogue. As $\rho \to 1$, the amplitude ratio is found to be very high for ϑ. This phenomenon is clearly analogous to the effect of the dead water due to surface gravity waves in a stratified fluid where the interfacial wave amplitude takes very large values as observed from equation (6.19). However, our main objective is to observe the difference due to consideration of bottom porosity. For $kh = 0.25$, as the bottom porosity increases, the amplitude ratio also increases. This is due to the fact that, for long waves, wave energy is uniform and a

TH-2746_176123008

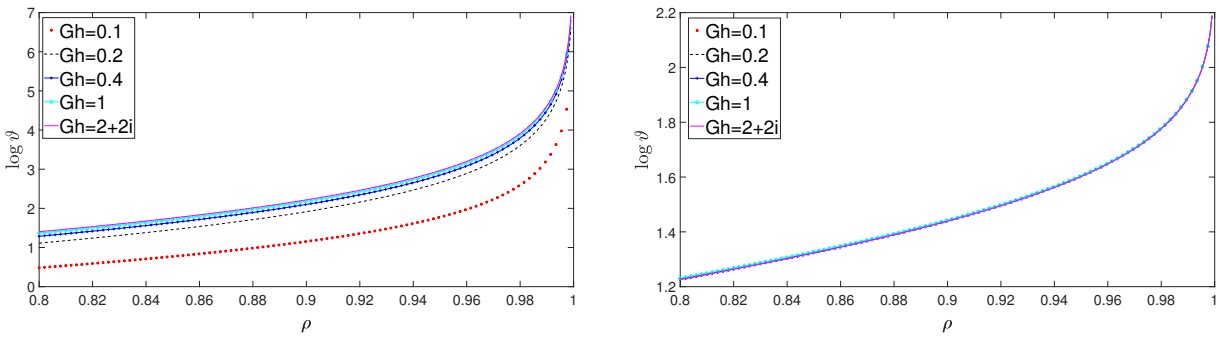

(a) (b)

Figure 6.2: Variation of $\log \vartheta$ against ρ for (a) $kh = 0.25$ and (b) $kh = 4$ corresponding to various values of porosity Gh with $d/h = 1/2$.

major part of the wave energy is dissipated due to the bottom porosity. However, for deep water waves ($kh = 4$), the concentration of the energy appears at the free surface and the effect of bottom porosity is negligible.

6.2.3 Analysis of the dispersion relation

Derivation and discussion

Now, the cases $\rho \to 1$ and $d \to 0$ or $d \to h$ in relation (6.16) present the dispersion relation in a homogeneous fluid over a porous bottom. The dispersion relation in equation (6.16) gets reduced to the dispersion relation for a two-layer fluid over an impermeable bed when $G = 0$. Corresponding to real values of G, the dispersion relation (6.16) gives rise to two positive real roots, say k_1 and k_2, restricted by $0 < k_1 < k_2$, which correspond to the propagating modes. This equation also has an infinite number of purely imaginary roots $k = k_n$ for $n = 3, 4, 5, \ldots$, which correspond to the evanescent modes where $k_n = \mathrm{i}t_n$, t_n is a real number. These evanescent modes do not contribute to wave propagation. Furthermore, those real and purely imaginary roots also have negative values which are also roots of this equation and they are wavenumbers of the waves propagating in the negative direction. Since the existence of exactly two positive roots k_1 and k_2 of (6.16) is ensured, it confirms the existence of two progressive propagating wave modes: (i) Free Surface Mode (SM) and (ii) Interface Mode (IM). Finding the roots of the dispersion relation (6.15) for real G by using the Newton-Raphson Method is a relatively common task. Finding the roots with complex G, on the other hand, is more difficult. The dispersion relation for complex G has complex roots given by $k_n = \pm a_n \pm \mathrm{i}b_n$ for $n = 1, 2, \ldots$, where all a_n and b_n are real. The roots nearer to the real axis correspond to the most prominent progressive waves in surface mode and interfacial mode where the dispersion relation given by equation (6.16) contains a pair of complex roots of opposite signs $\pm k_1$ and $\pm k_2$. It also contains an endless number of complex roots that are located

TH-2746_176123008

near the imaginary axis and have opposite signs $\pm k_n,\ n = 3, 4, \ldots$, and these correspond to the evanescent modes. In the case of the porous-effect parameter G being complex, all roots are complex in nature and they are close to the roots found corresponding to real G.

If we deeply analyse equation (6.16), we obtain a quadratic equation in ω^2 as follows:

$$\mathcal{A}\omega^4 - \mathcal{B}\omega^2 + \mathcal{C} = 0, \tag{6.20}$$

where

$$\begin{aligned}
\mathcal{A} =& k(\rho \tanh kd \tanh k(h-d) + 1) - G(\rho \tanh kd + \tanh k(h-d)),\\
\mathcal{B} =& gk\left[k(\tanh kd + \tanh k(h-d)) - G(\tanh kd \tanh k(h-d) + 1)\right],\\
\mathcal{C} =& g^2k^2(1-\rho)\tanh kd(k \tanh k(h-d) - G).
\end{aligned}$$

From equation (6.20), we obtain two propagating modes

$$\omega_{_1} = \pm\sqrt{\left(\frac{\mathcal{B} + \sqrt{\mathcal{B}^2 - 4\mathcal{A}\mathcal{C}}}{2\mathcal{A}}\right)},\ \ \omega_{_2} = \pm\sqrt{\left(\frac{\mathcal{B} - \sqrt{\mathcal{B}^2 - 4\mathcal{A}\mathcal{C}}}{2\mathcal{A}}\right)}, \tag{6.21}$$

where subscripts 1 and 2 refer to the propagating mode corresponding to the free surface and interface, respectively. An interesting fact lies here. For real G, wave modes result in the phase velocities in the form

$$c_{_1} = \frac{\omega_{_1}}{k} \ \text{ and } \ c_{_2} = \frac{\omega_{_2}}{k}. \tag{6.22}$$

Furthermore, the group velocities are given by

$$c_{g_{_1}} = \frac{\partial\omega_{_1}}{\partial k} \ \text{ and } \ c_{g_{_2}} = \frac{\partial\omega_{_2}}{\partial k}. \tag{6.23}$$

Wave energy propagation rate is proportional to the group velocity of the wave train. Hence, wave energy propagation stops when group velocity is 0 and this phenomenon is referred to as blocking.

For deep water waves for both layers of the fluid, $|kd| \gg 1$ and $|k(h-d)| \gg 1$ are valid which yield two ω^2 values from (6.21):

$$\omega^2 = gk,\ gk\frac{(1-\rho)}{(1+\rho)}, \tag{6.24}$$

which correspond to waves in the free surface and interface modes, respectively. Furthermore, it is self-evident that in deep water, the angular frequency in both surface and interface modes is unaffected by the porosity of the sea-bed. The phase velocities for

TH-2746_176123008

waves in the surface and interface modes are as follows:

$$c_1 = \sqrt{\frac{g}{k}} \text{ and } c_2 = \sqrt{\frac{g(1-\rho)}{k(1+\rho)}}, \tag{6.25}$$

which are the same as the wave flow in a two-layer fluid over rigid bottom. As a result, the bottom porosity can be ignored for deep water waves. The phase velocity for deep ocean waves is larger in the free surface mode ($c_1 > c_2$). The group velocities are as follows:

$$c_1^g = \frac{1}{2}\sqrt{\frac{g}{k}} \text{ and } c_2^g = \frac{1}{2}\sqrt{\frac{g(1-\rho)}{k(1+\rho)}}. \tag{6.26}$$

In a similar manner, for shallow water waves ($kd \ll 1$ and $k(h-d) \ll 1$), equation (6.20) yields

$$\begin{aligned}
\mathcal{A} &= k(\rho k^2 d(h-d)+1) - kG(\rho d + (h-d)),\\
\mathcal{B} &= gk\left[k^2 h - G(\, k^2 d(h-d)+1)\right],\\
\mathcal{C} &= g^2 k^3 (1-\rho) d\left[k^2(h-d) - G\right],
\end{aligned}$$

which can be used to find ω^2 as well as phase and group velocity.

It is interesting to observe what happens when $\mathcal{B}^2 - 4\mathcal{A}\mathcal{C} = 0$. This leads to the free surface and interfacial angular frequency to coincide, resulting in coalescence of both the propagating modes. For shallow water depth, $\mathcal{B}^2 - 4\mathcal{A}\mathcal{C} = 0$ leads to the algebraic equation

$$\begin{aligned}
g^2k^2\Big[\left\{k^2(h - Gd(h-d)) - G\right\}^2 - 4k^2 d(1-\rho)(k^2(h-d)-G)\left\{\rho d(h-d)k^2\right.\\
\left.+1 - G(\rho d + (h-d))\right\}\Big] = 0,
\end{aligned} \tag{6.27}$$

which implies the coincidence of wave modes. However, the important consequence is the sign change of $\mathcal{B}^2 - 4\mathcal{A}\mathcal{C}$. The coincidence of wave modes also raises the possibilities of mode swapping. It may be noted that, for $k\tanh k(h-d) - G = 0$, say $k = \pm k_c$, there is a situation of no wave propagation. In that case, $\omega_2 = 0$ and ω_1 satisfies

$$\omega_1^2 = \left(\frac{\mathcal{B}}{\mathcal{A}}\right). \tag{6.28}$$

Hence, for such wave modes, the system works as a homogeneous fluid system in the presence of the bottom porosity. We can term this as cut-off wave mode k_c. Physically, this can be defined as the effect of damping of the wave mode due to bed porosity. For shallow water waves, $k_c = \pm\sqrt{G/(h-d)}$.

The phase speed of the free surface wave mode and the interfacial wave mode are

TH-2746_176123008

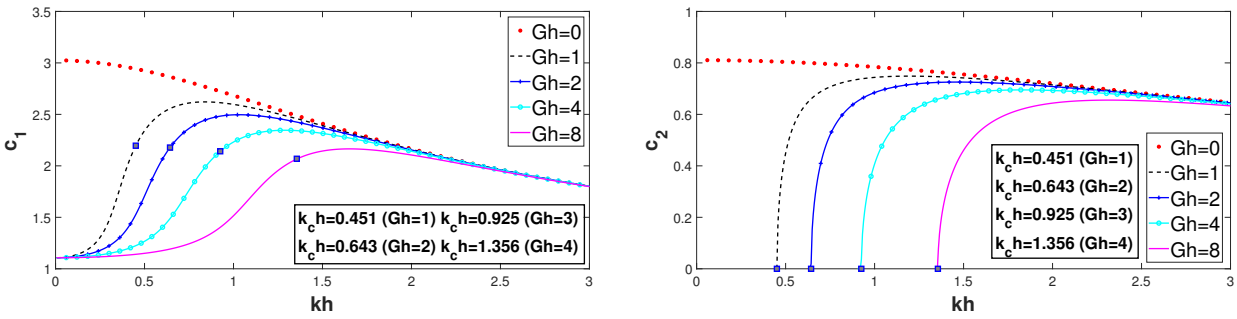

(a) (b)

Figure 6.3: Phase speeds in free surface and interface mode against non-dimensional length kh by varying Gh corresponding to various values of bed porosity with $\rho = 0.75$, $d/h = 1/2$ and k_c points are expressed in blue box.

computed and examined for various values of real sea-bed porosity in Figures 6.3(a) and 6.3(b). For zero porosity value, smooth change can be observed in both modes of phase velocity, but due to the bottom porosity, major changes can be observed. For moderate porosity values, phase velocity c_1 starts from a lower value and it attains its maximum. However, depending upon the porosity, certain phase shift of k_c as well maximum can be observed. Moreover, blocking is not observed with respect to wave modes. Maximum in wave modes may be observed due to the effect of bottom porosity. Larger values of bed porous-effect parameter G result in lower phase values in both modes. In Figure 6.3(b), phase speed in interfacial modes reaches its maximum value immediately after $k = k_c$ which shows that the damping reaches its minimum after $k = k_c$. But zero porosity shows a smooth phase speed reduction. Nature of c_1 changes for different Gh but it starts from the same point and converges after a certain kh. Similar behaviour is observed also for interfacial phase velocity.

Observation of mode swapping

The roots of dispersion relation (6.16) for real G may be found by using an available approach. However, this is not true in the case of complex G. In order to identify such roots, the algorithm of Mendez and Losada [68] is followed so that the roots get transformed from real G to complex G. The benefit of this methodology is that the propagating modes can be clearly differentiated, despite of the fact that they are all complex. Other techniques, such as homotopy perturbation (HP) method of Chang and Liou [18] can also be applied. We here adopt the methodology of Mendez and Losada [68] because of the consistency of the results in both ways, ignoring the computational cost. Furthermore, the direct application of the Newton-Raphson based algorithm through Matlab would definitely provide us the roots but it may be accompanied by a reasonable amount of complication while guessing the suitable initial value. In addition to that, for

$\mathcal{D}'(k) = 0$, with $'$ denoting differentiation, the Newton-Raphson method does not succeed. In a similar manner, the eigenfunction expansion also fails for these values of k. In this context, we apply the program Matlab 2019a to implement an algorithm, based on the Newton-Raphson method, to verify the complex roots whereas we find the initial guess for the roots by adopting the method of Mendez and Losada [68].

$Gh \Downarrow$	Err_1	Err_2	Err_3	Err_4	Err_5	Err_6
$10 + 5$i	0	0	$1.22 \cdot 10^{-5}$	$1.18 \cdot 10^{-5}$	$2.47 \cdot 10^{-5}$	$8 \cdot 10^{-6}$
$10 + 10$i	0	0	$2.73 \cdot 10^{-5}$	$3.6 \cdot 10^{-5}$	$1.14 \cdot 10^{-5}$	$3.14 \cdot 10^{-5}$
$10 + 15$i	0	0	$3.51 \cdot 10^{-5}$	$5.42 \cdot 10^{-5}$	$1.81 \cdot 10^{-5}$	$5.54 \cdot 10^{-5}$

Table 6.1: Difference of kh obtained by two different approaches, i.e., Err for different values of Gh with $d/h = 0.5$, $Kh = 0.63$ and $\rho = 0.9$.

In Table 6.1, the difference of the roots computed by the method of Mendez and Losada ($k^{(ML)}$) and the method of Newton-Raphson ($k^{(NR)}$) is compared by following the formula below:

$$Err_j = |k_j^{(ML)} h - k_j^{(NR)} h|.$$

The result shows no difference up to four places after decimal point.

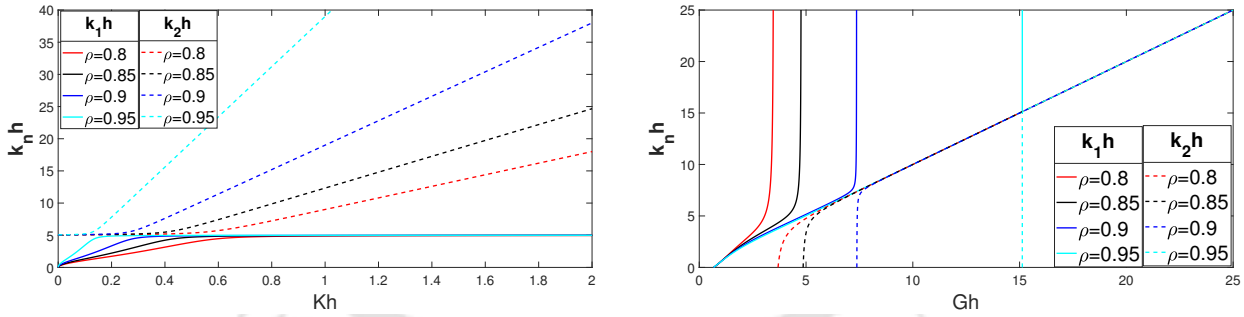

(a) (b)

Figure 6.4: Variation of non-dimensional wave modes in free surface and interface for various values of ρ (a) against non-dimensional Kh with the values $d/h = 1/2$ and $Gh = 5$ and (b) against non-dimensional Gh with the values $d/h = 1/2$ and $Kh = 0.19$.

The distribution of both the wave modes for non-dimensional frequency and non-dimensional porosity of the sea-bed is examined in Figures 6.4(a) and 6.4(b). No coalescence is found between these real propagating modes. Increasing Kh brings changes in k_1h for initial values only but no further major change is visible whereas k_2h initially starts from the same value and changes with an increase of Kh. Lower ρ results in lower values for both the modes. While changing the porosity, as observed from Figure 6.4(b), free surface mode starts initially from the same point and shoots up with an increase in

TH-2746_176123008

porous-effect parameter. Interfacial mode initially shows the difference but after $Gh \geq 5$, it exhibits no major difference. For real propagating modes for real G, the illustrations show that there is no coalescence between the modes, and the eigenfunction expansion can be carried forward while assuming distinct characteristics of the modes.

Figures 6.5(a) to 6.5(d) discuss the behaviour of the roots of the dispersion relation

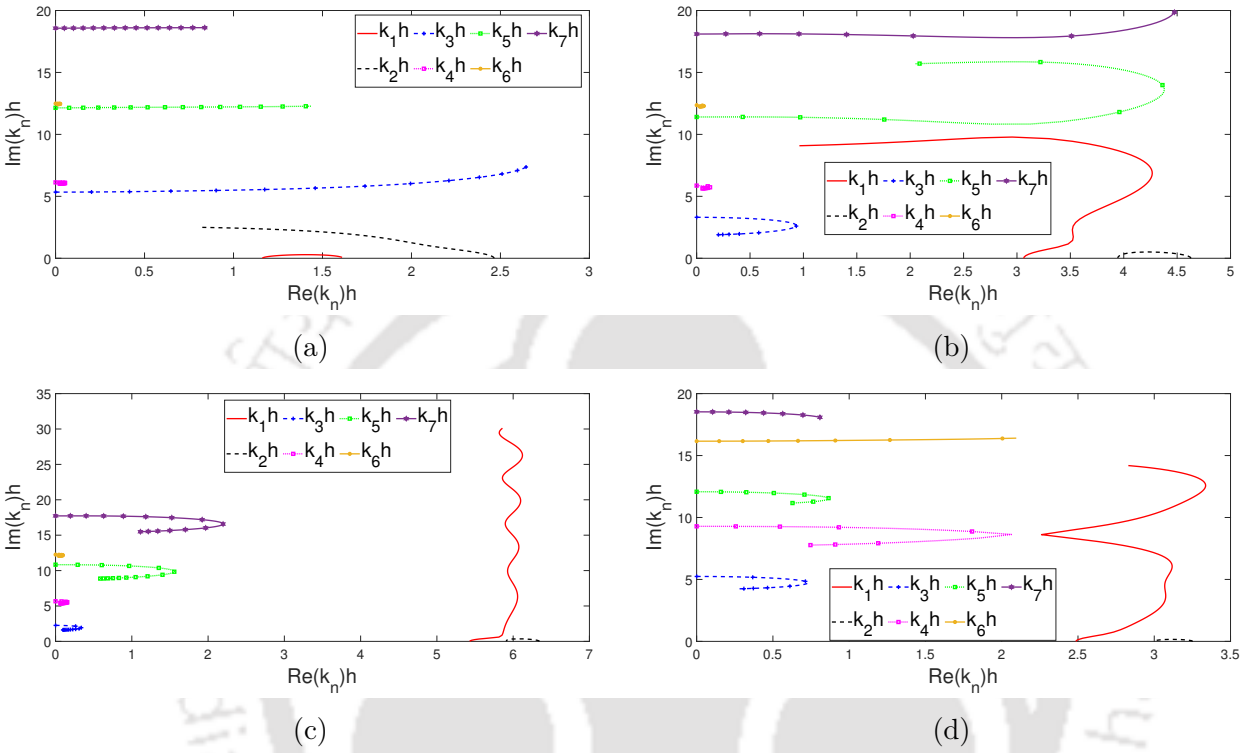

Figure 6.5: Roots of dispersion relation (6.16) corresponding to varying $\mathrm{Im}(G)$ in $[0, 5]$ corresponding to (a) $Kh = 0.0943$, (b) $Kh = 0.2515$, (c) $Kh = 0.3773$, (d) $Kh = 3.0182$ for $d/h = 1$.

against the dimensionless depth with the aim of examining whether there is any situation for which the eigenfunction solution fails. The figures depict the complex wavenumbers corresponding to the first seven non-dimensional modes $k_n h$, $n = 1, \ldots, 7$, for the values of $\mathrm{Re}(G) = 1$, $\mathrm{Im}(G)$ in the range $[0, 5]$ and different values of Kh. For $Kh = 0.0943$, Figure 6.5(a) shows the dimensionless wavenumbers due to complex G. For this case, real parts of k_1 and k_2 decrease with higher $\mathrm{Im}(G)$ but the real parts of the evanescent modes rise sharply for increasing $\mathrm{Im}(G)$. The real part of the evanescent mode k_3 crosses the values of $k_1 h$ and $k_2 h$ for higher values of $\mathrm{Im}(G)$, to be precise, for $\mathrm{Im}(G) > 2.68$. This implies that the plane-wave approximation does not have validity for large complex values of G corresponding to such values of Kh. Furthermore, no mode swapping appears to take place corresponding to shallow water. If there is any intersection between two curves, then we refer to it as mode swapping. For Figures 6.5(b) and 6.5(c), values of $Kh = 0.2515$ and $Kh = 0.3773$, respectively, are used and $k_1 h$ shows an increasing nature corresponding to

TH-2746_176123008

changing values of Kh whereas k_2h shows a decreasing pattern while changing the imaginary part of G. Evanescent modes first increase and then exhibit a decreasing nature corresponding to increasing values of Im(G). For the shallow depth, the curve corresponding to propagating modes passes below the dimensionless evanescent curves whereas for higher Kh, it maintains a significant distance from the non-dimensional evanescent curves. In Figure 6.5(b) also, the evanescent modes cross the propagating modes which renders the plain wave approximation invalid there. Figure 6.5(d) shows that, for deeper wave conditions, the possibility of coalescence disappears. If two roots are found to be overlapped, then the Green's function technique may be preferred in order to overcome the situation (as in Dalrymple et al. [25]). For the choice of parameters along with the value of G considered in the present work, the mode swapping does not take place.

6.3 Method of solution

6.3.1 Solution of the BVP

We express the spatial velocity potentials ϕ_j for $j = 1, 2$ by combining $\psi_j^{(1)}$ and $\psi_j^{(2)}$ in the following forms:

$$\phi_1 = \sum_{n=1}^{2} e^{\mathrm{i}q_n x} I_n(k_n, z) + \sum_{n=1}^{\infty} R_n e^{-\mathrm{i}q_n x} I_n(k_n, z), \tag{6.29}$$

$$\phi_2 = \sum_{n=1}^{\infty} T_n \left[\cos q_n(x - L) + \frac{G_w}{q_n} \sin q_n(x - L)\right] I_n(k_n, z), \tag{6.30}$$

where the unknown coefficients R_n are the reflection coefficients and T_n are the transmission coefficients. In $(-h, d)$, the eigenfunctions $I_n(k_n, z)$ in (6.15) are integrable and they form an orthogonal set with regard to the following inner product:

$$\langle I_n, I_m \rangle = \int_{-h}^{-d} I_n I_m \mathrm{d}z + \rho \int_{-d}^{0} I_n I_m \mathrm{d}z = \begin{cases} 0, & m \neq n, \\ W_n, & m = n, \end{cases} \tag{6.31}$$

where

$$W_n = \frac{(k_n^2 + G^2)\sinh 2k_n(h-d) + (2k_n^3 - 2G^2k_n)(h-d) + 2Gk_n(1 - \cosh 2k_n(h-d))}{4k_n^3} + Q_n \left[\frac{(k_n^2 + K^2)\sinh 2k_n d}{4k_n} - \frac{(K^2 - k_n^2)d + K(\cosh 2k_n d - 1)}{2}\right],$$

TH-2746_176123008

with

$$Q_n = \rho \left(\frac{\sinh k_n(h-d) - G/k_n \sinh k_n(h-d)}{K \cosh k_n d - k_n \sinh k_n d} \right)^2.$$

Utilizing the orthogonality of the eigenfunction in the continuity relation between $\dfrac{\partial \phi_1}{\partial x}$ and $\dfrac{\partial \phi_2}{\partial x}$ (from equations (6.7) and (6.13)), we get

$$\begin{aligned} R_n &= 1 + \alpha_n T_n, \quad \text{for } n = 1, 2, \\ R_n &= \alpha_n T_n, \qquad \text{for } n = 3, 4, \ldots, \end{aligned} \tag{6.32}$$

where $\alpha_n = \mathrm{i}(\sin q_n L + \frac{G_w}{q_n} \cos q_n L)$.

Substituting the potentials in (6.8) by using the condition from equation (6.32), we get

$$\zeta(z) = \sum_{n=1}^{4} C_n F_n(z) + \sum_{n=1}^{2} \mathbf{b}_n I_n + \sum_{n=1}^{\infty} \mathbf{a}_n T_n I_n, \text{ for } -a < z < 0, \tag{6.33}$$

with $\mathbf{a}_n = \dfrac{\mathrm{i}\Upsilon\omega p_n}{\hat{E} q_n^4 + \hat{Q} q_n^2 - \delta\omega^2}$ where $p_n = (\alpha_n - \cos q_n L + \frac{G_w}{q_n} \sin q_n L)$, $\mathbf{b}_n = \dfrac{2\mathrm{i}\Upsilon\omega}{\hat{E} q_n^4 + \hat{Q} q_n^2 - \delta\omega^2}$ and $F_n(z)$ are the independent solutions of the homogeneous ODE satisfied by ζ in (6.8). Further, in equation (6.33), the constants C_n for $n = 1, 2, 3, 4$ are given by

$$C_n = \begin{cases} C_n^1, \text{ for } -d < z < 0, \\ C_n^2, \text{ for } -a < z < -d. \end{cases}$$

If the barrier is non-interface-piercing in nature, then $C_n = C_n^1$.

Now, if we replace $\zeta(z)$ in equation (6.8), we obtain

$$\omega \sum_{n=1}^{4} C_n F_n(z) + \sum_{n=1}^{\infty} \beta_n T_n I_n + \sum_{n=1}^{2} \gamma_n I_n = 0, \text{ for } -a < z < 0, \tag{6.34}$$

where $\beta_n = \mathrm{i}(\omega \mathbf{a}_n - q_n \alpha_n - k_1 G_1 p_n)$ and $\gamma_n = \mathrm{i}(\omega \mathbf{b}_n - 2k_1 G_1)$.

Using the relation (6.32) in the equality condition of ϕ_1 and ϕ_2 (equation (6.13)), we get

$$\sum_{n=1}^{2} 2 I_n + \sum_{n=1}^{\infty} p_n T_n I_n = 0, \quad -h < z < -a. \tag{6.35}$$

To obtain the unknown coefficients in equations (6.34) and (6.35), Dalrymple and Martin [26] utilized the least square technique. A new quantity $S(z)$ is defined for this purpose

TH-2746_176123008

as follows:

$$S(z) = S_0(z) + \sum_{n=1}^{N+2} S_n^1(z) T_n + \sum_{n=1}^{4} S_n^2 C_n, \tag{6.36}$$

where

$$S_0(z) = \begin{cases} \sum_{n=1}^{2} \gamma_n I_n \text{ in } -a < z < 0, \\ \sum_{n=1}^{2} 2I_n \quad \text{in } -h < z < -a, \end{cases}, \quad S_n^1(z) = \begin{cases} \beta_n I_n & \text{in } -a < z < 0, \\ p_n I_n & \text{in } -h < z < -a, \end{cases}$$

$$S_n^2(z) = \begin{cases} \omega F_n(z) & \text{in } -a < z < 0, \\ 0 & \text{in } -h < z < -a. \end{cases}$$

This method requires that the following relation should hold:

$$\int_{-h}^{0} |S(z)|^2 \mathrm{dz} \quad \text{is minimum.} \tag{6.37}$$

Subsequently, minimizing the integral in equation (6.37) with respect to each $T_m (m = 1, 2, \ldots, N+2)$, the following integral equation is obtained:

$$\int_{-h}^{0} S^*(z) \frac{\partial S(z)}{\partial T_m} \mathrm{dz} = 0, \quad m = 1, 2, \ldots, N+2, \tag{6.38}$$

where $S^*(z)$ is the complex conjugate of $S(z)$.

After carrying out integration with respect to z, the following system of linear equations arises:

$$\sum_{n=1}^{N+2} X_{m,n}^1 T_n^* + \sum_{n=1}^{4} Y_{m,n} C_n^* = -Z_m, \text{ for } m = 1, 2, \ldots, N+2, \tag{6.39}$$

where $X_{m,n}^1 = \int_{-h}^{0} S_n^{1*} S_m^1 \mathrm{dz}$, $Y_{m,n} = \int_{-h}^{0} S_n^{2*} S_m^1 \mathrm{dz}$, $Z_m = \int_{-h}^{0} S_0^* S_m^1 \mathrm{dz}$.

As equation (6.39) contains 8 extra unknowns C_n^1 and C_n^2 $(n = 1, 2, 3, 4)$ for the interface-piercing barriers, this results in $(N+2)$ linear equations having $(N+10)$ unknowns such as

$$\sum_{n=1}^{N+2} X_{m,n}^1 T_n^* + \sum_{n=1}^{4} Y_{m,n}^{(1)} C_n^{1*} + \sum_{n=1}^{4} Y_{m,n}^{(2)} C_n^{2*} = -Z_m, \text{ for } m = 1, 2, \ldots, N+2, \tag{6.40}$$

where $Y_{m,n}^{(1)} = \int_{-d}^{0} S_n^{2*} S_m^1 \mathrm{dz}$ and $Y_{m,n}^{(2)} = \int_{-a}^{-d} S_n^{2*} S_m^1 \mathrm{dz}$.

TH-2746_176123008

The barrier edge conditions (equations (6.9) to (6.11)) and the barrier interface conditions (equation (6.12)) provide the additional eight equations. However, there are $(N+6)$ unknowns satisfying $(N+2)$ equations (equation (6.39)) for the non-interface-piercing barriers. The system of equation is

$$\sum_{n=1}^{N+2} X^1_{m,n} T^*_n + \sum_{n=1}^{4} Y^{(1)}_{m,n} C^{1*}_n = -Z_m, \text{ for } m = 1, 2, \ldots, N+2, \tag{6.41}$$

where $Y^{(1)}_{m,n} = \int_{-a}^{0} S^{2*}_n S^1_m \mathrm{d}z$.

By merging the systems of equations given by equation (6.39) along with these extra conditions, we can now build the following complex matrix system:

$$\mathbb{A}\mathbb{X} = \mathbb{B}, \tag{6.42}$$

where $\mathbb{A}$ is a $(N+10) \times (N+10)$ matrix and $\mathbb{X}$ is the unknown quantity as given below:

$$\mathbb{X} = \begin{bmatrix} T^*_1 & T^*_2 & \ldots & T^*_{N+2} & C^{1*}_1 & \ldots & C^{1*}_4 & C^{2*}_1 & \ldots & C^{2*}_4 \end{bmatrix}^T.$$

To acquire various physical values of interest, the unknown coefficients T^*_n are found by solving the given system of equations. The reflection coefficients R_1 and R_2 are computed by using the relation (6.32).

Taking $R_{SM} = |R_1|$ and $R_{IM} = |R_2|$, the reflection coefficients for free surface mode and interface mode $(N = 1, 2)$ are calculated. The local non-dimensional magnitude of the unit horizontal wave forces indicated by $\mathbb{F}_b$ and $\mathbb{F}_w$, respectively, acting on the poro-elastic barrier and the partially reflecting wall may also be calculated by using the following formulas:

$$\mathbb{F}_b = \frac{\omega}{gdh} \left| \int_{-a}^{-d} [\phi_2(0,z) - \phi_1(0,z)] \, \mathrm{d}z + \rho \int_{-d}^{0} [\phi_2(0,z) - \phi_1(0,z)] \, \mathrm{d}z \right|, \tag{6.43}$$

$$\mathbb{F}_w = \frac{\omega}{gdh} \left| \int_{-h}^{-d} \phi_2(L,z) \mathrm{d}z + \rho \int_{-d}^{0} \phi_2(L,z) \mathrm{d}z \right|. \tag{6.44}$$

With the assumption that the progressive waves in the surface and interfacial modes have the forms $\chi_j = \mathrm{Re}\left\{\eta_j e^{-\mathrm{i}\omega t}\right\}$ for $j = 1, 2$, the amplitudes are obtained, respectively, as

$$\eta_1 = \frac{\mathrm{i}}{\omega} \frac{\partial \phi_j(x,0)}{\partial z} \text{ and } \eta_2 = \frac{\mathrm{i}}{\omega} \frac{\partial \phi_j(x,-d)}{\partial z} \text{ for } j = 1, 2. \tag{6.45}$$

The run-up coefficient $\mathbb{K}_R$ is defined as the ratio of wave height at the free surface to the

TH-2746_176123008

wave height at the partially reflecting seawall. It is given by

$$\mathbb{K}_R = 2\frac{|\eta_1|}{\mathbb{I}_1}, \tag{6.46}$$

where $\mathbb{I}_1$ is the incident wave amplitude in SM.

The following formula can be used to calculate the non-dimensional pressure distribution at the surface of the porous structure in each layer:

$$\mathbb{D}_P = \left| \frac{\mathrm{i}\Upsilon}{\omega dh}(\phi_2(0,z) - \phi_1(0,z)) \right|. \tag{6.47}$$

The non-dimensional bending moment and shear force of the poro-elastic plate can be expressed as

$$Bd_M = \frac{a}{\omega}\left| \left(\frac{d^2}{dz^2} - \nu k_y^2 \right) \zeta(z) \right|, \tag{6.48}$$

$$S_F = \frac{a^2}{\omega \hat{E}}\left| \left(\hat{E}\left\{ \frac{d^2}{dz^2} - (2-\nu)k_y^2 \right\} \frac{d}{dz} + \hat{Q}\frac{d}{dz} \right) \zeta(z) \right|. \tag{6.49}$$

6.3.2 Energy identity

It is important that hydrodynamic relations such as energy identities are derived in the study of surface wave scattering by floating/submerged structures in order to comprehend the link between the scattered coefficients and then to check the accuracy and applicability of the computational findings. Green's integral theorem, often known as the rule of conservation of energy flux, is frequently used to construct the energy identities. In the linearized theory of water waves, the reflection and transmission coefficients R and T in any wave diffraction problem involving a finite number of bodies present in a homogeneous fluid with a free-surface satisfy the energy identity $|R|^2 + |T|^2 = 1$ which can be derived by a simple use of Green's integral theorem in the fluid region. For a two-layer fluid with a free surface, there exist two different modes at which time-harmonic progressive waves can propagate, and as such two energy identities involving reflection and transmission coefficients of two different modes corresponding to incident waves of again two different modes, can also be derived by using Green's integral theorem in both the fluid regions. Energy conservation principle for a two-layer fluid in the presence of the submerged bodies is not very familiar.

The whole fluid region is divided into two bounded contours as follows:

$$\tau_1 = \left\{ \begin{array}{c} x = -X, -d \le z \le 0;\ z = -d_+, -X \le x \le 0;\ z = -d_-, -X \le x \le 0 \\ x = -X, -h \le z \le -d;\ z = -h, -X \le x \le 0;\ x = 0, -h \le z \le -a \\ x = 0, -a \le z \le -d;\ x = 0, -d \le z \le 0;\ z = 0, -X \le x \le 0 \end{array} \right\},$$

TH-2746_176123008

$$\tau_2 = \left\{ \begin{array}{c} x = 0, -d \le z \le 0;\ x = 0, -d \le z \le -a;\ x = 0, -h \le z \le -a \\ z = -h, 0 \le x \le L;\ x = L, -h \le z \le -d;\ z = -d_-, 0 \le x \le L \\ z = -d_+, 0 \le x \le L;\ x = L, -d \le z \le 0; z = 0, 0 \le x \le L \end{array} \right\},$$

where $\pm$ refers to the upper and lower layer, respectively and the leftmost boundary is considered as $x = -X$.

Employing Green's integral theorem to the function $\phi_j(x, z)$ and its complex conjugate $\bar{\phi}_j(x, z)$, for $j = 1, 2$, bounded by the contours, it can be found that

$$\int_{\tau} \left(\phi \frac{\partial \bar{\phi}}{\partial n} - \bar{\phi} \frac{\partial \phi}{\partial n} \right) \mathrm{d}\tau = \sum_{\mathrm{j}=1}^{2} \int_{\tau_{\mathrm{j}}} \left(\phi_{\mathrm{j}} \frac{\partial \bar{\phi}_{\mathrm{j}}}{\partial \mathrm{n}} - \bar{\phi}_{\mathrm{j}} \frac{\partial \phi_{\mathrm{j}}}{\partial \mathrm{n}} \right) \mathrm{d}\tau = 0. \tag{6.50}$$

The approach of Das et al. [28] is used to find the contribution of (6.50) along each line. The contribution from the line $z = -d_{\pm}$ is 0 due to the property

$$\rho \left(\phi_j \frac{\partial \bar{\phi}_j}{\partial n} - \bar{\phi}_j \frac{\partial \phi_j}{\partial n} \right)_{z=-d_+} = \left(\phi_j \frac{\partial \bar{\phi}_j}{\partial n} - \bar{\phi}_j \frac{\partial \phi_j}{\partial n} \right)_{z=-d_-}.$$

The contribution from the line $x = -X$, by letting $X \to \infty$, yields

$$U_1 = 2\mathrm{i} \sum_{n=1}^{2} q_n (|R_n|^2 - 1) W_n. \tag{6.51}$$

If the side wall is assumed to be rigid, then the contribution from the wall is 0. Due to the partial reflection, the contribution from the line $x = L$, i.e., U_2 can be found as

$$U_2 = (G_w - G_w^*) \sum_{n=1}^{2} |T_n|^2 W_n. \tag{6.52}$$

There are no contribution along the lines $z = 0$ and $z = -h$ (for real G) in equation (6.50) due to the free surface and bottom boundary conditions. Combining Regions 1 and 2, the contribution from $x = 0$, i.e., U_3 is obtained as

$$\begin{aligned} U_3 = \mathrm{i}k_1 & \left[\rho \int_{-d}^{0} (G_1 + \bar{G}_1) |\phi_1 - \phi_2|^2 \mathrm{dz} + \int_{-a}^{-d} (G_1 + \bar{G}_1) |\phi_1 - \phi_2|^2 \mathrm{dz} \right] \\ - \mathrm{i}\omega & \left[\rho \int_{-d}^{0} \left\{ \zeta(\bar{\phi}_1 - \bar{\phi}_2) + \bar{\zeta}(\phi_1 - \phi_2) \right\} \mathrm{dz} + \int_{-a}^{-d} \left\{ \zeta(\bar{\phi}_1 - \bar{\phi}_2) + \bar{\zeta}(\phi_1 - \phi_2) \right\} \mathrm{dz} \right]. \end{aligned} \tag{6.53}$$

For $\rho \to 1$, we have $d \to 0$ and the energy balance equation for a homogeneous fluid can be achieved.

Thus, the energy balance relation due to the presence of a structure is derived by adding all the results related to the integral in equation (6.50):

$$\begin{aligned} & U_1 + U_2 + U_3 = 0 \\ \implies & \sum_{n=1}^{2} q_n |R_n|^2 W_n + \frac{\mathrm{i}(G_w^* - G_w)}{2} \sum_{n=1}^{2} |T_n|^2 W_n - \frac{\mathrm{i}}{2} U_3 = \sum_{n=1}^{2} q_n W_n. \end{aligned} \tag{6.54}$$

This energy identity relation given by equation (6.54) is different from the usual energy identity relations found otherwise. Let, $V_1 = \sum_{n=1}^{2} q_n |R_n|^2 W_n$, $V_2 = \frac{\mathrm{i}(G_w^* - G_w)}{2} \sum_{n=1}^{2} |T_n|^2 W_n$, $V_3 = -\frac{\mathrm{i}}{2} U_3$ and $V_4 = \sum_{n=1}^{2} q_n W_n$ where $|V_1|$ is considered as the reflected energy, $|V_2|$ is considered as the energy contribution from the partially reflecting wall and $|V_3|$ is considered to be energy contribution from the poro-elastic structure.

Kh	V_1	V_2	V_3	$(V_1 + V_2 + V_3)$	V_4
1.12	13.6595	10.443	18.8505	42.9531	42.9508
0.63	11.6277	8.0973	9.7565	29.4814	29.4812
0.4	19.353	8.498	3.554	31.049	31.051
0.28	15.2496	11.2985	24.2241	50.7722	50.772
0.2	25.1935	20.8676	40.2708	86.3319	86.3319

Table 6.2: Validation of Energy identity for various values of Kh with $d/h = 0.5$, $Gh = 10$, $G_1 = 1 + \mathrm{i}$, $a/h = 0.6, L/h = 2$, $R_w = 0.9$ and $\rho = 0.75$.

For various values of Kh, the energy contributions of reflection, transmission and poro-elastic barrier are estimated and presented in Table 6.2. It clearly shows the precision of different numerical simulations and provides quantitative data on energy loss when a poro-elastic barrier is present. Furthermore, these statistics show that the barrier and the reflecting wall cause a large amount of energy loss.

6.4 Results and discussion

In this section, we illustrate the numerical experiments for various hydrodynamic coefficients for different parameter values.

6.4.1 Validation and convergence study

We validate our current problem by comparing it to some previous efforts. The simplest way for establishing validation is to consider our results when the porosity of the sea-bed

TH-2746_176123008

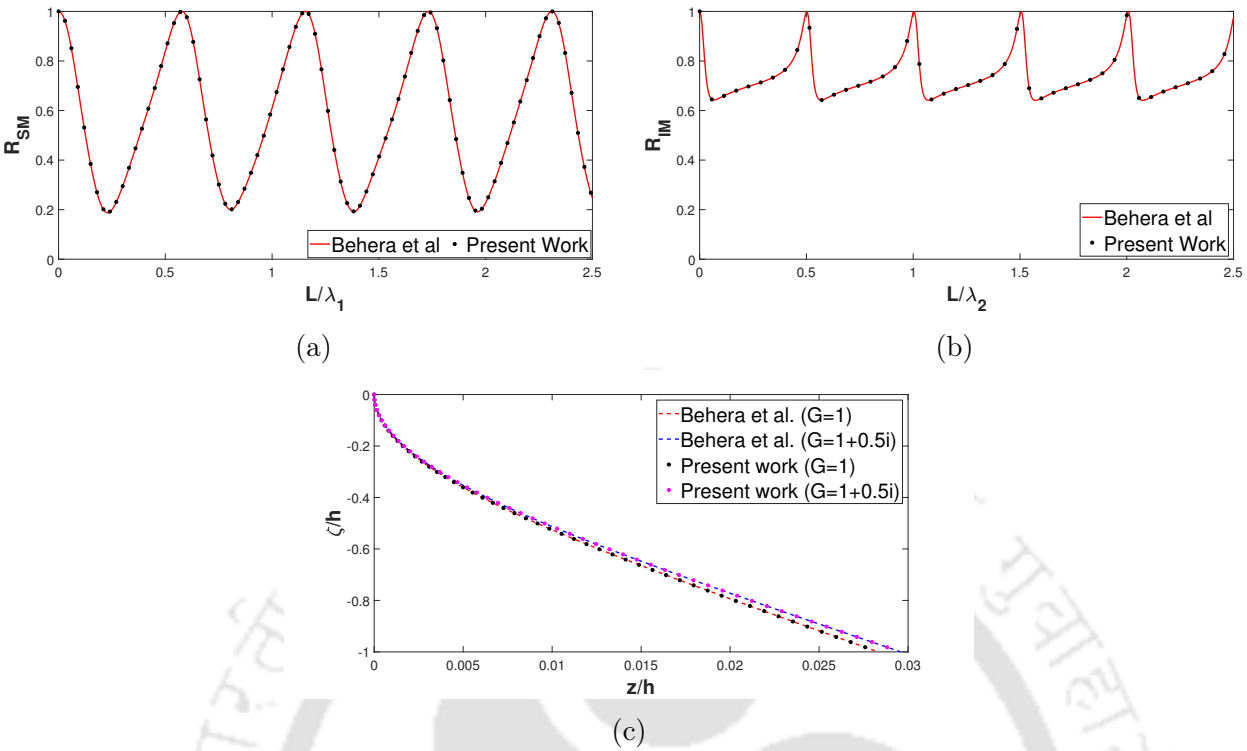

Figure 6.6: Reflection coefficients against non-dimensional length at (a) free surface and (b) interface and (c) non-dimensional poro-elastic plate deflection corresponding to the present result and Behera et al. [6].

is removed from the formulation. When the value of G is set to 0, the otherwise porous bottom arrangement is transformed into a rigid one. Apart from that, the partially reflecting wall turns into a stiff wall which allows the current model to be transformed to that of Behera et al. [6]. We take $G = 0$ and $R_w = 1$ for this purpose. The following parameter values are also taken into account: $d/h = 0.2$, $a/h = 0.8$, $h = 10$ meter, $T = 8$ sec, $g = 9.81$ m/s^2, $G_1 = 1 + 0.5$i, where the top edge is clamped and the bottom edge is deemed free. The plots of the reflection coefficients vs L/λ_j,where $\lambda_j = 2\pi/k_j$ (for $j = 1, 2$) are shown in Figures 6.6(a) and 6.6(b), and a comparison of the reflection coefficients between two studies reveals a high level of agreement between the result of Behera et al. [6] and the current result. Furthermore, non-dimensional plate elevation is also compared in Figure 6.6(c). For this, the values $d/h = 0.5$, $a/h = 1$ are considered. All three graphs clearly establish sufficient validation of our computed data. This implies that the present model is substantially accurate and may be used to solve a wide range of ocean infrastructure problems.

Convergence of evanescent modes

Before proceeding with numerical experiments, it is thought ideal to fix N, the number of evanescent modes. Table 6.3 clearly shows that the evanescent modes have a considerable

TH-2746_176123008

contribution to reflection coefficients compared to the case when they are not considered (i.e., $N = 0$). The convergence of the finding is validated. As the number of evanescent modes increases, the values of two subsequent reflection coefficients are almost the same. As a consequence, we estimate the number of evanescent modes to be $N = 16$ which can be considered as the ideal one for our subsequent computation, as supported by Table 6.3, which clearly establishes the convergence of the results.

$N \Rightarrow$ / R_{SM} $R_{IM} \Downarrow$	0	4	8	12	16	18	20	
R_{SM}	0.439	0.443	0.441	0.440	0.441	0.441	0.441	$\Leftarrow Kh = 1.1$
R_{IM}	0.460	0.474	0.471	0.470	0.472	0.472	0.472	
R_{SM}	0.459	0.460	0.461	0.461	0.460	0.460	0.460	$\Leftarrow Kh = 0.6$
R_{IM}	0.615	0.631	0.638	0.638	0.640	0.640	0.640	
R_{SM}	0.728	0.730	0.726	0.726	0.731	0.731	0.731	$\Leftarrow Kh = 0.4$
R_{IM}	0.848	0.967	0.977	0.982	0.988	0.988	0.988	

Table 6.3: Convergence study of R_{SM} and R_{IM} for different Kh with $d/h = 0.5$, $L/h = 1, a/h = 0.8$, and $Gh = 10$.

6.4.2 Numerical experiments

By using program Matlab R2019a, we solve the system of equations given by (6.42). For computing, fixed values of some parameters are considered as follows: $d/h = 0.5$; $a/h = 0.8$; $\rho = 0.9$; $\hat{E}/gh^4 = 0.1$; $\hat{Q}/gh^2 = 0.1; \delta/h = 0.1$; $Kh = 0.1$; $\theta = 30°$; $R_w = 0.5$; $\mathbb{S}_{moor} = 10^3$; $\Theta = 45°$; $\nu = 0.3$. For an in-depth information of selection of such parameter values, one can refer to Appendix D.

Effect of the confined region for various structural configuration of the poro-elastic barrier

Figures 6.7(a) and 6.7(b) show how the reflection coefficients fluctuate as per the variation of the structural arrangement for both propagating modes. The periodic nature of reflection in both propagating modes becomes more apparent as length L/h increases. In SM, different edge conditions result in significant differences in reflection coefficients, while in IM, the difference is negligible. In SM, the moored-moored edge yields higher reflection whilst the moored-free edge returns lesser reflection. In both propagating modes, the reflection trough has a period of $(j-1) < L/h < j$ for $j = 1, 2, \ldots$. In the case of IM, however, the greatest influence of reflection occurs for the starting length of L/h. The waveload on the reflecting harbour wall and the wave run-up indicate that the moored-free edge has the lowest impact and the moored-moored edge has the highest impact. $\mathbb{K}_R$ displays a waveload-specific return pattern. The size of the dip in each period decreases progressively as the length of the confined zone between the wall and the barrier grows

TH-2746_176123008

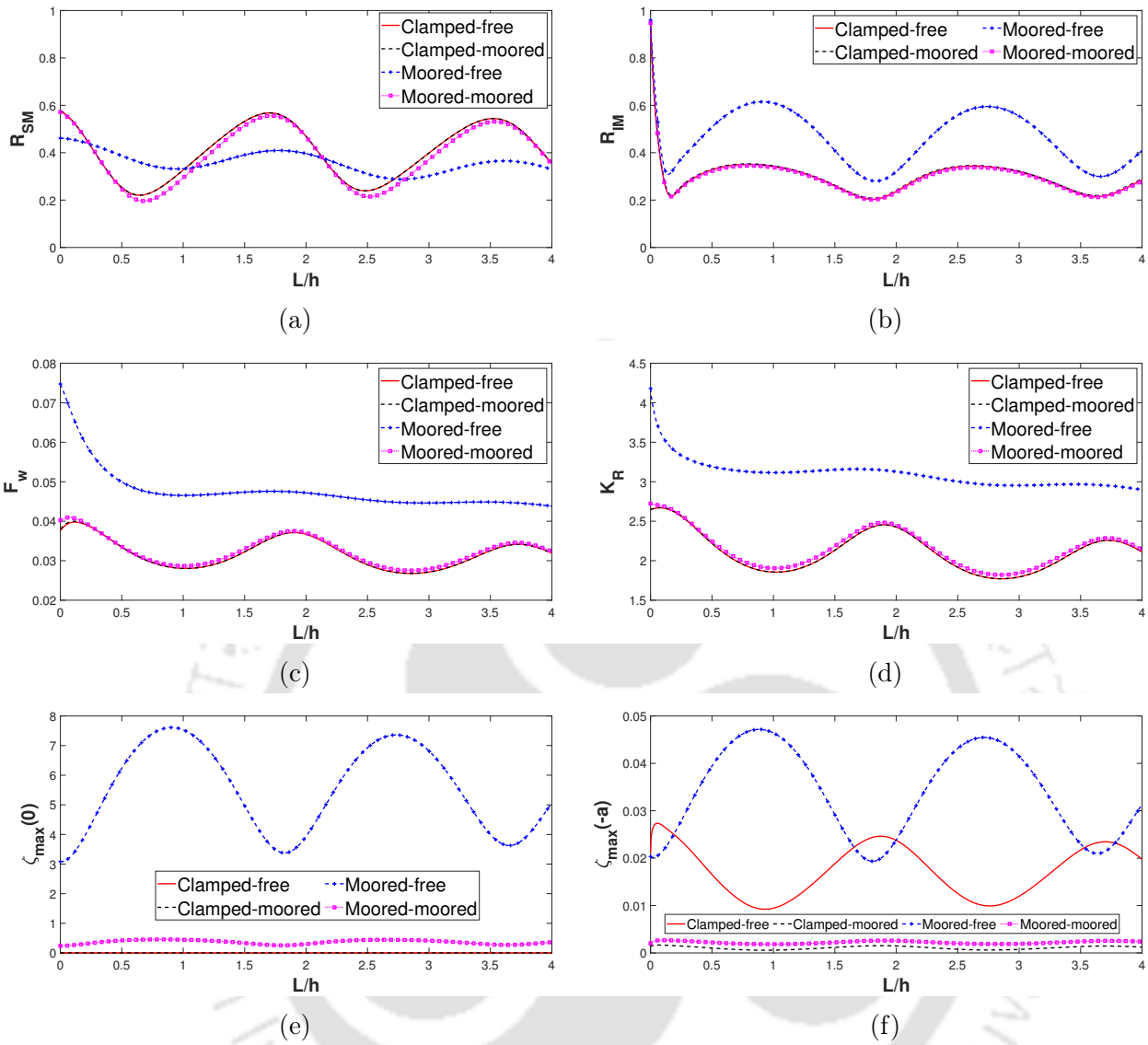

Figure 6.7: Behaviour of (a) R_{SM}, (b) R_{IM}, (c) $\mathbb{F}_w$, (d) $\mathbb{K}_R$, (e) $\zeta_{max}(0)$ and (f) $\zeta_{max}(-a)$ against incident non-dimensional distance L/h with $Gh = 10 + 10\mathrm{i}$, $\mathrm{G}_1 = 1 + \mathrm{i}$.

for both $\mathbb{F}_w$ and $\mathbb{K}_R$. Furthermore, the deflection of the poro-elastic barrier at both edges is plotted in Figures 6.7(e) and 6.7(f). For clamped upper edges, the least influence is observed for deflection. The clamped edge makes the deflection vanish which is clear from Figure 6.7(e). A periodic pattern may be observed in the deflection at both edges of the poro-elastic barrier with its upper edge anchored. For the clamped free condition, minimal periodicity is noticed due to the clamped upper edge whereas for clamped-moored edge, it almost vanishes in the lower edge. Despite of the fact that all situations result in a significant variation owing to structural construction, the optimal values for different configurations in reflection coefficients, waveload, and wave run-up may be seen at roughly the same restricted zone spacing. Furthermore, all of the hydrodynamic coefficients have

TH-2746_176123008

a consistent periodic behaviour with regard to the length L/h, indicating that at a certain value of spacing, a larger value of L/h has no significant effect on reflection and the associated hydrodynamic coefficients. Poro-elastic structures may be utilized as breakwaters by precisely integrating structural layout as well as spacing in order to achieve lower waveload and lower run-up, which would make it possible to safeguard maritime infrastructures.

Effect of the confined region on reflection for various structural height

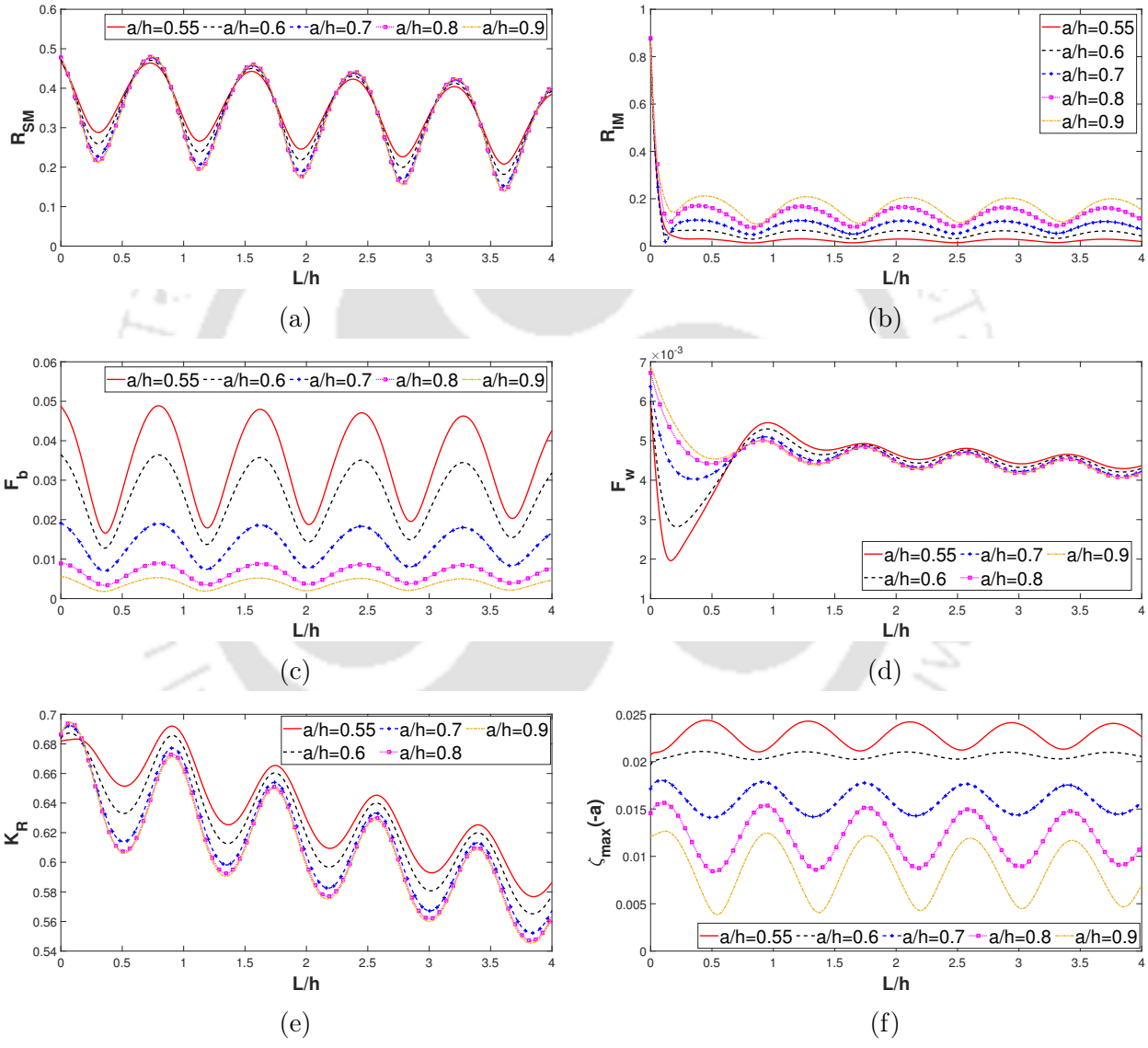

Figure 6.8: Behaviour of (a) R_{SM}, (b) R_{IM}, (c) $\mathbb{F}_b$, (d) $\mathbb{F}_w$, (e) $\mathbb{K}_R$ and (f) $\zeta_{max}(-a)$ against non-dimensional length L/h corresponding to various structural height a/h with $G_1 = 1, Gh = 10 + 10\mathrm{i}$.

The effect of the confined region spacing on wave hydrodynamic coefficients is examined in Figures 6.8(a) to 6.8(f) for various values of relative barrier height. The reflection

TH-2746_176123008

coefficients in both propagating modes show an undulating pattern. Wave trapping is a common result of standing waves, and it is characterized by a periodic dip in reflection. The trapped wave behaviour is said to be more dynamic due to different interactions of transmitted and reflected waves within the confined region. The π-shift of incident waves generated by the partially reflecting wall and the poro-elastic barrier causes the corresponding periodic peak in reflection. Less reflection is noticed when the barrier height is raised, which is due to the increased energy dissipation. However, when $a/h = 0.9,\ 0.95$, the barrier end edge seems to be closer to the bed, and as a result of mutual interaction between the reflected waves from the barrier and the bottom, reflection rises quickly in both propagating modes, which, for $a/h = 0.55$ and $a/h = 0.8$, appear to have the highest and the least amount of reflection, respectively. The higher dissipation of energy implies such a result. From Figure 6.8(c), it is clear that the waveload $\mathbb{F}_b$ on the structure reduces as the height of the structure increases. The trapping locations of reflection coefficients have a direct impact on the barrier force $\mathbb{F}_b$. This might be attributed to the flexible structure's optimum wave damping owing to its location where high wave energy resides. The total length of the confined region examined in this work is $L/h = 4$ and in the initial confined space, the minimum of each of $\mathbb{F}_w$ and $\mathbb{K}_R$, is achieved for different a/h, but after $L/h > 1/2$, the highest structural configuration results in the optima which may be termed an ideal structure height. Due to minimum wave damping, the lower the value of flexible structure height, the greater the value of $\mathbb{F}_w$ may occur which is clearly observed from Figure 6.8(d). The phase lag plays a key role in reducing the waveload on the wall, which is a consequence of partial reflection owing to the existence of a partially reflected harbour wall. The waveload $\mathbb{F}_w$ on the wall displays a similar pattern like the one seen in the run-up. The run-up coefficient is a complimentary phenomenon of waveload on the wall, and in the initial regime, a change in the optima of $\mathbb{F}_w$ and $\mathbb{K}_R$ is seen due to the inference of reflected waves to the harbour wall and transmitted waves via the flexible structure. The poro-elastic barrier is subjected to incident wave train, and the maximal relative structure height a/h illustrates the maximum deflection ζ_{max}, with the deflection coefficient decreasing as the height a/h gets lowered. The minimum deflection is observed for minimal height $a/h = 0.55,\ 0.6$, resulting in the higher reflection and waveload. As a consequence, the numerical findings of the investigation suggest that the size of the flexible structure does not ensure optimal performance. The length of the confined area as well as other physical characteristics of the barrier play important roles in producing the most desirable results.

Effect of (a) barrier height and (b) porosity on pressure distribution

The hydrodynamic pressure distribution $\mathbb{D}_P$ on the poro-elastic barrier is illustrated in Figures 6.9(a) and 6.9(b) for various values of depth ratio a/h and porous-effect parameter G_1, respectively. For any height ratio, the pressure distribution is lower near the inter-

TH-2746_176123008

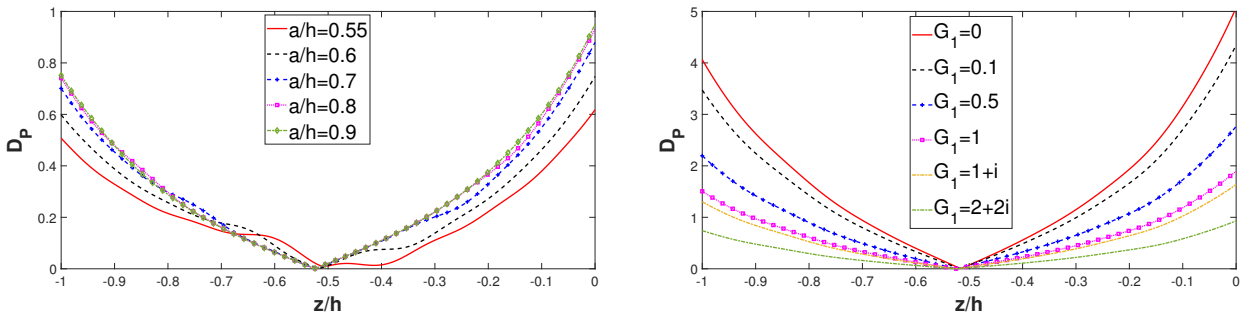

(a) (b)

Figure 6.9: Behaviour of $\mathbb{D}_P$ against non-dimensional length z/h corresponding to (a) various structural height a/h with $G_1 = 2 + 2\mathrm{i}$ and (b) various porosity G_1 with $Gh = 10 + 10\mathrm{i}$.

face in general. Furthermore, as compared to the bottom, the hydrodynamic pressure $\mathbb{D}_P$ is higher at the free surface. This clearly establishes the fact that the wave energy concentration is higher near the free surface. The pressure distribution increases as the depth ratio a/h rises, as seen in Figure 6.9(a). Again, when the barrier is placed nearer the bottom, the pressure distribution increases which can be justified by higher reflection and higher deflection $\zeta_{max}(-a)$ in Figures 6.8(a) and 6.8(f). For a range of z, the minimum pressure difference is obtained for a relative height $a/h = 0.8$. In Figure 6.9(b), $\mathbb{D}_P$ exhibits a similar pattern in the pressure distribution for different values of G_1. As the absolute value of the porous-effect parameter G_1 grows, the average hydrodynamic pressure $\mathbb{D}_P$ falls. This might be because greater values of G_1 allow more amount of wave energy to pass through the pores of the barrier.

Effect of the barrier porosity for varying incident angle θ

The ultimate objective of a flexible poro-elastic barrier is to achieve the lowest waveload on the wall by maximising wave dissipation. The incident wave dissipation coefficient is influenced by two important factors: (a) porosity, (b) fluid discharge through the flexible barrier. The barrier porosity and viscosity of the fluid define the fluid that flows through the structure. As a result, the porosity of the flexible structure is critical in the damping of incident wave trains. The barrier is considered to be made up of small pore spaces. Yu and Chwang [121], Chwang [20], Wu et al. [113] and Cho and Kim [19] have demonstrated that the typical velocity of the fluid propagating through a submerged poro-elastic barrier is linearly proportional to the dynamic pressure difference in the barrier occupied area. An ideal condition of moderate structural porosity induces critical damping which allows for modest fluid discharge through the flexible barrier and reduces the ensuing waveload on the wall.

TH-2746_176123008

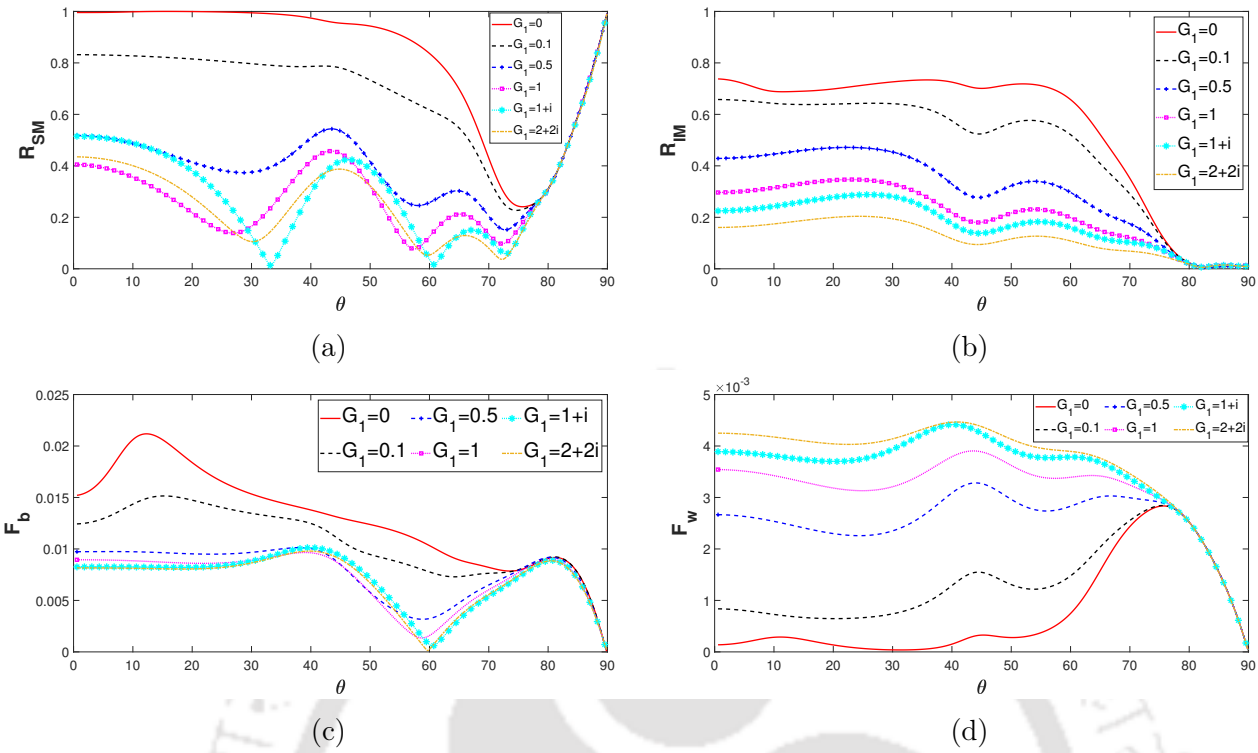

Figure 6.10: Behaviour of (a) R_{SM}, (b) R_{IM}, (c) $\mathbb{F}_b$ and (d) $\mathbb{F}_w$ against θ corresponding to different values of porosity G_1 with $a/h = 0.8$, $L/h = 2$ and $Gh = 10 + 10\mathrm{i}$.

Figures 6.10(a) to 6.10(d) show the effect of porous-effect parameter G_1 on hydrodynamic coefficients with respect to the incident angle θ. To reduce the remaining wave amplitudes transmitted by the barrier, it is suggested that a partially reflecting harbour wall be utilized. The reflection coefficients in both propagating modes have the same tendency in the form of greater amplitude fluctuations in the case of the smallest absolute value of the porous-effect parameter $G_1 = 0$ (impermeable barrier) and $G_1 = 0.1$ (very minimal porosity). In the presence of a rigid barrier, the incident wave contacts the barrier and is reflected towards the seaward far-field area. Consequently, the reflection coefficients are enhanced. Because of the enhanced wave decay, significant porosity in both propagating modes can result in a reduction in total wave reflection. The wave passes through the poro-elastic barrier, and the interaction between the fluid particles and the structure generates considerable wave damping, followed by wave entrapment beneath the barrier. As a result, the relevant hydrodynamic coefficients are regulated by wave damping when the orbit of the fluid particle is disturbed. Due to this, for producing the trapping modes with various porous-effect parameter values in both propagating modes, a slight change in the incident angle is required. Full reflection is observed for waves at $\theta \approx 90°$. In IM, however, the maximum porosity yields the highest value at nearly 80°. The non-dimensional wave forces $\mathbb{F}_b$ and $\mathbb{F}_w$ versus the oblique angle of incidence θ are plotted in Figures 6.10(c) and 6.10(d) for different values of the porous-effect parameter

TH-2746_176123008

G_1. In general, the force coefficient $\mathbb{F}_b$ drops as G_1 rises, whereas the force coefficient $\mathbb{F}_w$ behaves in an opposite manner. The porous flexible structure transmits more wave as the value of G_1 rises, and the incident wave smacks the partially reflecting harbour wall directly in the face. The waveload on the wall soon increases due to the increased porosity of the poro-elastic barrier. Furthermore, the waveload of the barrier is greater than that of the partly reflecting wall. Significant wave blockage is conceivable from a physical standpoint due to viscous damping through pore gaps. Local optima in waveloads are observed attenuately in both situations for varying values of angle of incidence θ. However, regardless of the value of G_1, $\theta = 90°$ results in zero minima for waveload $\mathbb{F}_w$. As shown in Figure 6.10(a), the optimality of waveload on the flexible structure can be observed in a similar manner. The reciprocal interaction of waves in free surface and interfacial modes might explain the local optima in wave forces.

Effect of the barrier porosity on wave elevation

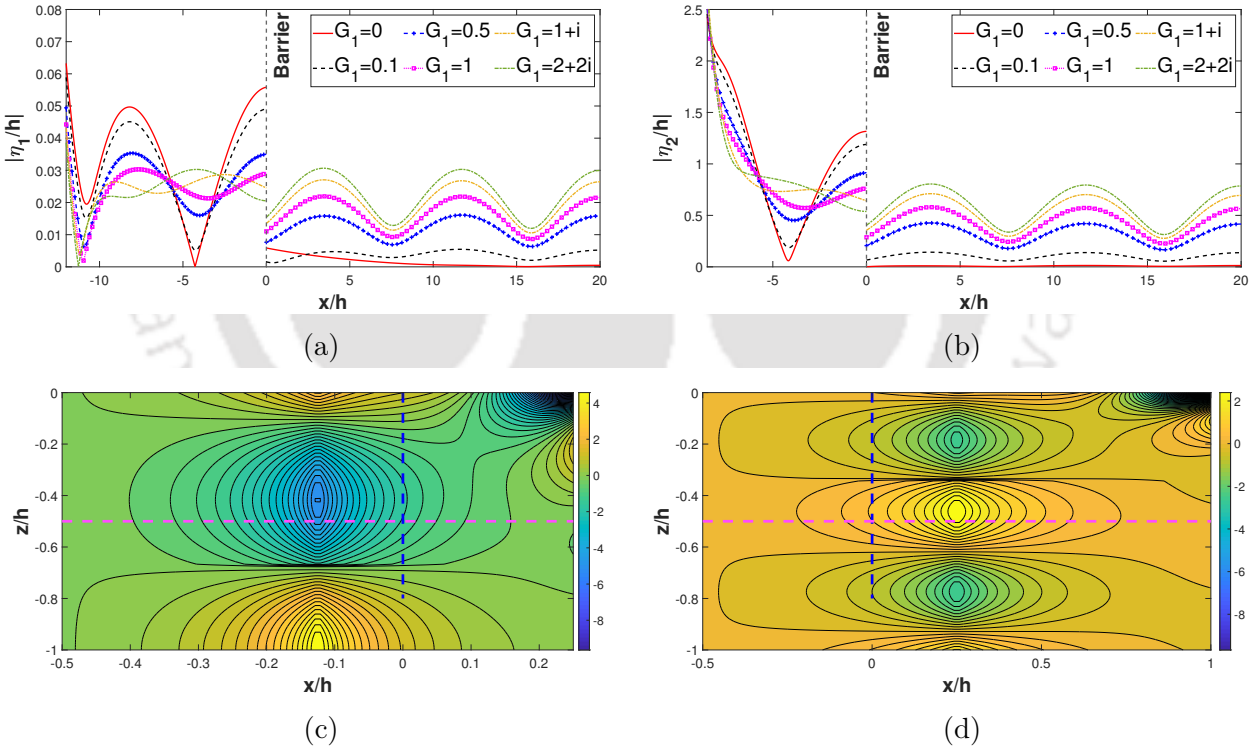

Figure 6.11: Non-dimensional elevation amplitude for (a) free surface and (b) interfacial modes versus x/h different values of G_1 and the contour plot of non-dimensional amplitude for (c) free surface and (d) interface modes corresponding for $L/h = 1$, $Gh = 10 + 10\mathrm{i}$, $G_1 = 2 + 2\mathrm{i}$ (for (c,d)).

Figures 6.11(a) and 6.11(b) show how the free surface and interfacial height undergo changes corresponding to different values of the porous-effect parameter G_1. The presence

TH-2746_176123008

of the poro-elastic structure reduces the elevation considerably in both propagating modes. This is owing to the fact that, for a surface-piercing barrier, wave energy dissipation is greater than for other barrier designs. Figure 6.11(b) demonstrates that the absolute value of $|\eta_2/h|$ exceeds $|\eta_1/h|$. We can infer that the resonant interaction between free surface waves and interfacial waves causes the difference in heights of these two modes. With an increase in the absolute value of G_1, the amplitude of oscillation in both propagating modes drops considerably. This happens because, for moderate values of the porous-effect parameter, when the porosity of the barrier rises, a significant portion of the incoming wave energy is dissipated, as already shown in Figure 6.9. Furthermore, when the absolute value of the porous-effect parameter G_1 changes, so does the phase shift in the free surface and interfacial elevation. This is due to a change in the argument of the complicated porous-effect parameter of the poro-elastic barrier. The flow distributions corresponding to the flexible structure are shown in Figures 6.11(c) and 6.11(d). In Figure 6.11(c), both constructive and destructive interference occur in front of the barrier. The flexible porous structure behaves like a kinetic barrier which blocks the fluid flow through wave damping and causes minimal deflection. On the other hand, the distance between the poro-elastic structure and the sea-wall is one of the incentives, which contributes to the multiple oscillatory peaks and troughs in elevation as observed in Figures 6.11(a) and 6.11(b). Changing the location of the reflecting wall causes constructive interference after the structure (Figure 6.11(d)). The existence of the structure causes energy dissipation, which might be the cause of such an occurrence. The damage to the barrier is significantly reduced with this sort of suitable reflecting wall position. Destructive interference may be seen in both situations when the waves are closer to the reflecting sea-wall. Such an event is caused by the interference of the reflected and absorbed waves.

Effect of non-dimensional length on energy identity terms

Figures 6.12(a) and 6.12(b) show the variations in $|V_2|$ and $|V_3|$ versus L/h for different values of a/h. Both figures exhibit oscillatory patterns with an increase in L/h. Similar occurrence was observed in Figures 6.8(a) to 6.8(d). The oscillatory patterns in the reflection, transmission, and dissipation coefficients are due to the combined effect of wave resonance occurring between the poro-elastic barrier and the partially reflecting wall. As a/h increases, the dissipation of wave increases which is clearly observed in the result. Optimum values occur in periodic positions. In $1 \leq L/h \leq 2.5$, the maximum energy dissipation can be observed which reduces after increasing L/h whereas the minimum value remains the same in our investigation area. Furthermore, increase of the barrier height also reduces the amount of waves in Region 2 which results in higher amount of energy contribution due to the partially reflecting wall. Optimum values for specific structural height remain the same while changing L/h. With an increase in the porous-

TH-2746_176123008

effect parameter, the poro-elastic plate becomes transparent to wave motion and thus the oscillatory trend diminishes.

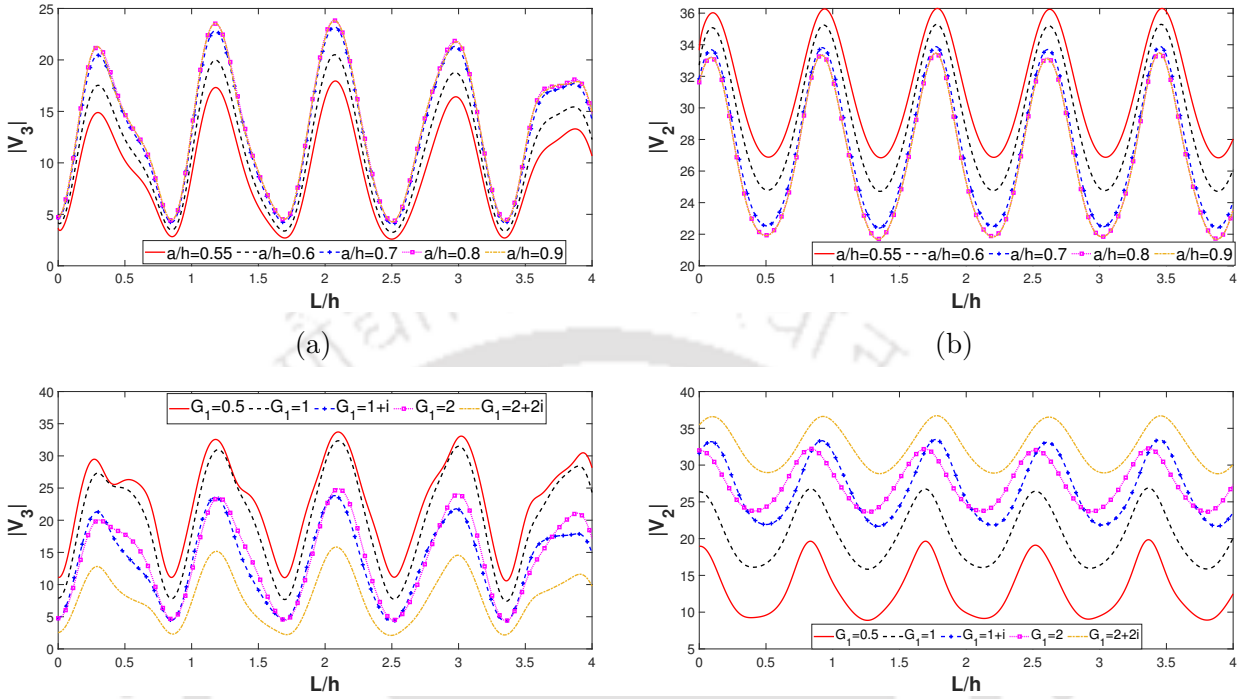

Figure 6.12: Effect of nondimensional L/h against energy contribution due to the (a) poro-elastic barrier and (b) partially reflecting wall corresponding to different values of a/h for $G_1 = 1 + \mathrm{i}, Gh = 10$ and effect of nondimensional L/h against energy contribution due to the (c) poro-elastic barrier and (d) partially reflecting wall corresponding to different values of G_1 for $a/h = 0.9, Gh = 10$.

The wave energy concentration is uniform along the horizontal direction, and the vertical porous plate helps to dissipate a major portion of the wave energy with an increase in the absolute value of the porous-effect parameter G_1. However, Figures 6.10(a) to 6.10(d) showed that the increase of porosity reduced the reflection and higher waveload on the structure. That is why higher energy dissipation can be observed for lower G_1. The combined effect of energy reflection and dissipation is greater for higher values of the complex porous-effect parameter, and the wave transmission is negligible since a major portion of the energy concentrated at the free surface and interface is reflected back in addition to the portion of the wave energy dissipated by the poro-elastic structure. As a result, the energy contribution $|V_3|$ is overall lower for low porous-effect parameter due to the combined effect of reflection and dissipation. Moreover, Figures 6.12(a) and 6.12(b) reveal that the optima of energy contribution, on changing the value of the complex porous-effect parameter, results in the same L/h.

TH-2746_176123008

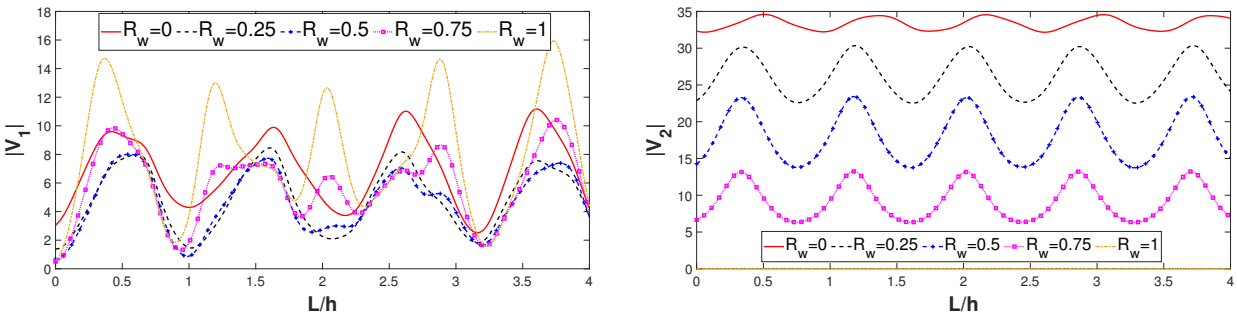

(a) (b)

Figure 6.13: Effect of non-dimensional L/h against energy contribution due to the (a) reflection coefficients and (b) sea-wall corresponding to different values of R_w for $G_1 = 1 + \mathrm{i}$, $a/h = 0.9$ and $Gh = 10$.

Figure 6.13(a) shows that, with a reduction in the reflectivity of sea-wall, the amplitude of oscillation in the energy contribution increases. This is because of the fact that, with an increase in the reflectivity, a major portion of the wave energy resonating between the barrier and wall is reflected back to Region 1. For a fully transmitting sea-wall, lower energy reflection can be observed. However, some part of the wave energy is transmitted in Region 2 which reveals that the oscillatory pattern in dissipation is stronger for a fully transmitting wall (Figure 6.13(b)).

Effect of the edge conditions and flexural rigidity on barrier characteristics

Figures 6.14(a), 6.14(c) and 6.14(e) show how the barrier deflection, bending moment and shear force, respectively, undergo changes corresponding to different edge conditions. Clamped edge condition is justified at $x = 0$ in Figure 6.14(a). Free edge gives the maximum deflection and clamped edge results in minimum deflection among all edge conditions. However, a periodic dip in deflection can be observed near the interface. It clearly shows that depending upon the edges, the optimum barrier deflection can be easily obtained. In Figure 6.14(c), the free and clamped edge conditions can be easily justified. However, a similar periodic pattern can be observed for moored and free edges, but due to the clamped edge, the bending moment at the edge differs. Similarly, as in Figure 6.14(a), a periodic dip can be observed near the interface. Moored edges result in overall lower deflection and bending moment. For shear force, the maximum can be observed near interface. Figures 6.14(b) to 6.14(f) show the influence of flexural rigidity on barrier coefficients. Up to moderate levels ($\hat{E}/gh^4 \leq 0.5$), an admissible difference owing to differing stiffness $\hat{E}$ may be detected except that, for larger flexural rigidity, all deflection coefficients show convergence to a fixed value in both propagating modes. It might be because bending a thin elastic plate possessing a high flexural stiffness is more challenging. As a result of the improved rigidity, zero deflection is achieved. Bd_M is shown

TH-2746_176123008

against several values of $\hat{E}/gh^4$ in Figure 6.14(d) which demonstrates that an insignificant change may be observed by increasing $\hat{E}/gh^4$. Irrespective of the rigidity, the periodic dip can be easily observed near the interface. It clearly shows that the barrier deflection goes into an destructive interference due to the interfacial wave attack. Decreased barrier rigidity lowers the amplitude of the shear force at the interface which shows that the maximum load of impact is observed due to the barrier rigidity at the interface. However, in all cases, the linear relationship with deflection, bending moment and shear force is clearly observed. As a result, selecting effective barrier settings for the poro-elastic barrier can improve its stability and subsequently give protection to diverse maritime structures.

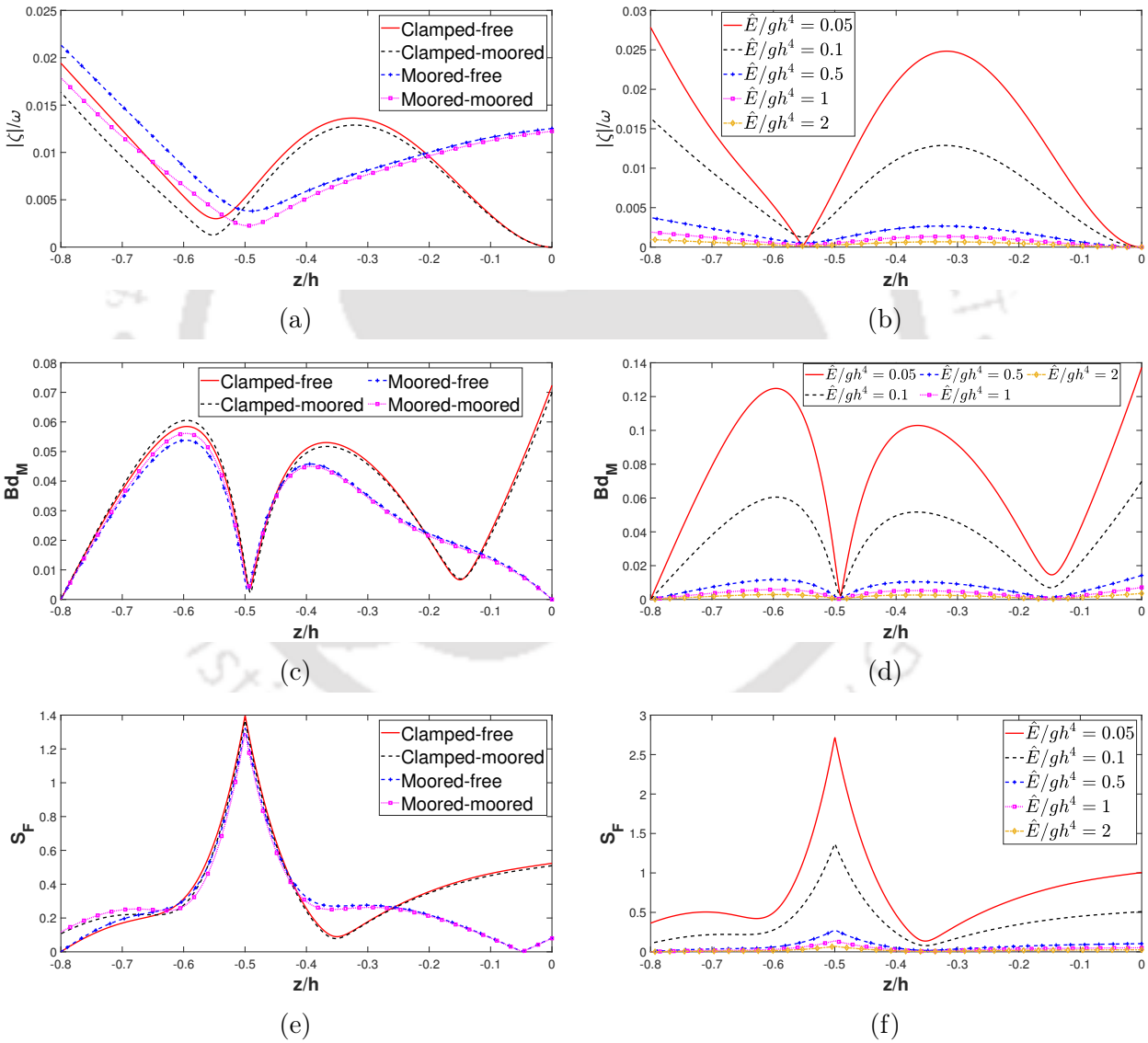

Figure 6.14: Behaviour of poro-elastic barrier (a,b) deflection $|\zeta|/\omega$, (c,d) bending moment Bd_M, and (e,f) shear force S_F against non-dimensional z/h corresponding to different values of edge conditions and flexural rigidity parameters with $a/h = 0.8, L/h = 4, Gh = 10 + 10\mathrm{i}$ and $G_1 = 2 + 2\mathrm{i}$.

TH-2746_176123008

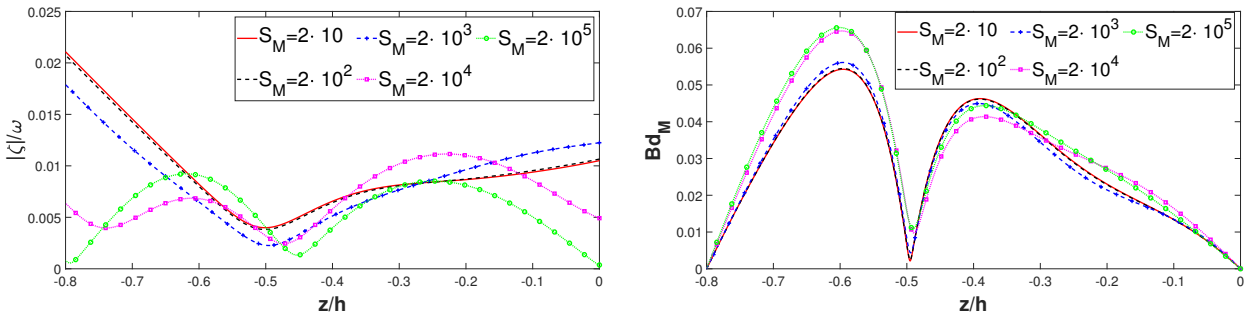

(a) (b)

Figure 6.15: Variation of poro-elastic barrier (a) deflection $|\zeta|/\omega$ and (b) bending moment Bd_M against non-dimensional z/h corresponding to different values of mooring stiffness parameters with $a/h = 0.8, L/h = 4, Gh = 10 + 10\text{i}$ and $G_1 = 2 + 2\text{i}$.

The effect of a mooring line in edges can be observed in overall plate characteristics in Figures 6.15(a) and 6.15(b). Stiffer edge results in lower deflection in the edges. Physically, higher mooring stiffness opposes the bending in the edges which produces lower deflection. However, the stiffer edge also presents minimum deflection. In Figure 6.15(b), B_M must have only zero value due to the conditions. However, for the lower part of the structure, higher stiffness of the plate results in higher bending moment and for the upper layer, the lowest stiffness results in maximum bending moment. It clearly justifies that, by appropriate mooring edge conditions, the optimal deflection and characteristics of the plate can be controlled which can help in obtaining higher reflection.

6.5 Conclusion

The present work takes up the study of oblique water wave interaction by a poro-elastic structure, placed near a partially reflecting sea-wall, in a two-layer fluid flowing over a porous sea bottom. By employing linear water wave theory and eigenfunction expansion, the solution of the corresponding scattering problem is found. By dividing the fluid region into a number of sub-regions and with the help of the given equations and matching conditions, a system of linear algebraic equations is obtained and solved. This allows to compute the potentials, the reflection coefficients and wave forces. By considering the contribution of complex conjugate wavenumbers, the resistance as well as the inertial effect of the sea-bed are also taken into account while finding the potential. Subsequently, some important results are obtained and analyzed. Some of the key points are highlighted below:

- Various types of edge conditions are analyzed for reflection coefficients, wave force, wave run-up and non-dimensional elevations. This study also leads to finding a much better reflection as well as optimum waveload on the leeside region. Clamped-free

TH-2746_176123008

and clamped moored conditions are appropriate choices for the structure, which presents that a porous structure is more efficient in possessing both reflective and dissipative characteristics.

- Taking into account moderate values of the structure length helps in achieving maximum wave reflection and minimum waveload on the wall while utilizing the porous structure under consideration as a breakwater. Furthermore, the pressure distribution in Region 1, for various structural length, helps in finding the lowest pressure distribution area.

- The structural elevation is examined for different elastic parameters of the structure, and minimum structural elevation can be achieved by the highly porous structures with higher flexural rigidity.

- By observing the flow field as well as the non-dimensional elevations, it is found that constructive and destructive interference occur in seaward and leeward region, respectively, depending upon the position of the sea-wall, which increases the wave reflection. However, most of the reflecting waves in the leeside undergo a destructive interference, resulting in the serene environment in surface flow in Region 2.

In a nutshell, the study of water wave interaction with poro-elastic structures makes it possible to clearly understand the effect of those structures that help in creating a tranquillity zone. It further demonstrates that there exists some kind of relationship among the optimum wave reflection by the porous structures, the optimum waveload on the sea-wall and on the porous structure. There is a clear observation that the use of a poro-elastic structure with suitable geometrical configuration in association with appropriate characteristics of the sea-bed is a very useful and feasible means in the creation of a tranquillity zone for appropriate protection of the coastal facilities.

TH-2746_176123008

TH-2746_176123008

CHAPTER 7

Water wave scattering and radiation due to a porous barrier in a two-layer fluid over a permeable sea-bed

7.1 Mathematical formulation

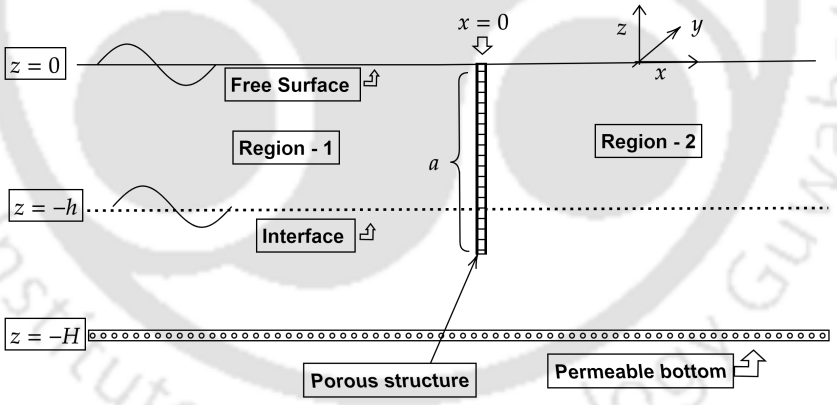

Figure 7.1: Definition sketch of wave interaction with a porous barrier.

In this work, surface wave interaction with a vertically standing thin porous barrier, over a permeable sea-bed is analyzed in the context of a right-handed Cartesian coordinate system. In a two-layer fluid flow with gravity acting on it, linear water wave theory in finite water depth, and irrotational and simple harmonic motion in an inviscid, incompressible fluid of two layers separated by a linear interface are considered. The coordinate system is considered in such a way that the z-axis considered points in the upward direction, $z = -h$ represents the fluid layer interface. $z = 0$ indicates the position of the mean surface of the upper layer fluid with density ρ_1 while $z = -H$ indicates the mean bottom

TH-2746_176123008

surface of the lower layer fluid with density ρ_2. From the earlier works, it is known that the wave force activity on the shoreline occurs repeatedly, and that introducing a suitable floating/submerged structure is an appropriate measure for reducing wave force on coastal areas. The thin porous barrier is considered at $x = 0$. The surface wave strikes it obliquely at an angle θ to the x-axis. It guarantees that velocity potentials $\Phi_j,\ j = 1, 2$ in Regions 1 and 2 (Figure 7.1) can be expressed as $\Phi_j(x, y, z, t) = Re[\phi_j(x, z)e^{i(k_y y-\omega t)}]$. To balance the velocity potentials along the vertical boundaries, the deviation of the potentials in the y-direction is assumed to be the same (due to Snell's Law). Moreover, the porous sea-bed is considered simply as a boundary surface in this work, and any fluid motion within it is not accounted for.

The spatial velocity potentials $\phi_j(x, z),\ j = 1, 2$ are divided along the z-direction in the following form for layer-wise clarity:

$$\phi_j = \left\{ \begin{array}{ll} \psi_j^{(1)}, & -h < z < 0, \\ \psi_j^{(2)}, & -H < z < -h, \end{array} \right\} \text{ for } j = 1, 2, \tag{7.1}$$

with the superscripts $^{(1)}$ and $^{(2)}$ representing the potentials corresponding to different layers.

Taking into account the above considerations, boundary value problems in $\phi_j, j = 1, 2$ can now be formulated using the modified Helmholtz equation

$$(\nabla^2_{x,z} - k_y^2)\phi_j = 0, \quad \text{for } j = 1, 2. \tag{7.2}$$

The linearized condition at the free surface $z = 0$ is

$$\frac{\partial \psi_j^{(1)}}{\partial z} - K\psi_j^{(1)} = 0, \quad j = 1, 2. \tag{7.3}$$

The boundary condition at the bottom $z = -h$ for the velocity potential $\psi_j^{(2)}$ is as follows:

$$\frac{\partial \psi_j^{(2)}}{\partial z} + G\psi_j^{(2)} = 0, \quad j = 1, 2. \tag{7.4}$$

In equation (7.4), G is the porous-effect parameter of the sea-bed that characterizes the bed permeability and is specified as $G = \dfrac{ib_B\rho_2\omega}{\mu}$ (See Section 1.4).

The ratio of the densities of the two fluids is denoted by $\rho(= \rho_1/\rho_2),\ 0 < \rho < 1$ and subsequently, the linearized boundary (matching) conditions at the mean interface

TH-2746_176123008

$z = -h$ have the following forms:

$$\begin{aligned} \frac{\partial \psi_j^{(1)}}{\partial z} &= \frac{\partial \psi_j^{(2)}}{\partial z}, \\ \rho\left(\frac{\partial \psi_j^{(1)}}{\partial z} - K\psi_j^{(1)}\right) &= \left(\frac{\partial \psi_j^{(2)}}{\partial z} - K\psi_j^{(2)}\right), \quad \text{for } j = 1, 2. \end{aligned} \tag{7.5}$$

Combining the potentials $\psi_j^{(1)}$ and $\psi_j^{(2)}$ into ϕ_j as provided in equation (7.1) for $j = 1, 2$, the matching conditions over the porous barrier at $x = 0$ yield

$$\frac{\partial \phi_1}{\partial x} = \frac{\partial \phi_2}{\partial x} = \mathrm{i}k_1 G_1(\phi_1 - \phi_2) \text{ for } -a < z < 0, \tag{7.6}$$

where $G_1 = \dfrac{\epsilon(f + \mathrm{i}m)}{k_1 b_p(f^2 + m^2)}$ (See Yu and Chwang [122], Yu [120], Lee and Chwang [21], Sahoo et al. [91]) is the porous-effect parameter of the barrier with ϵ as the porosity of the barrier, f the resistance force coefficient, m the inertial force coefficient, and b_p the thickness of the barrier.

Along the gap between Regions 1 and 2, the potentials satisfy the continuity of velocity and pressure which yield the following matching conditions:

$$\phi_1 = \phi_2, \quad \frac{\partial \phi_1}{\partial x} = \frac{\partial \phi_2}{\partial x} \text{ at } x = 0 \text{ for } -H < z < -a. \tag{7.7}$$

7.2 Plane wave approximation

It is essential to develop the equations for the velocity potentials associated with surface wave interaction for a finite depth porous sea-bed. Solutions for the potential are derived by using the equations from the preceding section. For $j = 1, 2$, the velocity potentials $\psi_j^{(1)}$ and $\psi_j^{(2)}$ that satisfy (7.2) and the respective boundary conditions (7.3)-(7.5) can be written as follows:

$$\phi_j = \begin{cases} \psi_j^{(1)} = \exp(\pm \mathrm{i}xq_n) I_n(k_n, z), & -h < z < 0, \\ \psi_j^{(2)} = \exp(\pm \mathrm{i}xq_n) I_n(k_n, z), & -H < z < -h, \end{cases} \tag{7.8}$$

with $q_n = \sqrt{k_n^2 - k_y^2}$, and eigenfunctions $I_n(k_n, z)$ given by

$$I_n(k_n, z) = \begin{cases} \dfrac{g(k_n)(K \sinh k_n z + k_n \cosh k_n z))}{(K \cosh k_n h - k_n \sinh k_n h)}, & -h < z < 0, \\ \cosh k_n(z + H) - \dfrac{G}{k_n} \sinh k_n(z + H), & -H < z < -h, \end{cases} \tag{7.9}$$

TH-2746_176123008

where $g(k_n) = \left(\sinh k_n(H-h) - \dfrac{G}{k_n}\cosh k_n(H-h)\right)$ and k_n in (7.9) can be computed from the dispersion relation which can be derived by using the second equation of (7.5) through

$$\begin{aligned} &k_n\left[K^2(\rho\tanh k_nh\tanh k_n(H-h)+1) - k_nK(\tanh k_nh+\tanh k_n(H-h))\right.\\ &\left.+\ {k_n}^2(1-\rho)\tanh k_nh\tanh k_n(H-h)\right] + G\left[(\rho-1){k_n}^2\tanh k_nh\right.\\ &\left.-K^2(\rho\tanh k_nh+\tanh k_n(H-h)) + k_nK(\tanh k_nh\tanh k_n(H-h)+1)\right] = 0, \quad (7.10)\end{aligned}$$

where k_n is assumed to be non-zero since zero propagating mode is not required to be considered.

7.3 Discussion of the dispersion relation

Now, the cases $\rho_1 \to \rho_2$ and $h \to 0$ in relation (7.10) present the dispersion relation in a homogeneous fluid over a porous bottom. The dispersion relation in equation (7.10) gets reduced to the one for a two-layer fluid over an impermeable bed when $G = 0$. Corresponding to real values of G, dispersion relation (7.10) gives rise to two positive real roots for $n = 1, 2$, say k_1 and k_2, restricted by $0 < k_1 < k_2$, which correspond to the propagating modes. This equation also has an infinite number of purely imaginary roots for $n = 3, 4, 5, \ldots$, which correspond to the evanescent modes where $k_n = \mathrm{i}t_n$, t_n is a real number. These evanescent modes do not contribute to wave propagation. Similar observation can be found in Sections 3.2.2 and 6.2.3. Furthermore, those real and purely imaginary roots also have negative values which are also roots of this equation and they are wavenumbers of the waves propagating in the negative direction. Since the existence of exactly two positive roots k_1 and k_2 of (7.10) is ensured, it confirms the existence of two progressive propagating wave modes: (i) Free Surface Mode (SM) and (ii) Interface Mode (IM). Finding the roots of dispersion relation (7.9) for real G by using the Newton-Raphson Method is a relatively common task and hence, it is not included in this study. Thorough analysis of the dispersion relation is already covered in Section 6.2.3.

7.4 Scattering Problem

In a two-layer fluid, we express the spatial velocity potentials ϕ_j for $j = 1, 2$ by combining $\psi_j^{(1)}$ and $\psi_j^{(2)}$ in the following forms:

$$\phi_1 = \sum_{n=1}^{2} e^{\mathrm{i}q_nx}I_n(k_n,z) + \sum_{n=1}^{\infty} R_ne^{-\mathrm{i}q_nx}I_n(k_n,z), \quad (7.11)$$

$$\phi_2 = \sum_{n=1}^{\infty} T_ne^{\mathrm{i}q_nx}I_n(k_n,z), \quad (7.12)$$

TH-2746_176123008

where the coefficients R_n and T_n are associated with the reflection and transmission, respectively. In $(-H, 0)$, the eigenfunctions $I_n(k_n, z)$ in (7.9) are integrable. Further, they form an orthogonal set with regard to the inner product as given below (See Section 6.3.1):

$$\langle I_n, I_m \rangle = \int_{-H}^{-h} I_n I_m \mathrm{d}z + \rho \int_{-h}^{0} I_n I_m \mathrm{d}z = \begin{cases} 0, & m \neq n, \\ W_n, & m = n. \end{cases} \tag{7.13}$$

Utilizing the orthogonality of the eigenfunction in the continuity relation between $\dfrac{\partial \phi_1}{\partial x}$ and $\dfrac{\partial \phi_2}{\partial x}$ (from equations (7.6) and (7.7)), we get

$$\begin{aligned} R_n &= 1 - T_n, \text{ for } n = 1, 2, \\ R_n &+ T_n = 0, \text{ for } n = 3, 4, \ldots \end{aligned} \tag{7.14}$$

Using the relation (7.14) for the second part of equation (7.6) and equality condition of ϕ_1 and ϕ_2 (equation (7.7)), we get

$$\sum_{n=1}^{\infty} \alpha_n T_n I_n = \beta_n \sum_{n=1}^{2} I_n, \quad -a < z < 0, \tag{7.15}$$

$$\sum_{n=1}^{\infty} T_n I_n = \sum_{n=1}^{2} I_n, \quad -H < z < -a, \tag{7.16}$$

where $\alpha_n = (q_n + 2k_1 G_1)$ and $\beta_n = 2k_1 G_1$.

To obtain the unknown coefficients in equations (7.15) and (7.16), Dalrymple and Martin [26] utilized the least square technique. A new quantity $S(z)$ is defined with fixed evanescent modes N for this purpose as follows:

$$S(z) \equiv \sum_{n=1}^{N+2} S_n^1(z) T_n - S_0(z), \tag{7.17}$$

where

$$S_0(z) = \begin{cases} \sum_{n=1}^{2} \beta_n I_n, & \text{for } -a < z < 0, \\ \sum_{n=1}^{2} I_n, & \text{for } -H < z < -a, \end{cases}, \quad S_n^1(z) = \begin{cases} \alpha_n I_n, & \text{for } -a < z < 0, \\ I_n, & \text{for } -H < z < -a. \end{cases}$$

The basic requirement of this method is that the following relation should hold:

$$\int_{-H}^{0} |S(z)|^2 \mathrm{d}z \quad \text{be minimized.} \tag{7.18}$$

TH-2746_176123008

As a result, minimizing the integral in equation (7.18) with respect to each T_m $(m = 1, 2, \ldots, N+2)$ gives the following integral equation:

$$\int_{-H}^{0} S^*(z) \frac{\partial S(z)}{\partial T_m} \mathrm{dz} = 0, \quad m = 1, 2, \ldots, N+2, \tag{7.19}$$

where $S^*(z)$ is the complex conjugate of $S(z)$.

Integration with respect to z gives rise to the following system of linear equations:

$$\sum_{n=1}^{N+2} X_{m,n} T_n^* = Z_m, \text{ for } m = 1, 2, \ldots, N+2, \tag{7.20}$$

where $X_{m,n} = \int_{-H}^{0} S_n^{1*} S_m^1 \mathrm{dz}$, $Z_m = \int_{-H}^{0} S_0^* S_m^1 \mathrm{dz}$.

Here $(N+2)$ unknowns satisfy $(N+2)$ equations from equation (7.20) which builds the following complex matrix system:

$$\mathbb{A}\mathbb{X} = \mathbb{B}, \tag{7.21}$$

where $\mathbb{A}$ is a $(N+2) \times (N+2)$ matrix and $\mathbb{X}$ is the unknown quantity as given below:

$$\mathbb{X} = \begin{bmatrix} T_1^* & T_2^* & \ldots & T_{N+2}^* \end{bmatrix}^T.$$

To acquire various physical values of interest, the unknown coefficients T_n^* are found by solving the given system of equations. The reflection coefficients R_1 and R_2 are computed by using the relation (7.14).

Taking $R_{SM} = |R_1|$ and $R_{IM} = |R_2|$, the reflection coefficients for free surface and interface modes $(N = 1, 2)$ are calculated. The local non-dimensional magnitude of the unit horizontal wave forces F_b acting on the porous barrier may also be calculated by using the following formula:

$$F_b = \frac{\omega}{ghH} \left| \int_{-a}^{-h} \left[\phi_2(0,z) - \phi_1(0,z)\right] \mathrm{d}z + \rho \int_{-h}^{0} \left[\phi_2(0,z) - \phi_1(0,z)\right] \mathrm{d}z \right|. \tag{7.22}$$

With the assumption that the progressive waves in the surface and interfacial modes have the form $\chi_j = \mathrm{Re}\left\{\eta_j e^{-\mathrm{i}\omega t}\right\}$ for $j = 1, 2$, the amplitudes are obtained, respectively, as

$$\eta_1 = \frac{\mathrm{i}}{\omega} \frac{\partial \phi_j(x,0)}{\partial z} \text{ and } \eta_2 = \frac{\mathrm{i}}{\omega} \frac{\partial \phi_j(x,-h)}{\partial z} \text{ for } j = 1, 2. \tag{7.23}$$

The following formula can be used to calculate the non-dimensional pressure distribution

TH-2746_176123008

at the surface of the porous structure in each layer:

$$D_P = \left| \frac{\mathrm{i}\Upsilon}{\omega h H}(\phi_2(0,z) - \phi_1(0,z)) \right|. \tag{7.24}$$

7.4.1 Energy identity for scattering problem

It is important that hydrodynamic relations such as energy identities are derived in the study of surface wave scattering by floating/submerged structures in order to comprehend the link between the scattered coefficients and then to check the accuracy and applicability of the computational findings. Green's integral theorem, often known as the rule of conservation of energy flux, is frequently used to construct the energy identities.

The whole fluid region is divided into two bounded contours as follows:

$$\tau_1 = \left\{ \begin{array}{c} x = -X, -h \le z \le 0;\ z = -h_+, -X \le x \le 0;\ z = -h_-, -X \le x \le 0 \\ x = -X, -h \le z \le -H;\ z = -H, -X \le x \le 0;\ x = 0, -H \le z \le -a \\ x = 0, -a \le z \le -h;\ x = 0, -h \le z \le 0;\ z = 0, -X \le x \le 0 \end{array} \right\},$$

$$\tau_2 = \left\{ \begin{array}{c} x = 0, -H \le z \le 0;\ x = 0, -h \le z \le -a;\ x = 0, -H \le z \le -a \\ z = -H, 0 \le x \le X;\ x = X, -H \le z \le -h;\ z = -h_-, 0 \le x \le X \\ z = -h_+, 0 \le x \le X;\ x = X, -h \le z \le 0; z = 0, 0 \le x \le X \end{array} \right\},$$

where $\pm$ refers to the upper and lower layer, respectively and the right and leftmost boundary is considered as $x = \pm X$.

Employing Green's integral theorem to the function $\phi_j(x,z)$ and its complex conjugate $\bar{\phi}_j(x,z)$, for $j = 1, 2$, bounded by the contours, it can be found that

$$\int_{\tau} (\phi \frac{\partial \bar{\phi}}{\partial n} - \bar{\phi} \frac{\partial \phi}{\partial n}) \mathrm{d}\tau = \sum_{\mathrm{j}=1}^{2} \int_{\tau_{\mathrm{j}}} (\phi_{\mathrm{j}} \frac{\partial \bar{\phi}_{\mathrm{j}}}{\partial \mathrm{n}} - \bar{\phi}_{\mathrm{j}} \frac{\partial \phi_{\mathrm{j}}}{\partial \mathrm{n}}) \mathrm{d}\tau = 0. \tag{7.25}$$

The approach of Das et al. [28] is used to find the contribution of (7.25) along each line. The contribution from the line $z = -h_{\pm}$ will be 0 due to the following property:

$$\rho \left(\phi_j \frac{\partial \bar{\phi}_j}{\partial n} - \bar{\phi}_j \frac{\partial \phi_j}{\partial n} \right)_{z=-h_+} = \left(\phi_j \frac{\partial \bar{\phi}_j}{\partial n} - \bar{\phi}_j \frac{\partial \phi_j}{\partial n} \right)_{z=-h_-}.$$

The contribution from the line $x = -X$, by letting $X \to \infty$, yields

$$U_1 = 2\mathrm{i} \sum_{n=1}^{2} q_n (|R_n|^2 - 1) W_n. \tag{7.26}$$

TH-2746_176123008

The contribution from the line $x = X$, by letting $X \to \infty$, gives us

$$U_2 = 2\mathrm{i}\sum_{n=1}^{2} q_n |T_n|^2 W_n. \tag{7.27}$$

There will not be any contribution along the lines $z = 0$ and $z = -h$ (for real G) in equation (7.25) due to the free surface and bottom boundary conditions. Combining Regions 1 and 2, the contribution from $x = 0$, i.e., U_3 is obtained as

$$U_3 = \mathrm{i}k_1 \left[\rho \int_{-h}^{0} (G_1 + \bar{G}_1)|\phi_1 - \phi_2|^2 \mathrm{d}z + \int_{-a}^{-h} (G_1 + \bar{G}_1)|\phi_1 - \phi_2|^2 \mathrm{d}z \right]. \tag{7.28}$$

For $\rho \to 1$ and $h \to 0$, the energy balance equation for a homogeneous fluid can be achieved.

Thus, the energy balance relation due to the presence of a structure is derived by adding all the results related to the integral in Eq. (7.25):

$$\begin{aligned} & U_1 + U_2 + U_3 = 0 \\ \implies & \sum_{n=1}^{2} q_n |R_n|^2 W_n + \sum_{n=1}^{2} q_n |T_n|^2 W_n - \frac{\mathrm{i}}{2} U_3 = \sum_{n=1}^{2} q_n W_n. \end{aligned} \tag{7.29}$$

This energy identity relation given by equation (7.29) is different from the usual energy identity relations found otherwise. Let $\mathrm{V}_1 = \sum_{n=1}^{2} q_n |R_n|^2 W_n$, $\mathrm{V}_2 = \sum_{n=1}^{2} q_n |T_n|^2 W_n$ and $\mathrm{V}_3 = -\frac{\mathrm{i}}{2} U_3$ where $|V_1|$ is considered as reflected energy, $|V_2|$ as transmitted energy and $|V_3|$ to be the energy dissipated by the structure.

7.5 Results and discussion

By using program Matlab R2019a, the system of equations (7.21) is solved. For computing, some parameter values are considered as follows: $h/H = 0.5$; $a/H = 0.75$; $\rho = 0.9$; $\theta = 30°$. For an in-depth information of selection of these parameter values, the readers are referred to Appendix D.

N	0	4	8	12	16	18	20
R_{SM}	0.293	0.292	0.291	0.291	0.291	0.291	0.291
R_{IM}	0.113	0.118	0.112	0.109	0.108	0.108	0.108

Table 7.1: Convergence study of $\mathrm{R_{SM}}$ and $\mathrm{R_{IM}}$ for $KH = 0.22$ with $a/H = 0.8$, and $GH = 10$.

TH-2746_176123008

Before proceeding with numerical experiments, it is thought ideal to fix N, the number of evanescent modes. Table 7.1 clearly shows that evanescent modes have a considerable contribution to reflection coefficients compared to the case when evanescent modes are not considered (i.e., $N = 0$). The convergence of the finding is validated. As the number of evanescent modes increases, the values of two subsequent reflection coefficients are almost the same. As a consequence, we estimate the number of evanescent modes to be $N = 16$ which can be considered as an ideal one for our subsequent computation, as supported by Table 7.1 which clearly establishes the convergence of the results.

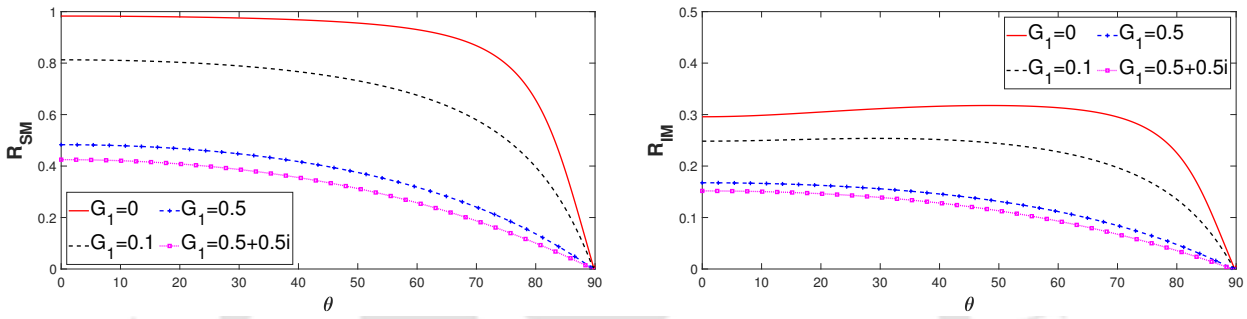

(a) (b)

Figure 7.2: Non-dimensional reflection coefficients (a) R_{SM} and (b) R_{IM} against non-dimensional incident angle θ corresponding to various structural porous-effect paramter values with $KH = 1$, $a/H = 1.5$, $GH = 10$.

An ideal condition of moderate structural porosity induces critical damping which allows for modest fluid discharge through the barrier and reduces the ensuing waveload on the shoreline. Figures 7.2(a) and 7.2(b) show the effect of porous-effect parameter G_1 on hydrodynamic coefficients with respect to the incident angle θ. The reflection coefficients in both propagating modes have the same tendency in the form of greater amplitude fluctuations in the case of the smallest absolute value of $G_1 = 0$ (impermeable barrier). In the presence of a rigid barrier, the incident wave contacts the barrier and is reflected towards the seaward far-field region. Consequently, the reflection coefficients are enhanced. Because of the enhanced wave decay, significant value of G_1 for both propagating modes can result in a reduction in total wave reflection. For both propagating modes, maximum reflection is observed for the waves at $\theta \approx 0^\circ$ and the zero minimum, irrespective of the value of the porous-effect parameter, is attained near 90°.

Influence of the porous-effect parameter on waveload F_b can be observed easily in Figure 7.3(a) for varying angular frequency. It is clear that the waveload F_b on the structure reduces as the value of the porous-effect parameter of the structure increases. Significant wave absorption is conceivable from a physical standpoint due to viscous damping through pore gaps which reduces the amount of wave resulting in such a behaviour of the waveload. The optimality of the waveload on the structure can be observed for lower

TH-2746_176123008

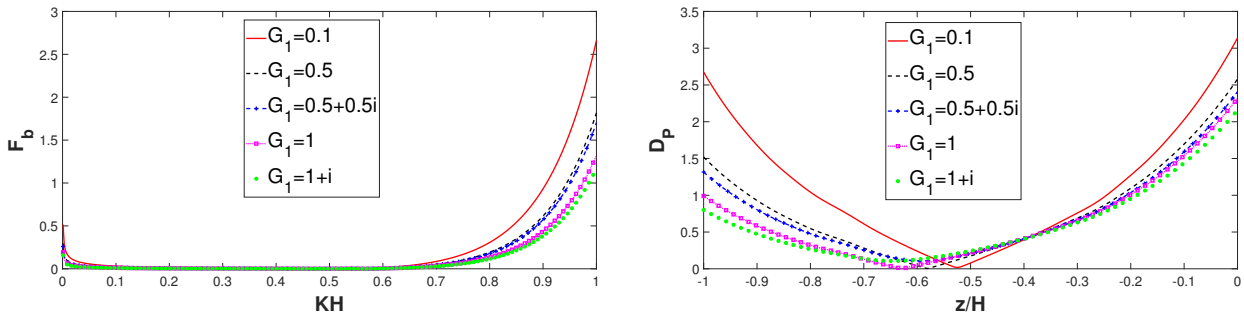

(a) (b)

Figure 7.3: Non-dimensional waveload on the structure (a) F_b vs KH and non-dimensional pressure distribution on the structure (b) D_P vs z/H corresponding to various structural porous-effect parameter values with $GH = 10$.

frequency waves as the increase in wave period enhances the amount of wave interaction. The hydrodynamic pressure distribution D_P on the porous barrier is illustrated in Figure 7.3(b) for various values of G_1. In Figure 7.3(b), D_P exhibits a similar pattern in the pressure distribution for different values of G_1. As the absolute value of G_1 grows, the average hydrodynamic pressure D_P falls which is a consequence of waveload characteristics. Moreover, as compared to the bottom, the hydrodynamic pressure D_P is higher at the free surface. The pressure distribution is lower near the interface in general. However, the minima of pressure distribution can be observed to shift towards the barrier end edge as porosity increases which shows the shift of energy due to the presence of the barrier.

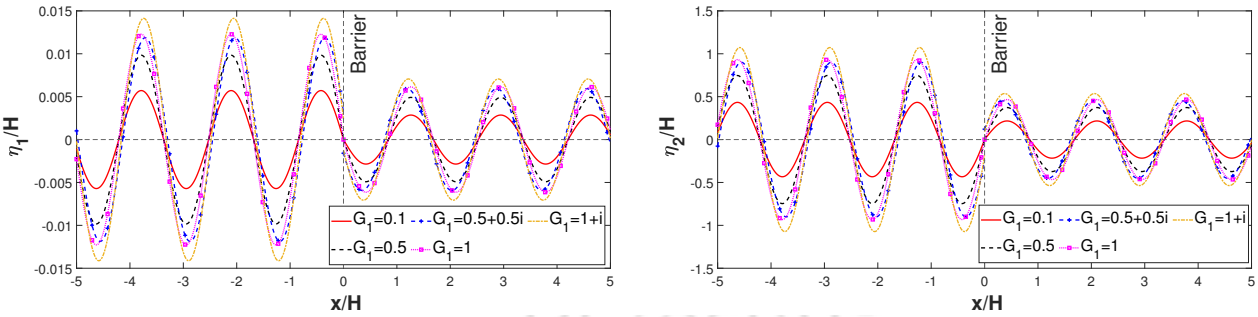

(a) (b)

Figure 7.4: Non-dimensional elevation amplitude for (a) free surface and (b) interfacial modes versus x/H different values of G_1 for $a/H = 0.6$ and $GH = 10$.

Figures 7.4(a) and 7.4(b) show how the free surface and interfacial height undergo changes corresponding to different values of the porous-effect parameter G_1. It is clear that the presence of the porous structure contributes in getting a considerable reduction in the elevation in both propagating modes. This is owing to the fact that, in the presence of a surface-piercing barrier, wave energy dissipation is greater than for other barrier designs.

TH-2746_176123008

Figure 7.4(b), on the other hand, demonstrates that the absolute value of $|\eta_2/H|$ exceeds $|\eta_1/H|$. We can infer that the resonant interaction between the free surface waves and interfacial waves causes the difference in heights of these two modes. With an increase in the absolute value of G_1, the amplitude of oscillation in both propagating modes drops considerably. This happens because, when the value of the porous-effect parameter is increased, a significant portion of the incoming wave energy is dissipated, as shown in Figure 7.3(a). Furthermore, when the absolute value of the porous-effect parameter G_1 changes, so does the phase shift of optima in the free surface and interfacial elevation. No major changes can be observed for real porosity values but difference can be clearly observed for complex values. This is due to a change in the argument of the complex porous-effect parameter of the porous barrier which enables damping due to the inertial effects.

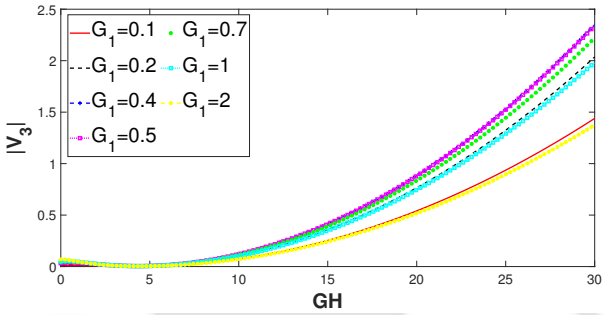

Figure 7.5: Effect of GH against Energy dissipation due to the barrier corresponding to different values of G_1 for $a/H = 0.9$.

Figure 7.5 shows the variation in $|\mathrm{V}_3|$ versus GH for different values of GH. The wave energy dissipation attains a minimum near $GH \approx 5$. This figure also helps to find out the major contribution of the bottom porosity in energy dissipation. The vertical porous barrier helps to dissipate wave energy as well as to reflect and transmit a major portion of wave. $GH \approx 5$, $G_1 = 0.4, 0.5$ give the highest dissipation and increasing bottom porosity lowers the energy distribution. This may be due to the effect of higher wave reflection and transmission rather than energy dissipation. Moreover, Figure 7.5 reveals that the energy contribution pattern shows the same on changing the value of the complex porous-effect parameter G_1. Here, $G_1 = 0.5$ can be termed as suitable plate porous-effect parameter value for attaining higher dissipation. This also justifies that, after the value of G_1, higher porosity of the barrier is not appropriate from the point of view of marine infrastructure.

7.6 Radiation Problem

A floating structure in water may experience six motions: three translational motions known as surge, sway, and heave in the mutually perpendicular $x-$, $y-$, and z-directions,

TH-2746_176123008

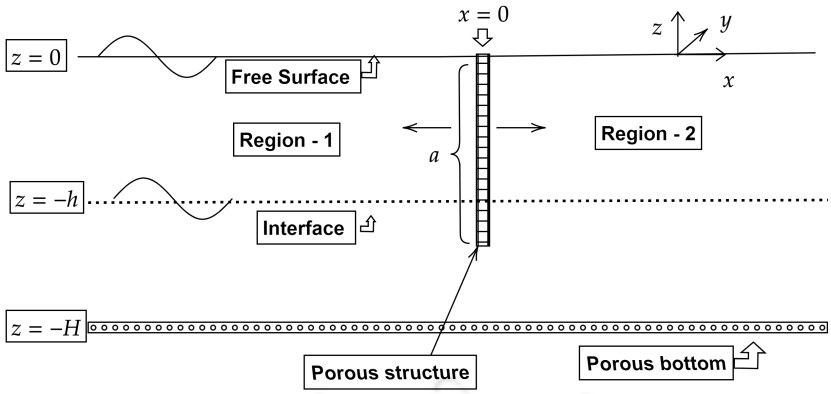

Figure 7.6: Schematic diagram of radiation problem

and three rotating motions known as roll, pitch, and yaw about the $x-$, $y-$, and z-axes, respectively. For the radiation problem considered here, the thin object is considered to be in motion. As shown in Figure 7.6, a vertical porous barrier is forced to oscillate horizontally with an angular frequency ω and a small displacement u_0 along the $x = 0$ axis. Basically, we can assume the porous barrier to be a mechanical wavemaker. This oscillating barrier generates outgoing water waves. Out of all motions, we consider only the surge motion here due to the structure configuration. The radiation problem considered here is solely based on mechanical wavemaker motion. Similar consideration can be observed in Lee and Chwang [53]. Why only surge motion is taken into account in this arrangement and not also the heave motion, the following explanation is provided for justification:
Because the wavemaker is thin, the waves interact with it in a negligible manner from the z-direction. Waves usually interact with vertical floating structures only if they have a firm foundation. With this in mind, heave motion for this structure is not taken into consideration since its impact would be negligible. We express the spatial radiation velocity potentials ϕ_j^R for $j = 1, 2$ in the following forms:

$$\phi_1^R = \sum_{n=1}^{\infty} A_n e^{-\mathrm{i}q_n x} I_n(k_n, z), \tag{7.30}$$

$$\phi_2^R = \sum_{n=1}^{\infty} B_n e^{\mathrm{i}q_n x} I_n(k_n, z), \tag{7.31}$$

where the coefficients A_n and B_n are the coefficients of the radiated potentials.

The porous structure has horizontal velocity $U(z,t) = -\mathrm{i}\omega u_0 e^{-\mathrm{i}\omega t}$ which generates outgoing waves on both sides. All other boundary conditions are still valid except equa-

TH-2746_176123008

tion (7.6) which is replaced by

$$\frac{\partial \phi_1^R}{\partial x} = \frac{\partial \phi_2^R}{\partial x} = -\mathrm{i}\omega u_0 + \mathrm{i}k_1 G_1(\phi_1^R - \phi_2^R). \tag{7.32}$$

Using orthogonality of depth function in $\dfrac{\partial \phi_1^R}{\partial x} = \dfrac{\partial \phi_2^R}{\partial x}$, we obtain

$$A_n = -B_n. \tag{7.33}$$

Using the relation (7.33) in equation (7.32) and equality condition of ϕ_1^R and ϕ_2^R (equation (7.7)), we get

$$\sum_{n=1}^{\infty} \alpha_n B_n I_n = -\omega u_0, \qquad -a < z < 0, \tag{7.34}$$

$$\sum_{n=1}^{\infty} B_n I_n = 0, \qquad -H < z < -a. \tag{7.35}$$

Similarly, $S(z)$ is defined with fixed evanescent modes N for this purpose as follows:

$$S(z) \equiv \sum_{n=1}^{N+2} S_n^1(z) B_n - S_0(z), \tag{7.36}$$

where

$$S_0(z) = \begin{cases} -u_0\omega, & \text{for } -a < z < 0, \\ 0, & \text{for } -H < z < -a, \end{cases}$$

$$S_n^1(z) = \begin{cases} \alpha_n I_n, & \text{for } -a < z < 0, \\ I_n, & \text{for } -H < z < -a. \end{cases}$$

Integrating with respect to z gives the following system of linear equations:

$$\sum_{n=1}^{N+2} X_{m,n}^1 B_n^* = Z_m^1, \text{ for } m = 1, 2, \ldots, N+2, \tag{7.37}$$

where $X_{m,n}^1 = \int_{-H}^{0} S_n^{1*} S_m^1 \mathrm{dz}$, $Z_m = \int_{-H}^{0} S_0^* S_m^1 \mathrm{dz}$.

Equation (7.37) can be written equivalently as the following complex matrix system:

$$\mathbb{A}_1 \mathbb{X}_1 = \mathbb{B}_1, \tag{7.38}$$

TH-2746_176123008

where $\mathbb{A}_1$ is a $(N+2)\times(N+2)$ matrix and $\mathbb{X}_1$ is the unknown quantity as given below:

$$\mathbb{X}_1 = \begin{bmatrix} B_1^* & B_2^* & \dots & B_{N+2}^* \end{bmatrix}^T.$$

The amplitude to stroke ratio, i.e., the ratio of amplitude of the radiated potential to the amplitude of wavemaker stroke in both propagating modes can be defined by $\mathrm{R}_1^{\mathrm{a}} = |A_1/u_0|$ and $\mathrm{R}_2^{\mathrm{a}} = |A_2/u_0|$.

The main hydrodynamic coefficients, such as added mass and damping coefficients, are obtained by solving the relevant radiation problems. The real and imaginary components of the hydrodynamic response loads on the body caused by the stipulated body movements give birth to these coefficients. The weight added to a system in a fluid owing to the fact that an accelerating or decelerating body must transport some volume of surrounding fluid with it as it moves is known as added mass. Damping is an effect that occurs inside or on an oscillatory system that reduces or restricts or prevents oscillations. By integrating the associated pressure across the structure, the hydrodynamic forces in the x-direction (i.e., for surge motion) owing to the motion may be determined. Moreover, following the procedure of Hsu and Wu [42], the non-dimensional form of added mass coefficient (μ) and the damping coefficient (λ) can be derived as follows:

$$\mu = \frac{\sqrt{gH}}{u_0\omega}\left(\int_{-a}^{-h} \mathrm{Im}\left(\phi_1^R(0,z) - \phi_2^R(0,z)\right)\mathrm{d}z + \rho\int_{-h}^{0} \mathrm{Im}\left(\phi_1^R(0,z) - \phi_2^R(0,z)\right)\mathrm{d}z\right), \quad (7.39)$$

$$\lambda = \frac{H}{u_0}\left(\int_{-a}^{-h} \mathrm{Re}\left(\phi_1^R(0,z) - \phi_2^R(0,z)\right)\mathrm{d}z + \rho\int_{-h}^{0} \mathrm{Re}\left(\phi_1^R(0,z) - \phi_2^R(0,z)\right)\mathrm{d}z\right). \quad (7.40)$$

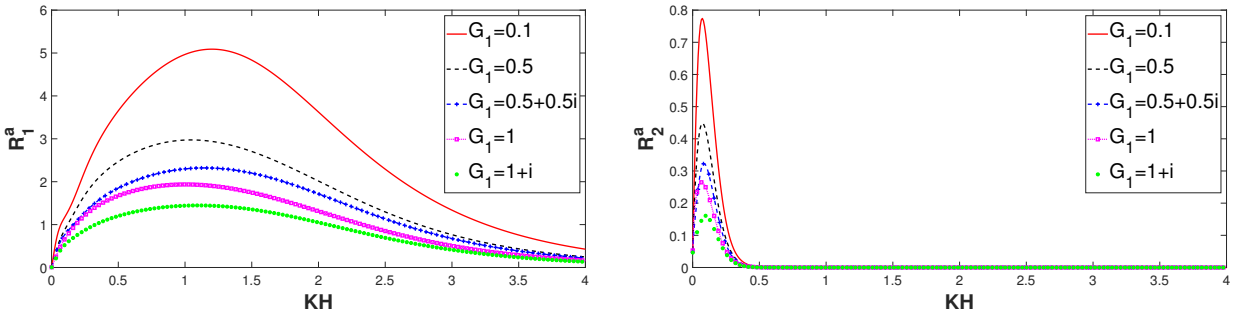

(a) (b)

Figure 7.7: Amplitude of stroke ratio for radiated potentials at (a) free surface and (b) interfacial modes versus KH different values of G_1 for $a/H = 0.8, u_0/H = 1$ and $GH = 1$.

The effectiveness of this type of wavemaker is examined by studying the variation of the amplitude to stroke ratio with respect to the dimensionless angular frequency KH

TH-2746_176123008

for different values of the porous-effect parameter G_1. Figures 7.7(a) and 7.7(b) show how the amplitude ratio changes as per the variation of the angular frequency for both propagating modes. Higher amplitude can be observed for lower frequency waves in both propagating modes. However, in both propagating modes, the amplitude ratio vanishes for higher frequency. For the free surface mode, it can be observed for higher values of $KH \approx 4$ and for interfacial mode, it can be observed after $KH = 0.5$. When KH is small, it means that the wavemaker oscillates very slowly. Moreover, the free surface amplitude ratio is higher than the interfacial one. This shows that the impact of radiated energy mostly carries out along the free surface waves. Consideration of different porous-effect parameters result in significant differences in radiation coefficients, while a rigid structure produces higher radiation amplitude as the higher porosity effect damps the wave as well as helps in higher fluid passage.

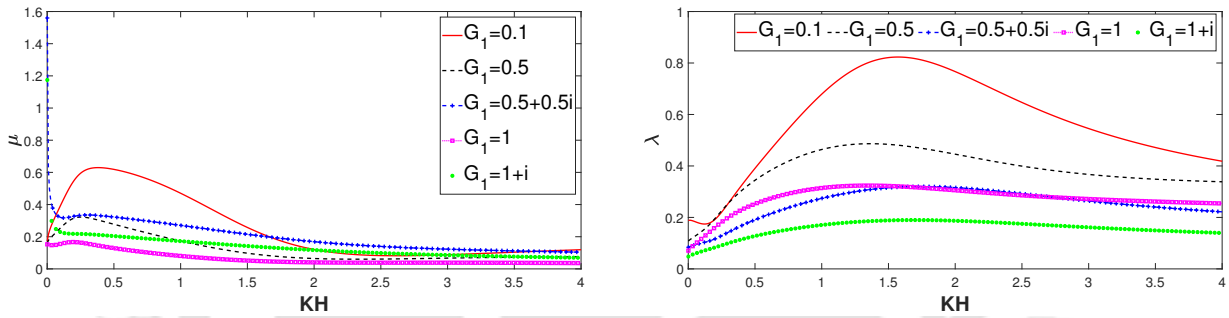

(a) (b)

Figure 7.8: (a) Added mass and (b) damping coefficient versus KH different values of G_1 for $a/H = 0.8, u_0/H = 1$ and $GH = 1$.

For the wavemaker, added mass and damping coefficient vary with respect to the dimensionless angular frequency KH for different porous-effect parameters (Figure 7.8). Added mass and damping coefficient increase sharply with the increase of oscillation amplitude. After $KH \approx 0.5$, an increase of oscillation frequency smoothly lowers added mass. Similar characteristics can be observed for the damping coefficient after $KH \approx 1.5$. A rigid wavemaker yields the highest wave elevation for both cases. Usually, we observe that a rigid wavemaker produces the highest pressure distribution. Therefore, it will give higher wave thrust which will result in higher amplitude for radiated potentials. However, comparing the real and complex porous-effect parameters of the barrier, the complex parameter produces higher added mass. This is due to the increasing inertial effect of the barrier. For damping coefficient, increasing porosity decreases the oscillation which is similar to what is observed in Figure 7.7.

TH-2746_176123008

7.6.1 Validation

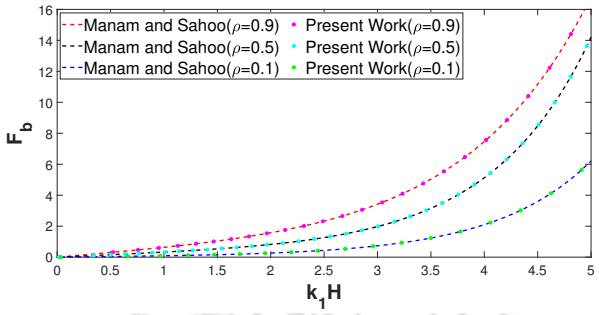

Figure 7.9: Non-dimensional wavload F_b corresponding to k_1H for various density ratio ρ.

We validate our current radiation problem by comparing it with a previous effort. The simplest way to establish the validation is to consider our result when the porosity of the sea-bed is removed from the formulation. When the value of G is set to 0, the otherwise porous bottom arrangement is transformed to a rigid one, and furthermore, consideration of $a = H$ allows the current model to be transformed to that of Manam and Sahoo [65]. Furthermore, Manam and Sahoo [65] has defined the effective waveload on a wavemaker as follows

$$\mathrm{F_b} = \frac{K^2}{u_0}\left|\int_{-a}^{-h}\left[\phi_2^R(0,z)-\phi_1^R(0,z)\right]\mathrm{d}z+\rho\int_{-h}^{0}\left[\phi_2^R(0,z)-\phi_1^R(0,z)\right]\mathrm{d}z\right|. \tag{7.41}$$

In this context, the following parameter values are also taken into account: $N = 0$, $u_0 = 1$, $h/H = 0.5$, $a/H = 1$, $\theta = 60°$, $G_1 = 1 + 0.5\mathrm{i}$. The plots of the non-dimensional waveload (F_b) vs k_1H for various density ratio (ρ) are shown in Figure 7.9, and a comparison of these two studies reveals a high level of agreement between them. This implies that the present model is substantially accurate and may be used to solve a wide range of ocean infrastructure problems.

7.7 Conclusion

The present work takes up a study of oblique water wave interaction by a porous barrier in a two-layer fluid flowing over a porous sea bottom. By employing linear water wave theory and eigenfunction expansion, the solution of the corresponding scattering problem is found. The fluid region is split into a number of sub-regions, and the utilization of the given equations and matching conditions gives a system of linear algebraic equations which is solved to obtain and analyze some important results which are summarized below:

TH-2746_176123008

- It is observed that, while energy undergoes a transformation, the porous effect of the sea-bed appears as embedded in the velocity potentials whereas the porous-effect parameter explicitly contributes in the energy transformation.

- By selecting suitable structural porous-effect parameters, it is possible to obtain (i) the maximum wave reflection by the structure, (ii) the maximum dissipation of energy by the porous structure, and (iii) the minimum value of the waveload on the wall. Moreover, it can be observed that a highly porous body results in lower wave elevation for both propagating modes. It is clear that a porous structure possesses more efficiency in producing higher dissipation and lower elevation as compared to a similar rigid one. Movement of low pressure area can be observed for different porosities of the structure.

- By observing the non-dimensional wave elevations, it is found that constructive and destructive interference occur in seaward and leeward region, respectively. However, most of the reflecting waves in the leeside undergo a destructive interference, resulting in the serene environment in surface flow in Region 2.

- From energy dissipation results for various porous-effect parameters, the following observations may be noted: (i) the reflective property of the breakwater produces higher reflection as well as transmission in both propagating modes, (ii) suitable porosity of the structure is to be followed so that wave energy dissipation can be the controlled.

- The current research is expected to add to our knowledge of the mechanism of a wavemaker in motion. The analysis of radiated potential amplitude establishes that the radiated potential in free surface mode contains higher wave flow of energy with increasing frequency. It also shows that the impact of the porous barrier produces lower radiated outgoing waves in both propagating modes.

- The analysis of added mass and damping coefficient establishes that the porosity of the barrier plays a crucial role in energy dissipation. Complex porous-effect parameter of the wavemaker may give rise to higher added mass. Higher frequency of the wavemaker results in a smooth nature for both of the characteristics.

In a nutshell, the study of water wave interaction with porous structures makes it possible to clearly apprehend the effect of those structures that help in creating a tranquillity zone for appropriate protection of the coastal facilities. The realistic scenario can be envisaged when both reflection and radiation are considered.

TH-2746_176123008

TH-2746_176123008

CHAPTER 8

Impact of porous breakwaters in mitigating wave forces acting on a floating dock in a two-layer fluid

8.1 Mathematical formulation

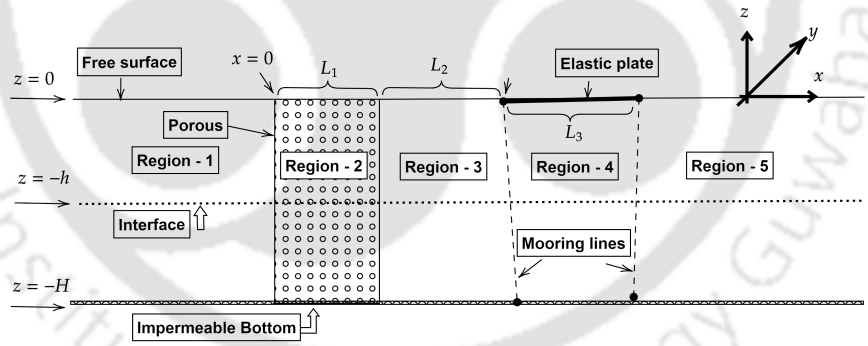

Figure 8.1: Definition sketch of wave scattering by a porous breakwater in front of a finite dock.

In a two-layer fluid, a porous breakwater is considered in front of a finite dock which is modelled in the form of a thin floating elastic plate. The oblique surface wave interaction with the structure is discussed by using linear water wave theory and small amplitude motion at finite ocean water depth. For the thin elastic plate, Euler-Bernoulli beam theory is used. The fluid is considered to be inviscid and incompressible consisting of two layers under gravity, and the motion is supposed to be irrotational and simple harmonic. The interface of the layers is represented as $z = -h$, with the z-axis pointing upwards, using a

TH-2746_176123008

right-handed coordinate system. Furthermore, the top fluid layer of density ρ_1 has a mean elastic plate surface/free surface/porous free surface at $z = 0$, but the lower fluid layer of density ρ_2 is confined in the region $-\infty < x < \infty$, $-H < z < -h$ with the bottom considered as impermeable. A porous region is considered for $(x, z) \in [0, L_1] \times [-H, 0]$. We analyse an obliquely incident wave with an inclination θ to the x-axis. Following that, velocity potentials Φ_j, $j = 1, 2, \ldots, 5$, which designate the velocity potentials in Regions 1, 2, ..., 5, may be expressed as $\Phi_j(x, y, z, t) = \mathrm{Re}[\phi_j(x, z)e^{\mathrm{i}(k_y y - \omega t)}]$. In Figure 8.1, the geometry of the problem is presented. In order to match all Φ_j along the vertical boundaries according to Snell's Law, the variation of each potential Φ_j $(j = 1, 2, \ldots, 5)$ in the y-direction is deemed to be the same.

$\phi_j(x, z)$ are separated in the following way so that the geometry of the problem may be comprehended layer by layer:

$$\phi_j = \begin{cases} \psi_j^{(1)}, & -h < z < 0, \\ \psi_j^{(2)}, & -H < z < -h, \end{cases} \quad \text{for } j = 1, 2, \ldots, 5, \tag{8.1}$$

where the upper and lower layers are denoted by the superscripts $^{(1)}$ and $^{(2)}$, respectively.

The boundary value problems for ϕ_j, $j = 1, 2, \ldots, 5$ are found to fulfill the modified Helmholtz equation as follows:

$$(\nabla_{x,z}^2 - {k_y}^2)\phi_j = 0. \tag{8.2}$$

Equation (8.2) is written as follows with the aid of equation (8.1):

$$\left.\begin{aligned} (\nabla_{x,z}^2 - {k_y}^2)\psi_j^{(1)} &= 0, \quad -h < z < 0, \\ (\nabla_{x,z}^2 - {k_y}^2)\psi_j^{(2)} &= 0, \quad -H < z < -h, \end{aligned}\right\} \text{ for } j = 1, 2, \ldots, 5. \tag{8.3}$$

The free surface condition for the plain water region yields

$$\frac{\partial \psi_j^{(1)}}{\partial z} = K\psi_j^{(1)}, \text{ for } j = 1, 3, 5, \tag{8.4}$$

where $K = \dfrac{\omega^2}{g}$.

The free surface condition for porous region gives

$$\frac{\partial \psi_2^{(1)}}{\partial z} = K\gamma\psi_2^{(1)}, \tag{8.5}$$

where γ is the porous impedance parameter of the porous structure as $\gamma = m + \mathrm{i}f$. For a full derivation and information regarding this porous impedance parameter and their relationship, one can refer to Appendix A.

TH-2746_176123008

We consider the deflection of the plate as $\tilde{\eta}(x,y,t) = \mathrm{Re}\left(\eta(x)e^{-\mathrm{i}(k_y y-\omega t)}\right)$. The dynamic pressure on the floating plate is given by

$$\left\{\hat{E}I\left(\frac{\partial^2}{\partial x^2}+\frac{\partial^2}{\partial y^2}\right)^2+\rho_p\hbar\frac{\partial^2}{\partial t^2}\right\}\tilde{\eta}=P_s \text{ on } z=0, \tag{8.6}$$

where $\hat{E}I$ is the flexural rigidity of the elastic plate with $\hat{E}$ as the Young's modulus, $I=\hbar^3/(12(1-\nu))$, ν as the Poisson's ratio, $\hbar$ as the thickness and ρ_p, as the density of the elastic plate.

The hydrodynamic pressure on the elastic plate at $z=0$ is given by

$$P_H=-\rho_1\left(\frac{\partial\Phi_2}{\partial t}+g\tilde{\eta}\right). \tag{8.7}$$

The hydrodynamic pressure P_H in equation (8.7) is equated to P_s in equation (8.6) for the upper layer having the elastic plate above it so that $P_s=P_H$ gives us

$$\left\{\hat{E}I\left(\frac{\partial^2}{\partial x^2}-k_y^2\right)^2-\rho_p\hbar\omega^2+\rho_1 g\right\}\tilde{\eta}=\mathrm{i}\omega\rho_1\Phi_4. \tag{8.8}$$

On the elastic plate, the kinematic boundary condition is given by

$$\frac{\partial\Phi_4}{\partial z}=\frac{\partial\tilde{\eta}}{\partial t}. \tag{8.9}$$

On the mean elastic plate position, we derive the linearized boundary condition as follows:

$$\left\{\hat{E}I\left(\frac{\partial^2}{\partial x^2}-k_y^2\right)^2-\rho_p\hbar\omega^2+\rho_1 g\right\}\frac{\partial\phi_4}{\partial z}=\omega^2\rho_1\phi_4. \tag{8.10}$$

Additionally, the following may be written explicitly as

$$\left\{E\left(\frac{\partial^2}{\partial x^2}-k_y^2\right)^2-\delta K+1\right\}\frac{\partial\psi_4^{(1)}}{\partial z}=K\psi_4^{(1)}, \tag{8.11}$$

where $E=\hat{E}I/\rho_1 g$ and $\delta=\rho_p\hbar/\rho_1$.

The impermeable bottom condition yields

$$\frac{\partial\psi_j^{(2)}}{\partial z}=0, \quad \text{for } j=1,2,\ldots,5. \tag{8.12}$$

Let us denote by $\rho=\rho_1/\rho_2<1$ the ratio of the density of respective fluid layers. Following

TH-2746_176123008

that, at $z = -h$, the linearized conditions have the following forms:

$$\left.\begin{aligned} \frac{\partial \psi_j^{(1)}}{\partial z} &= \frac{\partial \psi_j^{(2)}}{\partial z}, \\ \rho\left(\frac{\partial \psi_j^{(1)}}{\partial z} - K\psi_j^{(1)}\right) &= \left(\frac{\partial \psi_j^{(2)}}{\partial z} - K\psi_j^{(2)}\right), \end{aligned}\right\} \quad \text{for } j = 1, 3, 4, 5. \tag{8.13}$$

Due to the interface-piercing porous structure, the linearized conditions at $z = -h$ for Region 2 take the following forms:

$$\begin{aligned} \frac{\partial \psi_2^{(1)}}{\partial z} &= \frac{\partial \psi_2^{(2)}}{\partial z}, \\ \rho\left(\frac{\partial \psi_2^{(1)}}{\partial z} - K\gamma\psi_2^{(1)}\right) &= \left(\frac{\partial \psi_2^{(2)}}{\partial z} - K\gamma\psi_2^{(2)}\right). \end{aligned} \tag{8.14}$$

The matching conditions across the vertical boundaries $x = 0, L_j$ for $j = 1, 2, 3$ are then obtained by merging the potentials $\psi_j^{(1)}$ and $\psi_j^{(2)}$ into ϕ_j as stated in equation (8.1):

$$\phi_1 = \gamma\phi_2, \ \frac{\partial \phi_1}{\partial x} = \epsilon\frac{\partial \phi_2}{\partial x} \quad \text{at} \quad x = 0, \tag{8.15}$$

$$\gamma\phi_2 = \phi_3, \ \epsilon\frac{\partial \phi_2}{\partial x} = \frac{\partial \phi_3}{\partial x} \quad \text{at} \quad x = L_1, \tag{8.16}$$

$$\phi_j = \phi_{j+1}, \ \frac{\partial \phi_j}{\partial x} = \frac{\partial \phi_{j+1}}{\partial x} \quad \text{at} \quad x = \sum_{n=1}^{j-1} L_n, \ \text{ for } \ j = 3, 4, \tag{8.17}$$

where ϵ is the porosity of the porous region.

At $(x, z) = (L_1 + L_2, 0), (L_1 + L_2 + L_3, 0)$, the moored edge conditions are taken into account. This means that there is no bending moment, and the horizontal components of the dynamic mooring line tensions connect the restoring forces resulting from this load to the shearing forces, which are expressed as

$$\left(\frac{\partial^2}{\partial x^2} - \nu k_y^2\right)\frac{\partial \psi_4^{(1)}}{\partial z} = 0, \tag{8.18}$$

$$\left\{E\left(\frac{\partial^3}{\partial x^3} - (2-\nu)k_y^2\frac{\partial}{\partial x}\right) - E_d\right\}\frac{\partial \psi_4^{(1)}}{\partial z} = 0, \tag{8.19}$$

where $E_d = \dfrac{2S_{moor}}{\rho_1 g}\sin^2(\Theta)$ is the stiffness of the mooring line and Θ is the static mooring line angle at the static position. It could be observed that, when $\Theta = 0$, equation (8.19) along with equation (8.18) gives the free edge condition where the bending moment as well as the shear force both will be 0.

TH-2746_176123008

8.2 Plane wave approximation

The velocity potentials $\psi_j^{(1)}$ and $\psi_j^{(2)}$, $j = 1, 2, \ldots, 5$ satisfying the governing equations (8.3), subject to the respective boundary conditions equations (8.4) to (8.12), and the continuity of velocity conditions between the layers, i.e., the first equation of equations (8.13) and (8.14), have the following forms:

$$\phi_j = \begin{cases} \psi_j^{(j)} = \exp(\pm \mathrm{i}xq) I^{(1)}(k, z), \\ \psi_j^{(j)} = \exp(\pm \mathrm{i}xq) I^{(2)}(k, z), \end{cases} \quad \text{for } j = 1, 3, 5, \tag{8.20}$$

$$\phi_2 = \begin{cases} \psi_2^{(1)} = \exp(\pm \mathrm{i}x\hat{q}) \hat{I}^{(1)}(\hat{k}, z), \\ \psi_2^{(2)} = \exp(\pm \mathrm{i}x\hat{q}) \hat{I}^{(2)}(\hat{k}, z), \end{cases} \tag{8.21}$$

$$\phi_4 = \begin{cases} \psi_4^{(1)} = \exp(\pm \mathrm{i}x\tilde{q}) \tilde{I}^{(1)}(\tilde{k}, z), \\ \psi_4^{(2)} = \exp(\pm \mathrm{i}x\tilde{q}) \tilde{I}^{(2)}(\tilde{k}, z), \end{cases} \tag{8.22}$$

with $q = \sqrt{k^2 - {k_y}^2}$, $\hat{q} = \sqrt{\hat{k}^2 - {k_y}^2}$ and $\tilde{q} = \sqrt{\tilde{k}^2 - {k_y}^2}$. The eigenfunctions are given by

$$I(k, z) = \begin{cases} I^{(1)} = \dfrac{\sinh k(H-h)(K \sinh kz + k \cosh kz)}{(K \cosh kh - k \sinh kh)}, \\ I^{(2)} = \cosh k(z + H), \end{cases} \tag{8.23}$$

$$\hat{I}(\hat{k}, z) = \begin{cases} \hat{I}^{(1)} = \dfrac{\sinh \hat{k}(H-h)(K\gamma \sinh \hat{k}z + \hat{k} \cosh \hat{k}z)}{(K\gamma \cosh \hat{k}h - \hat{k} \sinh \hat{k}h)}, \\ \hat{I}^{(2)} = \cosh \hat{k}(z + H), \end{cases} \tag{8.24}$$

$$\tilde{I}(\tilde{k}, z) = \begin{cases} \tilde{I}^{(1)} = \dfrac{\sinh \tilde{k}(H-h)(K \sinh \tilde{k}z + \tilde{k}F(\tilde{k}) \cosh \tilde{k}z)}{(K \cosh \tilde{k}h - \tilde{k}F(\tilde{k}) \sinh \tilde{k}h)}, \\ \tilde{I}^{(2)} = \cosh \tilde{k}(z + H), \end{cases} \tag{8.25}$$

where $F(\tilde{k}) = (E\tilde{k}^4 + 1 - \delta K)$.

Using the second relation of equations (8.13) and (8.14), we can figure out the dispersion relations as follows:

$$K^2 (\rho + \coth kh \coth k(H-h)) + k^2(1-\rho) - kK (\coth kh + \coth k(H-h)) = 0, \tag{8.26}$$

$$K^2\gamma^2 \left(\rho + \coth \hat{k}h \coth \hat{k}(H-h)\right) + \hat{k}^2(1-\rho) - \hat{k}\gamma K \left(\coth \hat{k}h + \coth \hat{k}(H-h)\right) = 0, \tag{8.27}$$

$$K^2 \left(\rho + \coth \tilde{k}h \coth \tilde{k}(H-h)\right) + F(\tilde{k})\tilde{k}^2(1-\rho) - \tilde{k}K \left((1 - \rho(1 - F(\tilde{k}))) \coth \tilde{k}h + F(\tilde{k}) \coth \tilde{k}(H-h)\right) = 0. \tag{8.28}$$

TH-2746_176123008

8.2.1 Discussion on the roots of the dispersion relations

The dispersion relation for a homogeneous fluid with a comparable geometrical arrangement is given by the examples $\rho \to 1$ and $h \to 0$ in equations (8.26) to (8.28). The dispersion relation equation (8.26) has two symmetric real roots, say $\pm k_1$ and $\pm k_2$, and an infinite number of fully symmetric imaginary roots, provided by $\pm k_n = \mathrm{i}p_n$ for $n = 3, 4, 5, \ldots$, where p_n is real. Positive real roots, such as k_1 and k_2, where $0 < k_1 < k_2$, correspond to propagating modes and the purely imaginary roots to evanescent modes, respectively. The occurrence of precisely two positive zeros suggests that there are two wave modes (wavenumbers) propagating along the positive x-direction at the free surface (say, SM) and at the interface (say, IM). Because of the symmetry around $x = 0$, studying the wave properties corresponding to $x \geq 0$ is adequate. Waves propagating in the negative direction are represented by the negative values of real and totally imaginary roots.

For real γ, equation (8.27) results in two symmetric real roots, say, $\pm\hat{k}_1$ and $\pm\hat{k}_2$ which correspond to the propagating modes and an infinite number of purely imaginary roots given by $\pm\hat{k}_n = \mathrm{i}\hat{t}_n$ for $n = 3, 4, 5, \ldots$ which correspond to the evanescent modes. However, equation (8.27) gives rise to complex roots due to consideration of complex γ. Now, using the procedure of Mendez and Losada [68], the complex roots corresponding to complex γ can be obtained. The roots for real γ are used as initial guesses, and as γ turns into complex, the roots also get converted into complex ones.

For a given K, equation (8.28) yields two symmetric real roots, say $\pm\tilde{k}_1$ and $\pm\tilde{k}_2$; a pair of complex conjugate roots $\pm\tilde{k}_I = \pm a + \mathrm{i}b$, $\pm\tilde{k}_{II} = \pm a - \mathrm{i}b$; and an infinite number of purely imaginary roots $\pm\tilde{k}_n$. Positive real roots, such as $\tilde{k}_1$ and $\tilde{k}_2$, where $0 < \tilde{k}_1 < \tilde{k}_2$, correspond to propagating modes (wavenumbers) propagating along the positive x-direction at the elastic plate surface or flexural mode (say, FM) and at the interface (say, IM).

All the dispersion relations above can be written in the form

$$A\omega^4 - B\omega^2 + C = 0. \tag{8.29}$$

The solution of (8.29) yields two propagating modes as follows:

$$\omega_{_1} = \pm\sqrt{\left(\frac{B + \sqrt{B^2 - 4AC}}{2A}\right)}, \quad \omega_{_2} = \pm\sqrt{\left(\frac{B - \sqrt{B^2 - 4AC}}{2A}\right)}, \tag{8.30}$$

where subscripts 1 and 2 refer to the propagating mode corresponding to the free surface/plate and interface, respectively.

Further, the phase and group velocities, respectively, in plane water region can be

TH-2746_176123008

found from

$$c_{_1} = \frac{\omega_{_1}}{k} \text{ and } c_{_2} = \frac{\omega_{_2}}{k}, \tag{8.31}$$

$$c_{g_{_1}} = \frac{\partial \omega_{_1}}{\partial k} \text{ and } c_{g_{_2}} = \frac{\partial \omega_{_2}}{\partial k}. \tag{8.32}$$

For equations (8.26) and (8.28), a detailed discussion is already available in literature. Therefore, our main attention lies in the dispersion relation in the porous region. For equation (8.27), we have

$$A = \gamma^2 \left(\rho + \coth \hat{k}h \coth \hat{k}(H-h)\right), \tag{8.33}$$

$$B = g\hat{k}\gamma \left(\coth \hat{k}h + \coth \hat{k}(H-h)\right), \tag{8.34}$$

$$C = g^2\hat{k}^2(1-\rho). \tag{8.35}$$

Moreover, the wavenumber $\hat{k}$ is a real quantity which is also known as the wave propagation vector owing to its directional properties. Assume ω and $\hat{k}$ as real and complex numbers, respectively, as long as total energy is preserved throughout the wave-material interaction. There are, however, certain instances when the reverse convention of ω as a complex number and $\hat{k}$ as a real number has been used (see, e.g., dissipation of thermoelastic waves in solids [3]). In this work, we assume that the wave propagation vector $\hat{k}$ is complex, and that

$$\hat{k} = \hat{k}_r + \mathrm{i}\hat{k}_i, \ \hat{k}_r \geq 0 \text{ and } \hat{k}_i \geq 0, \tag{8.36}$$

where $\hat{k}_r$ is the wave velocity vector and $\hat{k}_i$ is the wave attenuation vector. Substituting equation (8.36) in equation (8.30), frequency ω can be obtained with the phase and group velocities given by the real part of $\hat{k}$ as

$$c = c_r = \frac{\omega}{\hat{k}_r} \text{ and } c_g = c_{g_r} = \frac{\mathrm{d}\omega}{\mathrm{d}\hat{\mathrm{k}}_{\mathrm{r}}}. \tag{8.37}$$

Attenuation

Due to the involvement of complex numbers in the coefficients in equation (8.36), the solutions of equation (8.30) will also be complex-valued. Let us denote the attenuations by the symbol τ. The attenuation coefficients are given by

$$\tau = \left| \frac{\omega}{\mathrm{Im}(c_i)} \right|, \tag{8.38}$$

where $Im(c_i) = \dfrac{\omega}{\hat{k}_i}$.

TH-2746_176123008

For deep water waves for both layers of the fluid, $\mathrm{Re}(\hat{k}h),\ \mathrm{Im}(\hat{k}h) \gg 1$ and $\mathrm{Re}(\hat{k}(H-h))\mathrm{Re}(\hat{k}(H-h)) \gg 1$ are valid which yield

$$A = \gamma^2\left(\rho+1\right),\ B = 2g\hat{k}\gamma \text{ and } C = g^2\hat{k}^2(1-\rho). \tag{8.39}$$

ω^2 values are as follows:

$$\omega = \sqrt{\frac{gk}{\gamma}} \text{ and } \sqrt{\frac{gk}{\gamma}\frac{(1-\rho)}{(1+\rho)}}. \tag{8.40}$$

In a similar manner, for shallow water waves, i.e., for $\mathrm{Re}(\hat{k}h),\ \mathrm{Im}(\hat{k}h) \ll 1$ and $\mathrm{Re}(\hat{k}(H-h))\mathrm{Re}(\hat{k}(H-h)) \ll 1$, equation (8.33) yields

$$A = \gamma^2\left(\rho+\frac{1}{\hat{k}^2h(H-h)}\right),\ \ B = g\gamma\frac{H}{h(H-h)} \text{ and } C = g^2\hat{k}^2(1-\rho),$$

which can be used to find ω^2 as well as phase and group velocity.

8.3 Method of solution

The velocity potentials $\phi_j(x,z)$ for each subdomain $j = 1,2,\ldots,5$ may be represented, by using the eigenfunction expansion approach, as follows:

$$\phi_1 = \sum_{n=1}^{2} e^{\mathrm{i}q_n x}I_n(k_n,z) + \sum_{n=1}^{\infty} R_n e^{-\mathrm{i}q_n x}I_n(k_n,z), \tag{8.41}$$

$$\phi_2 = \sum_{n=1}^{\infty}(A_n e^{\mathrm{i}\hat{q}_n x} + B_n e^{-\mathrm{i}\hat{q}_n(x-L_1)})\hat{I}_n(\hat{k}_n,z), \tag{8.42}$$

$$\phi_3 = \sum_{n=1}^{\infty}(C_n e^{\mathrm{i}q_n(x-L_1)} + D_n e^{-\mathrm{i}q_n(x-L_1-L_2)})I_n(k_n,z), \tag{8.43}$$

$$\phi_4 = \sum_{n=I,II,1}^{\infty}(E_n e^{\mathrm{i}\tilde{q}_n(x-L_1-L_2)} + F_n e^{-\mathrm{i}\tilde{q}_n(x-L_1-L_2-L_3)})\tilde{I}_n(\tilde{k}_n,z), \tag{8.44}$$

$$\phi_5 = \sum_{n=1}^{\infty} T_n e^{\mathrm{i}q_n(x-L_1-L_2-L_3)}I_n(k_n,z), \tag{8.45}$$

where R_n and T_n, $n = 1,2,\ldots$ are, respectively, the reflection and transmission coefficients.

Now, using the matching conditions (equations (8.15) to (8.17)) by considering N

TH-2746_176123008

evanescent modes and using the orthogonality of I_n, we get the following:

$$R_m W_m - \gamma \sum_{n=1}^{N+2} (A_n + B_n e^{\mathrm{i}\hat{q}_n L_1}) \hat{W}_{n,m} = -\sum_{j=1}^{2} \delta_{j,m} W_m, \tag{8.46}$$

$$R_m q_m W_m + \epsilon \sum_{n=1}^{N+2} (A_n - B_n e^{\mathrm{i}\hat{q}_n L_1}) \hat{q}_n \hat{W}_{n,m} = \sum_{j=1}^{2} \delta_{j,m} q_m W_m, \tag{8.47}$$

$$\gamma \sum_{n=1}^{N+2} (A_n e^{\mathrm{i}\hat{q}_n L_1} + B_n) \hat{W}_{n,m} - (C_m + D_m e^{\mathrm{i}q_m L_2}) W_m = 0, \tag{8.48}$$

$$\epsilon \sum_{n=1}^{N+2} (A_n e^{\mathrm{i}\hat{q}_n L_1} - B_n) \hat{q}_n \hat{W}_{n,m} - (C_m - D_m e^{\mathrm{i}q_m L_2}) q_m W_m = 0, \tag{8.49}$$

$$(C_m e^{\mathrm{i}q_m L_2} + D_m) W_m - \sum_{n=I,II,1}^{N+2} (E_n + F_n e^{\mathrm{i}\tilde{q}_n L_3}) \tilde{W}_{n,m} = 0, \tag{8.50}$$

$$(C_m e^{\mathrm{i}q_m L_2} - D_m) q_m W_m - \sum_{n=I,II,1}^{N+2} (E_n - F_n e^{\mathrm{i}\tilde{q}_n L_3}) \tilde{q}_n \tilde{W}_{n,m} = 0, \tag{8.51}$$

$$\sum_{n=I,II,1}^{N+2} (E_n e^{\mathrm{i}\tilde{q}_n L_3} + F_n) \tilde{W}_{n,m} - T_m W_m = 0, \tag{8.52}$$

$$\sum_{n=I,II,1}^{N+2} (E_n e^{\mathrm{i}\tilde{q}_n L_3} - F_n) \tilde{q}_n \tilde{W}_{n,m} - T_m q_m W_m = 0, \tag{8.53}$$

where

$$W_m = \int_{-H}^{-h} I_m^2 \mathrm{d}z + \rho \int_{-h}^{0} I_m^2 \mathrm{d}z,\ \hat{W}_{m,n} = \int_{-H}^{-h} I_m \hat{I}_n \mathrm{d}z + \rho \int_{-h}^{0} I_m \hat{I}_n \mathrm{d}z,$$

$$\tilde{W}_{m,n} = \int_{-H}^{-h} I_m \tilde{I}_n \mathrm{d}z + \rho \int_{-h}^{0} I_m \tilde{I}_n \mathrm{d}z,\ \text{and}\ \delta_{m,n} = \begin{cases} 1, \text{ for } m = n, \\ 0, \text{ when } m \neq n. \end{cases}$$

Now, equations (8.46) to (8.53) will yield a system of $(8N + 16)$ equations of $(8N + 20)$ unknowns as follows:

$$X = [R_1 \dots R_{N+2} A_1 \dots A_{N+2} B_1 \dots B_{N+2} C_1 \dots C_{N+2} D_1 \dots D_{N+2} E_I \dots E_{N+2} F_I \dots F_{N+2} \\ T_1 \dots T_{N+2}]^T.$$

Now, using the edge conditions as defined by (8.18) and (8.19) gives $(8N+20) \times (8N+20)$ equations yielding a linear system of equations

$$\mathbb{A}X = \mathbb{B}. \tag{8.54}$$

TH-2746_176123008

Determination of X permits us to discuss the whole reflection and transmission phenomena via the elastic plate and the porous structure. Reflection coefficients R_n $(n = 1, 2)$ are represented by the expressions $R_{SM} = |R_1|,\ R_{IM} = |R_2|$.

The elevations of the free surface and the interface are given by the formulas

$$\zeta_1 = \frac{\mathrm{i}}{\omega}\frac{\partial \phi_j(x,z)}{\partial z} \text{ at } z = 0, \tag{8.55}$$

$$\zeta_2 = \frac{\mathrm{i}}{\omega}\frac{\partial \phi_j(x,z)}{\partial z} \text{ at } z = -h, \tag{8.56}$$

which hold for the open water regions and porous region.
The deflection of the elastic plate is given by the formula

$$\eta = \frac{\mathrm{i}}{\omega}\frac{\partial \phi_4(x,z)}{\partial z} \text{ at } z = 0. \tag{8.57}$$

The non-dimensional bending moment B_M and shear force S_F on the elastic plate are obtained by using the formulas

$$B_M = \frac{H}{\omega}\left|\left(\frac{\partial^2}{\partial x^2} - \nu {k_y}^2\right)\frac{\partial \phi_4(x,z)}{\partial z}\right| \text{ at } z = 0, \tag{8.58}$$

$$S_F = \frac{H^2}{\omega}\left|\left(\frac{\partial^3}{\partial x^3} - (2-\nu){k_y}^2\frac{\partial}{\partial x}\right)\frac{\partial \phi_4(x,z)}{\partial z}\right| \text{ at } z = 0. \tag{8.59}$$

The local non-dimensional magnitude of the unit horizontal wave forces $\mathbb{F}_b$ acting on the elastic plate may be calculated by using the following formula:

$$\mathbb{F}_b = \frac{\omega}{ghH}\left|\int_{-H}^{-h}\phi_3(L_1+L_2,z)\mathrm{d}z + \rho\int_{-h}^{0}\phi_3(L_1+L_2,z)\mathrm{d}z\right|. \tag{8.60}$$

8.4 Results and discussion

By using program Matlab R2019a, we solve the system of equations given by (8.54). For computing purpose, fixed values of some parameters are considered as follows: $h/H = 0.5$; $\rho = 0.9$; $\theta = 60°$; $S_M = 1$; $\nu = 0.3$ and $\vartheta = 45°$.

8.4.1 Validation and convergence

We validate our current problem against two known results. The best way to establish the validation is to consider a present result when the elastic plate is altogether removed from the formulation. When the values of L_2 and L_3 are set to 0, the arrangement gets transformed to the porous structure interaction problem of Behera and Sahoo [8]. In this context, the following parameter values are also taken into account: $H = 5$ m, $h/H =$

TH-2746_176123008

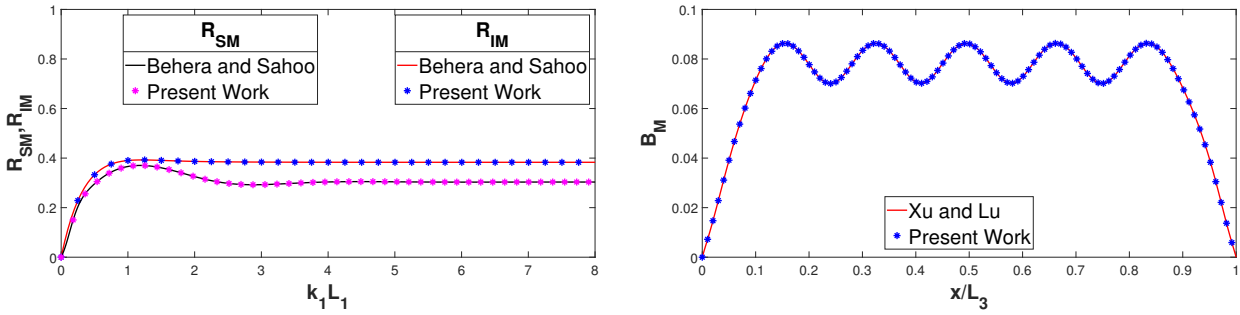

(a) R_{SM}, R_{IM} vs k_1L_1. (b) B_M vs x/L_3.

Figure 8.2: (a) Reflection coefficients against non-dimensional structure width k_1L_1 and (b) non-dimensional bending moment corresponding to non-dimensional plate length x/L_3.

0.5, $L_2 = L_3 = 0$, $\epsilon = 0.5$, $f = 1$, $\theta = 30°$, $T = 8$ s, $g = 9.81$ m/s^2. The plots of the reflection coefficients in both modes agianst k_1L_1 are shown in Figure 8.2(a), and a comparison of these two studies reveals a high level of agreement. Furthermore, removal of the porous structure from the model converts the present model to the one considered by Xu and Lu [114]. For this purpose, the following parameter values are also taken into account: $E/H^4 = 0.05, H = 5$ m, $h/H = 0.2$, $L_3/H = 6$, $\omega\sqrt{\frac{H}{g}} = 1.25$, $L_1 = L_2 = 0$, $\theta = 0°$, $g = 9.81$ m/s^2. Bending moment of the plate is plotted agianst x/L_3 as shown in Figure 8.2(b). The comparison of these two studies reveals a high level of agreement between them. This implies that the present model is substantially accurate and may be used to solve a wide range of ocean infrastructure problems.

	N	0	4	8	12	16	20	24
$KH = 0.31$	R_{SM}	0.436	0.293	0.283	0.281	0.28	0.28	0.28
	R_{IM}	0.174	0.234	0.236	0.237	0.238	0.238	0.238
$KH = 0.55$	R_{SM}	0.846	0.888	0.834	0.819	0.814	0.812	0.812
	R_{IM}	0.175	0.215	0.224	0.226	0.227	0.228	0.228

Table 8.1: Convergence study of R_{SM} for different Kh with $L/H = 2, \rho = 0.9$ and $E/H^4 = 0.1$.

Before proceeding with numerical experiments, it is deemed ideal to fix N, the number of evanescent modes. In comparison to the scenario when evanescent modes are not considered (i.e., $N = 0$), Table 8.1 clearly indicates that the evanescent modes have a significant contribution to the reflection coefficients. The finding's convergence is also confirmed as the values of two successive reflection coefficients are found to be almost the same as the number of evanescent modes grows. As a consequence, we estimate the number of evanescent modes to be $N = 20$ which can be considered as an ideal one for

TH-2746_176123008

our subsequent computation, as supported by Table 8.1, which clearly establishes the convergence of the results.

8.4.2 Numerical experiments

Effect of the porous structure width for varying friction and porosity

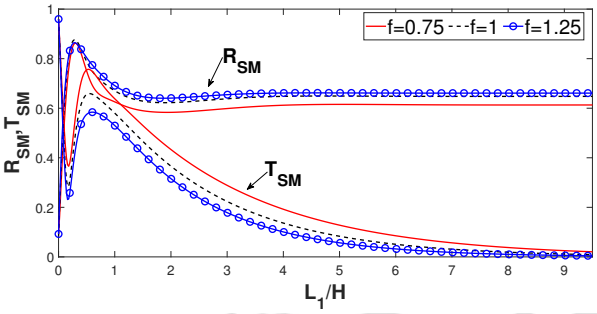

(a) R_{SM} vs L_1/H for various f

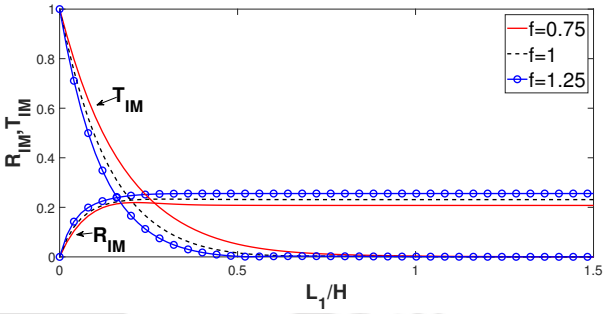

(b) R_{IM} vs L_1/H for various f

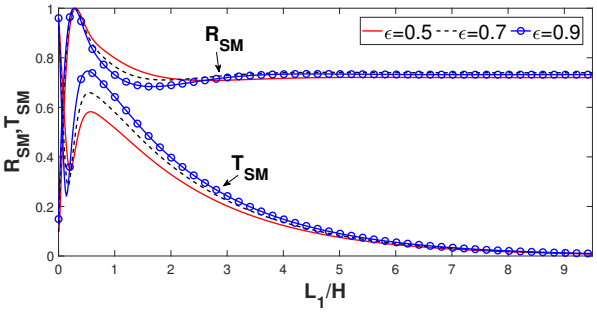

(c) R_{SM} vs L_1/H for various ϵ

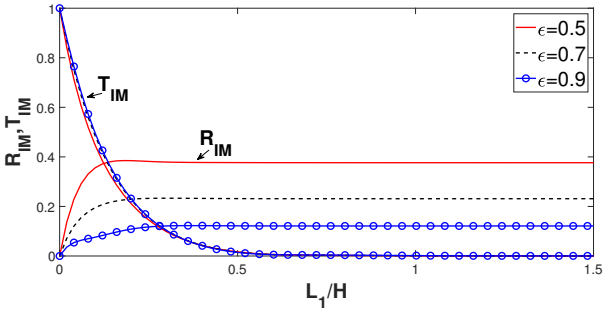

(d) R_{IM} vs L_1/H for various ϵ

Figure 8.3: Reflection coefficients R_{SM} and R_{IM} against non-dimensional structure width L_1/H: (a,b) corresponding to various values of f with $KH = 0.4$, $\epsilon = 0.7$ $L_2/H = 1$ and $L_3/H = 1/2$; (c,d) corresponding to various values of ϵ with $KH = 0.4$, $f = 1$, $L_2/H = 1$ and $L_3/H = 1/2$.

Figures 8.3(a) and 8.3(b) show how the reflection coefficients fluctuate as per the variation of the porous structure width for both propagating modes. Increasing nature of reflection in both propagating modes becomes more apparent as length L_1/H increases. However, for $L_1/H < 1$, free surface reflection attains maximum values. T_{SM} attains maximum value for zero structural width. For interfacial mode, non-existence of the structure gives the optimum results which clearly shows that there is a very less impact of the floating elastic plate in interfacial wave interaction. For both propagating modes, higher friction results in higher reflection and lower transmission. The reflection coefficients are plotted in Figures 8.3(c) and 8.3(d) for various porosity. Similar nature can be observed in both graphs when compared to Figures 8.3(a) and 8.3(b). In SM, a smooth increasing nature can be observed and they attain full reflection for $L_1/H \leq 1$. Hence, $L_1/H < 1$ can be

TH-2746_176123008

considered as the optimum breakwater width to achieve higher reflection. However, no major difference is observed in T_{IM} with respect to various porosity values. In both propagating modes, higher porosity values yield lower reflection and higher transmission which is due to the fact that the higher porosity values produce higher wave passage through the structure. In general, as L_1/H increases, R_{SM} attains a steady nature whereas T_{SM} tends to zero. It shows that, after the optimum width of the structure, major differences are not observed. From transmission perspective, for sufficiently large structures (here with regard to width) produce adequate wave reflection and dissipation which results in no transmission.

Effect of friction of the porous structure on wave elevation

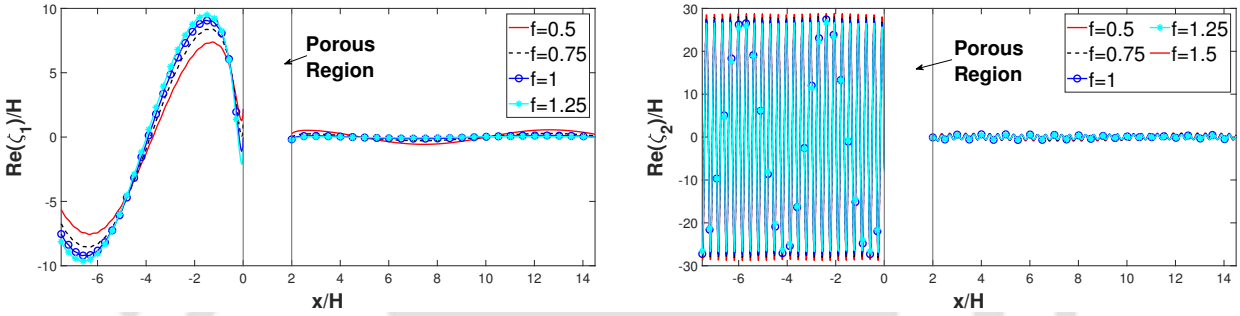

(a) $\mathrm{Re}(\zeta_1)/H$ vs x/H for various f (b) $\mathrm{Re}(\zeta_2)/H$ vs x/H for various f

Figure 8.4: Non-dimensional (a) $\mathrm{Re}(\zeta_1)$ and (b) $\mathrm{Re}(\zeta_2)$ against non-dimensional distance in the region 1 and 2 corresponding to various values of f with $\epsilon = 0.7$, $KH = 1$; $L_1/H = L_3/H = 1/2$ and $L_1/L_2 = 1/6$.

Figures 8.4(a) and 8.4(b) show the impact of the porous breakwater on wave elevation corresponding to different values of friction f. The presence of the breakwater helps to reduce the elevation considerably owing to a major wave dissipation. Periodic pattern can be observed for the elevation. However, the higher amplitude of interfacial elevation occurs due to dead water analogue which can be observed for $\rho = 0.9$. We can infer that the higher reflection due to higher friction value contributes to the major difference in heights of elevation (Figure 8.4(a)). However, no major differences can be observed in interfacial elevation for different friction values.

Effect of the plate length for various values of flexural rigidity

Figures 8.5(a) and 8.5(b) show reflection coefficients in both propagating modes for varying plate length. Increasing flexural rigidity results in higher values of reflection in SM. Higher flexural rigidity turns the plate to a rigid one, and it is known that a stiffer body yields higher reflection. For interfacial mode, no such variation can be observed for different rigidity which confirms the negligible impact of the floating elastic plate in interfacial

TH-2746_176123008

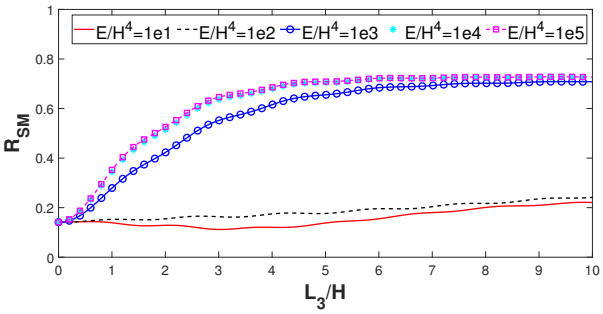

(a) R_{SM} vs L_3/H for various E/H^4

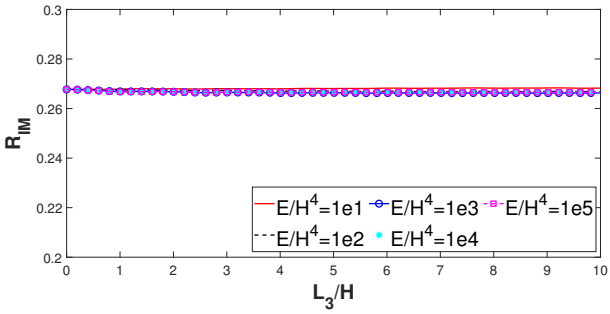

(b) R_{IM} vs L_3/H for various E/H^4

Figure 8.5: Reflection coefficients (a) R_{SM} and (b) R_{IM} against non-dimensional plate length L_3/H corresponding to various values of E/H^4 with $KH = 0.4$, $f = 1$, $\epsilon = 0.7$ $L_2/H = 1$ and $L_1/H = 1/2$.

wave interaction as observed in Figures 8.3(b) and 8.3(d). R_{SM} attains a steady state for higher plate length. It shows that, after the optimal length of the plate, no major differences can be observed in the wave plate interaction.

Effect of the flexural rigidity on deflection, bending moment and shear force of the plate

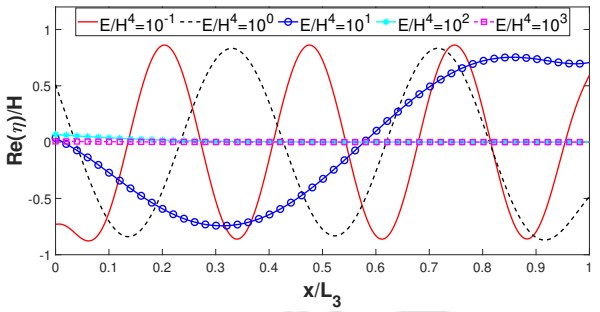

(a) Re(η/H) vs x/L_3 for various E/H^4

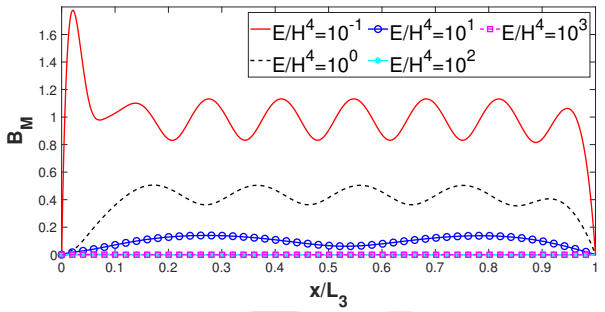

(b) B_M vs x/L_3 for various E/H^4

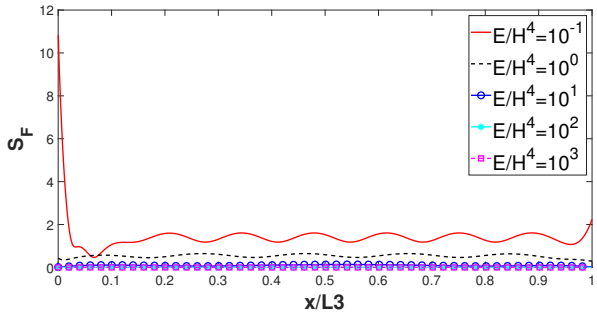

(c) S_F vs x/L_3 for various E/H^4

Figure 8.6: Non-dimensional (a) Re$(\eta)/H$, (b) B_M and (c) S_F against non-dimensional plate length L_3/H corresponding to various flexural rigidity E/H^4 with $KH = 1$, $\epsilon = 0.7$, $f = 1$, $L_1/H = L_3/H = 1/2$ and $L_2/H = 5$.

TH-2746_176123008

Figure 8.6 shows the impact of flexural rigidity on plate deflection, bending moment and shear force. Periodic nature of plate deflection can be observed. $\mathrm{Re}(\eta)/H$ decreases as E/H^4 increases and for $E/H^4 = 10^2, 10^3$, negligible plate deflection can be observed. Higher flexural rigidity results in a stiffer plate which is hard to bend. Figure 8.6(b) demonstrates that B_M attains the similar nature of higher values for lower rigidity. Zero B_M in the edges justifies our edge condition. In Figure 8.6(c), shear force attains the same nature. The linear relationship between deflection, bending moment and shear force can be easily inferred from the graphs. However, higher impact of mooring edge can be observed for less flexural rigid plates.

Effect of the mooring stiffness on reflection and deflection

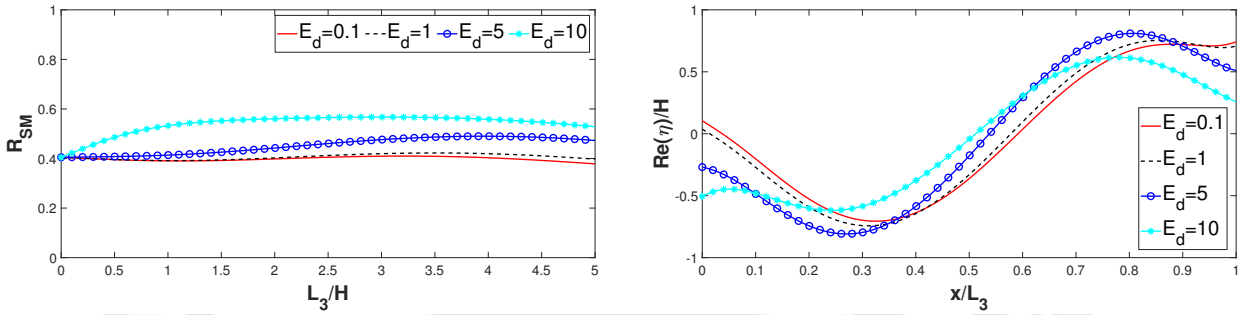

(a) R_{SM} vs L_3/H for various E_d (b) $\mathrm{Re}(\eta)/H$ vs x/L_3 for various E_d

Figure 8.7: Reflection coefficient (a) R_{SM} and non-dimensional (b) $\mathrm{Re}(\eta)/H$, against non-dimensional plate length L_3/H corresponding to various flexural rigidity E/H^4 with $KH = 0.4,\ \epsilon = 0.7,\ f = 1,\ L_1/H = 1/2$ and $L_2/H = 5$.

The effect of the mooring stiffness on free surface reflection R_{SM} and deflection $\mathrm{Re}(\eta)/H$ are examined in Figures 8.7(a) and 8.7(b). Stiffer moored edge produces higher reflection and less deflection, in general. This clearly shows that the plate reflection and deflection depends upon overall stiffness of the mooring line which controls the edges yielding the optimized plate deflection.

Effect of the breakwater width and confined region extent on waveload

The effect of the structure width (L_1) and confined region spacing (L_2) on waveload is examined in Figures 8.8(a) and 8.8(b) for various values of structural friction. Less waveload is noticed when the friction is raised, which is due to the increased energy dissipation. However, this also results in lower transmission as observed in Figure 8.3. As the structure width increases, the energy dissipation increases which shows a decreasing nature of waveload. In Figure 8.8(b), waveload shows an undulating pattern with respect to the confined Region 3 spacing. However, increasing friction diminishes the undulating

TH-2746_176123008

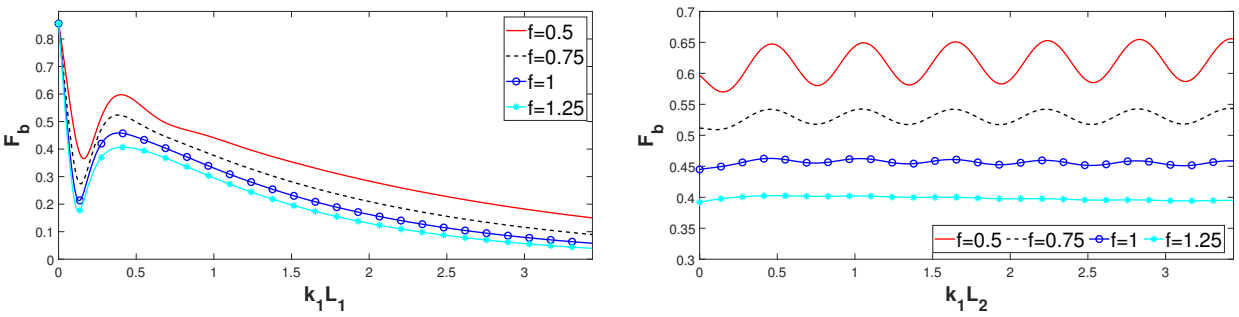

(a) F_b vs k_1L_1 for various f

(b) F_b vs k_1L_2 for various f

Figure 8.8: Non-dimensional waveload F_b against non-dimensional (a) structure width k_1L_1 and (b) non-dimensional spacing k_1L_2 of confined Region 3 corresponding to various f with $KH = 0.4$, $\epsilon = 0.7$ and $L_3/H = 1/2$.

pattern. Waveload $\mathbb{F}_b$ on the elastic plate reduces as the friction increases. This might be attributed to the optimum wave damping of the porous breakwater owing to its location where high wave energy resides. The periodic dip in the waveload also shows the existence of trapping due to the porous structure. The phase lag plays a key role in reducing the waveload on the structure, which is a consequence of reflection owing to the existence of the elastic plate. As a consequence, the numerical findings of the investigation suggest that the size of the structure does not ensure optimal performance. The length of the confined area as well as other physical characteristics of breakwater play important roles in producing the most desirable results.

8.5 Conclusion

The current research focuses on the interaction of oblique water waves with a floating dock, modelled as an elastic plate, in the presence of a porous breakwater in a two-layer fluid. The solution to the associated scattering issue is tackled by using linear water wave theory and the matching eigenfunction expansion method. A system of linear algebraic equations is produced and solved by splitting the fluid area into a number of sub-regions and using the specified equations and matching criteria. This permits the potentials, reflection and transmission coefficients and other hydrodynamic coefficients to be calculated. The impact of mooring edge circumstances and complex conjugate wavenumbers is taken into consideration while calculating the potential. Following that, certain significant findings and analyses are achieved, which are summarised below:

- Moderate values of the porous breakwater width aids in obtaining minimal wave transmission, optimal wave reflection and the minimal elevation by choosing appropriate structural parameters. Furthermore, negligible influence on interfacial

propagating modes is confirmed when a floating elastic body is associated with a porous breakwater.

- The reflection, deflection, bending moment and shear force of the elastic plate are investigated for various elastic parameters against plate length which suggests that greater flexural rigidity may produce higher reflection, lower plate deflection and associated hydrodynamic coefficients. Steady nature of the reflection coefficients establishes that an optimally chosen plate length is effective in attaining the desired reflection.

- Investigation of plate reflection and elevation for various moored edge conditions leads to the fact that optimization of hydrodynamic coefficients is possible by adopting appropriate mooring conditions which is more effective at both reflecting and deflecting.

In a nutshell, studying the interaction of water waves with an elastic plate in the presence of a porous breakwater allows one to understand in a much better way the influence of those features that aid in the safety of a floating structure. It also shows that the appropriate characteristics of the breakwater width along with a suitable positioning yields a lower impact on the elastic body. The employment of a breakwater with a proper geometrical arrangement is clearly seen to be a very valuable and viable method in the development of a floating elastic dock and such elastic bodies, e.g., solar panels, energy converters or other floating bodies for appropriate expansion of coastal infrastructure.

TH-2746_176123008

TH-2746_176123008

CHAPTER 9

Summary and future directions

This chapter provides a concise overview of the findings and contributions made by this thesis. Additionally, it offers a framework for future research works and expansions of the current study.

9.1 Summary

In this thesis, oblique water waves interaction by various types of structures in presence of various kinds of bottom topography in a two-layer fluid is investigated by using linear water wave theory.

Chapter 2 is concerned with the investigation of the problem of oblique water wave interaction with a porous structure over a step-like bottom in a two-layer fluid by assuming that the upper layer is free to the atmosphere. Applying linear water wave theory, the boundary value problems along with vertical matching conditions are formulated from which the velocity potentials are obtained by using eigenfunction expansion. The solution is obtained by the method of matched eigenfunction technique and solving a system of equations. From the computed hydrodynamic coefficients, it can be observed that the interaction between free surface and interfacial waves results in higher waveload acting on the sea-wall. Moreover, the outcomes of a composite porous structure are superior than those of a simple one. It can be concluded that as long as the structure's characteristics are adjusted correctly, it is possible to regulate both propagating modes and waveload on the wall's surface.

In **Chapter 3**, the vertically composite type breakwater problem is considered in which the lower fluid is bounded by a porous bottom surface. The reflection and trans-

TH-2746_176123008

mission coefficients are evaluated by the similar use of matched eigenfunction expansion technique as described in **Chapter 2**. Different parameters are considered in this chapter which are physically meaningful in practical scenario and the results are best presented graphically. We observe that a large amount of wave energy is dissipated due to the bottom porosity. Also, it is noted that the composite structure makes a significant effect on the reflected energy and waveload. Further, a perforated front wall is considered which increases the effectiveness of the breakwater.

Chapter 4 is concerned with the investigation of the problem of scattering of oblique incident water waves by a vertically single block caisson type breakwater located on an elastic sea-bed in a two-layer fluid in an ocean. Using the same mathematical procedure applied in **Chapters 1** and **2**, the boundary value problems are solved which are satisfied by the velocity potentials for the scattering of waves by the structure. The associated reflection and transmission coefficients are computed by carrying out appropriate numerical solutions for system of equations. Another method called linear algebraic method is also used in further verification of the solution. The complex mode-swapping is discussed concerning the wave propagation in a porous two-layer fluid flow. It is observed that the higher flexural rigidity converts the incident wave energy to the reflected and transmitted energy as similar as the rigid sea-bed problem. An interfacial wave mode is observed not to be influenced by the variations in the elastic parameter of the bottom. Furthermore, consideration of perforated sea-wall results in lower waveload due to the percolative property. However, no major changes are observed in reflection and transmission coefficients.

Chapter 5 is concerned with the extended problem of **Chapter 4** with oblique water wave scattering by a vertical caisson breakwater consisting multiple blocks and a perforated front wall. Following the Euler-Bernoulli beam equation, the elastic sea-bed is approximated as a thin elastic plate. The same mathematical procedure as applied in **Chapter 4** is used here to get the analytical solution of the scattering problem. Effectiveness of multiple blocks and the perforated-front wall is examined in the presence of bed-elasticity. The reflection coefficients and wave forces are plotted for different parameter values. When the length of the breakwater increases, a major part of waveload is dissipated.

Chapter 6 is concerned with a submerged thin vertical poro-elastic barrier placed at a finite distance from a partially-reflecting sea-wall above a porous sea-bed in a two-layer fluid flow system. The poro-elastic barrier is assumed to follow the elastic plate theory of thin plates. Time-harmonic propagating waves are assumed along the free surface and interface for any given frequency and the velocity potentials are expanded. Mode swapping due to porous impact of bed is discussed thoroughly. The reflection and transmission coefficients as well as the energy identity relation are computed and those are examined corresponding to various values of the parameters such as the porous-effect parameter, the submergence depth of barriers from free surface, the angle of incidence, the porosity

TH-2746_176123008

of the sea-bed, partial reflectivity of the wall. Impact of dead-water analogue is also illustrated in presence of porous bottom. It is demonstrated that a periodic oscillation is evident in trapping modes. Higher energy loss can be obtained by attenuating the inertial effect of the submerged poro-elastic barriers. Maximum energy loss is observed when the barriers of greater height just touch the porous sea-bed. Therefore, it can be inferred that a suitable positioning of the barriers is required in order to reduce the waveload and to create a tranquillity zone.

In **Chapter 7**, the previous work in **Chapter 6** is extended to a problem where the poro-elastic barrier is replaced by a porous wavemaker. The complete analytical solution, under the assumption of linear water wave theory and structural response, is acquired by employing eigenfunction expansion and least square method for the problem of gravity waves interacting with submerged porous barriers. The effect of various parameters such as the porous-effect parameters, the height of the porous barriers, the porosity of the sea-bed on scattering phenomenon is studied graphically. Wave energy dissipation is illustrated by following the derivation of energy identity. It is observed that a sufficient amount of the wave energy concentrated in the vicinity of the porous sea-bed undergoes reflection by the barrier while some amount of the wave energy gets dissipated when the waves pass through the porous barriers. Furthermore, considering the motion of the wavemaker, the radiation problem is also discussed. Impact of bed permeability on the amplitude stroke ratio, added mass and damping coefficient is analyzed. An important conclusion that can be drawn is that the wave energy propagation is higher for free surface, and the porous impact of the barrier produces lower radiated waves in both propagating modes. Furthermore, complex porous-effect parameter of the wavemaker results in higher added mass. This model can be considered to be very efficient for various applications in coastal engineering.

Chapter 8 deals with the investigation of scattering of oblique waves by totally submerged porous breakwater, placed at some distance from a finite dock in a two-layer fluid. Here the finite dock is considered as a thin elastic plate and the sea-bed is considered as an impermeable one. Computation for the reflection and transmission coefficients and wave forces is carried out and discussed for different parameter values corresponding to the elastic sheet, porous structure, angle of incidence. It is observed that, due to an increase in the width of the porous structure, the steadiness in wave reflection occur. The porous structure is found to dissipate a significant portion of the wave energy when an increase in the porous effect of the structure is affected. The hydrodynamic characteristic force on the dock also follows an oscillatory pattern and it decreases when the flexural rigidity is increased. Increase of the porous impact results in sufficient loss of waveload.

TH-2746_176123008

9.2 Future works

We now give some informal thoughts on how our current findings may be applied to other issues. We briefly discuss a few fascinating issues that may be addressed in the future. A two-layer fluid with varying densities is studied in this thesis, with the lowermost layer restricted to being covered by one of three options: a rigid bottom, a porous plate, or an elastic sheet. It might possibly be extended to a three-layer fluid. Additionally, a caisson-type construction may be expanded vertically by adding additional blocks in the works of **Chapters 2** to **5**.

Shear stress, strain and pressure may be found on almost all sea-beds along the coast because of their porous and elastic character. Poro-elastic or viscoelastic properties may be used to classify the structure as either partly adrift or completely adrift. A viscoelastic or poro-elastic sea-bed may be used to review the issues discussed in **Chapters 2, 3, 4,** and **5**. This is a challenging mathematical problem as well as a plausible physical reality. Such issues may also be attributed with the undulation of the bottom.

In **Chapters 6** and **7**, we look at how various types of poro-elastic or porous barriers affect water wave scattering in a two-layer fluid on a porous sea-bed. Viscoelastic and poro-elastic sea-beds are possible alternatives. Furthermore, a porous membrane construction may be used to solve these problems.

Chapter 8 discusses a finite dock and a thick porous structure. Expansion may be caused by a shift in the subsurface topography. In addition, shear current may be applied to all of the issues.

TH-2746_176123008

Bibliography

[1] S. Ali, D. Farhang, A. Ehsan, and M. Mojtaba. Dynamic behavior of a functionally graded plate resting on winkler elastic foundation and in contact with fluid. *Structural Engineering and Mechanics*, 50(1):53–71, 2014.

[2] E. Askari and F. Daneshmand. Free vibration of an elastic bottom plate of a partially fluid-filled cylindrical container with an internal body. *European Journal of Mechanics - A/Solids*, 29(1):68–80, 2010.

[3] D. K. Banerjee and Y. Pao. Thermoelastic waves in anisotropic solids. *The Journal of the Acoustical Society of America*, 56(5):1444–1454, 1974.

[4] M. Bayat, L. Andersen, L. Ibsen, and J. Clausen. Influence of pore water in the seabed on dynamic response of offshore wind turbines on monopiles. *Soil Dynamics and Earthquake Engineering*, 100:233–248, 2017.

[5] G. Bee. *Beam buckling on random elastic foundations*. PhD thesis, Colorado School of Mines, 2013.

[6] H. Behera, S. Mandal, and T. Sahoo. Oblique wave trapping by porous and flexible structures in a two-layer fluid. *Physics of Fluids*, 25(11):112110, 2013.

[7] H. Behera, C. O. Ng, and T. Sahoo. Oblique wave scattering by a floating elastic plate over a porous bed in single and two-layer fluid systems. *Ocean Engineering*, 159:280–294, 2018.

[8] H. Behera and T. Sahoo. Gravity wave interaction with porous structures in two-layer fluid. *Journal of Engineering Mathematics*, 87:73–97, 2014.

TH-2746_176123008

[9] M. Belorgey, M. R. Jean, and G. Carpentier. Perforated breakwaters, Dieppe harbour Jarlan caisson: general schedule and acquired experience. *In Proceedings of 13th International Offshore and Polar Engineering Conference*, pages 850–857, 2003.

[10] L. Bjerrum. Geotechnical problems involved in foundations of structures in the North Sea. *Geotechnique*, 23:319–358, 1973.

[11] B. H. Buck and R. Langan. Aquaculture perspective of multi-use sites in the open ocean: The untapped potential for marine resources in the anthropocene. *Springer International Publishing*, 2018.

[12] P. G. Chamberlain and D. Porter. Wave scattering in a two-layer fluid of varying depth. *Journal of Fluid Mechanics*, 524:207–228, 2005.

[13] A. Chanda. *Water wave interaction with different structures and obstacles due to various types of bottom topography in a homogeneous fluid and a two-layer fluid.* PhD thesis, Indian Institute of Technology Guwahati, 2021.

[14] A. Chanda and S. N. Bora. Effect of a porous sea-bed on water wave scattering by two thin vertical submerged porous plates. *European Journal of Mechanics - B/Fluids*, 84:250–261, 2020.

[15] A. Chanda and S. N. Bora. Propagation of oblique waves over a small undulating elastic bottom topography in a two-layer fluid flowing through a channel. *International Journal of Applied Mechanics*, 12(02):2050023, 2020.

[16] A. Chanda and S. N. Bora. Scattering of linear oblique water waves by an elastic bottom undulation in a two-layer fluid. *Zeitschrift für angewandte Mathematik und Physik*, 71:107, 2020.

[17] A. Chanda and S. N. Bora. Investigation of water wave scattering by an elastic sea-bed of varying depth in two superposed fluids covered by an ice-sheet. *Ocean Engineering*, 221:108510, 2021.

[18] H. K. Chang and J. C. Liou. Solving wave dispersion equation for dissipative media using homotopy perturbation technique. *Journal of Waterway, Port, Coastal, and Ocean Engineering, ASCE*, 132(1):28–35, 2006.

[19] I. H. Cho and M. H. Kim. Interactions of horizontal porous flexible membrane with waves. *Journal of Waterway, Port, Coastal, and Ocean Engineering, ASCE*, 126(5):245–253, 2000.

[20] A. T. Chwang. A porous-wavemaker theory. *Journal of Fluid Mechanics*, 132:395–406, 1983.

TH-2746_176123008

[21] A. T. Chwang and M. M. Lee. Scattering and radiation of water waves by permeable barriers. *Physics of Fluids*, 12:54–65, 2000.

[22] A. D. D. Craik. *Wave Interactions and Fluid Flows*. Cambridge Monographs on Mechanics. Cambridge University Press, 1986.

[23] A. D. D. Craik. The origins of water wave theory. *Annual Review of Fluid Mechanics*, 36:1–28, 2004.

[24] C. W. Curry, R. H. Bennett, M. H. Hulbert, K. J. Curry, and R. W. Faas. Comparative study of sand porosity and a technique for determining porosity of undisturbed marine sediment. *Marine Georesources & Geotechnology*, 22:231–252, 2004.

[25] R. A. Dalrymple, M. A. Losada, and P. A. Martin. Reflection and transmission from porous structures under oblique wave attack. *Journal of Fluid Mechanics*, 224:625–644, 1991.

[26] R. A. Dalrymple and P. A. Martin. Wave diffraction through offshore breakwaters. *Journal of Waterway, Port, Coastal, and Ocean Engineering, ASCE*, 116(6):727–741, 1990.

[27] D. Das and B. N. Mandal. A note on solution of the dispersion equation for small-amplitude internal waves. *Archives of Mechanics*, 57(6):493–501, 2005.

[28] D. Das, B. N. Mandal, and A. Chakrabarti. Energy identities in water wave theory for free-surface boundary condition with higher-order derivatives. *Fluid Dynamics Research*, 40(4):253–272, 2007.

[29] L. Das and S. Mohapatra. Effects of flexible bottom on radiation of water waves by a sphere submerged beneath an ice-cover. *Meccanica*, 54:985–999, 2019.

[30] L. Das and S. Mohapatra. Analytical study of exciting forces acting on a rigid sphere in a fluid with the flexible base surface of the fluid. *ZAMM - Zeitschrift für Angewandte Mathematik und Mechanik*, 100(10):e202000052, 2020.

[31] S. Das, H. Behera, and T. Sahoo. Flexural gravity wave motion over poroelastic bed. *Wave Motion*, 63:135–148, 2016.

[32] S. Das and S. N. Bora. Reflection of oblique ocean water waves by a vertical porous structure placed on a multi-step impermeable bottom. *Applied Ocean Research*, 47:373–385, 2014.

[33] S. Das and S. N. Bora. Reflection of oblique ocean water waves by a vertical rectangular porous structure placed on an elevated horizontal bottom. *Ocean Engineering*, 82:135–143, 2014.

TH-2746_176123008

[34] T. H. Dawson. Wave propagation over a deformable sea floor. *Ocean Engineering*, 5(4):227–234, 1978.

[35] S. Earnshaw. The mathematical theory of the two great solitary waves of the first order. *Transactions of the Cambridge Philosophical Society*, 8:326–341, 1847.

[36] H. G. Gade. Effects of a non-rigid, impermeable bottom on plane surface waves in shallow water. *Journal of Marine Research*, 16:61–82, 1958.

[37] J. M. Garrido and J. R. Medina. New neural network-derived empirical formulas for estimating wave reflection on Jarlan-type breakwaters. *Coastal Engineering*, 62:9–18, 2012.

[38] G. Green. On the motion of waves in a variable canal of small depth and width. *Transactions of the Cambridge Philosophical Society*, 6:457–462, 1838.

[39] S. M. Hasheminejad and M. M. Mohammadi. Hydroelastic response suppression of a flexural circular bottom plate resting on pasternak foundation. *Acta Mechanica*, 228:4269–4292, 2017.

[40] R. C. Heath. Basic ground-water hydrology. *U. S. Geological Survey*, 1983.

[41] M. Hetenyi. *Beams on elastic foundation; theory with applications in the fields of civil and mechanical engineering*. Ann Arbor: University of Michigan Press, 1946.

[42] H.-H. Hsu and Y.-C. Wu. The hydrodynamic coefficients for an oscillating rectangular structure on a free surface with sidewall. *Ocean Engineering*, 24(2):177–199, 1997.

[43] Z. Huang, Y. Li, and Y. Liu. Hydraulic performance and wave loadings of perforated/slotted coastal structures: A review. *Ocean Engineering*, 38(10):1031–1053, 2011.

[44] M. Isaacson, J. Baldwin, N. Allyn, and S. Cowdell. Wave interactions with perforated breakwater. *Journal of Waterway, Port, Coastal, and Ocean Engineering, ASCE*, 126(5):229–235, 2000.

[45] M. Isaacson and S. Qu. Waves in a harbour with partially reflecting boundaries. *Coastal Engineering*, 14(3):193–214, 1990.

[46] R. B. Kaligatla, Manisha, and T. Sahoo. Wave trapping by dual porous barriers near a wall in the presence of bottom undulation. *Journal of Marine Science and Application*, 16:286–297, 2017.

TH-2746_176123008

[47] P. Kelland. On the theory of waves. *Report of the British Association for the Advanced of Science*, pages 50–52, 1840.

[48] S. Khuntia and S. Mohapatra. Effects of ice-floe on surface wave interaction with an irregular flexible seabed. *European Journal of Mechanics - B/Fluid*, 84:357–366, 2020.

[49] D. V. Kondratov, L. I. Mogilevich, V. S. Popov, and A. A. Popova. Hydroelastic oscillations of a circular plate, resting on winkler foundation. *Journal of Physics: Conference Series*, 944(012057), 2018.

[50] T. Kumagai and M. A. Foda. Analytical model for response of seabed beneath composite breakwater to wave. *Journal of Waterway, Port, Coastal, and Ocean Engineering, ASCE*, 128(2):62–71, 2002.

[51] N. P. Kurian, K. Rajith, T. S. Shahul Hameed, L. Sheela Nair, M. V. Ramana Murthy, S. Arjun, and V. R. Shamji. Wind waves and sediment transport regime off the south-central kerala coast, india. *Natural Hazards*, 49:325–345, 2009.

[52] J. F. Lee and Y. J. Lan. On waves propagating over poro-elastic seabed. *Ocean Engineering*, 29(8):931–946, 2002.

[53] M. M. Lee and A. T. Chwang. Scattering and radiation of water waves by permeable barriers. *Physics of Fluids*, 12(1):54–65, 2000.

[54] Q. Lin, Q. R. Meng, and D. Q. Lu. Waves propagating over a two-layer porous barrier on a seabed. *Journal of Engineering Mathematics*, 30(3):453–462, 2018.

[55] C. M. Linton and J. R. Cadby. Scattering of oblique waves in a two-layer fluid. *Journal of Fluid Mechanics*, 461:343–364, 2002.

[56] C. M. Linton and J. R. Cadby. Trapped modes in a two-layer fluid. *Journal of Fluid Mechanics*, 481:215–234, 2003.

[57] C. M. Linton and M. McIver. The interaction of waves with horizontal cylinders in two-layer fluids. *Journal of Fluid Mechanics*, 304:213–229, 1995.

[58] Y. Liu, Y. C. Li, B. Teng, and S. Dong. Wave motion over a submerged breakwater with an upper horizontal porous plate and a lower horizontal solid plate. *Ocean Engineering*, 35(16):1588–1596, 2008.

[59] I. J. Losada, R. A. Dalrymple, and M. A. Losada. Water waves on crown breakwaters. *Journal of Waterway, Port, Coastal, and Ocean Engineering, ASCE*, 119(4):367–380, 1993.

TH-2746_176123008

[60] R. C. MacCamy and R. A. Fuchs. *Wave forces on piles: a diffraction theory*. Number 69 in Technical memorandum (United States. Beach Erosion Board). Dept. of the Army, Corps of Engineers, Beach Erosion Board, 1954.

[61] P. Madsen. Wave reflection from a vertical permeable wave absorber. *Coastal Engineering*, 7(4):381–396, 1983.

[62] P. Maiti and B. Mandal. Water wave scattering by bottom undulations in an ice-covered two-layer fluid. *Applied Ocean Research*, 30(4):264–272, 2008.

[63] P. Maiti and B. Mandal. Water wave scattering by an elastic plate floating in an ocean with a porous bed. *Applied Ocean Research*, 47:73–84, 2014.

[64] W. Mallard and R. Dalrymple. Water waves propagating over a deformable bottom. *In: Proc. Ninth Annual Offshore Technology Conference, (Houstan, U.S.A.; May 2-5, 1977)*, 3 , Houston, U.S.A., Offshore Technology Conference, 1977:141–146, January 1977.

[65] S. Manam and T. Sahoo. Waves past porous structures in a two layer fluid. *Journal of Engineering Mathematics*, 52:355–377, 2005.

[66] S. C. Martha, S. N. Bora, and A. Chakrabarti. Oblique water-wave scattering by small undulation on a porous sea-bed. *Applied Ocean Research*, 29(1):86–90, 2007.

[67] S. R. Massel. *Internal gravity waves in the shallow seas*. GeoPlanet: Earth and Planetary Sciences. Springer, first edition, 2015.

[68] F. J. Mendez and I. J. Losada. A perturbation method to solve dispersion equations for water waves over dissipative media. *Coastal Engineering*, 51:81–89, 2004.

[69] Q. R. Meng and D. Q. Lu. Scattering of gravity waves by a porous rectangular barrier on a seabed. *Journal of Hydrodynamics*, 28:519–522, 2016.

[70] Q. R. Meng and D. Q. Lu. Wave-induced hydrodynamic responses of a rigid body connected with elastic plates floating on a two-layer fluid. *Journal of Fluids and Structures*, 68:295–309, 2017.

[71] Q. R. Meng and D. Q. Lu. Scattering of flexural-gravity waves by a group of elastic plates floating on a stratified fluid. *European Journal of Mechanics - B/Fluids*, 67:329–340, 2018.

[72] K. S. Miller. Complex linear least squares. *SIAM Review*, 15(4):706–726, 1973.

TH-2746_176123008

[73] T. Miloh, M. P. Tulin, and G. Zilman. Dead-water effects of a ship moving in stratified seas. *Journal of Offshore Mechanics and Arctic Engineering, ASME*, 115(2):105–110, 05 1993.

[74] S. Mohapatra. Effects of elastic bed on hydrodynamic forces for a submerged sphere in an ocean of finite depth. *ZAMP - Zeitschrift for angewandte Mathematik und Physik*, 68:91, 2017.

[75] S. Mohapatra and S. N. Bora. Exciting forces due to interaction of water waves with a submerged sphere in an ice-covered two-layer fluid of finite depth. *Applied Ocean Research*, 34:187–197, 2012.

[76] S. C. Mohapatra and T. Sahoo. Surface gravity wave interaction with elastic bottom. *Applied Ocean Research*, 33(1):31–40, 2011.

[77] S. C. Mohapatra and G. C. Soares. Interaction of surface gravity wave motion with elastic bottom in three-dimensions. *Applied Ocean Research*, 57:125–139, 2016.

[78] M. A. Mustapa, O. B. Yaakoba, M. A. Yasser, K. R. Chang, K. K. Kohb, and A. A. Faizul. Wave energy device and breakwater integration: A review. *Renewable and Sustainable Energy Reviews*, 77:43–58, 2017.

[79] B. L. Méhauté. Progressive wave absorber. *Journal of Hydraulic Research*, 10(2):153–169, 1972.

[80] A. C. Narayana, C. F. Jago, P. Manojkumar, and R. Tatavarti. Nearshore sediment characteristics and formation of mudbanks along the kerala coast, southwest india. *Estuarine, Coastal and Shelf Science*, 78(2):341–352, 2008.

[81] E. Noda. Water waves generated by landslides. *Journal of the Waterways, Harbors and Coastal Engineering Division, ASCE*, 96(4):835–855, 1970.

[82] M. A. Rahman and A. Akter. The effect of porosity of submerged and emerged breakwater on wave transmission. *International Journal of Environmental Science and Development*, 5:473–478, 2014.

[83] B. Rayleigh. On waves. *Philosophical Magazine*, 5:257–279, 1876.

[84] S. Rojanakamthorn, M. Isobe, and A. Watanabe. A mathematical model of wave transformation over a submerged breakwater. *Coastal Engineering*, 32(2):299–234, 1989.

[85] D. M. P. Romero, M. O. Sanchez, A. Monino, and M. A. Losada. Characteristic friction coefficient and scale effects in oscillatory porous flow. *Coastal Engineering*, 56:931–939, 2009.

TH-2746_176123008

[86] J. S. Russell and S. J. Robinson. Report on waves. *Report of the British Association for the Advanced of Science*, pages 417–496, 1837.

[87] S. Saha and S. N. Bora. Trapped modes in a two-layer fluid of finite depth bounded above by a rigid lid. *Wave Motion*, 50:1050–1060, 2013.

[88] S. Saha and S. N. Bora. Flexural gravity waves trapped in a two-layer fluid of finite depth. *Applied Ocean Research*, 44:1–12, 2014.

[89] S. Saha and S. N. Bora. Elastic bottom effect on trapped waves in a two-layer fluid. *International Journal of Applied Mechanics*, 07(02):1550028, 2015.

[90] G. Sahoo, S. Singla, and S. Martha. Scattering of oblique water waves by thick porous structure and thin elastic plate. *Ocean Engineering*, 248:110526, 2022.

[91] T. Sahoo, M. M. Lee, and A. T. Chwang. Trapping and generation of waves by vertical porous structures. *Journal of Engineering Mechanics, ASCE*, 126(10):1074–1082, 2000.

[92] M. R. Sarangi and S. Mohapatra. Investigation on the effects of versatile deformating bed on a water wave diffraction problem. *Ocean Engineering*, 164:377–387, 2018.

[93] A. Sarkar and S. N. Bora. Interaction of water waves with a semiporous bottom-mounted cylindrical storage tank containing a cylindrical pile. *Journal of Waterway, Port, Coastal, and Ocean Engineering, ASCE*, 147(6):04021029, 2021.

[94] B. Sarkar, S. Paul, and S. De. Effects of flexible bed on oblique wave interaction with multiple surface-piercing porous barriers. *ZAMP - Zeitschrift for angewandte Mathematik und Physik*, 72:83, 2021.

[95] C. K. Sollitt and R. H. Cross. Wave transmission through permeable breakwaters. *Coastal Engineering Proceedings*, 1(13):99, Jan. 1972.

[96] G. G. Stokes. On the theory of oscillatory waves. *Transactions of the Cambridge Philosophical Society*, 8:441–455, 1847.

[97] W. Sulisz. Wave reflection and transmission at permeable breakwaters of arbitrary cross section. *Coastal Engineering*, 9(4):371–386, 1985.

[98] S. Tabssum, R. B. Kaligatla, and T. Sahoo. Gravity wave interaction with a porous breakwater in a two-layer ocean of varying depth. *Ocean Engineering*, 196:106816, 2020.

[99] S. A. Thorpe. *An Introduction to Ocean Turbulence*. Cambridge University Press, 2007.

TH-2746_176123008

[100] C. L. Ting, M. C. Lin, and C. Y. Cheng. Porosity effects on non-breaking surface waves over permeable submerged breakwaters. *Coastal Engineering*, 50:213–224, 2004.

[101] A. Toffoli and E. M. B. Gregersen. *Types of Ocean Surface Waves, Wave Classification*, pages 1–8. John Wiley & Sons Ltd., 2017.

[102] Y. T. Tsai, W. G. McDougal, and C. K. Sollitt. Response of finite depth seabed to waves and caisson motion. *Journal of Waterway, Port, Coastal, and Ocean Engineering, ASCE*, 116(1):1–20, 1990.

[103] S. W. Twu, C. C. Liu, and C. W. Twu. Wave damping characteristics of vertically stratified porous structures under oblique wave action. *Ocean Engineering*, 29(11):1295–1311, 2002.

[104] V. Venkateswarlu and D. Karmakar. Wave scattering by vertical porous block placed over flat and elevated seabed. *Marine Systems & Ocean Technology*, 14:85–109, 2019.

[105] V. Venkateswarlu and D. Karmakar. Significance of seabed characteristics on wave transformation in the presence of stratified porous block. *Coastal Engineering Journal*, 62(1):1–22, 2020.

[106] V. Venkateswarlu and D. Karmakar. Wave motion over stratified porous absorber combined with seaward vertical barrier. *Proceedings of the Institution of Mechanical Engineers, Part M: Journal of Engineering for the Maritime Environment*, 234:830–845, 2020.

[107] V. Venkateswarlu and D. Karmakar. Numerical investigation on the wave dissipating performance due to multiple porous structures. *ISH Journal of Hydraulic Engineering*, 27(sup1):202–219, 2021.

[108] V. Venkateswarlu, K. Praveen, and D. Karmakar. Surface gravity wave scattering by multiple energy absorbing structures of variable horizontal porosity. *Coastal Engineering Journal*, 62(4):504–526, 2020.

[109] K. H. Wang and X. Ren. An effective wave-trapping system. *Ocean Engineering*, 21(2):155–178, 1994.

[110] J. C. Ward. Turbulent flow in porous media. *Journal of the Hydraulics Division, ASCE*, 90:1–12, 1964.

[111] E. Winkler. *Die Lehre von der Elasticitaet und Festigkeit mit besondere Ruecksicht auf ihre Anwendung in der Technik.* fuer polytechnische Schuhlen, Bauakademien, Ingenieure, Maschienenbauer, Architecten, etc. , H. Dominicus, Prague, 1867.

TH-2746_176123008

[112] J. Wu, Z. Wan, and Y. Fang. Wave reflection by a vertical wall with a horizontal submerged porous plate. *Ocean Engineering*, 25(9):767–779, 1998.

[113] J. Wu, Z. Wan, and Y. Fang. Wave reflection by a vertical wall with a horizontal submerged porous plate. *Ocean Engineering*, 25(9):767–779, 1998.

[114] F. Xu and D. Lu. Wave scattering by a thin elastic plate floating on a two-layer fluid. *International Journal of Engineering Science*, 48(9):809–819, 2010.

[115] T. Yamamoto. On the response of a coulomb-damped poroelastic bed to water waves. *Marine Geotechnology*, 5(2):93–130, 1983.

[116] Z. Yana, C. Chen, P. Fan, and M. Wang. Pore structure characterization of ten typical rocks in China. *Electronic Journal of Geotechnical Engineering*, 20:479–494, 2015.

[117] J. H. Ye and D. S. Jeng. Response of porous seabed to nature loadings: Waves and currents. *Journal of Engineering Mechanics, ASCE*, 138:601–613, 2012.

[118] T. L. Yip and A. T. Chwang. Water wave control by a pitching plate. *Journal of Engineering Mechanics, ASCE*, 123(8):800–807, 1997.

[119] T. L. Yip and A. T. Chwang. Perforated wall breakwater with internal horizontal plate. *Journal of Engineering Mechanics, ASCE*, 126(5):533–538, 2000.

[120] X. Yu. Diffraction of water waves by porous breakwaters. *Journal of Waterway, Port, Coastal and Ocean Engineering, ASCE*, 121:275–282, 1995.

[121] X. Yu and A. T. Chwang. Water waves above submerged porous plate. *Journal of Engineering Mechanics, ASCE*, 120(6):1270–1282, 1994.

[122] X. Yu and A. T. Chwang. Wave induced oscillation in harbor with porous breakwaters. *Journal of Waterway, Port, Coastal, and Ocean Engineering*, 120(2):125–144, 1994.

[123] X. Yu and A. T. Chwang. Wave motion through porous structures. *Journal of Engineering Mechanics, ASCE*, 120:989–1008, 1994.

[124] Y. Zhao, H. J. Li, and Y. Liu. Oblique wave scattering by a submerged porous breakwater with a partially reflecting sidewall. *Journal of Marine Science and Technology*, 25(4):383–392, 2017.

[125] D. Zhou and Y. K. Cheung. Vibrations of elastic bottom plate of a sealed rectengular conatained fully filled with liquid. *International Journal of Structural Stability and Dynamics*, 01(01):145–162, 2001.

TH-2746_176123008

[126] D. Zhu and S. Zhu. Impendance analysis of hydrodynamic behoviors for a perforated-wall caisson breakwater under regular orthogonal attack. *Coastal Engineering*, 57:722–731, 2010.

[127] S. Zhu. Water waves within a porous medium on an undulating bed. *Coastal Engineering*, 42:87–101, 2001.

TH-2746_176123008

TH-2746_176123008

Appendices

TH-2746_176123008

TH-2746_176123008

APPENDIX A

Evaluation of porous impedance parameter

Small amplitude wave motion in three dimensions is considered within an undeformable porous medium. It is assumed that the porous structure is homogeneous and isotropic (uniform properties of the material in all directions). The fluid motion follows the continuity equation and the equation of motion in terms of the seepage fluid velocity $\vec{U}$, fluid density ρ^* and dynamic pressure P and are given by

$$\nabla.\vec{U} = 0, \tag{A.1}$$

$$\frac{\partial \vec{U}}{\partial t} = -\frac{\nabla P}{\rho^*} + \text{resistance forces.} \tag{A.2}$$

The resistance forces in equation (A.2) are evaluated by combining known steady and unsteady stress relationships. Under steady state flow conditions, the pressure drop through the porous medium is specified by Ward [110] as

$$-\frac{\nabla P}{\rho^*} = \frac{v_k}{K_p}\epsilon\vec{U} + \frac{C_f}{\sqrt{K_p}}\epsilon^2\vec{U}|\vec{U}|, \tag{A.3}$$

where v_k is the kinematic viscosity, K_p is the intrinsic permeability, ϵ is the porosity and C_f is a dimensionless turbulent resistance coefficient of the medium. It is hypothesized by Sollitt and Cross [95] that unsteadiness may be accounted for by introducing an additional term which evaluates the added resistance caused by the virtual mass of discrete grains within the medium. The resistance force due to the virtual mass is equal to the product of the displaced fluid mass, the virtual mass coefficient and the acceleration in the approach velocity. The resulting force is distributed over the fluid mass within the pore so that the

TH-2746_176123008

force per unit mass of fluid simply becomes

$$\frac{1-\epsilon}{\epsilon}C_M\frac{\partial\vec{U}}{\partial t}. \tag{A.4}$$

Combining equations (A.3) and (A.4), and replacing the resistance force in equation (A.2) by them, we get

$$\begin{aligned}\frac{\partial\vec{U}}{\partial t} &= -\frac{\nabla P}{\rho^*} - \frac{v_k}{K_p}\epsilon\vec{U} - \frac{C_f}{\sqrt{K_p}}\epsilon^2\vec{U}|\vec{U}| - \frac{1-\epsilon}{\epsilon}C_M\frac{\partial\vec{U}}{\partial t}\\ \implies m\frac{\partial\vec{U}}{\partial t} &= -\frac{\nabla P}{\rho^*} - \frac{v_k}{K_p}\epsilon\vec{U} - \frac{C_f}{\sqrt{K_p}}\epsilon^2\vec{U}|\vec{U}|,\end{aligned} \tag{A.5}$$

where $m = 1 + C_M\frac{1-\epsilon}{\epsilon}$. The parameter m is physically a dimensionless quantity which signifies the inertial force acting on the porous medium. It is worth mentioning that $m = 1$ accounts for two different cases, namely, $m = 1$, i.e., the absence of any structure and $C_M = 0$, i.e., the presence of an inviscid fluid.

Now, linearization of equation (A.5) is necessary in order to find an analytical solution and hence, the dissipative stress term is replaced by a linear stress term in U by the following form:

$$\frac{v_k}{K_p}\epsilon\vec{U} + \frac{C_f}{\sqrt{K_p}}\epsilon^2\vec{U}|\vec{U}| \to f\omega\vec{U}. \tag{A.6}$$

Combination of equation (A.5) and equation (A.6) leads to

$$m\frac{\partial\vec{U}}{\partial t} + \frac{\nabla P}{\rho^*} + f\omega\vec{U} = 0. \tag{A.7}$$

The friction coefficient f is a scalar quantity which can be found by the linearized equality condition and it is the ratio of two forces. This coefficient is directly connected to the resistance. In the structure, this coefficient contributes in the resistance against fluid flow. In order to evaluate f, Lorentz principle of equivalent work is applied which states that the average rate of energy dissipation should be identical whether evaluated by using the true non-linear resistance law or its linearized equivalent. The porous bed is assumed to be very thin for our consideration and therefore, the variation of the pressure across its thickness may be approximated as linear. Since the resistance terms of the above relation represent friction force per unit mass acting at a point in the flow field, the following equality (energy dissipation) holds:

$$\int_V \epsilon\mathrm{d}V\int_t^{t+T} f\omega\vec{U}\cdot\rho^*\vec{U}\mathrm{d}t = \int_V \epsilon\mathrm{d}V\int_t^{t+T}\left(\frac{v_k}{K_p}\epsilon\vec{U} + \frac{C_f}{\sqrt{K_p}}\epsilon^2\vec{U}|\vec{U}|\right)\cdot\rho^*\vec{U}\mathrm{d}t, \tag{A.8}$$

TH-2746_176123008

where V is the volume of the flow field and T is the wave period. Now assuming f to be constant throughout the flow field, the following expression for f can be written:

$$f = \frac{1}{\omega} \frac{\int_V \mathrm{d}V \int_t^{t+T} \epsilon^2 \left(\frac{\nu_k \vec{U}^2}{K_p} + \frac{C_f \epsilon}{K_p} \epsilon |\vec{U}|^3 \right) \mathrm{d}t}{\int_V \mathrm{d}V \int_t^{t+T} \epsilon \vec{U}^2 \mathrm{d}t}. \tag{A.9}$$

TH-2746_176123008

TH-2746_176123008

APPENDIX B

Analysis of the dispersion relations and their roots

The dispersion relation in a two-layer fluid region is given by equation (1.27). Now assuming $\tau = h/h_I$, $\mu = \tau - 1$ and $kh_I = z_1$, we can write (1.27) as

$$f_{_R}(z_1) \equiv \frac{Kh_I z_1 \coth z_1 - (1-\rho)z_1^2 - \rho(Kh_I)^2}{Kh_I(Kh_I \coth z_1 - z_1)} = \coth \mu z_1. \tag{B.1}$$

We can easily obtain the real roots of (1.27) graphically if we plot $y(x) = \coth \mu x$ and $y(x) = f_{_R}(x)$ from where we can show that (1.27) has four real roots (two positive and two symmetrically negative ones) since (1.27) remains unchanged if k is replaced by $-k$. Now, replacing k by ik in (1.27) gives us

$$f_{_I}(z_1) \equiv -\frac{Kh_I z_1 \cot z_1 + (1-\rho)z_1^2 - \rho(Kh_I)^2}{Kh_I(Kh_I \cot z_1 + z_1)} = \cot \mu z_1. \tag{B.2}$$

Similarly, by using the graphical method, the purely imaginary roots of (1.27) can also be obtained by plotting $y(x) = \cot \mu x$ and $y(x) = f_{_I}(x)$, from where we can show that there exist purely imaginary roots of (1.27) given by $\pm \mathrm{i}t_n$ $(n = 1, 2, \ldots)$.

Further, (1.27) can be rewritten as

$$F_1(z_1) + F_2(z_1) = 0, \qquad \begin{cases} F_1(z_1) = (z_1 - Kh_I \coth z_1)(z_1 - Kh_I \coth \mu z_1), \\ F_2(z_1) = -\rho\big(z_1^2 - (Kh_I)^2\big). \end{cases} \tag{B.3}$$

Apart from the graphical method, we can use Rouche's theorem as defined by Das and Mandal [27] to show that dispersion equation (1.27) has four real roots, an infinite number of purely imaginary roots and no other roots. To find the number of roots of (1.27), Das

TH-2746_176123008

and Mandal [27] defined a square contour where $F_2(z_1)$ had four real roots and infinite purely imaginary roots. They then used Rouche's theorem to show that $F_1(z_1) + F_2(z_1)$ and $F_2(z_1)$ have the same number of zeros on that fixed square contour.

From dispersion relation (1.53) in the porous medium, by solving for K, we obtain

$$K_{\pm} = \frac{\beta \pm \sqrt{\beta^2 - 4\alpha c}}{2\alpha}, \tag{B.4}$$

where

$$\begin{aligned}
\alpha =& \gamma(\rho + \coth kh_I \coth k(h - h_I)),\\
\beta =& k\gamma(\coth kh_I + \coth k(h - h_I)),\\
c =& k^2(1 - \rho).
\end{aligned}$$

In (B.4), the subscript $\pm$ refers to the free surface mode and interface mode, respectively as defined in [65]. If we substitute $K\gamma$ by $\mathcal{K}$, then dispersion relation (2.21) can be transformed into a similar form like (B.3) from which we can show that both (1.27) and (1.53) have the same number of roots. Further, Mendez and Losada [68] showed in their algorithm that, as the dissipation factor (here γ which is real for plain water region) changes from real to complex (in porous region), the corresponding dispersive roots of the pure water region also gets converted to the roots of dispersion equation in the porous region. Moreover, the form of K clearly indicates that the associated wavenumber within the porous medium is complex in nature due to the effect of the complex porous impedance parameter γ. After evaluating the roots numerically in the porous region, the absolute error can be found as

$$Error^{\pm} = \left| \frac{\omega^2}{g}\gamma - \frac{\beta \pm \sqrt{\beta^2 - 4\alpha c}}{2\alpha} \right|. \tag{B.5}$$

These are valid for all the problems in the thesis.

TH-2746_176123008

APPENDIX C

Perturbation method by Mendez and Losada

Mendez and Losada [68] described a perturbation method to find the roots in a porous medium. We briefly discuss this approach. First, we apply the dimensional analysis and convert the dispersion relation (1.53) as

$$\Upsilon(z_1, K_1, \upsilon, \varsigma) = K_1^2(\rho + \coth z_1 \coth \mu z_1) - K_1 \varsigma z_1(\coth z_1 + \coth \mu z_1) + z_1^2 \varsigma^2(1-\rho) = 0, \tag{C.1}$$

where $\varsigma = 1/(m + \mathrm{i}f), z_1 = kh_I,\ \tau = h/h_I,\ \mu = (\tau - 1)$ and $K_1 = Kh_I$.
Now, following the algorithm, a small perturbation $\delta\varsigma$ in ς results in a small change δz_1 where z_1 is the dimensionless wavenumber. We can explicitly write δz_1 in the following form:

$$\delta z_1 = -\delta\varsigma \left(\frac{\partial \Upsilon}{\partial \varsigma}\right) \Big/ \left(\frac{\partial \Upsilon}{\partial z_1}\right). \tag{C.2}$$

Then, the following iterative method finds z_1 for a given ς:

- $\delta\varsigma = (\varsigma - \varsigma^0)/M,\ M$ =number of steps,
- Calculate δz_1^i from (C.2) as a function of $z_1^{i-1}, \varsigma^{i-1}$ and $\delta\varsigma$,
- $z_1^i = z_1^{i-1} + \delta z_1^i$,
- Repeat the procedure until $\varsigma^M = \varsigma^{M-1} + \delta\varsigma$ is found.

We consider $\varsigma_0 = 1$ which corresponds to the dispersion relation for the water medium while the corresponding z_1^0 can be obtained by any readily available method for solving such a dispersion relation.

TH-2746_176123008

This method has been adopted in the thesis wherever required.

TH-2746_176123008

APPENDIX D

Selection of appropriate parameter values

As selection of physically meaningful parameter values is essential for solving a physical problem like the ones considered in this thesis, the following explanation is expected to provide an in-depth understanding about the same.

- For a two-layer fluid consisting of freshwater and salt water, the value of $\rho = \rho_1/\rho_2$ would ideally be around 0.97. The same qualitative features as in the present work can be observed for such a density ratio too, but from a computational point of view, the effects of the interface are observed to be too small to be noticed. To be precise, the values of the two roots of dispersion equation approach the same value and the whole region would act like a single-layer fluid of finite depth if we take the ratio of the two densities nearer to 0.97. However, the entire analytical study for the problem consisting of a two-layer fluid of finite depth over a porous bed becomes inappropriate unless two wavenumbers exist. For clear observation of the features, the density ratio of the fluids is chosen as 0.9. The same consideration is also observed in the works of Linton and McIver [57], Linton and Cadby [55] and Mohapatra and Bora [75]. In fact, the first two works mentioned above considered the density ratio as 0.5 and the third one considered the value 0.9.

- Following Appendix A, it is found that $m = 1 + C_M\frac{1-\epsilon}{\epsilon}$. It is worth mentioning that $m = 1$ accounts for two different cases, namely, $m = 1$, i.e., the absence of any structure and $C_M = 0$, i.e., the presence of an inviscid fluid. Due to the consideration of inviscid fluid, $m = 1$ is chosen.

- Consideration of the non-dimensional values of Gh such as $0.5, 0.25, 0.05$ is inspired from works such as those in [63, 7, 14] where the bed porosity has been assumed

TH-2746_176123008

more or less in this range or higher. Ye and Jeng [117] considered the water depth 20 meters and porosity of coarse sand and fine sand as 0.3 and 0.2, respectively, in their numerical work. The average porosity of 36 samples of marine sand collected from Fort Walton Beach, Florida, and embedded with resin was determined to be 41.30% and from the review of published data, the average porosity of sand was determined to be $37.7\% - 46.3\%$, for a range of sorting coefficients and grain sizes (Curry et al. [24]). From the report of Heath [40], it is known that the porosity of the soil, clay, sand, gravel, limestone, sandstone (unconsolidated), granite and Basalt (young) are, respectively, 55%, 50%, 25%, 20%, 20%, 11%, 0.1% and 11%. Therefore, the considered non-dimensional porosity value in the present work seems to be realistic based on those references.

- In our case, we are mainly focused upon the gravity waves whose period band is $(1, 20)$ sec (see [101]) with wind being the generating force and gravity the restoring force. Now, taking $g = 9.81\ m/s^2$ and $T = (1, 20)$ sec gives the range of $K = (0.01, 4)$. Therefore, multiplying by an appropriate depth level, the choice of K in our work looks appropriate.

- If we consider the friction parameter f, then from Romero et al. [85], it can be seen that $f = \upsilon_c(\mathscr{D}_p k_1)^{-0.57}$, where υ_c is a constant and $\mathscr{D}_p$ the characteristic pore diameter. Based on a series of experiments, they obtained this linearized equation for the friction term where υ_c varied in the range $0.21 \leq \upsilon_c \leq 0.46$. In practical life, a breakwater usually consists of large pieces of rock (granite). The granite rock of type 1 and 2 found in Nanjing, China, has their average pore diameters 0.26 mm and 0.48 mm, respectively (Yana et al. [116]). Using the formula of Romero et al. [85], with appropriate dispersive roots, the friction parameter can be found to be in the range $[0, 2]$. Moreover, many works have utilized this range of friction parameters ([8], [32], [106] etc.) and many for range higher than this ([104] etc.). Considering the other elements which are used more or less in the construction of breakwater or barrier consists of pore diameter equal to or higher than 0.1 mm which will also validate our purpose to consider this friction range. Romero et al. [85] also considered coarse sand with the porosity 0.374 in their investigation. Ting et al. [100] investigated the effects of porosity of submerged breakwaters by experimenting on eight model geometries each with six different porosities, from 0.421 to 0.912. Rahman and Akter [82] experimented at 50 cm still water depth for a fixed vertical porous breakwater of three different porosity (0.45, 0.51 and 0.7) having three different structure heights (40 cm, 50 cm and 60 cm). Theoretically, the value of porosity stands between 0 to 1. But practically, for most rocks, porosity varies from less than 1% to 40%. The porosity of a rock depends on many factors, including the rock type and how the grains of a rock are arranged. For example, crystalline rocks such as granite

TH-2746_176123008

has a very low porosity ($< 1\%$) since the only pore spaces are the tiny, long, thin cracks between the individual mineral grains. Sandstones, typically, have much higher porosities (10-35%) because the individual sand or mineral grains do not fit together closely, allowing larger pore spaces. Moreover, following the works in [8, 32] etc., the choice of porosity for our numerical calculation can be considered suitable.

- The choice of elastic parameter values is also justified here. Physically, the flexural rigidity has a very high value. From Yamamoto [115] and Lee and Lan [52], we find that, for a fine elastic sand bottom, we can take $\nu = 0.33$, $\rho_2 = 1024$ kg m^{-3}, $\rho_p/\rho_2 \approx 2.7$. Following that, we consider the bottom flexural rigidity as 47×10^9 N m^2 for numerical computation as considered by Mohapatra and Sahoo [76], Mohapatra and Soares [77], Das et al. [31].

The above considerations of justification of certain parameter values are spread across the seven works in the thesis; all of them do not necessarily appear in a single work. So, only some of the parameters may arise in connection with a specific work.

TH-2746_176123008

TH-2746_176123008

APPENDIX E

Practical validation of the caisson type breakwater upon elastic bottom model

It is important to visually justify the schematic model before the very crude mathematical model is solved. To physically test our schematic model in Chapters 4 and 5, we refer to some works as well as add legitimate reasoning.

- The primary aim of our proposed study is to develop an elastic bottom to replace the conventional flat and rigid bottom. A fluid base surface encases the lower surface in our work. When it comes to describing soil mechanics, there are primarily two kinds of methods (continuum approach and modelling approach). The soil medium is idealized by Winkler [111] as a series of equal but mutually distinct, closely spaced, isolated, linearly elastic springs. Based on this principle, we choose a thin elastic plate to represent the sea-bed. The plate's diameter is insignificant in relation to the wavelength of the normal incident waves propagating horizontally. As a result, structural slenderness is a reasonable expectation.

- The forced hydroelastic oscillations of a circular plate lying on an elastic base were studied by Kondratov and his colleagues [49]. To explain the soil-pile relationship in the ocean, Bayat et al. [4] suggested the Winkler theory in which the pile was modelled as beam components. Bee [5] used beam on elastic base buckling theory to investigate the effect of the seafloor on the buckling load of an undersea pipeline. To reflect the seafloor as a simplified elastic support, the Winkler foundation was selected. Due to the physical complexities inherent in soil dynamics, a more complex elastic base model is not warranted. Despite its simplicity, Hetenyi [41] claimed that the Winkler principle could much more reliably reflect the conditions in soil founda-

TH-2746_176123008

tions than more complicated models in which the structure is seen as a continuous isotropic elastic body. The thin elastic plate principle, which has been extensively considered for problems on wave-structure/ice-sheet interface problems, can be used for the elastic sea bottom by considering a significant length of the bottom.

- When deciding on the Euler-Bernoulli beam principle, the edge conditions are critical. The work on a crude model for sea-bed modelling may reflect the use of an arbitrary edge condition. For example, when a slab is lying on a beam and all building components behave independently, an unrestrained plate state can be considered. It is totally immobile due to the clamped end on one side. It maintains an orthogonal relationship with the boundary. The edges of the breakwater would be rigid as a scour protection is created on the bed to create the breakwater, ensuring the structure's stability. Wave reflection by a rigid wall in a channel of finite width and depth along with semi-infinite duration with elastic bed was studied by Mohapatra and Soares [77] and they used the free edge boundary state. When using clamped edge conditions, the modelling seems to be mechanically meaningful in our situation. The clamped edge elastic plate bottom with rigid side walls was used by Askari and Daneshmand [2] and Zhau and Cheung [125]. In the Pasternak foundation, Hasheminejad and Mohammadi [39] considered an elastic bottom plate with clamped edge action. The dynamic action of an elastic plate lying on a Winkler elastic base and in contact with fluid with certain boundary conditions was studied by Ali et al. [1]. Clamped edge situations can be mechanically feasible when point loads can be modelled at the end of operation.

- Only the thin bottom surface has been included in this study; the underneath thick section has been left out. Apart from the above evidence, this form of elastic model adoption is prevalent in soil mechanics and ocean wave propagation. An abyssal plain is an underwater plain on the deep ocean floor that is the flattest, smoothest, and least visited regions on the Earth, if we consider the seafloor structure carefully. Abyssal plains are important geologic features of oceanic basins, and no matter how large they are, we can only perceive the sea-beds as the bottom zone in terms of ocean engineering. Huge floating oil storage vessels, boats, and aircraft, for example, can resist localized vibrations, and large-capacity oil containers in the petrochemical industry can survive earthquakes, thanks to the free vibration properties of the fluid-structure relationship. For a homogeneous fluid, Mohapatra and Sahoo [76] and Mohapatra and Soares [77] came to the same conclusion. Several attempts have been made to study the elastic ocean-bed or ice-covered seafloor in a two-layer fluid by Saha and Bora [89], Chanda and Bora [16, 17]. Recently, Khuntia and Mohapatra [48], Mohapatra [74], Das and Mohapatra [29, 30], Sarangi and Mohapatra [92], Sarkar et al. [94] and others have worked on wave interaction issues

TH-2746_176123008

based on similar bottom characteristics.

- When investigating the impact of porous breakwater on wave interaction, our primary focus is on a crude porous model lying on the base. If the base is subjected to a partly spread surface loading, the springs would not be disturbed outside the loaded field, according to the Winkler idealisation. Given this, constructing a porous system that extends past the filled plate would have little effect on the sea-floor. When we look at the construction of different marine structures, such as traditional rubble mound breakwaters, caisson style on rock foundations, vertical breakwaters, and so on, we can see that the base is often designed to be rigid. By obstructing the movement of sand ions, the foundation configuration prevents erosion of the ground and sea-bed. On the sea-bed, a rigid rock foundation, namely, a caisson foundation can be usually observed. Bridges, piers, dams, and other buildings that require underwater protection often use caisson foundations. The construction loads are carried by the caisson foundations at their lower ends. Vertical breakwaters, for example, have a thin stone bedding structure, while vertical composite breakwaters have a high rubble foundation. To prevent erosion, the stone armor between the breakwater base and bed is often solid. Scour defence must be established before making the choice of any breakwater. Constructing toe defence in concrete filled jute bags has been observed in practice. A sheet of loose or silty sand or mud may also be seen on top of a strong hard bottom. Assuming this, we consider porous regions to have an impermeable bottom, and the elastic bottom effect is limited to the plain water regions only.

As a result, when studying the ocean bottom surface only, we can use the Euler-Bernoulli beam equation to model the elastic base surface as a thin elastic plate lying on such a Winkler basis and scientifically acceptable and justified edge conditions.

It may be noted that the above validation of the physical model pertains to the ones appearing in Chapters 4 and 5. A similar validation for other physical models can also be caried out.

TH-2746_176123008

TH-2746_176123008

APPENDIX F

Matrix form of system of equations

Given the system of equations given by (5.37) in compact form $\mathbb{A}X = \mathbb{B}$ with X already defined. The explicit forms of the matrices $\mathbb{A}$ and $\mathbb{B}$ can be written as follows:

$$\mathbb{A} = \Big[\mathbb{M}_{m,n}\Big]_{(2pN+4p+2)\times(2pN+4p+2)}$$

such that

$$\left.\begin{aligned} &\mathbb{M}_{m,n} = q_{1,n}\hat{b}^2_{n,m}, \mathbb{M}_{N+2+m,n} = (q_{1,n} + k_{1,1}G)b^2_{n,m}, \\ &\mathbb{M}_{2p(N+2)+1,n} = q_{1,n}k_{1,n},\ \mathbb{M}_{2p(N+2)+2,n} = k_{1,n}, \end{aligned}\right\} \begin{aligned} &\text{for} \quad m = 1,\ldots,N+2, \\ &\qquad\ n = I, II, 1,\ldots,N+2, \end{aligned}$$

$$\left.\begin{aligned} &\mathbb{M}_{m,N+4+m} = -e^{\mathrm{i}q_{2,m}l_1}\mathbb{M}_{m,2N+6+m} = \epsilon_2 q_{2,m}a^2_m, \\ &\mathbb{M}_{N+2+m,N+4+m} = e^{\mathrm{i}q_{2,m}l_1}\mathbb{M}_{N+2+m,2N+6+m} = -k_{1,1}G\gamma_2 a^2_m, \end{aligned}\right\} \text{for } m = 1,\ldots,N+2,$$

$$\underbrace{\begin{aligned} &e^{\mathrm{i}q_{j,n}l_{j-1}}\mathbb{M}_{j(N+2)+m,(j-1)(N+2)+n+2} = \mathbb{M}_{j(N+2)+m,j(N+2)+n+2} = \epsilon_j b^{j+1}_{n,m}, \\ &\mathbb{M}_{j(N+2)+m,(j+1)(N+2)+m+2} = -e^{\mathrm{i}q_{j+1,m}l_j}\mathbb{M}_{j(N+2)+m,(j+2)(N+2)+m+2} = -\epsilon_{j+1}q_{j+1}a^{j+1}_m e^{\mathrm{i}q_{j,n}l_{j-1}}, \\ &\mathbb{M}_{(p-2+j)(N+2)+m,(j-1)(N+2)+n+2} = \mathbb{M}_{(p-2+j)(N+2)+m,j(N+2)+n+2} = \gamma_j b^{j+1}_{n,m}, \\ &\mathbb{M}_{(p-2+j)(N+2)+m,(j+1)(N+2)+m+2} = e^{\mathrm{i}q_{j+1,m}l_j}\mathbb{M}_{(p-2+j)(N+2)+m,(j+2)(N+2)+m+2} = -\gamma_{j+1}a^{j+1}_m, \end{aligned}}_{\text{for } j=2,3,\ldots,p-1,\ m,n=1,\ldots,N+2,}$$

$$\underbrace{\begin{aligned} &e^{\mathrm{i}q_{p,n}l_{p-1}}\mathbb{M}_{(2p-2)(N+2)+m,(p-2)(N+2)+(N+4)+n} = \mathbb{M}_{(2p-2)(N+2)+m,(p-1)(N+2)+N+4+n} = \epsilon_p b^{p+1}_{n,m}, \\ &\mathbb{M}_{(2p-1)(N+2)+m,(p-2)(N+2)+N+4+n} = \mathbb{M}_{(2p-1)(N+2)+m,(p-1)(N+2)+N+4+n} = \gamma_p b^{p+1}_{n,m}, \\ &\mathbb{M}_{(2p-2)(N+2)+m,p(N+2)+(N+4)+m} = \mathrm{i}\epsilon_{p+1}\sin(q_{p+1,m}l_p)a^{p+1}_m, \\ &\mathbb{M}_{(2p-1)(N+2)+m,p(N+2)+N+4+m} = -\gamma_{p+1}\cos(q_{p+1,m}l_p)a^{p+1}_m, \end{aligned}}_{m,n=1,\ldots,N+2.}$$

TH-2746_176123008

and

$$\mathbb{B} = \left[\hat{B}_m\right]_{2pN+4p+2}$$

such that

$$\left.\begin{array}{l} \hat{B}_m = \sum_{n=1}^{2} q_{1,n}\hat{b}_{n,m}^2,\ \hat{B}_{N+2+m} = \sum_{n=1}^{2}(q_{1,n} - k_{1,1}G)b_{n,m}^2, \\ \hat{B}_{2p(N+2)+1} = \sum_{n=1}^{2} q_{1,n}k_{1,n},\ \hat{B}_{2p(N+2)+2} = -\sum_{n=1}^{2} k_{1,n}, \end{array}\right\} \text{for } m = 1, 2, \ldots, N+2.$$

Status of manuscripts out of the thesis

A. Published:

1. K. K. Barman and S. N. Bora, "Linear water wave interaction with a composite porous structure in a two-layer fluid flowing over a step-like sea-bed", Published in Geophysical and Astrophysical Fluid Dynamics (Taylor & Francis), 115(5-6), 577-611, 2021, doi: 10.1080/03091929.2020.1842391.

2. K. K. Barman and S. N. Bora, "Scattering and trapping of water waves by a composite breakwater placed on an elevated bottom in a two-layer fluid flowing over a porous sea-bed", Published in Applied Ocean Research (Elsevier), 113, 102544, 2021, doi:10.1016/j.apor.2021.102544. (18 pages)

3. K. K. Barman and S. N. Bora, "Interaction of oblique water waves with a single chamber caisson type breakwater for a two-layer fluid flow over an elastic bottom", Published in Ocean Engineering (Elsevier), 238, 109766, 2021, doi:10.1016/j.oceaneng.2021.109766. (18 pages)

4. K. K. Barman and S. N. Bora, "Elastic bottom effects on ocean water wave scattering by a composite caisson-type breakwater placed upon a rock foundation in a two-layer fluid", Published in International Journal of Applied Mechanics (World Scientific), 13(10), 2150114, doi:10.1142/S1758825121501143. (33 pages)

5. K. K. Barman and S. N. Bora, "Analysis of wave reflection, waveload and pressure distribution due to a poro-elastic structure in a two-layer fluid over a

TH-2746_176123008

porous sea-bed", Published in Journal of Ocean Engineering and Marine Energy (Springer Nature), doi:10.1007/s40722-022-00235-0.

B. Revised version submitted:

1. K. K. Barman and S. N. Bora, "Water wave scattering and radiation due to a porous barrier in a two-layer fluid over a permeable sea-bed", Journal of Engineering Mechanics (ASCE).

C. Communicated:

1. K. K. Barman and S. N. Bora, "Mitigation of wave-energy due to presence of a porous breakwater in front of a floating elastic plate in a two-layer fluid", European Journal of Mechanics - B/Fluids (Elsevier).

TH-2746_176123008

TH-2746_176123008